

Multi-Objective Optimization of Stochastic Engine Models

Von der Fakultät für Maschinenbau, Elektro- und Energiesysteme
der Brandenburgischen Technischen Universität Cottbus - Senftenberg
zur Erlangung des akademischen Grades eines
Doktors der Ingenieurwissenschaften
genehmigte Dissertation

vorgelegt von

Master of Science
Tim Franken
geboren am 23. Oktober 1987 in Engelskirchen

Vorsitzender: Prof. Dr.-Ing. Peter Berg
Gutachter: Prof. Dr.-Ing. Fabian Mauß
Gutachter: Univ.-Prof. Dr.-Ing. Jakob Andert
Tag der mündlichen Prüfung: 20.12.2023

"I have a truly marvelous demonstration of this proposition that this margin is too narrow to contain."

Pierre de Fermat

Contents

1	Abstract	6
2	Nomenclature	7
3	Introduction	17
3.1	Publications related to this PhD thesis	17
3.2	Objectives of the thesis	19
3.3	Outline of the thesis	20
4	Stochastic Reactor Models for compression ignition and spark ignition engines	21
4.1	The mass density function	21
4.2	Modeling of general phenomena in internal combustion engines	22
4.2.1	Convective heat transfer coefficient	22
4.2.2	Stochastic heat transfer algorithm	25
4.2.3	Direct injection and vaporization	29
4.2.4	Gas exchange through valves	32
4.2.5	Particle mixing	33
4.2.6	Chemical reaction	35
4.3	Modeling of spark ignition engine	36
4.3.1	$k - \epsilon$ turbulence model	36
4.3.2	Turbulent flame propagation	45
4.3.3	Stochastic combustion model	54
4.3.4	Crevice model	56
4.3.5	Cyclic variation model	59
4.4	Modeling of compression ignition engine	62
4.4.1	$k - \epsilon$ turbulence model	62
4.5	Numerical solution method	72
4.5.1	Explicit Runge-Kutta Solver	72
4.5.2	Operator split method	73
4.6	Conclusions for stochastic reactor models	74
5	The Multi-Objective Optimization Platform	76
5.1	General idea of optimization	76
5.2	Error calculation	78
5.3	Space filling algorithms	79
5.4	Response surface models	80
5.5	Multi-criteria decision making	82
5.6	Optimization algorithms	83
5.7	Conclusions for multi-objective optimization	93

6	Optimization of a spark ignition engine model	95
6.1	Engine specifications	95
6.2	Physical properties of gasoline fuel	96
6.3	Operating conditions	97
6.4	Chemistry model	100
6.5	Optimization sensitivity study	101
6.6	Final validation	108
6.7	Verification with 3D CFD	117
6.8	Conclusions for spark ignition engine model optimization	126
7	Optimization of a compression ignition engine model	128
7.1	Engine specifications	128
7.2	Physical properties of diesel fuel	128
7.3	Operating conditions	129
7.4	Chemistry model	131
7.5	Optimization sensitivity study	132
7.6	Final validation	138
7.7	Conclusions for compression ignition engine model optimization	146
8	Conclusions and Outlook	148
9	Appendix	151
9.1	Thermodynamic polynomials	151
9.2	Cylinder wall temperature correlation function	151
9.3	Start of vaporization correction function	152
9.4	Early flame propagation correlation function	152
9.5	Piston speed	153
9.6	Tumble ratio	154
9.7	Swirl ratio	154
9.8	Uniformity measure	154
9.9	3D CFD simulation setup	155
9.10	Liquid thermophysical properties	156
	References	162

1 Abstract

This thesis summarizes the author's developments of combustion models and multi-objective optimization methods for gasoline and diesel engines. The combustion models belong to the family of zero-dimensional stochastic reactor models introduced in the 1990s to improve the prediction of emissions with detailed chemistry in partially stirred reactors.

The first part introduces the fundamentals of the physical and chemical models describing the combustion process. As a novelty, $k - \epsilon$ turbulence models were implemented in the stochastic reactor model to predict the turbulent time and length scales in gasoline and diesel engines. This development allowed an improvement of the models for convective heat transfer, fuel evaporation, gas exchange across the valves, turbulent flame propagation and crevice flow, which depend on the turbulent time and length scales.

In the second part, the multi-objective optimization platform for automatic training of the stochastic reactor model is presented. The optimization method considers multiple operating points to find a set of model parameters that predict performance and emissions over the entire engine map. The Non-domination Sorting Genetic Algorithm II is combined with the stochastic reactor model and response surface models to find the best Pareto front. Multi-criteria decision making is used to select the best designs from the Pareto front.

Finally, the third part of this thesis deals with the validation of the stochastic reactor model and the multi-objective optimization platform. For this purpose, experiments of two single-cylinder research engines with spark ignition, one passenger car engine with compression ignition and one heavy duty engine with compression ignition are used. For the spark ignition engines, a set of model parameters was found that predicts well the power and emissions over the whole engine map. The calculated turbulent kinetic energy, dissipation, and angular momentum follow the trends of the three-dimensional computational fluid dynamic simulations to a good approximation for various operating points. For the two compression ignition engines, the prediction of combustion progress and nitrogen oxide emissions are in good agreement with the experiments. Larger discrepancies were found for the prediction of carbon monoxide and unburned hydrocarbon. Optimization of the soot model parameters improves the prediction of soot mass for operating points throughout the engine map.

Keywords: Stochastic Reactor Model, Multi-Objective Optimization, Turbulence Modelling, Emissions, Internal Combustion Engine

2 Nomenclature

Latin symbols

Parameter	Unit	Description
A	m^2	Area
A	m^2	Cross-sectional area
a_4	—	Peters turbulent flame propagation model parameter ($a_4=0.78$)
A_i	—	Molecular mixing source term
a_{in}	—	Intake flow parameter ($a_{in}=20$)
$A^{(n)}$	—	Thermodynamic polynomial
A_R	m^2	Flow reference area
A_T	m^2	Turbulent flame surface area
b_1	—	Peters turbulent flame propagation model parameter ($b_1=2.0$)
b_3	—	Peters turbulent flame propagation model parameter ($b_3=1.0$)
b_{in}	—	Intake flow parameter ($b_{in}=0.2$)
B_v	—	Function of edge weight $B_v=2 \cdot w_v$
C	—	Simple turbulent flame propagation model parameter ($C=2.5$)
c_1	—	Peters turbulent flame propagation model parameter
c_2	—	Peters turbulent flame propagation model parameter
c_3	—	Peters turbulent flame propagation model parameter
C_{axial}	—	Axial flow parameter ($C_{axial}=0.2$)
C_{Blint}	—	Flame thickness model parameter ($C_{Blint}=2.0$)
C_d	—	Discharge coefficient
$C_{friction}$	—	Friction force parameter ($C_{friction}=1.5$)
C_h	—	Stochastic heat transfer coefficient ($C_h=1$)
C_{inj}	—	Direct injection parameter ($C_{inj}=0$)
$C_{kin,sq}$	—	Scaling parameter for kinetic energy of squish flow ($C_{kin,sq}=0.3$)
C_m	—	Kolla turbulent flame propagation model parameter ($C_m=0.7$)
c_m	m/s	Mean piston velocity
c_p	J/kgK	Contant pressure heat capacity

c_{pis}	m/s	Instantaneous piston velocity
c_v	J/kgK	Constant volume heat capacity
C_ε	—	Dissipation parameter ($C_\varepsilon=1.0$)
C_{ε_1}	—	Turbulent length scale parameter ($C_{\varepsilon_1}=7.0$)
C_{ε_2}	—	Turbulent length scale parameter ($C_{\varepsilon_2}=3.0$)
C_μ	—	$k - \varepsilon$ model parameter ($C_\mu=0.09$)
C_ϕ	—	Scalar mixing time parameter ($C_\phi=1.0$)
$C_{\phi,u}$	—	Scalar mixing time parameter of unburnt zone ($C_{\phi,u}=1.0$)
$C_{\phi,b}$	—	Scalar mixing time parameter of burnt zone ($C_{\phi,b}=1.0$)
$C_{\tau,k,inflow}$	—	Inflow time scale parameter ($C_{\tau,k,inflow}=0.019$)
$C_{\tau,m}$	—	Squish flow time scale parameter ($C_{\tau,m}=0.5$)
D	m^2/s	Molecular diffusivity
D_t	m^2/s	Turbulent diffusivity
Da	—	Damköhler number
d_B	m	Cylinder bore diameter
d_{bowl}	m	Piston bowl diameter
d_{EV}	m	Exhaust valve diameter
d_{IV}	m	Intake valve diameter
e_{bowl}	m^2/s^2	Kinetic energy of secondary flow in piston bowl
$E_{kin,in}$	m^2/s^2	Kinetic energy of inflow
$E_{kin,out}$	m^2/s^2	Kinetic energy of outflow
$e_{kin,axial}$	m^2/s^2	Kinetic energy of axial flow
$e_{kin,sec}$	m^2/s^2	Kinetic energy of secondary flow
$e_{kin,sq}$	m^2/s^2	Kinetic energy of squish flow
\mathcal{F}	—	Cumulative distribution function
f	—	Probability density function
\vec{f}	—	Optimization objective functions
$f_{in,k}$	—	Kinetic energy conversion parameter of inflow
$f_{T,spin-up}$	—	Tumble spin-up model parameter ($f_{T,spin-up}=1.0$)
g_j	—	Optimization constraints
G_i	—	Chemical reaction source term
h	K	Temperature fluctuation
h_{bowl}	m	Bowl depth
H_1	m	Instantaneous distance between piston and cylinder head
$h_{f,l}$	J/kg	Specific liquid fuel enthalpy

$h_{f,s}$	J/kg	Specific fuel enthalpy at saturation temperature
H_g	J	Gas enthalpy
$H_{(n)}$	J	Enthalpy of notional particle
$h_{(n)}$	J/kg	Specific enthalpy of notional particle
$h_{(n),g}$	J/kg	Specific enthalpy at gas temperature
$h_{(n),s}$	J/kg	Specific enthalpy at saturation temperature
H_v	J	Vaporization enthalpy
h_s	m	Instantaneous piston stroke
h_v	J/kg	Specific vaporization enthalpy
J_S	kgm^2	Moment of inertia of swirl flow
J_T	kgm^2	Moment of inertia of tumble flow
k	m^2/s^2	Turbulent kinetic energy
k	–	Early flame propagation model parameter (k=5)
$k_{max,crev}$	m^2/s^2	Maximum limit of turbulent kinetic energy of crevice model
$k_{min,crev}$	m^2/s^2	Minimum limit of turbulent kinetic energy of crevice model
Ka	–	Karlovitz number
Ka_δ	–	Karlovitz number at the Kolmogorov scale
L	m	Characteristic length scale
l	m	Turbulent length scale
l_{bowl}	m	Characteristic bowl length scale
$l_{cyl,1}$	m	Characteristic cylinder length scale
L_{EV}	m	Characteristic length scale of exhaust valve flow
l_{EV}	m	Instantaneous lift of exhaust valve
l_G	m	Gibson length scale
l_I	m	Integral length scale
l_{IV}	m	Instantaneous lift of intake valve
L_{IV}	m	Characteristic length scale of intake valve flow
l_{rod}	m	Connecting rod length
L_S	kgm^2/s	Angular momentum of swirl flow
l_{sq}	m	Characteristic length scale of squish flow
L_T	kgm^2/s	Angular momentum of tumble flow
$l_{turb,avg}$	m	Turbulent length scale of inflow
$l_{turb,sq}$	m	Turbulent length scale of squish flow
$l_{turb,vol}$	m	Turbulent length scale of system volume
$l_{turb,IV}$	m	Turbulent length scale of inflow through intake valves

$l_{turb,EV}$	m	Turbulent length scale of inflow through exhaust valves
l_{vol}	m	Turbulent length scale of system volume
M	g/mol	Molar weight
m	kg	Mass
m_g	kg	Gaseous mass
\dot{m}_{air}	kg/s	Air mass flow
\dot{m}_f	kg/s	Fuel mass flow
$\dot{m}_{g,in}$	kg/s	Massflow into the cylinder
$\dot{m}_{g,out}$	kg/s	Massflow out of the cylinder
$\dot{m}_{back,sq}$	kg/s	Squish back flow
m_{inflow}	kg	Accumulated mass of inflow
$m_{inflow,IV}$	kg	Accumulated mass of inflow through intake valves
$m_{inflow,EV}$	kg	Accumulated mass of inflow through exhaust valves
\dot{m}_{IV}	kg/s	Massflow through intake valves
m_v	kg	Vapor mass
m_{vol}	kg	System volume mass
$m^{(n)}$	kg	Notional particle mass
m_{sq}	kg	Squish volume mass
N	—	Number of iterations
n	rpm	Engine speed
n	—	Simple turbulent flame propagation model exponent ($n=0.9$)
N_C	—	Number of stochastic cycles
N_{crev}	—	Number of notional particles in the crevice zone
N_{EV}	—	Number of exhaust valves
N_{hot}	—	Number of iterations in the hot phase
N_{iter}	—	Number of iterations in the stochastic vaporization model
N_{IV}	—	Number of intake valves
N_P	—	Number of notional particles
$N_{P,in}$	—	Number of notional particles of the intake flow
n_S	$1/s$	Swirl flow rotation speed
n_T	$1/s$	Tumble flow rotation speed
N_T	—	Number of notional particles in the mixing state
$N_{P,t+\Delta t}$	—	Number of notional particles of the next time step

Nu	–	Nusselt number
$P_{k,in}$	$m^2/s^2/s$	Turbulent kinetic energy production term of inflow
p	Pa, bar	Pressure
p_s	Pa	Saturation pressure
$Q_{i,ht}$	W	Convective heat transfer
Pr	–	Prandtl number
Re	–	Reynolds number
\vec{R}	–	Linear rank value
R^2	–	Correlation coefficient
r_f	m	Flame radius
$r_{in,IV}$	m	Characteristic length scale of intake valve flow
$r_{in,EV}$	m	Characteristic length scale of exhaust valve flow
\bar{R}_{gas}	J/molK	Universal gas constant (8.314 J/molK)
RN	–	Random number
RN_{res}	–	Residual random number
S	J/K	Entropy
s_L	m/s	Laminar flame speed
s_T	m/s	Turbulent flame speed
S_{Tipp}	–	Tippelmann swirl number
ΔSOV	°CA	Shift of start of vaporization
t	s	Time
T_{ad}	K	Adiabatic flame temperature
T_g	K	Gas temperature
t_{jump}	s	Time jump parameter
$T^{(n)}$	K	Temperature of notional particle
T_l	K	Liquid temperature
T_{oil}	K	Oil temperature
T_s	K	Saturation temperature
t_{sub}	s	Sub time step
T_{Tipp}	–	Tippelmann tumble number
T_u	K	Unburnt gas temperature
T_w, T_{wall}	K	Wall temperature
ΔT	K	Temperature difference
Δt	s	Time step size
U	K/s	Convective heat transfer source term
UD	–	Uniformity measure
U^*	m/s	Local tangential velocity
u_{axial}	m/s	Axial flow velocity
u_{cc}	m/s	Combustion velocity

$u_{sq,axial}$	m/s	Axial squish flow velocity
$u_{sq,radial}$	m/s	Radial squish flow velocity
u'	m/s	Turbulence fluctuation of velocity
u_η	m/s	Kolmogorov velocity
V	m^3	Volume
v	m/s	Velocity
V_{bowl}	m^3	Bowl volume
v_{IV}	m/s	Velocity of flow through intake valves
w_j	—	Weight of optimization errors
$W_{(n)}$	—	Notional particle weight
$W_{(p)}$	—	Weight of notional particle (p)
$W_{(q)}$	—	Weight of notional particle (q)
w_{mod}	m/s	Heat transfer velocity term
w_v	—	Edge weight
\vec{x}	—	Optimization parameters
$Y_{(n)}$	—	Mass fraction of notional particle
Z	—	Mixture fraction

Greek symbols

Parameter	Unit	Description
α	W/m^2K	Heat transfer coefficient
α	—	Rate of variance decay of scalars
α_{inflow}	—	Inflow time scale exponent ($\alpha_{inflow}=-2/3$)
α_{th}	m^2/s	Thermal diffusivity
$\alpha_{tke,crev}$	—	Scaling parameter of crevice model
β	—	Geometry parameter in the local tumble turbulent kinetic energy production term
β'	—	Kolla turbulent flame propagation model parameter ($\beta'=6.7$)
γ	—	Polytropic coefficient
Δ_{mod}	—	Heat transfer combustion term
δ	—	Kronecker delta
δ	—	Dimensionless length scale of the inner layer
δ_i	m	Inner layer length scale
δ_L	m	Thermal flame thickness
$\delta_{L,t}$	m	Flame brush thickness
ε	m^2/s^3	Dissipation
ε	—	Optimization error
ε_{CR}	—	Compression ratio

η, μ	$Pa \cdot s$	Dynamic viscosity
η	m	Kolmogorov length scale
η_0	m	Transition length scale
η_c	m	Early flame propagation model parameter ($\eta_c=0.003$)
θ	$^{\circ}CA$	Crank angle
θ_{SOI}	$^{\circ}CA$	Start of injection
θ_{ST}	$^{\circ}CA$	Spark timing
κ	—	Flame front curvature
λ	W/mK	Thermal conductivity
λ	—	Relative air-fuel ratio
ν_t	m^2/s	Turbulent viscosity
ρ	kg/m^3	Density
ρ_f	kg/m^3	Density of fuel
ρ_u	kg/m^3	Unburnt gas density
σ	—	Flame surface area ratio
$\sigma_{\theta_{ST}}$	$^{\circ}CA$	Standard deviation of spark timing
$\sigma_{u'}$	m/s	Standard deviation of turbulence fluctuation
$\bar{\sigma}_t$	—	Turbulent part of flame surface area ratio
τ	s	Time scale
τ	—	Ratio of burnt and unburnt temperature
τ_{axial}	s	Axial flow time scale
τ_c	s	Chemical time scale
$\tau_{inflow,k}$	s	Time scale of inflow
$\tau_{m,sq}$	s	Time scale of squish flow
τ_{ϕ}	s	Scalar mixing time
$\tau_{\phi,u}$	s	Scalar mixing time of unburnt zone
$\tau_{\phi,b}$	s	Scalar mixing time of burnt zone
ϕ	—	Scalar
$\langle \phi \rangle$	—	Mean of scalar
$\langle \phi'^2 \rangle$	—	Variance of scalar
ψ	—	Sample variable
$\dot{\omega}$	mol/s	Reaction rate

Index

Index	Description
0	Initial state
0	Inner layer state
<i>axial</i>	Axial flow

<i>compressibility</i>	Compressibility
CR	Compression ratio
<i>crev</i>	Crevice
<i>cylinder</i>	Cylinder
<i>cyl</i>	Cylinder
<i>eff</i>	Effective
EV	Exhaust valve
<i>f</i>	Fuel
<i>friction</i>	Friction force
<i>geom</i>	Geometry
<i>in</i>	Inflow
<i>inflow</i>	Inflow
<i>init</i>	Initial
<i>inj</i>	Injection
<i>injection</i>	Injection
<i>iter</i>	Iteration
IV	Intake valve
<i>local tumble</i>	Local tumble flow
<i>manifold</i>	Intake and exhaust manifold
<i>max</i>	Maximum
<i>min</i>	Minimum
<i>mot</i>	Motored
(<i>n</i>)	Notional particle
OxO ₂	Oxidation by O ₂
OxOH	Oxidation by OH
PI	Particle inception
<i>pilot1</i>	First pilot injection close to main injection
<i>pilot2</i>	Second pilot injection close to first pilot injection
<i>prop</i>	Flame propagation
<i>ref</i>	Reference
<i>rpm</i>	rotation per minute
S	Swirl
<i>s</i>	Species
<i>shear</i>	Shear force
<i>sim</i>	Simulation
<i>spin – up</i>	Tumble spin-up
<i>squish</i>	Squish flow
<i>swirl</i>	Swirl flow
T	Tumble
TDC	Top dead center
<i>therm</i>	Thermodynamic

Tipp
tumble

Tippelmann
Tumble flow

Abbreviations

Abbreviation	Description
0D	Zero-dimensional
1D	One-dimensional
3D	Three-dimensional
C	Carbon atom
CA	Crank angle
CFD	Computational fluid dynamics
CI	Compression ignition
CN	Cetane number
CO	Carbon monoxide
CO ₂	Carbon dioxide
DI	Direct injection
DNS	Direct numerical simulation
EAF	Empirical attainment function
EGR	Exhaust gas recirculation
EMST	Euclidean minimum spanning tree
ETRF	Ethanol toluene reference fuel
EVO	Exhaust valve opening
FAST	RSM-based multi-objective optimization
fsSoot	Fuel specific soot mass
H	Hydrogen atom
HC	Hydrocarbon
HCCI	Homogeneously charged compression ignition
HRR	Heat release rate
ID	Identification number
ICE	Internal combustion engine
IMEP	Indicated mean effective pressure
ISF	Incremental space filler
IVC	Intake valve closure
KPP	Kolmogorov-Petrovsky-Piskunov
LHV	Lower heating value
LTC	Laminar-to-turbulent conversion
MCDM	Multi-criteria decision maker
mdf	Mass density function
MOGA	Multi-objective genetic algorithm

MON	Motored octane number
MOO	Multi-objective optimization
MOPSO	Multi-objective particle swarm optimization
MOSA	Multi-objective simulated annealing
NO	Nitrogen monoxide
NO _x	Nitrogen oxide
NLT	No laminar-to-turbulent conversion
NSGA	Non-dominated sorting genetic algorithm
O	Oxygen atom
O ₂	Oxygen
OH	Hydroxyl radical
OP	Operating point
PAH	Polycyclic aromatic hydrocarbons
PaSR	Partially stirred reactor
PCP	Peak cylinder pressure
PCPCA	Peak cylinder pressure crank angle
pdf	Probability density function
RANS	Reynolds Averaged Navier Stokes
RBF	Radial basis function
RMSE	Root mean squared error
RON	Research octane number
RSM	Response surface model
SA	Simulated annealing
SI	Spark ignition
SOI	Start of injection
SOV	Start of vaporization
SRM	Stochastic Reactor Model
SVD	Singular value decomposition
TRF	Toluene reference fuel
ULHC	Uniform Latin Hypercube
var	Variable
ZMP	Zone mass proportion

3 Introduction

This thesis summarizes the author's developments in numerical engine models and multi-objective optimization methods for spark ignition and compression ignition engines. The numerical engine model belongs to the family of zero-dimensional (0D) stochastic reactor models (SRMs) developed in the 1990s to improve emission prediction with detailed chemistry for partially stirred reactors. Some of the results presented here have already been presented in international journals, research project reports, and at national and international conferences. The scientific papers, books, and dissertations with the most impact on this work have been published by Deb et al. [1, 2], Peters [3], Bhave et al. [4], Kozůch [5], Su [6], De Bellis et al. [7, 8], Dulbecco et al. [9], Bossung [10], Yang [11] and Bozza et al. [12]. Some of the models described in this thesis were developed by colleagues and have already been published in other forms. Their developments will be acknowledged here:

- "Stochastic heat transfer algorithm", Bhave et al. [4]
- "Direct injection and vaporization", Samuelsson [13] and Tunér [14]
- "Gas exchange through valves", Pasternak [15]
- "Curl particle mixing model", Tunér [14]
- "Euclidean minimum spanning tree mixing model", Matrisciano [16]
- "Kolla turbulent flame propagation model", Bjerkborn et al. [17, 18]
- "Cyclic variation model", Netzer et al. [19]
- "Tabulated chemistry model", Matrisciano [16]

3.1 Publications related to this PhD thesis

At the time of submitting the PhD thesis I published several works in the field of combustion modeling and multi-objective optimization. While this thesis is written as autonomous monography the work is related to previous publications. The models presented herein are based on the work of Franken et al. (2017) [20], Matrisciano et al. (2017) [21], Franken et al. (2020) [22], Matrisciano et al. (2020) [23] and Franken et al. (2020) [24]. All publications which are (co-)authored by myself are treated as any other publication.

Publications in reviewed journals and proceedings:

1. Netzer, C., Franken, T., Mauss, F., Seidel, L., Lehtiniemi, H., and Kulzer, A. C. (2018). Numerical analysis of the impact of water injection on combustion and thermodynamics in a gasoline engine using detailed chemistry. *SAE International Journal of Engines*, 11(6), 1151-1166.
2. Gern, M. S., Kauf, G. M., Vacca, A., Franken, T., and Kulzer, A. C. (2019). Ganzheitliche methode zur bewertung der wassereinspritzung im ottomotor. *MTZ-Motortechnische Zeitschrift*, 80(7), 124-129.

3. Franken, T., Netzer, C., Mauss, F., Pasternak, M., Seidel, L., Borg, A., Lehtiniemi, H., Matrisciano, A., and Kulzer, A. C. (2019). Multi-objective optimization of water injection in spark-ignition engines using the stochastic reactor model with tabulated chemistry. *International Journal of Engine Research*, 20(10), 1089-1100.
4. Franken, T., Mauss, F., Seidel, L., Gern, M. S., Kauf, M., Matrisciano, A., and Kulzer, A. C. (2020). Gasoline engine performance simulation of water injection and low-pressure exhaust gas recirculation using tabulated chemistry. *International Journal of Engine Research*, 21(10), 1857-1877.
5. Matrisciano, A., Franken, T., Gonzales Mestre, L. C., Borg, A., and Mauss, F. (2020). Development of a Computationally Efficient Tabulated Chemistry Solver for Internal Combustion Engine Optimization Using Stochastic Reactor Models. *Applied Sciences*, 10(24), 8979.
6. Franken, T., Klauer, C., Kienberg, M., Matrisciano, A., and Mauss, F. (2020). Prediction of thermal stratification in an engine-like geometry using a zero-dimensional stochastic reactor model. *International Journal of Engine Research*, 21(9), 1750-1763.
7. Franken, T., Seidel, L., Matrisciano, A., Mauss, F., Kulzer, A. C., and Schuerg, F. (2020). Analysis of the Water Addition Efficiency on Knock Suppression for Different Octane Ratings. *SAE Int. J. Adv. & Curr. Prac. in Mobility*, 2(5), 2531-2552.
8. Picerno, M., Lee, S. Y., Pasternak, M., Siddareddy, R., Franken, T., Mauss, F., and Andert, J. (2021). Real-Time Emission Prediction with Detailed Chemistry under Transient Conditions for Hardware-in-the-Loop Simulations. *Energies*, 15(1), 261.

Publications in conference proceedings with review (included in Scopus):

1. Franken, T., and Mauss, F. (2016). Development of methodology for predictive diesel combustion simulation using 0D stochastic reactor model. No. 2016-01-0566. SAE Technical Paper.
2. Franken, T., Sommerhoff, A., Willems, W., Matrisciano, A., Lehtiniemi, H., Borg, A., Netzer, C., and Mauss, F. (2017). Advanced predictive diesel combustion simulation using turbulence model and stochastic reactor model. No. 2017-01-0516. SAE Technical Paper.
3. Matrisciano, A., Franken, T., Perlman, C., Borg, A., Lehtiniemi, H., and Mauss, F. (2017). Development of a computationally efficient progress variable approach for a direct injection stochastic reactor model. No. 2017-01-0512. SAE Technical Paper.
4. Vacca, A., Bargende, M., Chiodi, M., Franken, T., Netzer, C., Gern, M. S., Kauf, M., and Kulzer, A. C. (2019). Analysis of water injection strategies to exploit the thermodynamic effects of water in gasoline engines by means of a 3D-CFD virtual test bench (No. 2019-24-0102). SAE Technical Paper.

5. Franken, T., Duggan, A., Matrisciano, A., Lehtiniemi, H., Borg, A., and Mauss, F. (2019). Multi-Objective Optimization of Fuel Consumption and NO_x Emissions with Reliability Analysis Using a Stochastic Reactor Model (No. 2019-01-1173). SAE Technical Paper.
6. Franken, T., Matrisciano, A., Sari, R., Robles, A. F., Monsalve-Serrano, J., Pintor, D. L., Pasternak, M., Garcia, A., and Mauss, F. (2021). Modeling of Reactivity Controlled Compression Ignition Combustion Using a Stochastic Reactor Model Coupled with Detailed Chemistry (No. 2021-24-0014). SAE Technical Paper.
7. Leon de Syniawa, L., Siddareddy, R., Oder, J., Franken, T., Guenther, V., Rottengruber, H., Mauss, F. (2023). Real-Time Simulation of CNG Engine and After-Treatment System Cold Start. Part 2: Tail-Pipe Emissions Prediction Using a Detailed Chemistry Based MOC Model (No. 2023-01-0364). SAE Technical Paper.
8. Siddareddy, R., Franken, T., Pasternak, M., Leon de Syniawa, L., Oder, J., Rottengruber, H., Mauss, F. (2023). Real-Time Simulation of CNG Engine and After-Treatment System Cold Start. Part 1: Transient Engine-Out Emission Prediction Using a Stochastic Reactor Model (No. 2023-01-0183). SAE Technical Paper.

3.2 Objectives of the thesis

The starting point of this work is the Stochastic Reactor Model (SRM) developed by Su [6] and Pasternak [15]. Their fundamental work paved the way for zero-dimensional (0D) simulations of non-premixed and premixed combustion using a probability density function (*pdf*) approach. In addition, the work of Matrisciano [16] in tabulated chemistry enabled the use of the SRM with multi-objective optimization methods on meaningful time scales.

From here, the question arose of how to train the SRM for the entire operation map to use it for engine operation extrapolation. This issue was already addressed by Pasternak et al [25] and the author [26]. However, a drawback of these approaches was the lack of physical basis of turbulent time and length scales in engines. This realization led to the definition of the **first objective of this thesis**, to implement a $k - \varepsilon$ turbulence model for spark ignition (SI) and compression ignition (CI) engines in order to calculate the turbulent time and length scales. The integration of a $k - \varepsilon$ turbulence model into SRM enabled the models for turbulent flame propagation, convective heat transfer, valve flow, direct injection, crevice flow, and molecular mixing to be linked across the turbulent time and length scales. Thus, the **second objective of this thesis** was to implement new physically based models and to extend existing models. This should make it possible to improve combustion and emission prediction for different operating points in the engine map.

The final obstacle was determining the model parameters of the SRM for the entire operation map of a given engine. Manual training requires the simultaneous input of a large number of values and an associated time-consuming iteration loop to approximate the experiments. If the investigated operating range was extended and the prediction worsened, the training has to be repeated which results in additional time consumption. This led to the definition of the **third objective of this thesis**, the development of a multi-objective optimization platform for

the automatic training of the model parameters of the SRM considering multiple operating points of the engine map.

3.3 Outline of the thesis

In addition to the introduction and the appendix, the thesis is divided into five main chapters. **Chapter 4** describes the fundamentals of SRM for engine simulation. The physics-based models for convective heat transfer, direct injection, vaporization, valve flow, molecular mixing, chemical reactions, turbulent flame propagation, crevice flow, and micro- and macro-scale flow in the cylinder are explained in detail. **Chapter 5** describes the multi-objective optimization platform, including optimization objective functions*, space filler algorithms, response surface models, multi-criteria decision making, and optimization algorithms. In **Chapter 6**, the performance of the multi-objective optimization platform for automatic model training of an SI research engine is investigated. The trained model parameters are validated using experimental data from a second SI research engine. Then, the $k - \varepsilon$ turbulence model results are verified using three-dimensional (3D) computational fluid dynamics (CFD) simulation results. In **Chapter 7**, the performance of the multi-objective optimization platform for model training of a CI passenger car engine is investigated. The trained model parameters are validated using experimental data from a second heavy-duty CI engine. **Chapter 8** summarizes the results and conclusions of this work and provides an outlook for future development work in the area of turbulence modeling, Runge-Kutta solvers, vaporization models, wall film models, crevice flow, spark ignition models, and turbulent flame propagation.

*In the text the optimization objective functions are also named errors.

4 Stochastic Reactor Models for compression ignition and spark ignition engines

The SRM is introduced to describe the partially mixing of molecules and its effect on reactive mixtures. Therefore, the mixture in a defined volume is discretized into a number of notional particles N_p each of which containing the information of species composition $y_{(n)}$ and enthalpy $H_{(n)}$. A particle mixing process is introduced which is depending on the mixing time scale τ_ϕ and describes the exchange frequency of information between the notional particles. With $\tau_\phi \rightarrow 0$ the mixture would be perfectly mixed, while with $\tau_\phi \rightarrow \infty$ the mixture stays segregated. The stochastic of the model is introduced by a Monte Carlo process which selects the notional particles that can mix with each other. Correa [27] and Correa and Braaten [28] introduced the partially stirred reactor model (PaSR) based on this theory to investigate the sensitivity of NO and CO formation towards turbulent stirring rates. Chen [29] extended the PaSR model by introducing the probability density function $\mathcal{F}_\phi(\psi, t)$ for multiple reactive scalars ϕ based on the joint scalar *pdf* from Pope [30]. Kraft [31] introduced two new models for the PaSR and partially stirred plug flow reactor (PaSPFR) and discussed new numerical solution methods for the SRM.

4.1 The mass density function

In the following years the SRM is introduced by several groups for internal combustion engine (ICE) applications. Tunér [14] published the SRM for different engine applications and performed a thorough analysis of the influence of number of notional particles, time step size, number of stochastic cycles and scalar mixing time on the numerical solution. Su [6] conducted a detailed analysis of SRM for homogeneously charged compression ignition (HCCI) engines and investigated new types of particle mixing, fuel vaporization and crevice flow models. Pasternak [15] investigated the SRM for diesel engine applications and developed a new method to describe the time dependent solution of the mixing time in engines.

The mass density function $\mathcal{F}_\phi(\psi, t)$ for variable density flows is introduced by Pope [30]. The mass density function (*mdf*) how it is formulated in this work is outlined in the following equation.

$$\begin{aligned}
\frac{\partial}{\partial t} \mathcal{F}_\phi(\psi, t) = & \underbrace{-\frac{1}{V} \frac{dV}{dt} \mathcal{F}_\phi(\psi, t)}_{\text{Piston Movement}} - \underbrace{\sum_{i=1}^{s+1} \frac{\partial}{\partial \psi_i} [G_i(\psi) \mathcal{F}_\phi(\psi, t)]}_{\text{Chemical Reaction}} - \underbrace{\frac{\partial}{\partial \psi_{s+1}} [U(\psi_{s+1}) \mathcal{F}_\phi(\psi, t)]}_{\text{Convective Heat Transfer}} \\
& + \underbrace{\sum_{i=1}^{s+1} \frac{\partial}{\partial \psi_i} [A_i(\psi) \mathcal{F}_\phi(\psi, t)]}_{\text{Mixing}} + \underbrace{\frac{\mathcal{F}_{\phi, in}(\psi, t) - \mathcal{F}_\phi(\psi, t)}{\tau_{in}}}_{\text{Gas Exchange}} + \underbrace{\frac{\mathcal{F}_{\phi, inj}(\psi, t)}{\tau_{inj}}}_{\text{Injection and Vaporization}} \\
& + \underbrace{\frac{\mathcal{F}_{\phi, crev}(\psi, t)}{\tau_{crev}}}_{\text{Crevice}} + \underbrace{\frac{\mathcal{F}_{\phi, prop}(\psi, t)}{\tau_{prop}}}_{\text{Flame Propagation}}
\end{aligned} \tag{4.1}$$

The individual terms of the *mdf* in equation (4.1) will be discussed in the following sections. Only the *piston movement* term won't be explained in detail because it simply describes the change of volume due to the reciprocal movement of the piston and a description can be found in [14].

The initial conditions in equation (4.2) and the boundary conditions have to be provided for the respective engine which is under investigation. They are required to be able to solve the *mdf*.

$$\mathcal{F}(\psi, 0) = \mathcal{F}_0(\psi) \tag{4.2}$$

4.2 Modeling of general phenomena in internal combustion engines

The subsection about *general phenomena* comprises the model description of fundamental physics and chemistry processes of non-premixed and premixed combustion in ICE. For simplicity the combustion chamber will be denoted as *system* in the subsequent sections. Beside the description of the physical and chemical phenomena, a detailed explanation of its implementation into the SRM framework is provided.

4.2.1 Convective heat transfer coefficient

The temperature change over time of the bulk gas is denoted as U in equation (4.1) and applies for the scalar ψ_{s+1}^* which is the temperature of the system. The unit of U is $\frac{K}{s}$. U is derived from the energy balance in equation (4.3) where the left hand side describes the change of energy of the bulk gas, and the right hand side describes the convective heat transfer. The negative sign of the right hand side is because convective heat transfer is commonly treated as a loss in the system.

$$U \cdot m \cdot c_p = -\alpha \cdot A \cdot (T_g - T_{wall}) \tag{4.3}$$

*s denotes the number of species of the reaction mechanism applied

Convective heat transfer is governed by the temperature difference between bulk gas T_g and temperature at the wall T_{wall} . The amount of heat transferred is also dependent of the system surface size A and the heat transfer coefficient α . As shown in equation (4.4) the heat transfer coefficient α can be determined based on the thermal conductivity λ of the gas and the characteristic length L of the system. The proportionality factor Nu is well known as the dimensionless Nusselt number.

$$\alpha = Nu \cdot \frac{\lambda}{L} \quad (4.4)$$

The Nusselt number Nu can be determined based on the ratio of inertial forces $v \cdot L^\dagger$ and viscous forces v^* described by the dimensionless Reynolds number Re and the ratio of the kinematic viscosity ν and thermal conductivity λ described as the dimensionless Prandtl number Pr .

$$Nu = C \cdot Re^m \cdot Pr^n \quad (4.5)$$

Introducing the definitions of Nu , Re and Pr in equation (4.5) one obtains equation (4.6), where the constant C and the exponents m and n have to be determined for the geometry under investigation.

$$\frac{\alpha \cdot L}{\lambda} = C \cdot \left(\frac{\rho \cdot v \cdot L}{\eta} \right)^m \cdot \left(\frac{\eta \cdot c_p}{\lambda} \right)^n \quad (4.6)$$

This equation was the starting point for Woschni [32], Hohenberg [33] and Heinle [34] to develop convective heat transfer models for 0D modeling applications. Based on extensive engine experiments Woschni correlated the characteristic length with the cylinder bore $L \sim d_B$, the density and viscosity with the cylinder pressure $\rho, \eta \sim p$ and the thermal conductivity and heat capacity with the cylinder temperature $\lambda, c_p \sim T$. The velocity is correlated with the mean piston velocity in axial direction and a pressure difference term induced by combustion $v \sim c_m \cdot (p - p_{mot})$ as shown in equation (4.7).

$$\alpha_{Woschni} = C \cdot d_B^{-0.2} \cdot p^{0.8} \cdot T^{-0.53} \cdot \left[C_1 \cdot c_m + C_2 \cdot \frac{V \cdot T_0}{p_0 \cdot V_0} \cdot (p - p_{mot}) \right]^{0.8} \quad (4.7)$$

Therein, V is the instantaneous cylinder volume, T_0 is the initial temperature, p_0 is the initial pressure and V_0 is the initial volume. The pressure difference term is calculated based on the instantaneous cylinder pressure p and the motored cylinder pressure p_{mot} . The constants C , C_1 and C_2 are adjustable and the default values are summarized in table 5.

Hohenberg proposed another heat transfer model in equation (4.8) where he correlated the characteristic length with the cylinder volume $L \sim V$ and introduced a constant C_2 for

[†] v denotes the velocity of the flow

^{*} ν denotes the kinematic viscosity of the gas

Parameter	Value
C	3.26
C_1	2.28
C_2	0.0035

Table 5: Woschni heat transfer model parameters.

the velocity due to combustion. The remaining terms of the equations are similar compared to the Woschni model.

$$\alpha_{Hohenberg} = C_1 \cdot V^{-0.06} \cdot p^{0.8} \cdot T^{-0.53} \cdot \left[T^{0.163} \cdot (c_m + C_2) \right]^{0.8} \quad (4.8)$$

The Hohenberg model parameters C_1 and C_2 are adjustable and the default values are outlined in table 6.

Parameter	Value
C_1	130
C_2	1.4

Table 6: Hohenberg heat transfer model parameters.

The Heinle heat transfer model in equation (4.9) is developed more recently and similarly to the Hohenberg model it correlates the characteristic length with the cylinder volume $L \sim V$. The exponents were adjusted to gain a better fit with the convective heat transfer in modern combustion engines.

$$\alpha_{Heinle} = C^* \cdot V^{-0.073} \cdot p^{0.78} \cdot T^{-0.477} \cdot w_{mod}^{0.78} \cdot \Delta_{mod} \quad (4.9)$$

The remaining terms will not be explained in detail at this point but can be found in [34] and [22]. Only the velocity term $w_{mod}^{-0.78}$ will be illuminated further. The corresponding equation is outlined in (4.10) and shows that the Heinle model considers the influence of turbulent kinetic energy k in the convective heat transfer. This is important for modern downsized combustion engines which show a higher level of turbulent kinetic energy compared to historic engines investigated during the times of Woschni and Hohenberg.

$$w_{mod} = \sqrt{\frac{8}{3} \cdot k + c^2 + u_{cc}^2} \quad (4.10)$$

The investigation of the performance of the three heat transfer models for an engine-like geometry is part of this work and was published in [22]. At this point only some of the results are outlined here. The initial and boundary conditions from the direct numerical simulation (DNS) experiment by Schmitt [35] are used to set up the SRM. The Woschni, Hohenberg and Heinle heat transfer models are used with default settings and the simulation is performed for a compression stroke at 560 rpm engine speed. The default Hohenberg and default Heinle models only slightly under-predict the DNS experiment, while the Woschni

model significantly under-performs as shown in figure 1. This trend is attributed to the difference in correlating the characteristic length L where the Hohenberg and Heinle models use the cylinder volume V . Close to top dead center (TDC) the default Hohenberg model satisfactorily predicts the strong rise in heat transfer rate, while the default Heinle and default Woschni models under-perform at this point.

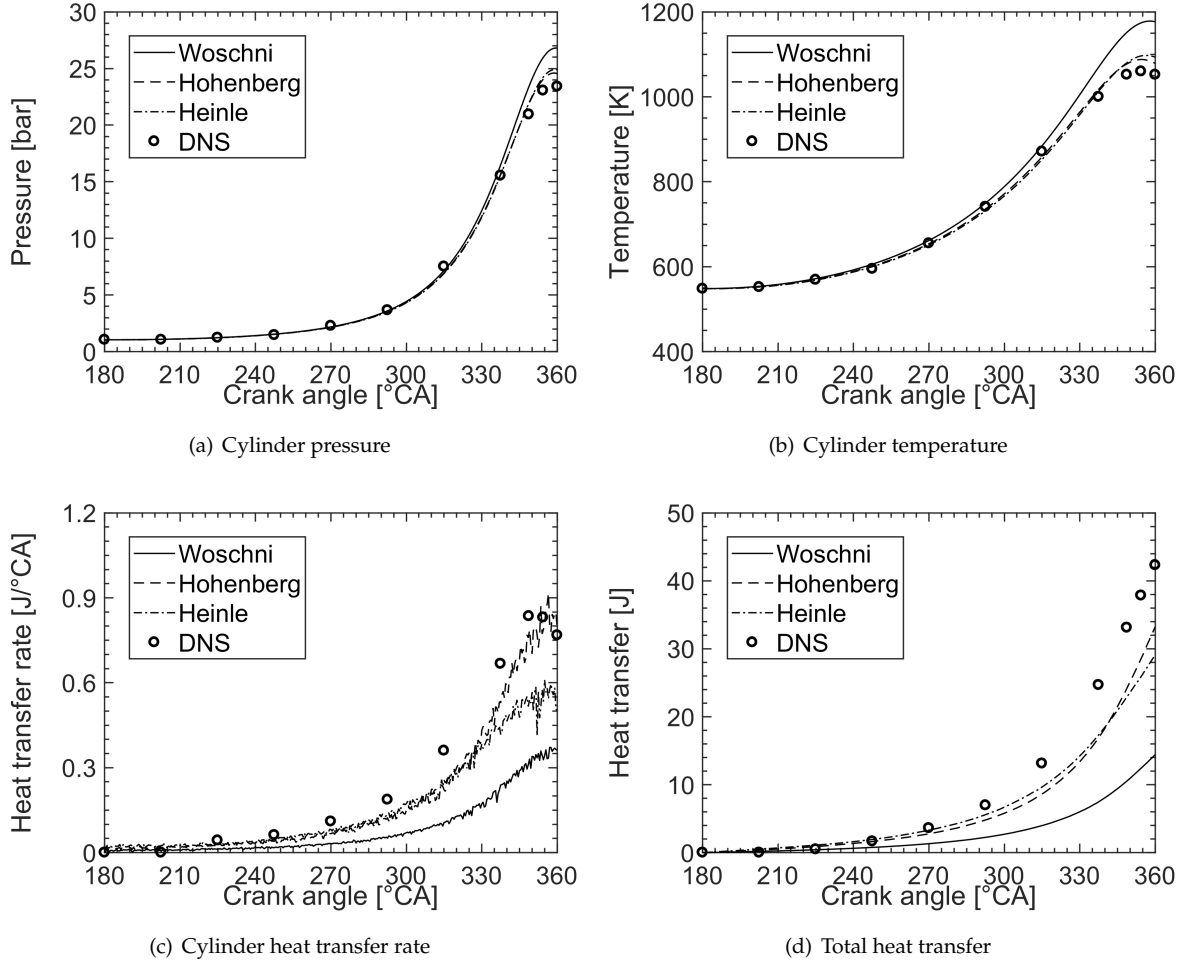


Figure 1: Comparison of Woschni, Hohenberg and Heinle heat transfer models with DNS experiment by Schmitt [35]. Top dead center is at $360^\circ CA$.

Optimized parameters of the heat transfer models are published in [22] to obtain a better match with the DNS experiments. In the subsequent section the updated stochastic heat transfer algorithm is discussed and only the heat transfer simulation results of the optimized Heinle model are shown.

4.2.2 Stochastic heat transfer algorithm

The stochastic heat transfer algorithm for the SRM was first introduced by Bhave et al. [4] for natural gas fuelled HCCI engines. It reflects the stochastic transport process of bulk gas entering in the wall boundary layer and exchanging heat with the walls. In equation (4.1) the convective heat transfer term $U(\psi_{s+1})\mathcal{F}(\psi, t)$ is replaced by a differencing scheme including the temperature fluctuation h . If $U(\psi_{s+1})$ becomes negative which means heat is transferred from the bulk gas to the walls, the temperature fluctuation h is subtracted from the gas

temperature ψ_{s+1} as shown in equation (4.11).

$$\frac{1}{h} [U(\psi_{s+1})\mathcal{F}(\psi, t) - U(\psi_{s+1} - h)\mathcal{F}(\psi_{1..s}, \psi_{s+1} - h, t)], \text{ if } U(\psi_{s+1}) < 0 \quad (4.11)$$

If $U(\psi_{s+1})$ becomes positive which means heat is transferred from the walls to the bulk gas, the temperature fluctuation h is added to the gas temperature ψ_{s+1} as shown in equation (4.12).

$$\frac{1}{h} [U(\psi_{s+1})\mathcal{F}(\psi, t) - U(\psi_{s+1} + h)\mathcal{F}(\psi_{1..s}, \psi_{s+1} + h, t)], \text{ if } U(\psi_{s+1}) > 0 \quad (4.12)$$

The stochastic heat transfer algorithm is updated in this work introducing a random number RN in the calculation of the temperature fluctuation of the notional particle $h_{(n)}$. Further, a residual random number RN_{res} is determined to distribute the remaining temperature fluctuation from the current heat transfer time step. The comparison of the SRM simulation using the updated stochastic heat transfer algorithm and the optimized Heinle heat transfer model with the DNS experiment is shown in figure 2.* The SRM simulations are conducted with 1000 notional particles, 1 stochastic cycle, 0.5°CA time step size, $C_h=1.0$ and $C_\phi=100$. The SRM shows a close match with the DNS experiment while the fluctuations in the heat transfer rate originate from the stochastic heat transfer algorithm. As it is shown in [22] increasing the number of stochastic cycles to 15 would cause a significant reduction of the variation of heat transfer rate.

The temperature distribution of the notional particles predicted by the SRM is compared to the DNS experiment in figure 3. The initial temperature distribution of the DNS experiment is mapped to the notional particles of SRM. During the early stage of the compression stroke at 225°CA the temperature distribution remains narrow for both cases. With progress in the compression stroke the bulk gas temperature increases while the gas close to the cylinder walls remain cooler because of heat loss. This effect leads to a broader temperature distribution for both cases. At TDC the temperature distribution spans from 700K to 1200K showing a pronounced temperature stratification. The SRM closely predicts the DNS experiment outlining its capability to capture spatial inhomogeneity effects.

Implementation of the stochastic heat transfer algorithm Initialize the algorithm by setting the sub time step $t_{sub,0} = 0$. The algorithm is repeated for each surface A_i which defines the combustion chamber. Following, the time jump parameter t_{jump} is calculated based on the stochastic heat transfer coefficient C_h , the notional particle number N_p and the total convective heat transfer $Q_{i,ht}$. The total convective heat transfer is calculated using one of the models outlined in section 4.2.1.

$$t_{jump} = \frac{C_h \cdot N_p}{-Q_{i,ht}} \quad (4.13)$$

*All results of the updated stochastic heat transfer algorithm can also be found in [22].

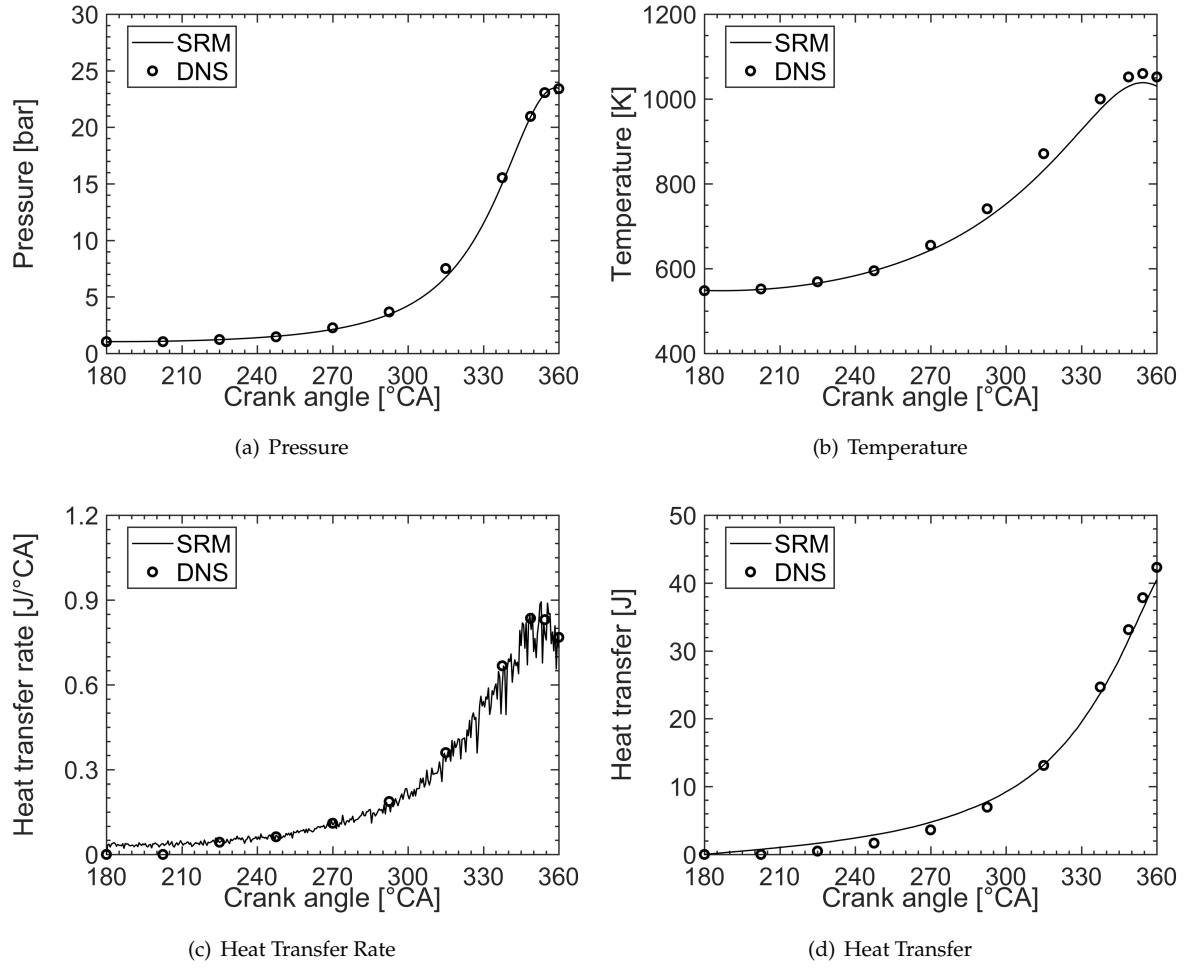


Figure 2: Comparison of DNS and SRM simulation pressure, temperature, heat transfer rate and accumulated heat transfer. Top dead center is at $360^\circ CA$.

A homogeneously distributed random number RN is drawn in the range of 0 and 1.

$$RN \in \{0, 1\} \quad (4.14)$$

The advance of the sub time step $t_{sub,j+1}$ is determined by increasing $t_{sub,j}$ by the reciprocal of the time jump parameter t_{jump} times the random number RN .

$$t_{sub,j+1} = t_{sub,j} + \frac{1}{t_{jump}} \cdot RN \quad (4.15)$$

If $t_{sub,j+1} < \Delta t$ then pick a random notional particle (n) out of the interval of notional particles $[1, N_p]$. Calculate the amount of heat $h_{(n)}$ to be transferred between notional particle and combustion chamber wall and assign the new temperature $T_{(n)}$ to the notional particle.

$$h_{(n)} = \frac{(T_{(n)} - T_{i,wall}) \cdot RN}{C_h} \quad (4.16)$$

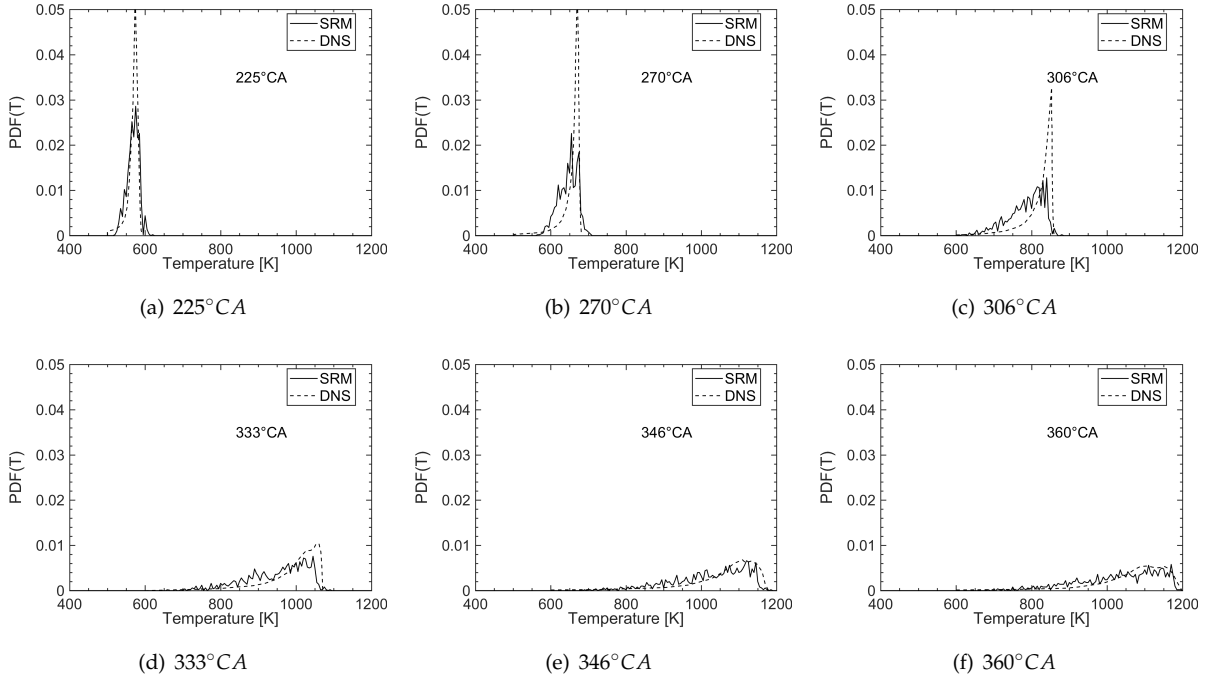


Figure 3: Comparison of DNS and SRM temperature pdf for different crank angles. Top dead center is at 360°CA.

$$T_{(n)} = T_{i,wall} - h_{(n)} \quad (4.17)$$

If $t_{sub,j+1} \geq \Delta t$ then pick a random notional particle (n) out of the interval of notional particles $[1, N_p]$. Calculate a residual random number RN_{res} to determine the remaining heat to be transferred between notional particle and combustion chamber wall and assign the new temperature $T_{(n)}$ to the notional particle.

$$T_{(n)} = T_{i,wall} - h_{(n)} \quad (4.18)$$

$$RN_{res} = (t_{sub,j+1} - t_{sub,j}) \cdot t_{jump} \quad (4.19)$$

$$h_{(n)} = \frac{(T_{(n)} - T_{i,wall}) \cdot RN_{res}}{C_h} \quad (4.20)$$

$$T_{(n)} = T_{i,wall} - h_{(n)} \quad (4.21)$$

Finally, exit the loop.

The parameter $h_{(n)}$ describes the fluctuation of the temperature, while the mean temperature is conserved. The magnitude of these fluctuations is defined by the stochastic heat transfer coefficient C_h . On one hand, a low C_h value means less notional particles are exchanging heat with the cylinder walls over a longer period of time. On the other hand, a high C_h value means that more notional particles are exchanging heat

with the combustion chamber walls over a shorter period of time. The purpose of the implemented stochastic heat transfer algorithm is to mimic the effects of the thermal boundary layer and the inhomogeneous distribution of heat transfer in the SRM.

4.2.3 Direct injection and vaporization

The direct injection and vaporization model is introduced in the SRM code by Samuelsson [13] and Tunér [14]. In this thesis the model is extended to calculate the early direct injection of spark ignited engines. Figure 4 shows a comparison of a SRM simulation* and 3D CFD Reynolds Averaged Navier Stokes (RANS) simulation for direct injection of gasoline E10 in a spark ignition engine. The injection starts at -300°CA with 200bar injection pressure. The SRM simulation uses the same injection rate as the 3D CFD RANS simulation. The liquid properties of gasoline E10 outlined in table 51 are used for the simulation. At -250°CA and -160°CA the SRM shows a faster mixing compared to 3D CFD RANS wherefor the second peak of the probability density function $f(\phi)$ is shifted to the lean side. Further, the 3D CFD RANS simulation shows formation of liquid wall film during injection which inhibits the mixing of air and fuel. At -100°CA and -20°CA the ϕ distribution of SRM converges towards the 3D CFD RANS solution wherefor similar mixture conditions can be achieved at spark ignition.

Implementation of the stochastic vaporization algorithm The stochastic vaporization model assumes that the enthalpy required for the vaporization $H_v(T)$ of the injected liquid fuel is completely extracted from the gas in the cylinder $H_g(T)$. The enthalpy balance is outlined in the following equation:

$$H_v(T) = H_g(T) \quad (4.22)$$

The enthalpy balance can also be expressed by using the specific enthalpy of vaporization $h_v(T)$ and constant pressure heat capacity $c_p(T)$ of the bulk gas.

$$m_v \cdot h_v(T) = m_g \cdot c_p(T) \cdot \Delta T \quad (4.23)$$

A homogeneously distributed random number RN is drawn to select the notional particle with index (n) out of the interval $[1, N_p]$ that will be mixed with the injected fuel mass. The notional particle should contain sufficient enthalpy for the fuel vaporization and its reaction progress c should be lower than 0.001. Hence, auto-igniting notional particles are excluded from the selection.

$$RN \in \{0, 1\} \quad (4.24)$$

*Simulation was performed with 500 notional particles, 0.5°CA time step size and Curl mixing model. The mixing time was calculated using the Bossung turbulence model.

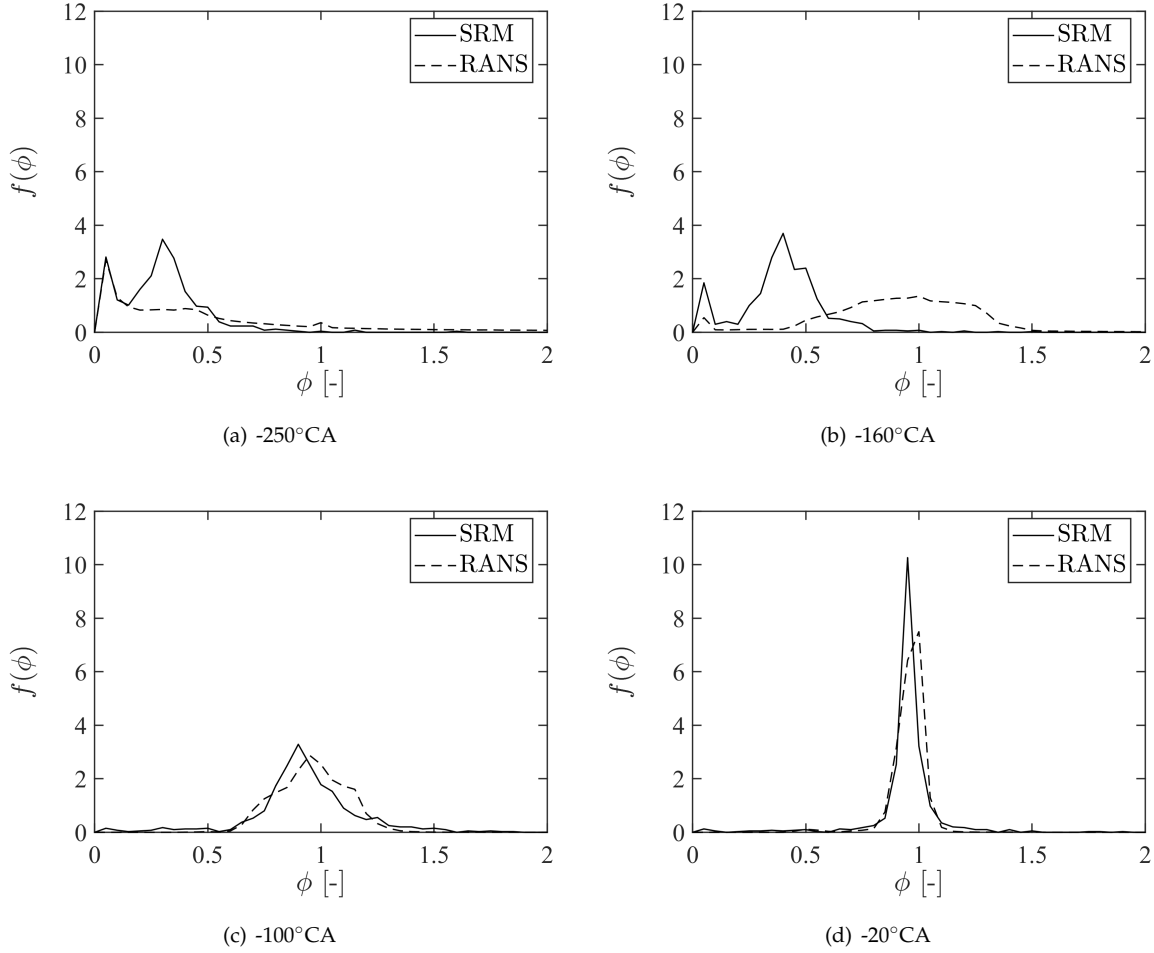


Figure 4: Comparison of 3D CFD RANS and 0D SRM equivalence ratio distribution at 2000 rpm 6 bar IMEP for a SI engine. Firing top dead center is at 0°CA.

The mass of the selected notional particle (n) is determined by multiplying its weight $W_{(n)}$ with the total cylinder mass m_g .

$$W_{(n)} = \frac{m_{(n)}}{m_g} \quad (4.25)$$

The maximum available enthalpy for vaporization of the notional particle (n) is determined by the specific enthalpy difference between notional particle temperature $T_{(n),g}$ and saturation temperature T_s . By multiplication with the notional particle mass the total enthalpy $H_{(n),g}$ is determined.

$$H_{(n),g} = \left[h_{(n),g}(T_{(n),g}) - h_{(n),s}(T_s) \right] \cdot m_{(n),g} \quad (4.26)$$

The total vaporization enthalpy H_v is determined by the difference between fuel specific enthalpy at saturation point $h_{f,s}(T_s)$ and the liquid fuel specific enthalpy $h_{f,l}(T_l)$. The mass m_v denotes the mass available for vaporization in the current time step of the

operator split.

$$H_v = [h_{f,s}(T_s) - h_{f,l}(T_l)] \cdot m_v \quad (4.27)$$

If $H_{(n),g} > H_v$ then all available mass m_v will be vaporized and assigned to the selected notional particle (n). In this case the remaining vaporization mass $m_{v,remain}$ will be zero.

$$m_{v,*} = m_v \quad (4.28)$$

If $H_{(n),g} < H_v$ then only a part of the available mass m_v will be vaporized and assigned to the selected notional particle (n). The mass to be vaporized $m_{v,*}$ will be determined by the quotient of the total notional particle enthalpy $H_{(n),g}$ and the specific enthalpy difference $h_{f,s}(T_s) - h_{f,l}(T_l)$.

$$m_{v,*} = \frac{H_{(n),g}}{h_{f,s}(T_s) - h_{f,l}(T_l)} \quad (4.29)$$

The remaining mass for vaporization $m_{v,remain}$ is determined as the difference between the available vaporization mass m_v and the actual vaporized mass $m_{v,*}$.

$$m_{v,remain} = m_v - m_{v,*} \quad (4.30)$$

The new mass $m_{(n),t+\Delta t}$ of the selected notional particle (n) is increased by the actual vaporized mass $m_{v,*}$.

$$m_{(n),t+\Delta t} = m_{(n)} + m_{v,*} \quad (4.31)$$

If $m_{v,remain} = 0$ the new specific enthalpy $h_{(n),g,t+\Delta t}$ of the notional particle (n) is determined by subtracting the enthalpy required for vaporization.

$$h_{(n),g,t+\Delta t} = h_{(n),g} - \frac{H_v}{m_{(n)}} \quad (4.32)$$

If $m_{v,remain} > 0$ the new specific enthalpy $h_{(n),g,t+\Delta t}$ of the notional particle (n) is set equal the enthalpy at saturation temperature T_s .

$$h_{(n),g,t+\Delta t} = h_{(n),s}(T_s) \quad (4.33)$$

The new thermodynamic polynomials $A_{(n),t+\Delta t}$ (see section 9.1) of the notional particle (n) are determined by accounting for the mass fraction of the notional particle $\frac{m_{(n)}}{m_{(n)}+m_{v,*}}$ and vaporized fuel mass $\frac{m_{v,*}}{m_{(n)}+m_{v,*}}$ and the thermodynamic polynomials of the notional

particle $A_{(n)}$ and the gaseous fuel $A_{f,g}$.

$$A_{(n),t+\Delta t} = \frac{A_{(n),g} \cdot m_i + A_{f,g} \cdot m_{v,*}}{m_{(n)} + m_{v,*}} \quad (4.34)$$

The new notional particle weight $W_{(n),t+\Delta t}$ is determined by the increase of the notional particle mass $m_{(n)} + m_{v,*}$ and the total mass $m_g + m_{v,*}$.

$$W_{(n),t+\Delta t} = \frac{m_{(n)} + m_{v,*}}{m_g + m_{v,*}} \quad (4.35)$$

The remaining vaporization mass $m_{v,remain}$ will be assigned for another vaporization loop in the current time step.

If the number of iterations reaches $N_{iter} > 10$ the remaining vaporization mass $m_{v,remain}$ is saved in the liquid fuel mass $m_{f,l}$ variable and will be assigned to the available vaporization mass $m_{v,t+\Delta t}$ of the next time step $t + \Delta t$.

4.2.4 Gas exchange through valves

The gas exchange model is implemented according to Heywood [36] for a poppet valve geometry. It distinguishes two cases depending on the pressure difference between manifold and cylinder. If the pressure in the manifold is larger than in the cylinder $p_{manifold} > p_{cylinder}$ the mass is flowing into the cylinder and the mass flow rate $\dot{m}_{g,in}$ can be calculated according to the following equation.

$$\dot{m}_{g,in} = \frac{C_d \cdot A_R \cdot p_{manifold}}{(R_{gas} \cdot T_{manifold})^{\frac{1}{2}}} \left(\frac{p_{cylinder}}{p_{manifold}} \right)^{\frac{1}{\gamma}} \cdot \left[\frac{2\gamma}{\gamma - 1} \cdot \left(1 - \left(\frac{p_{cylinder}}{p_{manifold}} \right)^{\left(\frac{\gamma-1}{\gamma} \right)} \right) \right]^{\frac{1}{2}} \quad (4.36)$$

Therein, the discharge coefficient C_d describes the ratio of the real mass flow to the ideal mass flow and it usually has a value lower than 1. For poppet valves C_d is provided as a function of valve lift. The reference flow area A_R is calculated according to the geometry of the valve, the runners and the current valve lift.*

If the pressure in the manifold is lower than in the cylinder $p_{manifold} < p_{cylinder}$ the mass is flowing out of the cylinder and the mass flow rate $\dot{m}_{g,out}$ can be calculated according to the following equation.

$$\dot{m}_{g,out} = \frac{C_d \cdot A_R \cdot p_{cylinder}}{(R_g \cdot T_{cylinder})^{\frac{1}{2}}} \left(\frac{p_{manifold}}{p_{cylinder}} \right)^{\frac{1}{\gamma}} \cdot \left[\frac{2\gamma}{\gamma - 1} \cdot \left(1 - \left(\frac{p_{manifold}}{p_{cylinder}} \right)^{\left(\frac{\gamma-1}{\gamma} \right)} \right) \right]^{\frac{1}{2}} \quad (4.37)$$

*The polytropic coefficient γ is calculated as the ratio of constant pressure heat capacity c_p and constant volume heat capacity c_v of the gas in the manifold.

In the case $p_{cylinder}/p_{manifold}$ is larger than $[2/(\gamma + 1)]^{\gamma/(\gamma-1)}$ the incoming flow becomes choked and the mass flow $\dot{m}_{g,in}$ is calculated instead according to the following equation.

$$\dot{m}_{g,in} = \frac{C_d \cdot A_R \cdot p_{manifold}}{(R_{gas} \cdot T_{manifold})^{\frac{1}{2}}} \gamma^{\frac{1}{2}} \left(\frac{2}{\gamma + 1} \right)^{\frac{\gamma+1}{2(\gamma-1)}} \quad (4.38)$$

In the case $p_{manifold}/p_{cylinder}$ is larger than $[2/(\gamma + 1)]^{\gamma/(\gamma-1)}$ the outgoing flow becomes choked and the mass flow $\dot{m}_{g,out}$ is calculated instead according to the following equation.

$$\dot{m}_{g,out} = \frac{C_d \cdot A_R \cdot p_{cylinder}}{(R_{gas} \cdot T_{cylinder})^{\frac{1}{2}}} \gamma^{\frac{1}{2}} \left(\frac{2}{\gamma + 1} \right)^{\frac{\gamma+1}{2(\gamma-1)}} \quad (4.39)$$

If $\dot{m}_{g,in} > 0$ the total mass in the cylinder is increased by $m_{g,t+\Delta t} = m_g + m_{g,in}$ and new notional particles are added according to $N_{p,t+\Delta t} = N_p + N_{p,in}$.[†] After the incoming mass $m_{g,in}$ is added to the total mass in the cylinder m_g the weight $W_{(n)}$ of the notional particles is updated as shown in the following equation.

$$W_{(n),t+\Delta t} = W_{(n)} \cdot \frac{m_g}{m_{g,t+\Delta t}} \quad (4.40)$$

If $\dot{m}_{g,out} > 0$ the total mass in the cylinder is decreased by $m_{g,t+\Delta t} = m_g - m_{g,out}$. Therefore, a notional particle is selected randomly by drawing a homogeneously distributed random number RN in the range of $RN \in \{0, 1\}$ and it is erased from the system. This procedure is repeated until the outgoing mass $m_{g,out}$ is fully consumed. After the procedure the new weight $W_{(n),t+\Delta t}$ of the remaining notional particles is calculated according to equation (4.40). The performance of the gas exchange model in SRM is evaluated by comparing the predicted intake and exhaust valve mass flow with 3D CFD RANS simulation results in figure 5. The 3D CFD calculations are performed for two operating points at 1500 rpm and 2000 rpm engine speed and 6 bar IMEP. The predicted exhaust valve mass flow of SRM between 120 °CA and 360 °CA follows the trend of the 3D CFD RANS simulation. However, the strong fluctuations during the open valve phase are not captured by the gas exchange model. For the predicted intake valve mass flow of SRM between 360 °CA and 600 °CA the match with the 3D CFD RANS simulation is good while some fluctuations of the 3D CFD RANS are not captured by the gas exchange model. The total valve mass for 3D CFD RANS is predicted slightly higher for the intake and exhaust valve. Overall the gas exchange model in SRM is able to follow the predictions of the 3D CFD RANS simulation.

4.2.5 Particle mixing

In this thesis two particle mixing models are considered for closure of the molecular mixing term in equation (4.1). The coalescence/dispersal (C/D) model or Curl mixing model and the Euclidean Minimum Spanning Tree (EMST) mixing model. The Curl mixing model was initially proposed by Curl [37] and further improved by Janicka et al. [38]. The model was

[†]The number of new notional particles added is determined according to the incoming mass $m_{g,in}$, the total mass in the cylinder m_g and the weight $W_{(n)}$ of the existing notional particles $N_{p,in} = m_{g,in} / (W_{(n)} \cdot m_g)$.

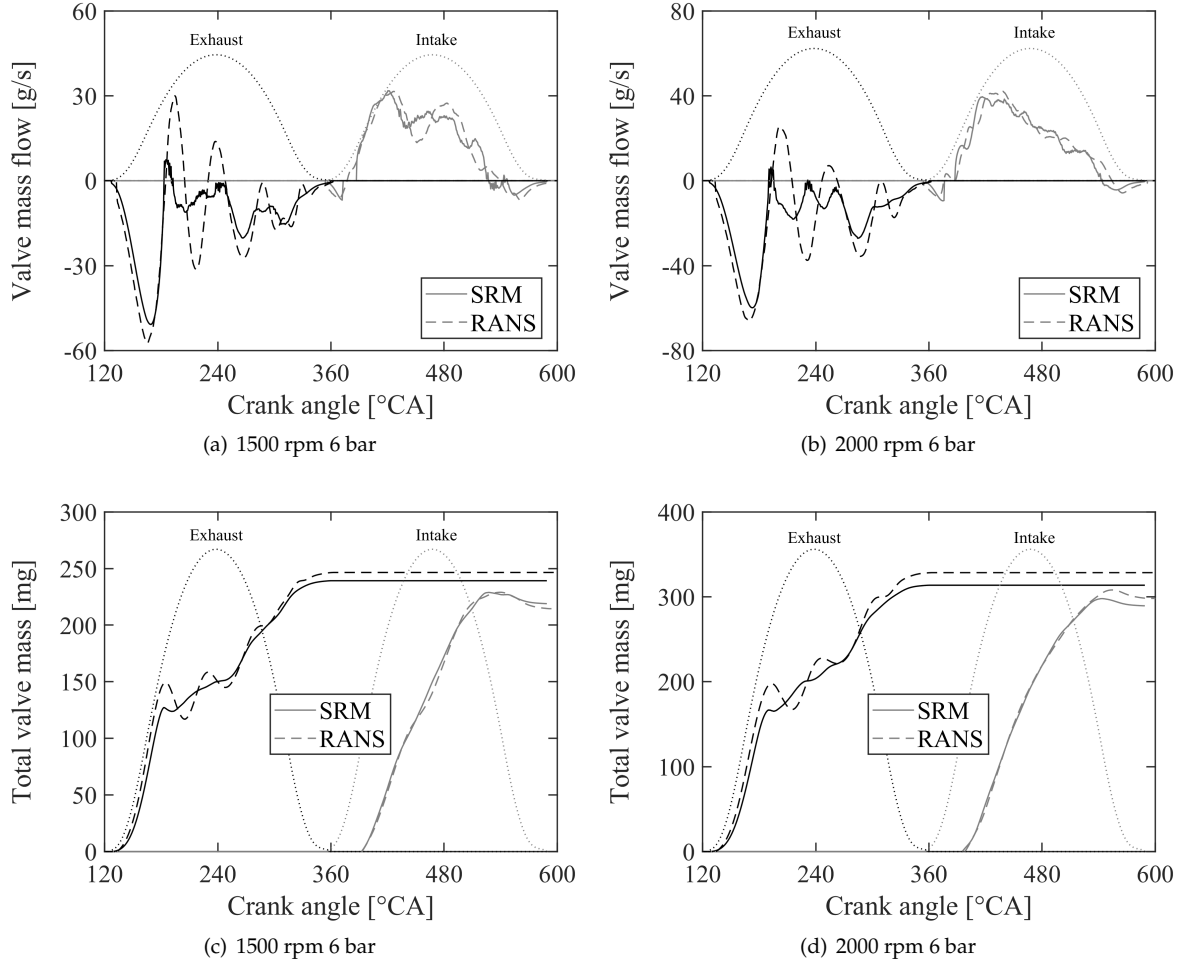


Figure 5: Comparison of 3D CFD and 0D SRM intake and exhaust valve mass flow and total valve mass at 1500 rpm 6 bar IMEP and 2000 rpm 6 bar IMEP for a SI engine. Gas exchange top dead center is at 360°CA.

implemented by Tunér [14] in SRM code and updated to consider the particle weights $W_{(q)}$ and $W_{(p)}$ of the notional particles (q) and (p). The calculation of the median of scalar ϕ of two randomly selected particles (q) and (p) is shown in equation (4.41). The Curl mixing model implementation in SRM is investigated by Tunér [14], Pasternak [15] and Matrisciano [16].

$$\begin{aligned} \frac{d\phi_{(p)}(t)}{dt} &= \frac{W_{(q)} \cdot \phi_{(q)}(t) - W_{(p)} \cdot \phi_{(p)}(t)}{W_{(q)} + W_{(p)}}, \\ \frac{d\phi_{(q)}(t)}{dt} &= \frac{W_{(p)} \cdot \phi_{(p)}(t) - W_{(q)} \cdot \phi_{(q)}(t)}{W_{(q)} + W_{(p)}} \end{aligned} \quad (4.41)$$

The EMST mixing model was introduced by Subramaniam and Pope [39] to consider the local gas composition in particle mixing. The EMST mixing model was first introduced in SRM by Su [6]. Later the model was modified to only consider mixture fraction (Z) and enthalpy (H) as scalars for the mixing process. The Z-EMST model* was investigated in detail by Franken et al. [20], Svensson [40] and Matrisciano [16], while the H-EMST model was investigated in [22] and [41].

*The mixture fraction based EMST mixing model is named Z-EMST and the enthalpy based EMST mixing model is named H-EMST.

The time evolution of scalars ϕ of notional particle (i) is described by equation (4.42). For the Z-EMST and H-EMST mixing models the mixing problem reduces to a simple unordered list where each notional particle (i) has two neighboring particles n_v and m_v . Only the two notional particles at the edges of the list have one neighboring particle.

$$W_{(i)} \frac{d\phi_{(i)}}{dt} = \alpha \sum_{v=1}^{N_T-1} B_v \left[\left(\phi_{(i)} - \phi_{(n_v)} \right) \delta_{im_v} + \left(\phi_{(i)} - \phi_{(m_v)} \right) \delta_{in_v} \right] \quad (4.42)$$

Therein, B_v is a function of the edge weight w_v and δ is the Kronecker delta. N_T denotes the number of particles which are currently in the mixing state. The model parameter α describes the rate of variance decay of scalars [39]. Its definition can be derived for a single conserved passive scalar field with mean $\langle \phi \rangle$ and variance $\langle \phi'^2 \rangle$. The mean value is not changing due to mixing wherefore the following equation holds true.

$$\frac{d\langle \phi \rangle}{dt} = 0 \quad (4.43)$$

The change of variance follows an exponential decay law in equation (4.44) based on the scalar mixing time τ_ϕ . The scalar mixing time τ_ϕ can be calculated using the $k - \varepsilon$ turbulence models in SRM [20].

$$\frac{d\langle \phi'^2 \rangle}{dt} = -\frac{\langle \phi'^2 \rangle}{\tau_\phi} \quad (4.44)$$

Following, α is selected so that the decay rate of the ensemble scalar variance $\langle \phi'^2 \rangle_N$ implied by the EMST mixing model follows the decay law in equation (4.44).

$$\frac{d\langle \phi'^2 \rangle_N}{dt} = \sum_{i=1}^{N_T} W_{(i)} 2\phi'_{(i)} \frac{d\langle \phi'_{(i)} \rangle}{dt} = -\alpha \sum_{i=1}^{N_T} W_{(i)} 2\phi'_{(i)} \overline{M}_{ij} \phi'_j \quad (4.45)$$

where \overline{M}_{ij} is quotient of the interaction matrix M_{ij} and α .

$$\overline{M}_{ij} = \frac{1}{\alpha} M_{ij} \quad (4.46)$$

$$M_{ij} = -\alpha \sum_{v=1}^{N_T-1} B_v \{ \delta_{im_v} \delta_{jn_v} + \delta_{jm_v} \delta_{in_v} \} \text{ with } j \neq i \quad (4.47)$$

Equating the two decay rates in (4.44) and (4.45) yields the final definition of α :

$$\alpha = \frac{\langle \phi'^2 \rangle_N}{\tau_\phi \sum_{i=1}^{N_T} \sum_{j=1}^N W_{(i)} 2\phi'_{(i)} \overline{M}_{ij} \phi'_j} \quad (4.48)$$

4.2.6 Chemical reaction

The SRM incorporates detailed kinetic models to calculate the change of gas composition in equation (4.49) and change of enthalpy in equation (4.50) due to chemical reactions. The

kinetic model contains among other things the information of species molar weight M_i and the reaction rate parameters of the elementary reactions. The parameters are used to determine the reaction rate $\dot{\omega}_i$ of species i . The heat capacity c_p , enthalpy H and entropy S of the mixture are calculated using the species specific coefficients of the thermodynamic NASA polynomials.

$$G_i = \frac{M_i \dot{\omega}_i}{\rho}, i = 1, \dots, s \quad (4.49)$$

$$G_{s+1} = -\frac{1}{\rho c_p} \sum_{i=1}^s u_i M_i \dot{\omega}_i - \frac{V}{m c_p} \frac{dp}{dt} \quad (4.50)$$

During the SRM simulation a non-linear equation system is solved using a backward differential function method combined with a Newton algorithm [14]. Depending on the number of species and number of reactions of the reaction mechanism the computational cost of the SRM simulation is rising [15].

Lehtiniemi et al. [42, 43] and Matrisciano [16] developed the combustion progress variable (CPV) tabulated chemistry model for prediction of ignition processes and emission formation with low computational costs. Tabulated chemistry implies that the data is stored in look-up tables where the information is extracted during the simulation runtime. To reconstruct the reaction path for the table look-up for different thermodynamic conditions, the combustion progress variable c is introduced and it is determined based on the latent enthalpy of formation h_{298} [16].*

4.3 Modeling of spark ignition engine

The SRM for spark ignition engines (SI-SRM) distinguishes the combustion chamber into three zones: Unburnt zone (uz), burnt zone (bz) and crevice zone (cz). The gas composition and enthalpy of each zone is described by the ensemble of notional particles belonging to each zone. The mass transport between the zones is governed by specific models for turbulent flame propagation and crevice flow which will be described in the following section. The turbulence in the system is modeled using a $k - \varepsilon$ model which calculates the production and dissipation of turbulent kinetic energy k and the change of angular momentum of tumble flow L_T . Finally, a cyclic variation model is incorporated to account for influence of turbulence variation and ignition kernel size variation on combustion progress and emission formation.

4.3.1 $k - \varepsilon$ turbulence model

The $k - \varepsilon$ turbulence model for SI engines is implemented according to the work of Bossung [10] and the derived equations are based on Wilcox [44]. The model calculates the change of turbulent kinetic energy dk/dt by a set of differential terms which describe the production and dissipation of k in a cylinder-shaped geometry with a tumble flow motion around the cross-axis of the cylinder. The differential terms for valve flow, axial flow, tumble flow motion,

*The latent enthalpy of formation h_{298} is found to be a suitable progress variable since it has a steady progress during the two stage ignition process.

direct injection, compressibility and dissipation outlined in equation (4.51) will be described more in detail.

$$\frac{dk}{dt} = \left(\frac{dk}{dt}\right)_{inflow} + \left(\frac{dk}{dt}\right)_{axial} + \left(\frac{dk}{dt}\right)_{tumble} + \left(\frac{dk}{dt}\right)_{injection} + \left(\frac{dk}{dt}\right)_{compressibility} - \varepsilon \quad (4.51)$$

The production of turbulent kinetic energy from valve flow is related to the production term $P_{k,inflow}$ which is normalized by the total mass m_g of the system.

$$\left(\frac{dk}{dt}\right)_{inflow} = \frac{P_{k,inflow}}{m_g} \quad (4.52)$$

The production term $P_{k,inflow}$ is defined as the exponential decay of the effective kinetic energy $E_{kin,inflow,eff}$ with the time scale $\tau_{inflow,k}$.[†]

$$P_{k,in} = \frac{E_{kin,inflow,eff}}{\tau_{inflow,k}} \quad (4.53)$$

The effective kinetic energy $E_{kin,inflow,eff}$ in the system is changing over time depending on the rate of kinetic energy flowing into the system $\frac{dE_{kin,in,eff}}{dt}$, flowing out of the system $\frac{dE_{kin,out}}{dt}$ and due to production of turbulent kinetic energy $P_{k,in}$.

$$\frac{dE_{kin,inflow,eff}}{dt} = \frac{dE_{kin,in,eff}}{dt} + \frac{dE_{kin,out}}{dt} - P_{k,in} \quad (4.54)$$

The rate of kinetic energy of the inflow $\frac{dE_{kin,in}}{dt}$ is calculated based on the intake mass flow \dot{m}_{IV} and inflow velocity v_{IV} which are calculated by the gas exchange model in section 4.2.4.

$$\frac{dE_{kin,in}}{dt} = \frac{1}{2} \cdot \sum_{i=1}^{N_{IV}} \dot{m}_{IV} \cdot v_{IV}^2 \quad (4.55)$$

The rate of kinetic energy of inflow is scaled by a conversion parameter $f_{in,k}$ to obtain the rate of effective kinetic energy of inflow $\frac{dE_{kin,in,eff}}{dt}$ which is relevant for turbulent kinetic energy production.

$$\frac{dE_{kin,in,eff}}{dt} = f_{in,k} \cdot \frac{dE_{kin,in}}{dt}, \quad \dot{m}_{in/out} \geq 0 \quad (4.56)$$

The conversion parameter $f_{in,k}$ is defined as a linear function depending on the instantaneous intake valve lift l_{IV} and has a value between 0 and 1.*

$$f_{in,k} = a_{in} \cdot l_{IV} + b_{in} \quad (4.57)$$

The influence of the model parameters a_{in} and b_{in} on turbulent kinetic energy k and production of turbulent kinetic energy is shown in figure 6 (a) and (b). Increasing the parameters leads to higher production of kinetic energy from inflow which increases the

[†]The time scale is defined as $\tau_{inflow,k} = C_{\tau,k,inflow} \cdot (n/60)^{\alpha_{inflow}}$, where n is the engine speed, $C_{\tau,k,inflow}$ is set to 0.019 and α_{inflow} is set to $-2/3$.

*The default value for a_{in} is set to 20 and the default value for b_{in} is set to 0.2.

production rate of turbulent kinetic energy and dissipation. The a_{in} and b_{in} model parameters mostly influences the production of turbulent kinetic energy during valve opening while a minor decrease of k can be observed during combustion at 0°CA .

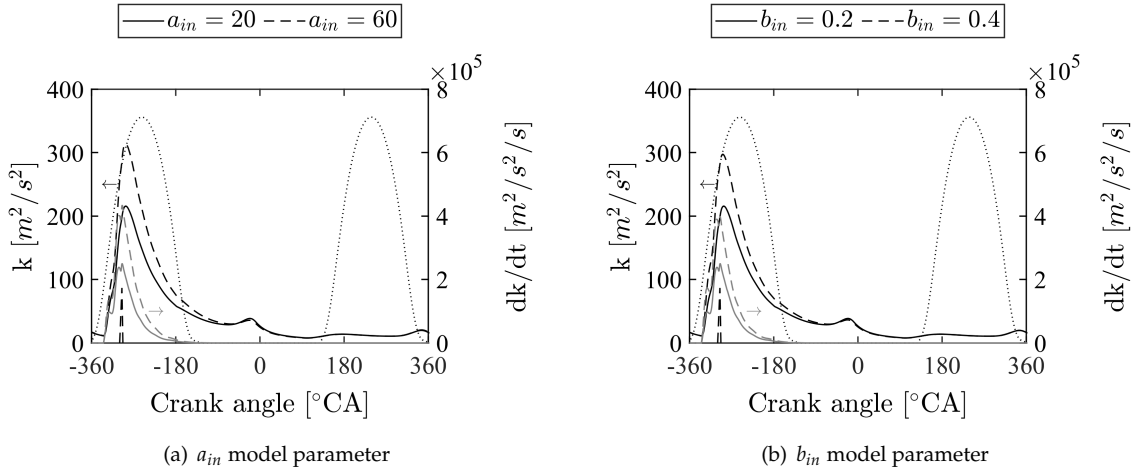


Figure 6: Turbulent kinetic energy and inflow production term in dependence of a_{in} and b_{in} parameters at 2000 rpm and 6 bar IMEP. The dashed lines highlight the intake and exhaust valve lift. The start of fuel injection is at -300°CA .

The flow of kinetic energy out of the system is a sink in the balance equation (4.54) and is proportional to the outflow rate \dot{m}_{out} and the effective kinetic energy $E_{kin,inflow,eff}$.

$$\frac{dE_{kin,out}}{dt} = \frac{\dot{m}_{out}}{m_{gas}} \cdot E_{kin,inflow,eff}, \quad \dot{m}_{in/out} < 0 \quad (4.58)$$

The piston movement in axial direction induces a flow field with the kinetic energy $e_{kin,axial}$ and which is proportional to the instantaneous piston speed c_{pis} .[†]

$$e_{kin,axial} = \frac{1}{6} \cdot c_{pis}^2 \quad (4.59)$$

When the axial kinetic energy decays during the deceleration of the piston, secondary flow motions are induced with the kinetic energy $e_{kin,sec}$. Therefor, a negative rate $\frac{de_{kin,axial}}{dt}$ means the production of kinetic energy of secondary flow motions and the production of turbulent kinetic energy means the decay of kinetic energy of the secondary flow motions.

$$\frac{e_{kin,sec}}{dt} = \max\left(-\frac{de_{kin,axial}}{dt}, 0\right) - \left(\frac{dk}{dt}\right)_{axial} \quad (4.60)$$

The decay of the secondary flow motion leads to the production of turbulent kinetic energy as described in equation (4.61). Thereby, it is assumed that the exponential decay of the secondary flow motion follows a characteristic time scale τ_{axial} which is proportional to the piston stroke and mean piston speed.*

$$\left(\frac{dk}{dt}\right)_{axial} = \frac{e_{kin,sec}}{\tau_{axial}} \quad (4.61)$$

[†]The instantaneous piston speed c_{pis} is calculated according to section 9.5.

*The time scale is calculated according to $\tau_{axial} = C_{axial} \cdot \frac{h_s}{c_m}$ where C_{axial} is a model parameter, h_s is the stroke and c_m is the mean piston speed.

The time scale τ_{axial} can be modified by tuning the model parameter C_{axial} . Decreasing C_{axial} leads to a reduced time scale and consequently a stronger production of turbulent kinetic energy due to secondary flow decay. The highest production rate of turbulent kinetic energy is found close to TDC where the piston is decelerating.

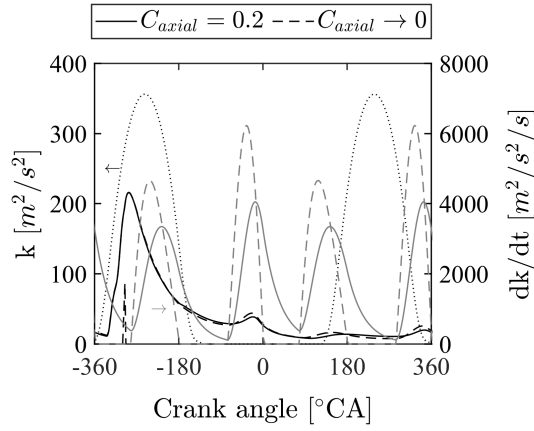


Figure 7: Turbulent kinetic energy and axial flow production term in dependence of C_{axial} parameter at 2000 rpm and 6 bar IMEP. The dashed lines highlight the intake and exhaust valve lift. The start of fuel injection is at -300 °CA.

The production of turbulent kinetic energy due to direct injection is described by equation (4.62). The turbulent kinetic energy is proportional to the injection velocity and injection mass. The Bernoulli equation is applied to determine the injection velocity in dependence of the pressure difference $p_{inj} - p_{cyl}$ and the density of the fuel ρ_f . The fuel mass flow \dot{m}_f and injection pressure p_{inj} are determined by the injection and vaporization model in section 4.2.3. The turbulent kinetic energy is normalized by the total mass m_g .

$$\left(\frac{dk}{dt}\right)_{injection} = C_{inj} \cdot \dot{m}_f \cdot \frac{p_{inj} - p_{cyl}}{\rho_f} \cdot \frac{1}{m_g} \quad (4.62)$$

The model parameter C_{inj} is introduced to control the contribution of direct injection to the production of turbulent kinetic energy. The results of turbulent kinetic energy and the production term for different C_{inj} model parameter values are outlined in figure 8. Increasing the value of C_{inj} leads to an increase of turbulent kinetic energy and production rate during injection. The increase of C_{inj} shows no effect on the turbulent kinetic energy during combustion.

The contribution of tumble flow motion decay to production of turbulent kinetic energy is described by equation (4.63). The tumble flow motion is a rotating flow motion around the cross-axis of the cylinder within the x-z plane. Its rotational energy can be determined by the angular momentum of a rotating cylinder L_T with its length equal to the cylinder bore d_B and its radius equal to the instantaneous distance between piston and cylinder head H_1 .*

$$\left(\frac{dk}{dt}\right)_{tumble} = \frac{9 \cdot \pi^8}{1024} \cdot \nu_t \cdot \frac{(d_B^2 + H_1^2)^2}{d_B^8 \cdot H_1^6} \cdot \frac{1}{\rho^2} \cdot L_T^2 \quad (4.63)$$

Therein, ν_t is the turbulent viscosity which is calculated based on turbulent kinetic energy

*The instantaneous distance between piston and cylinder head is calculated with $H_1 = \frac{V}{\pi \cdot \frac{d_B^2}{4}}$.

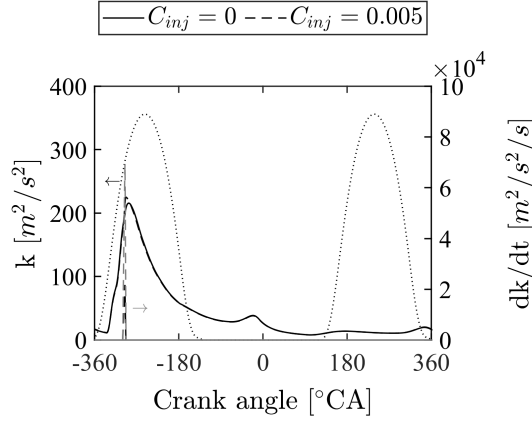


Figure 8: Turbulent kinetic energy and direct injection production term in dependence of C_{inj} parameter at 2000 rpm and 6 bar IMEP. The dashed lines highlight the intake and exhaust valve lift. The start of fuel injection is at -300°CA .

and dissipation in equation (4.64). C_μ is a model parameter with the default value of 0.09 for standard $k - \varepsilon$ models.

$$v_t = C_\mu \cdot \frac{k^2}{\varepsilon} \quad (4.64)$$

The change of angular momentum of the tumble flow motion L_T is described by the equation (4.65). Angular momentum can be produced due to inflow through the valves and spin-up due to piston acceleration. Angular momentum decays due to outflow out of the system and shear forces.

$$\frac{dL_T}{dt} = \left(\frac{dL_T}{dt}\right)_{in} + \left(\frac{dL_T}{dt}\right)_{out} + \left(\frac{dL_T}{dt}\right)_{shear} + \left(\frac{dL_T}{dt}\right)_{spin-up} \quad (4.65)$$

The production of angular momentum L_T due to inflow is proportional to the mass flow \dot{m}_{in} , the density ρ and the bore diameter d_B as shown in equation (4.66). Thereby, the angular momentum is scaled by the Tippelmann tumble number T_{Tipp} .

$$\left(\frac{dL_T}{dt}\right)_{in} = \frac{2 \cdot T_{Tipp} \cdot \dot{m}_{in}^2}{d_B \cdot \rho}, \quad \dot{m}_{in} \geq 0 \quad (4.66)$$

T_{Tipp} is a model parameter and can change for different operating conditions and engines. Increasing T_{Tipp} increases the angular momentum and tumble ratio* as shown in figure 9 (b). The higher angular momentum during the intake valve opening also increases the angular momentum during compression stroke and combustion.

The decay of angular momentum due to outflow out of the system is proportional to the mass flow out of the system \dot{m}_{out} and the instantaneous angular momentum L_T .

$$\left(\frac{dL_T}{dt}\right)_{out} = L_T \cdot \frac{\dot{m}_{out}}{m_g} \quad (4.67)$$

Equation (4.68) describes the decay of angular momentum due to shear forces and the production of turbulent kinetic energy.

*The calculation of the tumble ratio is outlined in section 9.6.

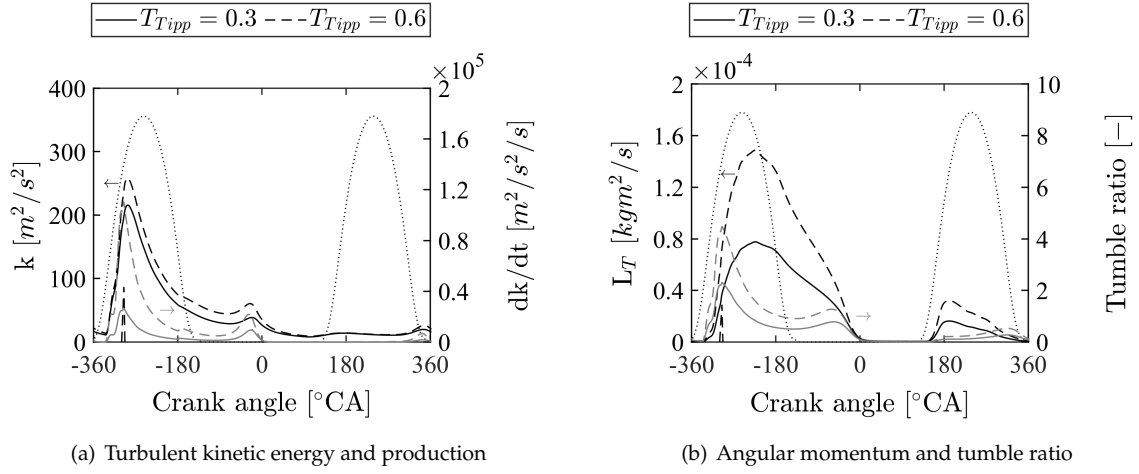


Figure 9: Turbulent kinetic energy, tumble flow production term, angular momentum and tumble ratio in dependence of T_{Tipp} parameter at 2000 rpm and 6 bar IMEP. The dashed lines highlight the intake and exhaust valve lift. The start of fuel injection is at -300 °CA.

$$\left(\frac{dL_T}{dt}\right)_{shear} = -sign(L_T) \cdot \frac{2048}{9 \cdot \pi^6} \cdot \frac{d_B^6 \cdot H_1^4}{\frac{3}{4}d_B^2 + H_1^2} \cdot \frac{\rho^2}{2 \cdot |L_T|} \cdot \left(\frac{dk}{dt}\right)_{tumble} \quad (4.68)$$

The last term on the right hand side of equation (4.65) describes the tumble flow motion during compression. The model parameter $f_{T,spin-up}$ can be changed and is defined in the range of 0 and 1.

$$\left(\frac{dL_T}{dt}\right)_{spin-up} = f_{T,spin-up} \cdot \frac{d_B^2}{d_B^2 \cdot H_1 + \frac{4}{3} \cdot H_1^3} \cdot L_T \cdot \frac{dh_s}{dt} \quad (4.69)$$

When $f_{T,spin-up}$ is equal to 1 the tumble flow experiences no acceleration while when $f_{T,spin-up}$ is equal to 0 the tumble is accelerated during compression and reaches a maximum shortly before TDC as shown in figure 10.

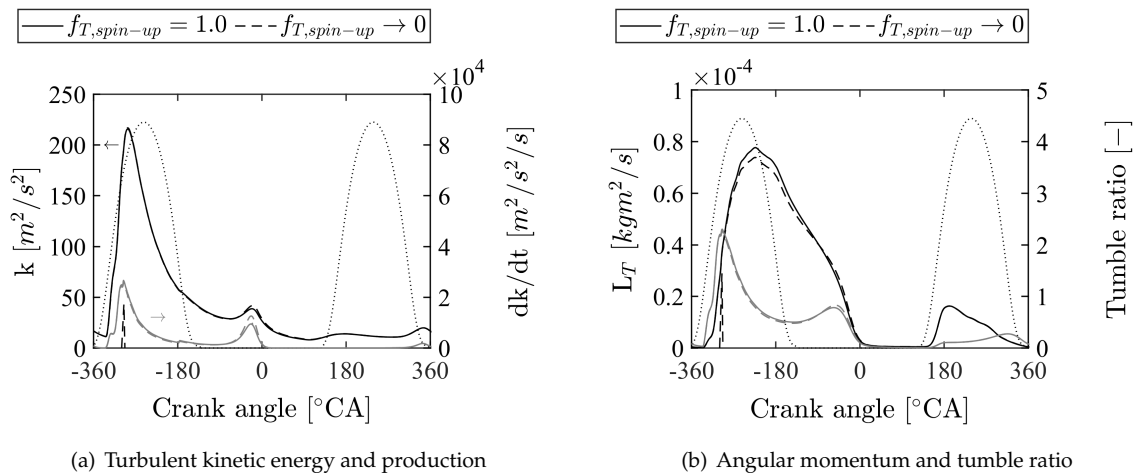


Figure 10: Turbulent kinetic energy, tumble flow production term, angular momentum and tumble ratio in dependence of $f_{T,spin-up}$ parameter at 2000 rpm and 6 bar IMEP. The dashed lines highlight the intake and exhaust valve lift. The start of fuel injection is at -300 °CA.

For the compressible case the Boussinesq approximation introduces two terms for the

closure of the Reynolds stress tensor [44]. The first term describes the production of turbulent kinetic energy due to shear forces and is assumed to be zero for the case of isentropic compression. The second term describes the influence of compressibility on the production of turbulent kinetic energy. Using the continuity equation the term can be described in dependence of density changes. If it is further assumed that the mass in the system is constant ($m_g = const$) then the influence of compressibility can be described by volume changes [10] as outlined in the following equation.

$$\left(\frac{dk}{dt}\right)_{compressibility} = -\frac{2}{3} \cdot \frac{dV}{dt} \cdot \frac{k}{V} \quad (4.70)$$

The last term of equation (4.51) describes the destruction of turbulent kinetic energy due to dissipation. According to Wilcox [44] the dissipation is proportional to the turbulent kinetic energy k and inversely proportional to a turbulent length scale l . Therefore, dissipation ε can be determined according to the following equation [10].

$$\varepsilon = C_\varepsilon \cdot \frac{k^3}{l_I} \quad (4.71)$$

Therein, l_I is the integral length scale that describes the dimension of the large flow structure in the system. The model parameter C_ε reflects the proportionality between dissipation ε , turbulent kinetic energy k and integral length scale l_I . The ratio of C_ε and C_μ reflects the proportionality of the integral length scale l_I to the turbulent length scale l .

$$l_I = \frac{C_\varepsilon}{C_\mu} \cdot l \quad (4.72)$$

The increase of the model parameter C_ε leads to a decrease of the turbulent kinetic energy and dissipation over the full engine cycle as shown in figure 11.

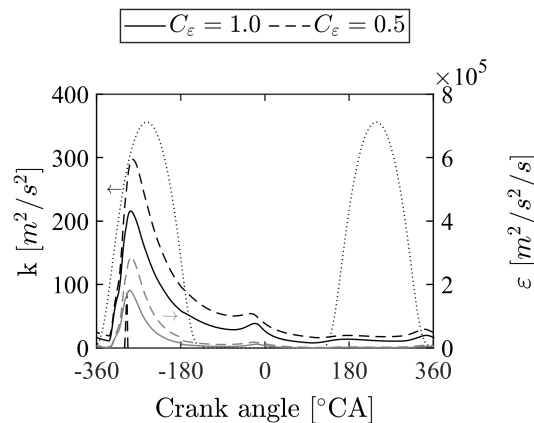


Figure 11: Turbulent kinetic energy and dissipation in dependence of C_ε parameter at 2000 rpm and 6 bar IMEP. The dashed lines highlight the intake and exhaust valve lift. The start of fuel injection is at -300°CA .

The turbulent length scale l is determined according to Qirui [45] and accounts for the system volume length scale l_{vol} and valve flow length scale $l_{turb,avg}$. The contribution of each

length scale is based on its mass m_{vol}^* and m_{inflow}^\dagger in relation to the total mass in the system m_g .

$$l = \frac{m_g}{\left(\frac{m_{vol}}{l_{vol}} + \frac{m_{inflow}}{l_{turb,avg}}\right)} \quad (4.73)$$

The length scale l_{vol} is determined according to a sphere whose volume is equal to the instantaneous volume of the system V .

$$l_{vol} = \frac{C_\mu}{C_{\varepsilon_1}} \cdot \left(6 \cdot \frac{V}{\pi}\right)^{\frac{1}{3}} \quad (4.74)$$

The model parameters C_μ and C_{ε_1} account for the proportionality between the turbulent length scale l and the characteristic length scale L . The model parameter C_μ is set equal to 0.09 while the model parameter C_{ε_1} can be adjusted. Decreasing the value of C_{ε_1} leads to an increase of the turbulent length scale l for the full engine cycle. The turbulent kinetic energy is increasing during the gas exchange while it decreases before firing TDC at 0°CA .

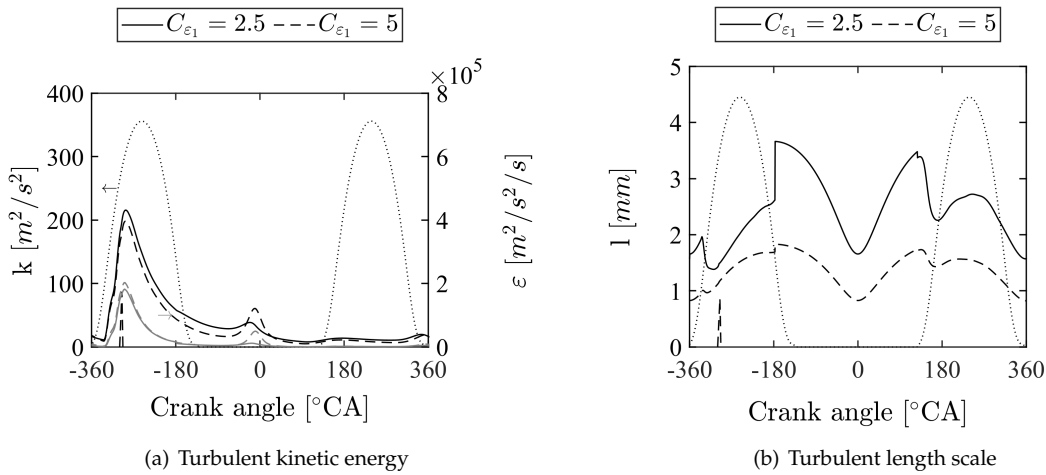


Figure 12: Turbulent kinetic energy, dissipation and turbulent length scale in dependence of C_{ε_1} parameter at 2000 rpm and 6 bar IMEP. The dashed lines highlight the intake and exhaust valve lift. The start of fuel injection is at -300°CA .

The length scale $l_{turb,avg}$ is determined based on the intake valve length scale $l_{turb,IV}$ and the exhaust valve length scale $l_{turb,EV}$.

$$l_{turb,avg} = \frac{l_{turb,IV} \cdot m_{inflow,IV} + l_{turb,EV} \cdot m_{inflow,EV}}{m_{inflow}} \quad (4.75)$$

The two length scales can be calculated according to equation (4.76) and (4.77). They are depending on a characteristic length scale L_{IV} and L_{EV} which are influenced by the valve lifts l_{IV} and l_{EV} . The proportionality between the turbulent length scale l and characteristic length scale L is governed by the model parameters C_μ and C_{ε_2} .

*The mass m_{vol} is calculated according to $m_{vol} = m_g - m_{inflow}$.

†The mass m_{inflow} is calculated based on the accumulated inflow masses through the intake ($m_{inflow,IV}$) and exhaust valve ($m_{inflow,EV}$) using the following definition $m_{inflow} = \sum m_{inflow,IV} + \sum m_{inflow,EV}$.

$$l_{turb,IV} = \frac{C_\mu}{C_{\varepsilon_2}} \cdot L_{IV} \quad (4.76)$$

$$l_{turb,EV} = \frac{C_\mu}{C_{\varepsilon_2}} \cdot L_{EV} \quad (4.77)$$

The increase of the model parameter C_{ε_2} leads to a decrease of the turbulent length scale l during the valve opening as shown in figure 13. At the same time the turbulent kinetic energy is decreasing during valve opening while it increases close to firing TDC at 0°CA .

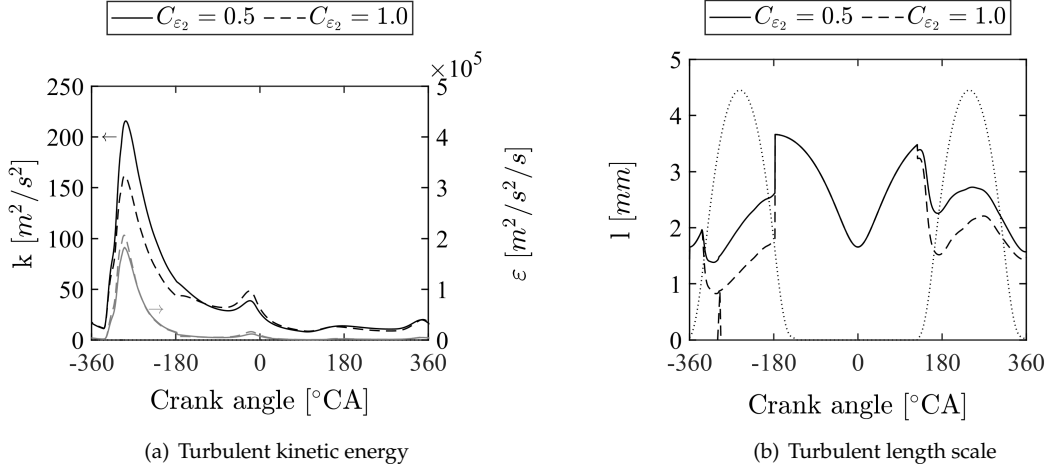


Figure 13: Turbulent kinetic energy, dissipation and turbulent length scale in dependence of C_{ε_2} parameter at 2000 rpm and 6 bar IMEP. The dashed lines highlight the intake and exhaust valve lift. The start of fuel injection is at -300°CA .

The calculated turbulent kinetic energy and dissipation are used to determine the turbulent mixing time of the unburnt mixture. The turbulent mixing time is proportional to the scalar mixing time $\tau_{\phi,u}$ which is the time scale that governs the particle mixing as explained in section 4.2.5. Equation (4.78) outlines the calculation of the scalar mixing time and introduces the proportionality parameter $C_{\phi,u}$ which can be adjusted according to the investigated application.

$$\tau_{\phi,u} = C_{\phi,u} \cdot \frac{k}{\varepsilon} \quad (4.78)$$

The scalar mixing time of burnt mixture $\tau_{\phi,b}$ is determined using an additional scaling factor $C_{\phi,b}$. The value of $C_{\phi,b}$ is usually in the range of 0.001 – 0.1.

$$\tau_{\phi,b} = C_{\phi,b} \cdot \tau_{\phi,u} \quad (4.79)$$

The turbulent kinetic energy is further used to calculate the turbulence fluctuation u' [44] which is an input parameter for the turbulent flame propagation in section 4.3.2. Additionally, the integral length scale l_I is used as an input in the turbulent flame propagation to determine the turbulence and flame interaction.

$$u' = \sqrt{\frac{2}{3} \cdot k} \quad (4.80)$$

4.3.2 Turbulent flame propagation

The combustion regime diagram in figure 14 is introduced by Peters [3]. It distinguishes the different regimes based on turbulence fluctuation u' , laminar flame speed s_L , integral length scale l_I and flame thickness δ_L . For the investigations in this thesis two regimes are relevant: The corrugated flamelets and thin reactions regimes. Damköhler already described these regimes in his work [46] and denoted them as areas of large scale turbulence and small scale turbulence.

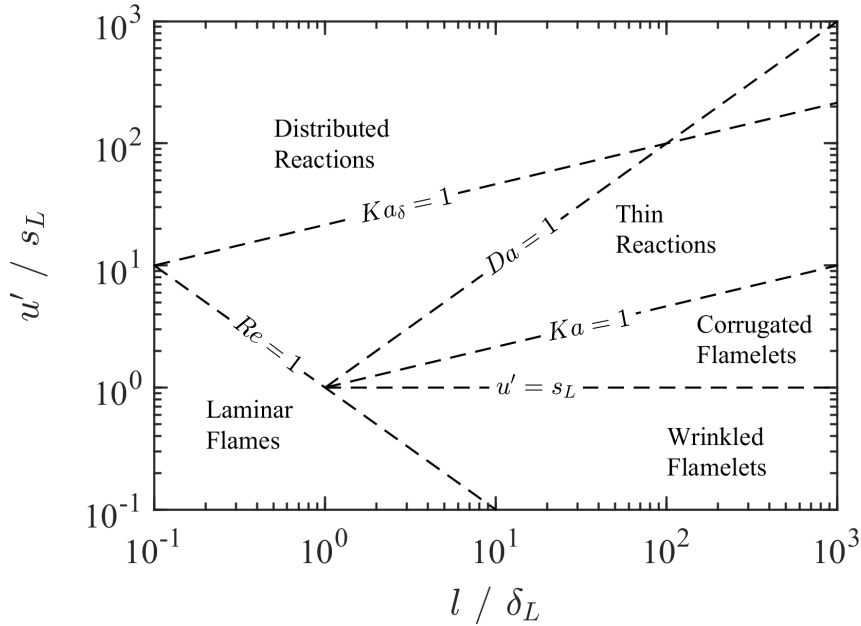


Figure 14: Regimes of turbulent premixed combustion in the Borghi-Peters diagram.

The boundaries of the two combustion regimes can be determined by the Reynolds number, the Damköhler number and the Karlovitz number. The Reynolds number is defined according to equation (4.81).

$$Re = \frac{u' \cdot l}{s_L \cdot \delta_L} \quad (4.81)$$

Therein, u' is the turbulence fluctuation and l is the turbulent length scale which are calculated according to equations (4.73) and (4.80). The flame thickness δ_L is defined as the ratio of thermal diffusivity α_{th} and laminar flame speed s_L . The thermal conductivity λ_0 and heat capacity $c_{p,0}$ are defined for the inner layer of the flame and the density ρ_u is defined for the unburnt mixture [3]. The laminar flame speed s_L is defined based on the properties of the unburnt mixture.

$$\delta_L = \frac{\alpha_{th}}{s_L} = \frac{\left(\frac{\lambda_0}{c_{p,0} \cdot \rho_u} \right)}{s_L} \quad (4.82)$$

In the SRM the thermal diffusivity α_{th} in equation (4.82) is not defined based on the inner

layer but on the unburnt mixture properties wherefor it is corrected according to the definition by Blint [47] in equation (4.83).

$$\delta_L = 2 \cdot \frac{\alpha_{th}}{s_L} \cdot \left(1 + \frac{(T_{ad} - T_u)}{T_u}\right)^{0.7} \quad \text{with } \alpha_{th} = \left(\frac{\lambda}{c_p \cdot \rho}\right)_u \quad (4.83)$$

The Damköhler number is defined by equation (4.84) and denotes the ratio of turbulent time scales and chemical time scales.

$$Da = \frac{l \cdot s_L}{u' \cdot \delta_L} \quad (4.84)$$

Peters [3] introduced two Karlovitz numbers Ka and Ka_δ to distinguish the combustion regimes. Ka is the ratio of the flame scales δ_L and the Kolmogorov scales η . It can also be described as the ratio of the Kolmogorov velocity u_η and the laminar flame speed s_L . For $Ka = 1$ the Kolmogorov scale becomes equal to the flame scale $\eta = \delta_L$. In figure 14 this condition separates the corrugated flamelet regime from the thin reactions regime. The corrugated flamelet regime is further defined for decreasing Ka and is limited downwards by the condition $u' = s_L$ where the turbulent fluctuation cannot compete anymore with the laminar flame propagation.

$$Ka = \frac{\delta_L^2}{\eta^2} = \frac{u_\eta^2}{s_L^2} \quad (4.85)$$

The second Karlovitz number Ka_δ describes the ratio of the inner layer scale δ_i and the Kolmogorov scale. It can be related to the first Karlovitz number Ka by the dimensionless scale δ of the inner layer.* For $Ka_\delta = 1$ the Kolmogorov scale becomes equal to the inner layer scale $\eta = \delta_i$. In figure 14 this condition separates the thin reactions regime from the distributed reactions regime. The thin reactions regime is further defined by decreasing Ka numbers and is limited downwards by the condition $Ka = 1$ where the smallest turbulent eddies become too large to interact with the reaction zone.

$$Ka_\delta = \frac{\delta_i^2}{\eta^2} = \delta^2 \cdot Ka \quad (4.86)$$

The Karlovitz number can also be expressed based on the turbulence fluctuation u' , the laminar flame speed s_L , the turbulent length scale l and the flame thickness δ_L .

$$Ka = \left(\frac{\left(\frac{u'}{s_L}\right)^3}{\frac{l}{\delta_L}} \right)^{\frac{1}{2}} \quad (4.87)$$

Simple model According to Damköhler [46] the mass flux \dot{m} through a turbulent flame surface area A_T can be equated to mass flux through a cross-sectional area A of a pipe by

*The dimensionless scale δ is defined as the ratio of the inner layer thickness δ_i and the flame thickness δ_L .

using the laminar s_L and turbulent flame speed s_T and the density of the unburnt mixture ρ_u *

$$\dot{m} = \rho_u \cdot A_T \cdot s_L = \rho_u \cdot A \cdot s_T \quad (4.88)$$

For constant density ($\rho_u = \text{const}$) one obtains the following relationship

$$\frac{A_T}{A} = \frac{s_T}{s_L} \quad (4.89)$$

For the corrugated flamelet regime Damköhler [46] stated that the interaction of the flame front and turbulence is purely kinematic and he derived the following relationship

$$\frac{A_T}{A} \sim \frac{u'}{s_L} \quad (4.90)$$

Considering equation (4.89) and (4.90) one obtains that the turbulent flame speed s_T is in the same order of magnitude than the turbulence fluctuation u' . This relationship was confirmed for the G-equation modeling by Peters [3].

$$s_T \sim u' \quad (4.91)$$

For the thin reactions regime Damköhler [46] stated that the turbulence modifies the transport between reaction zone and unburnt gas. Based on the relationship between laminar flame speed s_L and molecular diffusivity D in equation (4.92), he proposed a similar relationship for the turbulent flame speed s_T and the turbulent diffusivity D_t in equation (4.93). Thereby, it is assumed that the chemical time scale τ_c is not affected by the turbulence [3].

$$s_L \sim \left(\frac{D}{\tau_c} \right)^{1/2} \quad (4.92)$$

$$s_T \sim \left(\frac{D_t}{\tau_c} \right)^{1/2} \quad (4.93)$$

Based on equation (4.92) and (4.93) Damköhler derived a relationship of the turbulent flame speed and laminar flame speed.

$$\frac{s_T}{s_L} \sim \left(\frac{D_t}{D} \right)^{1/2} \quad (4.94)$$

Using the proportionality of turbulent diffusivity and the product of turbulence fluctuation and turbulent length scale $D_t \sim u' l$ and the proportionality of molecular diffusivity and product of laminar flame speed and flame thickness $D \sim s_L \delta_L$ one obtains the relationship in equation (4.95). Based on a similarity analysis with the G-equation model Peters [3] stated that the thin reactions regime is governed by scalar dissipation.

$$\frac{s_T}{s_L} \sim \left(\frac{u' l}{s_L \delta_L} \right)^{1/2} \quad (4.95)$$

*Assumption of an idealized premixed steady flame in a pipe according to Peters [3].

Based on equation (4.95) the expression in equation (4.96) is derived which introduces an exponent n^* and a constant C which is expected to be dependent on the ratio l/δ_L [3]. The first term on the right hand side includes the condition $u' \rightarrow 0$ where $s_T = s_L$.

$$\frac{s_T}{s_L} = 1 + C \cdot \left(\frac{u'}{s_L} \right)^n \quad (4.96)$$

The best practice parameters in the SRM which were used in [48] and [24] are summarized in table 7.

Parameter	Value
C	2.5
n	0.9

Table 7: Model parameters for the simple turbulent flame propagation model.

Peters model Peters introduced the G-equation model in equation (4.97) to describe the turbulent premixed combustion in the corrugated flamelet and thin reactions regime [3].

$$\rho \frac{\partial G}{\partial t} + \rho \mathbf{u} \cdot \nabla G = (\rho s_L^0) \sigma - (\rho D) \kappa \sigma \quad \text{with } G(\mathbf{x}, t) = G_0 \quad (4.97)$$

Therein, ρ is the density, \mathbf{u} is the velocity vector, s_L^0 is the unstretched laminar burning velocity, \mathbf{x} is the location, t is the time, σ is defined as the gradient $|\nabla G|$ of the G-field and κ is the curvature. Peters [3] introduced $G = G_0$ as the instantaneous flame front which is related to the instantaneous flame front surface area A_T . For a two-dimensional representation of the flame front denoted by $G = G_0$ he derived the relationship between a differential section dS of G , a differential section dy of the cross-sectional area A and the gradient σ .

$$\frac{dS}{dy} = \sigma \quad (4.98)$$

Therefor, σ can also be denoted as the flame surface area ratio. Following, he then derived a transport equation for σ similar to equation (4.97).

$$\frac{\partial \sigma}{\partial t} + \mathbf{u} \cdot \nabla \sigma = -\mathbf{n} \cdot \nabla \mathbf{u} \cdot \mathbf{n} \sigma + s_L^0 (\kappa \sigma + \nabla^2 G) + D \mathbf{n} \cdot \nabla (\kappa \sigma) \quad (4.99)$$

Therein, \mathbf{n} is the normal vector to the flame front $G = G_0$ and D is the molecular diffusivity. The terms on the left hand side describe the accumulation and convection term. The first term on the right hand side describes the production of σ because of straining by the flow field. The second term describes the kinematic influence and the third term describes the scalar dissipation influence. Peters introduced an averaging of $\bar{\sigma}$ and obtained a mean gradient of the G-field $|\nabla \tilde{G}|$ and a turbulent part $\bar{\sigma}_t$.

$$\bar{\sigma} = |\nabla \tilde{G}| + \bar{\sigma}_t \quad (4.100)$$

By insertion of definition (4.100) into equation (4.99) he obtained a transport equation for the turbulent part of the flame surface area ratio $\bar{\sigma}_t$. The transport equation can be simplified

*The value of exponent n is usually in the range of 0.5 – 1.0.

by considering a steady planar flame which allows to eliminate the accumulation, convection and tangential transport term. Further, the production term due to mean velocity gradients is eliminated by assuming that the result of mean velocity production is much smaller than the result of turbulent production.

$$c_1 \cdot \frac{D_t}{\delta_{L,t}^2} - c_2 \cdot \frac{s_L^0}{\delta_{L,t}} \frac{\bar{\sigma}_t}{|\nabla \tilde{G}|} - c_3 \cdot \frac{D}{\delta_{L,t}^2} \frac{\bar{\sigma}_t^2}{|\nabla \tilde{G}|^2} = 0 \quad (4.101)$$

The constants c_1, c_2, c_3 and the flame brush thickness $\delta_{L,t}$ and the turbulent diffusivity D_t are replaced with suitable terms based on the turbulent length scale l and the turbulence fluctuation u' . Following, for the case of constant density the difference of the turbulent and laminar flame speed is introduced.

$$\Delta s = s_T - s_L = s_L \frac{\bar{\sigma}_t}{|\nabla \tilde{G}|} \quad (4.102)$$

The following quadratic equation is obtained after insertion of above solutions and additional conversions.

$$\left(\frac{\Delta s}{s_L}\right)^2 + \frac{a_4 b_3^2 l}{2b_1 \delta_L} \left(\frac{\Delta s}{s_L}\right) - a_4 b_3^2 \frac{u'l}{s_L \delta_L} = 0 \quad (4.103)$$

Solving the quadratic equation only the positive solution of the quadratic equation is considered since the negative solution has no physical significance.

$$\frac{\Delta s}{s_L} = -\frac{a_4 b_3^2 l}{2b_1 \delta_L} + \left[\left(\frac{a_4 b_3^2 l}{2b_1 \delta_L} \right)^2 + a_4 b_3^2 \frac{u'l}{s_L \delta_L} \right]^{1/2} \quad (4.104)$$

Conversion of the equation and insertion of the Damköhler number Da^* yields the following equation for the ratio of turbulent and laminar flame speed.

$$\frac{s_T}{s_L} = 1 + \frac{u'}{s_L} \left\{ -\frac{a_4 b_3^2}{2b_1} Da + \left[\left(\frac{a_4 b_3^2}{2b_1} Da \right)^2 + a_4 b_3^2 Da \right]^{\frac{1}{2}} \right\} \quad (4.105)$$

The model parameters a_4, b_3 and b_1 are defined according to Peters [3] and are summarized in table 8.

Parameter	Value
a_4	0.78
b_3	1.0
b_1	2.0

Table 8: Model parameters for the Peters turbulent flame propagation model.

*Here equation (4.84) is inserted.

Kolla model In his thesis Kolla [49] proposed an algebraic scalar dissipation rate model which is valid for large Da numbers.

$$\tilde{\varepsilon}_c \simeq \frac{1}{\beta'} \left([2K_c^* - \tau C_4] \frac{s_L}{\delta_L} + C_3 \frac{\tilde{\varepsilon}}{k} \right) \tilde{c}'^{1/2} \quad (4.106)$$

Following, the KPP theorem [50, 51] provided an equation of turbulent flame speed (4.107) which could be used to validate the new scalar dissipation rate model.

$$s_T = 2 \sqrt{\frac{\nu_t}{\rho_u S c_c} \left(\frac{\partial \bar{\omega}}{\partial \tilde{c}} \right)_{\tilde{c} \rightarrow 0}} \quad (4.107)$$

Therein, ν_t is the turbulent viscosity which is defined by equation (4.63), ρ_u is the density of the unburnt mixture, $S c_c$ is the Schmidt number of the progress variable \tilde{c} and $\bar{\omega}$ is the average reaction rate. Bray [52] introduced a relationship between the reaction rate $\bar{\omega}$ and the scalar dissipation rate $\tilde{\varepsilon}_c$.

$$\bar{\omega} = \frac{2}{(2C_m - 1)} \bar{\rho} \tilde{\varepsilon}_c \quad (4.108)$$

Therein, C_m has typically a value of 0.7 [53]. The term $\tilde{c}'^{1/2}$ in equation (4.106) is approximated with $\tilde{c}'^{1/2} \approx \tilde{c}(1 - \tilde{c})$ for high Da numbers [49]. After some adjustments the equation (4.109) is obtained for the ratio of turbulent and laminar flame speed. The model parameters are outlined in table 9. The model was implemented and validated by Bjerkborn et al. in SRM [17, 18].

$$\frac{s_T}{s_L} = \left\{ \frac{18 \cdot C_\mu}{\beta' \cdot (2C_m - 1)} \left[[2K_c^* - \tau \cdot C_4] \left(\frac{u'l}{s_L \delta_L} \right) + \frac{2C_3}{3} \left(\frac{u'}{s_L} \right)^2 \right] \right\}^{1/2} \quad (4.109)$$

Parameter	Value
C_μ	0.09
β'	6.7
C_m	0.7
K_c^*/τ	> 0.8 (for methane-air flames)
τ	$(T_{ad} - T_u)/T_u$
C_4	$1.1 (1 + Ka)^{-0.4}$
C_3	$1.5/(1 + Ka^{-0.5})$

Table 9: Model parameters for the Kolla turbulent flame propagation model.

The performance of the three turbulent flame propagation models is compared in figure 15. The turbulence fluctuation u' is calculated based on the integral length scale and scalar mixing time according to $u' = l_I/\tau_\phi$ where $l_I = 0.014m$ and $\tau_\phi = 2.6ms$. The Simple model incorporates the ratio of integral length scale and flame thickness indirectly by the model constant C_* . For the Peters and Kolla model the flame thickness is set to $0.01mm$. The Simple and Peters model show a similar trend for the calculated flame radius and turbulent flame speed. The Kolla model calculates a higher turbulent flame speed wherefor the calculated

*For this investigation the model constant C is set to 2.5.

flame radius becomes higher. Kolla et al. showed in their publication [54] that the model predicts higher s_T/s_L values at higher u'/s_L values in comparison to the Peters model wherefor the trend shown in figure 15 is in agreement.

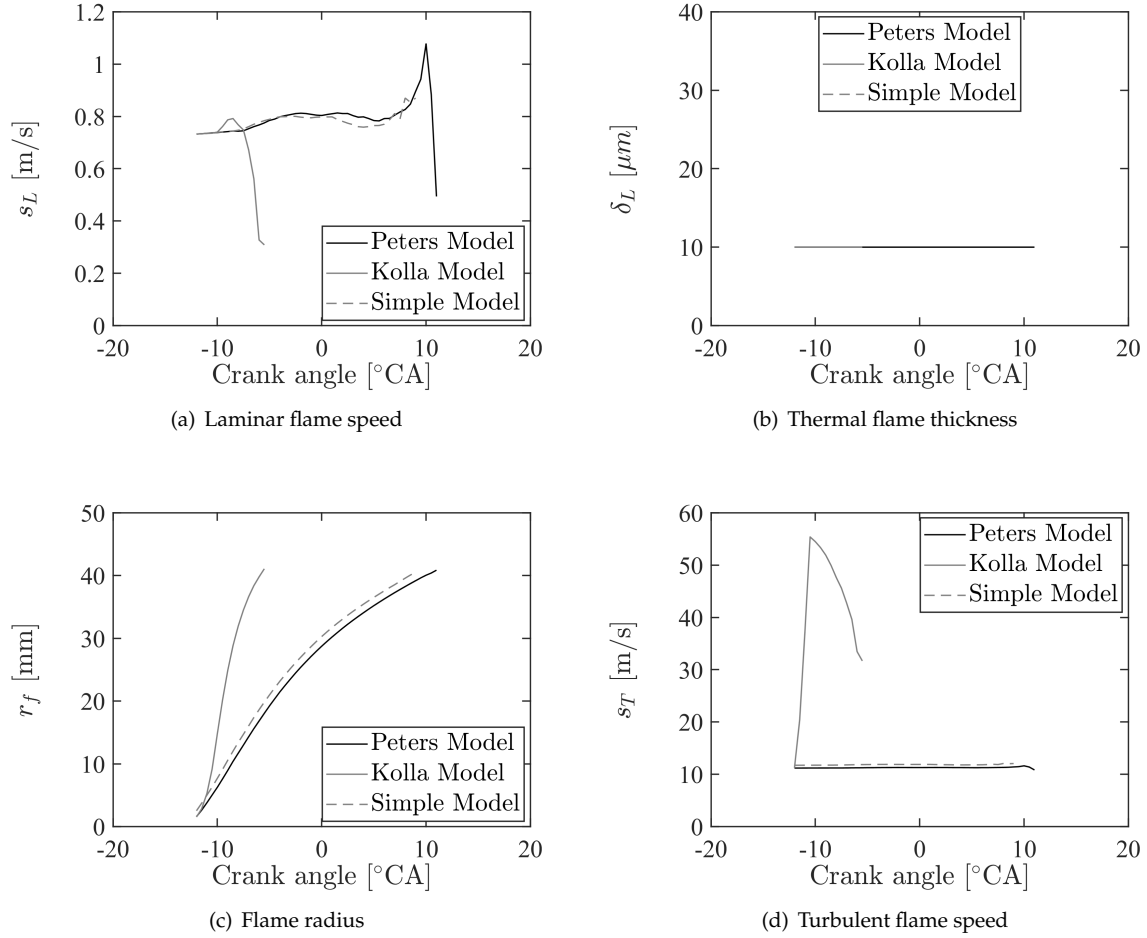


Figure 15: Comparison of the laminar flame speed, flame thickness, flame radius and turbulent flame speed for Simple, Peters and Kolla turbulent flame propagation models at 2000 rpm and 6 bar IMEP. The spark timing is at -13.3°CA .

Early flame propagation The early flame propagation model is implemented based on the work of Su et al. [55] and a similar approach was proposed by Keum et al. [56]. The laminar-to-turbulent transition is characterized by the transition scale η_0 .

$$\eta_0 = k \cdot l_G + \eta_c \quad (4.110)$$

The transition scale η_0 is a function of the Gibson scale l_G defined by Peters [3] and the correction parameter η_c defined by Su et al. [55]. The Gibson scale is defined as the smallest eddy size where the eddy still interacts with the flame front. It is derived for the condition that the turnover velocity of the turbulent eddy u_η is equal to the laminar flame speed s_L . The correction factor η_c accounts for inaccuracies of the transition prediction introduced by near-wall turbulence effects at the spark plug [55]. The constant k is larger than 1 and should have the same value for all operating points of the engine investigated.

The Gibson scale is calculated based on the laminar flame speed s_L and the dissipation ε . The dissipation ε is determined according to the equation (4.52) of the $k - \varepsilon$ turbulence model.

$$l_G = \frac{s_L^3}{\varepsilon} \quad (4.111)$$

The transition between laminar flame velocity s_L and turbulent flame velocity s_T is governed by the parameter w .

$$s_T = (1 - w) \cdot s_L + w \cdot s_T \quad (4.112)$$

It is modeled as a function of the flame radius r_f , the flame thickness δ_L and the transition scale η_0 .

$$w = \frac{1}{2} \cdot \left\{ \tanh \left[\frac{4(r_f - \delta_L)}{\eta_0 - \delta_L} - 2 \right] + 1 \right\} \quad (4.113)$$

The two model parameters that can be adjusted to match the flame propagation of the experiments are summarized in table 10.

Parameter	Value
k	5.0
η_c	3 mm

Table 10: Model parameters of the early flame propagation model by Su et al. [55].

The effect of the variation of the model constant k and the near-wall correction factor η_c on the flame radius r_f is outlined in figure 16. The increase of the value of the model constant k extends the Gibson scale to larger eddy sizes, wherefor the laminar-to-turbulent transition takes longer time. The same effect can be observed by increasing the value of the correction factor η_c since both parameters affect the transition scale η_0 .

In figure 17 the performance of the early flame propagation model (LTC) is compared to a case without transition (NLT). For the LTC case the model constant k is set to 5^{*}, while the correction factor η_c is set to 9mm[†]. For the NLT case the spark timing is delayed by 5.5°CA to match the center of combustion of both cases. Further, the flame thickness δ_L is defined as a constant and is set to 40μm. During the initial phase after spark ignition until -3°CA both cases show a constant laminar flame speed s_L . The LTC case shows a slight decrease in the flame thickness δ_L and a steady increase of the flame radius r_f . The turbulent flame speed s_T of the LTC case shows a stronger increase at the start because of the initialization of the ignition kernel. The ignition kernel is initialized with 0.002% of the total mass or 3% of the injected fuel mass. Subsequently, s_T is slowly accelerating according to the laminar-to-turbulent transition in equation (4.113). After the flame propagation becomes fully turbulent

^{*}This value is also used by Su et al. [55].

[†]Su et al. [55] used a value of 1.5mm.

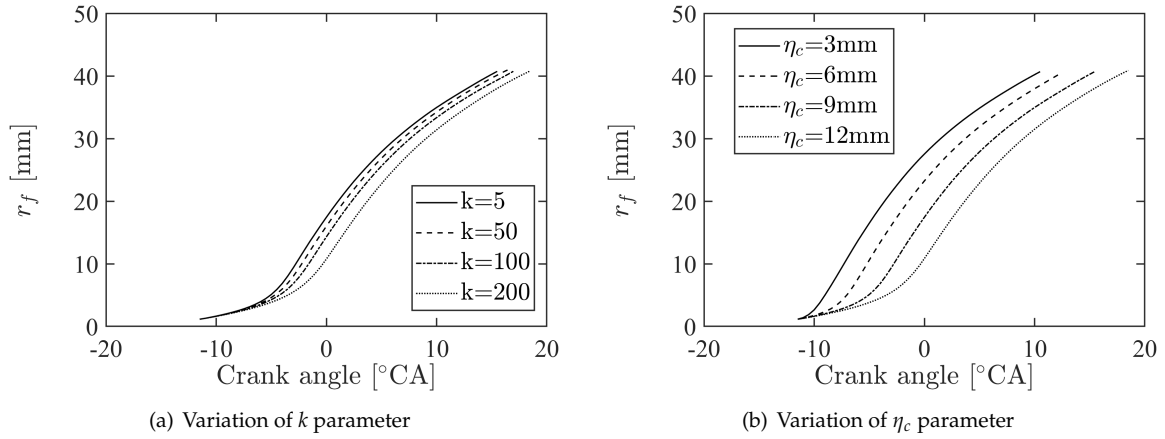


Figure 16: Comparison of temporal evolution of the flame radius r_f for different k and η_c parameter values of the early flame propagation model at 2000 rpm and 6 bar IMEP.

at -3°CA the flame thickness is decreasing even more becomes of the increase of laminar flame speed s_L and unburnt temperature T_u . The NLT case starts with fully turbulent flame propagation from the start and the range of s_T and r_f is similar to the LTC model. This was achieved by adjusted the constant flame thickness of the NLT model to the value of $40\mu\text{m}$.

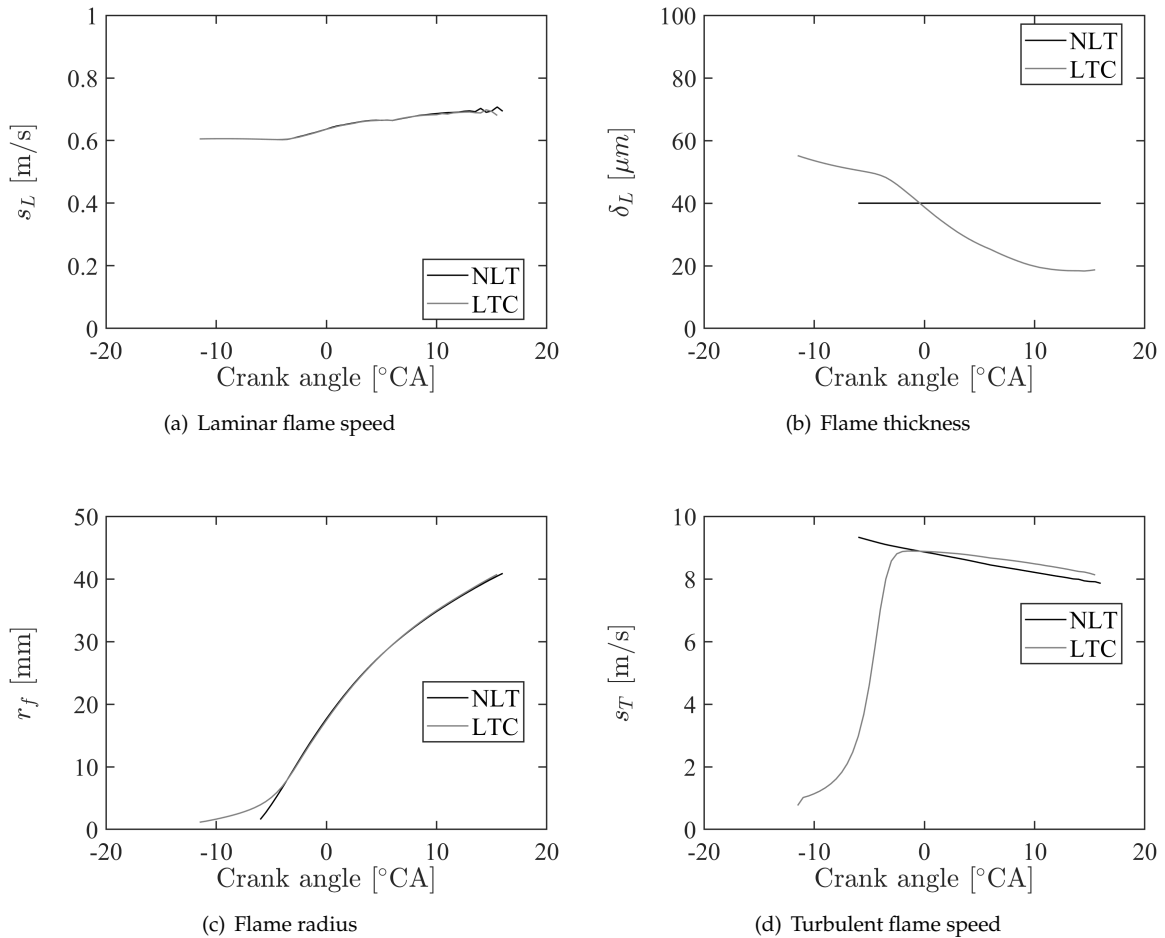


Figure 17: Comparison of temporal evolution of the laminar flame speed, thermal flame thickness, flame radius and turbulent flame speed for NLT and LTC at 2000 rpm and 6 bar IMEP.

4.3.3 Stochastic combustion model

Direct injection of fuel in SI engines can lead to inhomogeneous mixtures ahead of the flame front which affect the local flame propagation. Hélie et al. [57] performed DNS calculations of a mean stoichiometric mixture with various degree of inhomogeneity of the composition. They showed that the local mass burning rate per unit premixed flame surface area is affected by the variance of the mixture composition. The overall reaction rate was 20% lower compared to a homogeneously premixed case. Pasquier et al. [58] performed experimental optical measurements of homogeneous and stratified propane-air mixtures to determine the local flame propagation velocities. They stated that local flame propagation of stoichiometric equivalence ratio is only slightly affected by stratified conditions. For lean equivalence ratios their results revealed an enhancement of local flame propagation in locally lean mixtures. This effect is attributed to the burning of locally rich regions which increase the burnt temperature. The higher burnt temperature improved the heat conduction into the locally lean mixtures wherefor flame propagation was enhanced.

The stochastic combustion model accounts for the effect of equivalence ratio inhomogeneity on the mass burn rate by incorporating a probability density function $f(\phi)$ shown in figure 18. The distribution $f(\phi)$ is determined according to the s_L -profile of a gasoline flame at 15bar pressure and 800K temperature.* The stochastic combustion algorithm implemented in SRM in explained below.

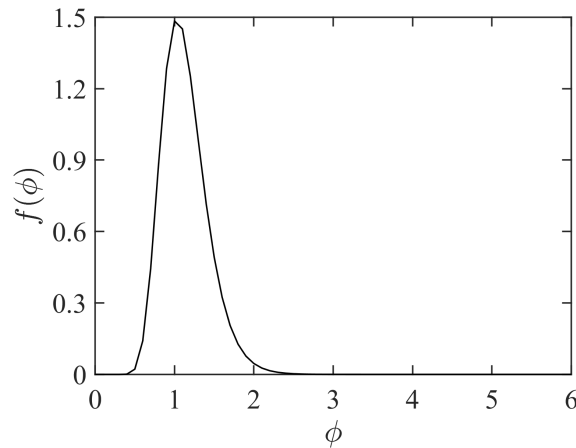


Figure 18: Probability density function based on equivalence ratio of gasoline for stochastic combustion algorithm in SRM.

The stochastic algorithm is evaluated in comparison to an averaging algorithm for two different relative air-fuel ratios $\lambda=1.0$ and $\lambda=1.5$ in figure 19. The averaging algorithm calculates the mean properties of the unburnt notional particles and creates a new burnt notional particle with the properties of the mean unburnt mixture.† The stochastic algorithm selects randomly an unburnt notional particle and moves it to the burnt zone. The scalar mixing time factor $C_{\phi,u}$ is increased to create an inhomogeneous mixture and the burnt scalar

*These conditions should reflect a mean condition in the operation of a SI engine.

†This algorithm is applied in SRM by Pasternak et al. [48] and Netzer et al. [59] to investigate SI engine performance.

mixing time factor $C_{\phi,b}$ is set to 0.001 which makes the burnt notional particles mix fast. For the $\lambda=1.0$ case the stochastic model burns rich at 10% combustion progress because the distribution $f(\phi)$ is skewed to the rich side (see figure 18). Further, the maximum burnt temperature is lower compared to the averaging model and the combustion progress is delayed. At 50% combustion progress more rich particles are burnt for the stochastic model compared to the averaging model. However, the equivalence ratio of the burnt particles approaches the averaging model results. For lean conditions at $\lambda=1.5$ the stochastic model burns close to stoichiometric conditions at 10% progress and the maximum burnt temperature is higher compared to the averaging model. At 50% progress the burnt equivalence ratio of the stochastic model approaches the result of the averaging model while the burnt temperature remains higher.

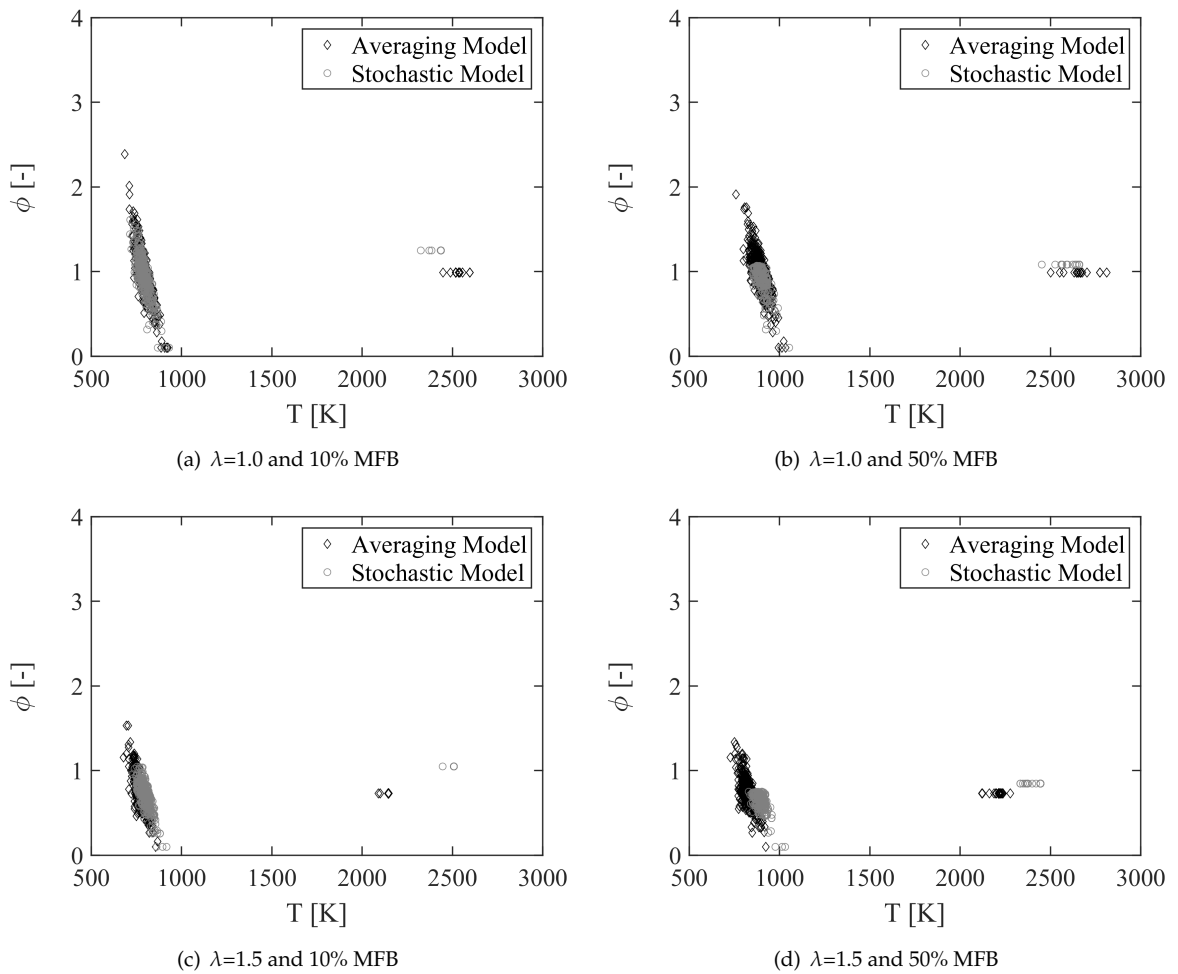


Figure 19: ϕ -T maps at 10% and 50% combustion progress for $\lambda=1.0$ and $\lambda=1.5$ at 2000 rpm and 6 bar IMEP.

Stochastic combustion algorithm During the initialisation step of the stochastic algorithm the cumulative distribution function $F(\phi)$ is calculated based on the user-provided probability density function $f(\phi)$ in figure 18.

$$F(\phi) = \int f(\phi) d\phi \quad (4.114)$$

where ϕ represents the equivalence ratio of the unburnt mixture.

After spark timing the flame propagation is initiated by establishing the ignition kernel at the spark plug. The stochastic combustion algorithm is called and generates a homogeneously distributed random number RN in the range between 0 and 1.

$$RN \in \{0,1\} \quad (4.115)$$

Using the random number RN the respective probability of equivalence ratio ϕ_{RN} is determined based on $F(\phi)$ in equation (4.114).

$$RN = F(\phi) \rightarrow \phi_{RN} \quad (4.116)$$

Next the algorithm loops over the number of notional particles of the unburnt zone to determine the notional particle * whos equivalence ratio is closest to the randomly selected ϕ_{RN} .

$$\phi^* = \min(|\phi_i - \phi_{RN}|) \quad (4.117)$$

According to the notional particle mass and the calculated burnt mass for the current time step t the notional particle is moved partially or completely from the unburnt to the burnt zone.

4.3.4 Crevice model

The crevice volume at the piston ring land of spark ignition engines contributes to the unburnt hydrocarbon engine-out emissions [60]. The early injected gasoline fuel penetrates into the crevice volume during the compression stroke and becomes inaccessible for the flame [61]. During the expansion stroke the unburnt fuel mass is released from the crevice volume to the bulk gas and burns only partially wherefor unburnt hydrocarbon emissions are increased. The crevice volume is implemented as a third zone into the SRM. The specifications of the implementation are highlighted in the paragraph below. The crevice volume is treated adiabatically and the reactants trapped are not participating in chemical reactions. Mass can be pushed to the crevice volume or extracted from it wherefor the zone mass proportions (ZMP) are changing over time as shown in figure 20 (a). The maximum percentage of total mass trapped in the crevice volume is approximately 5% at the time of maximum cylinder pressure. The temperature in the crevice zone follows the one from the unburnt mixture as shown in figure 20 (b). In contrast Malfi et al. [62] determined the temperature in the crevice volume in between the unburnt and burnt temperature using an in-house developed model.

The volume of the crevice can differ for different engines. Hence, the model parameter C_{crev} is introduced in SRM to scale the volume up or down. The effect of the crevice volume factor is shown in figure 21.* During the compression stroke the HC mole fraction is increasing and reaches its maximum shortly before TDC as shown in figure 21 (a). The size of the crevice

*The default crevice volume is 2% of the clearance volume.

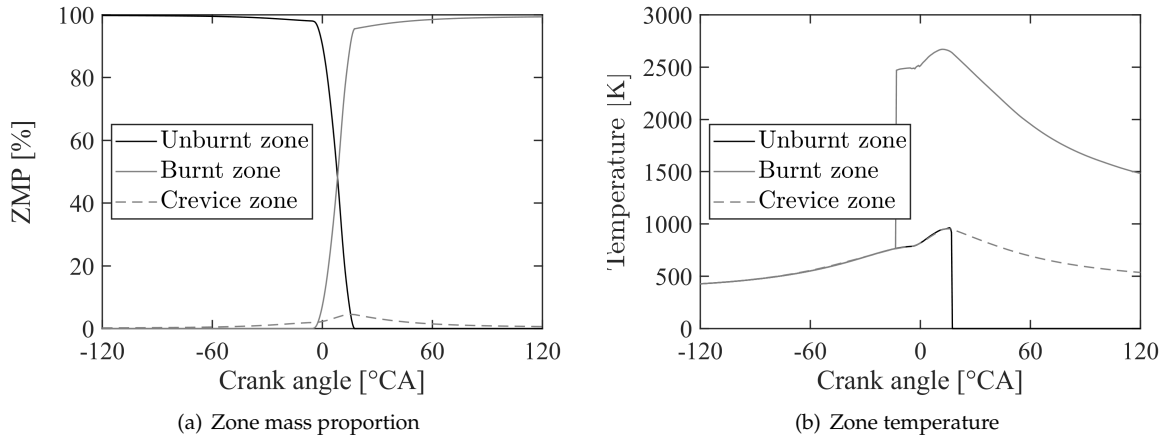


Figure 20: Comparison of zone mass proportion and temperature of unburnt zone, burnt zone and crevice zone at 2000 rpm and 6 bar IMEP.

volume shows no distinct effect for the HC mole fraction in the crevice. During the expansion stroke the HC mole fraction is only slightly decreasing. The overall HC mole fraction in figure 21 (b) is increasing during the beginning of direct injection at -120 °CA and is composed of unburnt fuel species. Subsequently the HC mole fractions remain constant until start of combustion shortly before TDC. During the combustion the fuel is oxidized and the HC mole fractions decrease rapidly. At the end of combustion at 20 °CA the consumption of HC is slowing down and a clear effect of the crevice volume size is observed. The larger crevice volume ($C_{crev}=4.0$) shows higher HC mole fractions at the end of combustion because more unburnt HC mass is trapped in the crevice volume. The unburnt HC is released from the crevice volume during the expansion stroke but can only be partially oxidized because of the low temperatures. Malfi et al. [62] reported similar results of the release of unburnt hydrocarbons during the expansion stroke as a potential source of HC emissions in lean-burn engines.

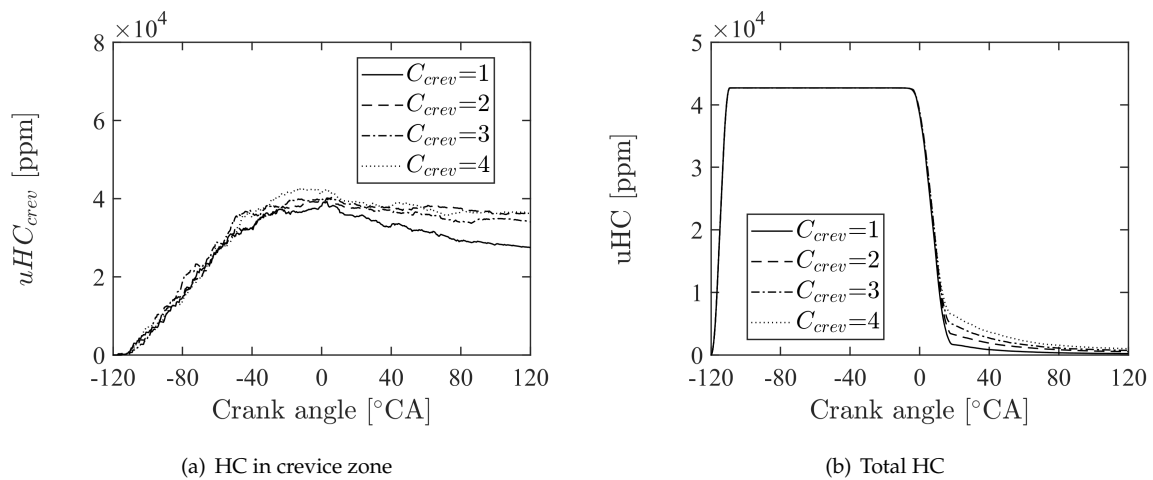


Figure 21: Comparison of unburnt hydrocarbon mole fraction in the crevice zone and in total for different C_{crev} values at 2000 rpm and 6 bar IMEP. Start of fuel injection is at -120 °CA. Firing top dead center is at 0 °CA.

Crevice zone algorithm The geometrical volume $V_{crev,geom}$ of the piston crevice is set as 2% of the clearance volume $V_{clearance}$ and can be modified by the factor C_{crev} in the following equation.

$$V_{crev,geom} = C_{crev} \cdot 0.02 \cdot V_{clearance} \quad (4.118)$$

The thermodynamic volume $V_{crev,therm}$ of the crevice is determined by assuming ideal gas for the notional particles in the crevice N_{crev} using the following equation:

$$V_{crev,therm} = \sum_{i=1}^{N_{crev}} \frac{R \cdot W_i \cdot m_{gas} \cdot T_i}{p \cdot M_i} \quad (4.119)$$

The difference between the two volumes ΔV_{crev} drives the mass transfer between bulk and crevice.

$$\Delta V_{crev} = V_{crev,geom} - V_{crev,therm} \quad (4.120)$$

If the $\Delta V_{crev} > 1$ then mass from the unburnt zone is moved to the crevice zone. The notional particle moved partially or completely to the crevice zone is selected according to a homogeneously distributed random number RN . However, if the reaction progress c of the selected notional particle is larger than 0.001 due to auto-ignition another notional particle is randomly selected.

$$RN \in \{0,1\} \quad (4.121)$$

If the $\Delta V_{crev} < 1$ then mass from the crevice zone is moved to the unburnt zone. If the unburnt zone is completely consumed ($ZMP=0$) then the mass is moved to the burnt zone.

The extension of the crevice zone algorithm allows to account for the influence of turbulent kinetic energy on the amount of unburnt hydrocarbons to be trapped in the crevice zone. To achieve this, a scaling parameter $\alpha_{tke,crev}$ based on the turbulent kinetic energy k is defined:

$$\alpha_{tke,crev} = \frac{k - k_{min,crev}}{k_{max,crev} - k_{min,crev}} \quad (4.122)$$

where k is calculated based on equation (4.51) and $k_{min,crev}$ and $k_{max,crev}$ are model constants. Following, a scaling factor for the unburnt hydrocarbons (HC) is defined as well:

$$\alpha_{y_{HC,(n),crev}} = \frac{y_{HC,(n)} - y_{HC,min,crev}}{y_{HC,max,crev} - y_{HC,min,crev}} \quad (4.123)$$

where $y_{HC,(n)}$ is the mass fraction of unburnt hydrocarbons of the notional particle with index (n) and $y_{HC,min,crev}$ and $y_{HC,max,crev}$ are the respective minimum and maximum mass fractions of unburnt hydrocarbons of all the notional particles $[1..N_p]$ at the cur-

rent time step.

Finally, the notional particle (n) to be moved to the crevice zone is selected by determining the minimum difference between the two scaling factors of equations (4.122) and (4.123).

$$\min \left(|\alpha_{tke,crev} - \alpha_{y_{HC,(n),crev}}| \right) \rightarrow (n) \quad (4.124)$$

The parameter $k_{max,crev}$ of the extended crevice model will therefor control the upper limit and the parameter $k_{min,crev}$ will control the lower limit of turbulent kinetic energy at which HC-rich particles are preferably pushed to the crevice volume.*

Increasing the model parameter $k_{max,crev}$ will decrease the probability to push HC-rich notional particles to the crevice volume wherefor the HC mole fraction is decreasing in the crevice as shown in figure 22 (a).[†] For the case with $k_{max,crev} = 100$ the HC mole fraction is increasing strongest during the compression stroke because the value of $k_{max,crev} = 100$ is close to the calculated turbulent kinetic energy in the system. Shortly before TDC at 0°CA the HC mole fraction is dropping because of a decline in the turbulent kinetic energy wherefor less HC-rich notional particles are moved to the crevice volume. The decrease of $k_{max,crev}$ shows a small effect for the overall HC mole fractions in figure 22 (b). The most noticeable increase in HC mole fraction at the end of combustion at 20°CA is observed for case $k_{max,crev} = 100$.

Increasing the model parameter $k_{min,crev}$ will decrease the probability to push HC-rich notional particles to the crevice volume.[‡] However, figure 22 (c) show a slight increase of HC mole fraction in the crevice while no significant impact is found for the total HC mole fraction in figure 22 (d). For the subsequent investigations the $k_{max,crev}$ model parameter is set to 500 and the $k_{min,crev}$ model parameter is set to 1.

4.3.5 Cyclic variation model

The cyclic variation model was introduced by Netzer et al. [19] in SRM to investigate the influence on knocking combustion in a spark ignition engine. They applied normal distributions for the scalar mixing time factor C_ϕ and the spark timing delay $\Delta\theta_{ST}$ to account for stochastic variation in the turbulent mixing and initial flame kernel development close to the spark plug. Pera et al. [63] reported similar results for their two-dimensional DNS simulation of the early flame kernel development for a stoichiometric and lean mixture. They reported the strongest influence on cyclic variation for stoichiometric mixtures by initial kernel size and turbulence structure while turbulence intensity and integral length scale had a reduced effect. For lean mixtures the influence of initial kernel size, turbulence intensity and integral length scale is increasing while for the turbulence structure it is decreasing.

The effect of turbulence intensity on the cyclic variation is accounted for by applying a normal

*Turbulent kinetic energy is used as an indicator for the strength of the large scale flow motion. It is assumed that a strong flow motion will lead to more transport of unburnt fuel towards the crevice volume.

[†]The model parameter $k_{min,crev}$ is set to 1 for this investigation.

[‡]The model parameter $k_{max,crev}$ is set to 500 for this investigation.

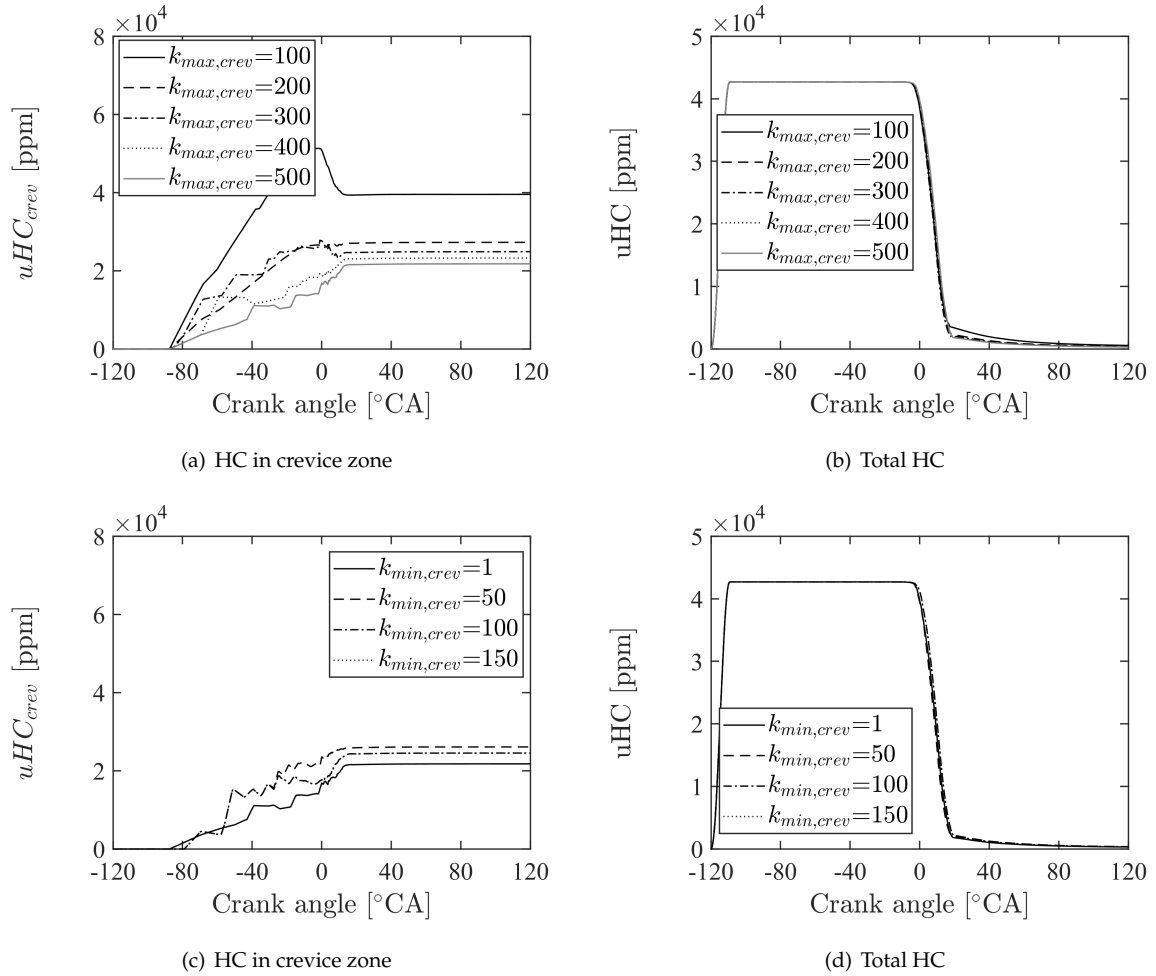


Figure 22: Comparison of unburnt hydrocarbon mole fraction in the crevice zone and in total for different $k_{max,crev}$ and $k_{min,crev}$ values at 2000 rpm and 6 bar IMEP. Start of fuel injection is at -120 °CA. Firing top dead center is at 0 °CA.

distribution $f(u')$ as shown in figure 23 (a). The standard deviation $\sigma_{u'}$ is set in the range of 0.1 - 0.3 m/s. The effect of initial kernel size variance is indirectly captured by accounting for slower or faster initial flame kernel propagation using a normal distribution $f(\theta_{ST})$ for the spark timing θ_{ST} as shown in figure 23 (b). The standard deviation $\sigma_{\theta_{ST}}$ is usually set in the range of 1 - 5 °CA.

The simulation results of a SI engine operated at 2000 rpm and 20 bar IMEP are compared to the experiments in figure 24.* The standard deviation $\sigma_{\theta_{ST}}$ is set to 1.1 °CA and the standard deviation $\sigma_{u'}$ is set to 0.1 m/s. The SRM shows a close match of the experiment cylinder pressure in figure 24 (a). The cyclic variation of the maximum cylinder pressure p_{max} and the crank angle of maximum cylinder pressure $\theta_{p_{max}}$ shown in figure 24 (b) to (d) is well matched. However, the findings of Pera et al. [63] suggest that the choice of u' for modeling of cyclic variations seem not to be ideal. The largest effect on cyclic variation is reported for the variance in turbulence structure wherefor the choice of Netzer et al. [19] using the scalar mixing time τ_{ϕ} as variance parameter is probably better.

*SRM simulations are performed with 500 notional particles, 0.5 °CA time step size, 150 stochastic cycles and Curl mixing model.

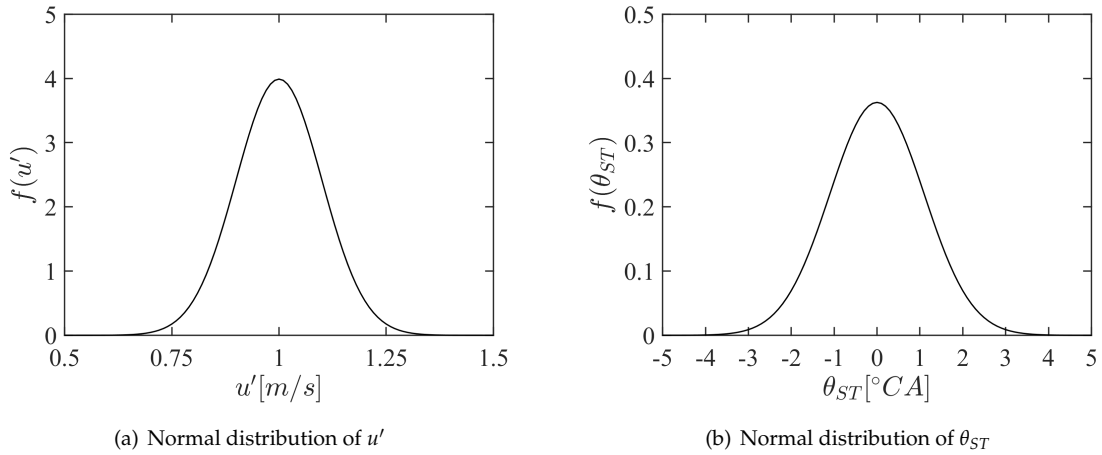


Figure 23: Normal distribution of u' and θ_{ST} of the cyclic variation model.

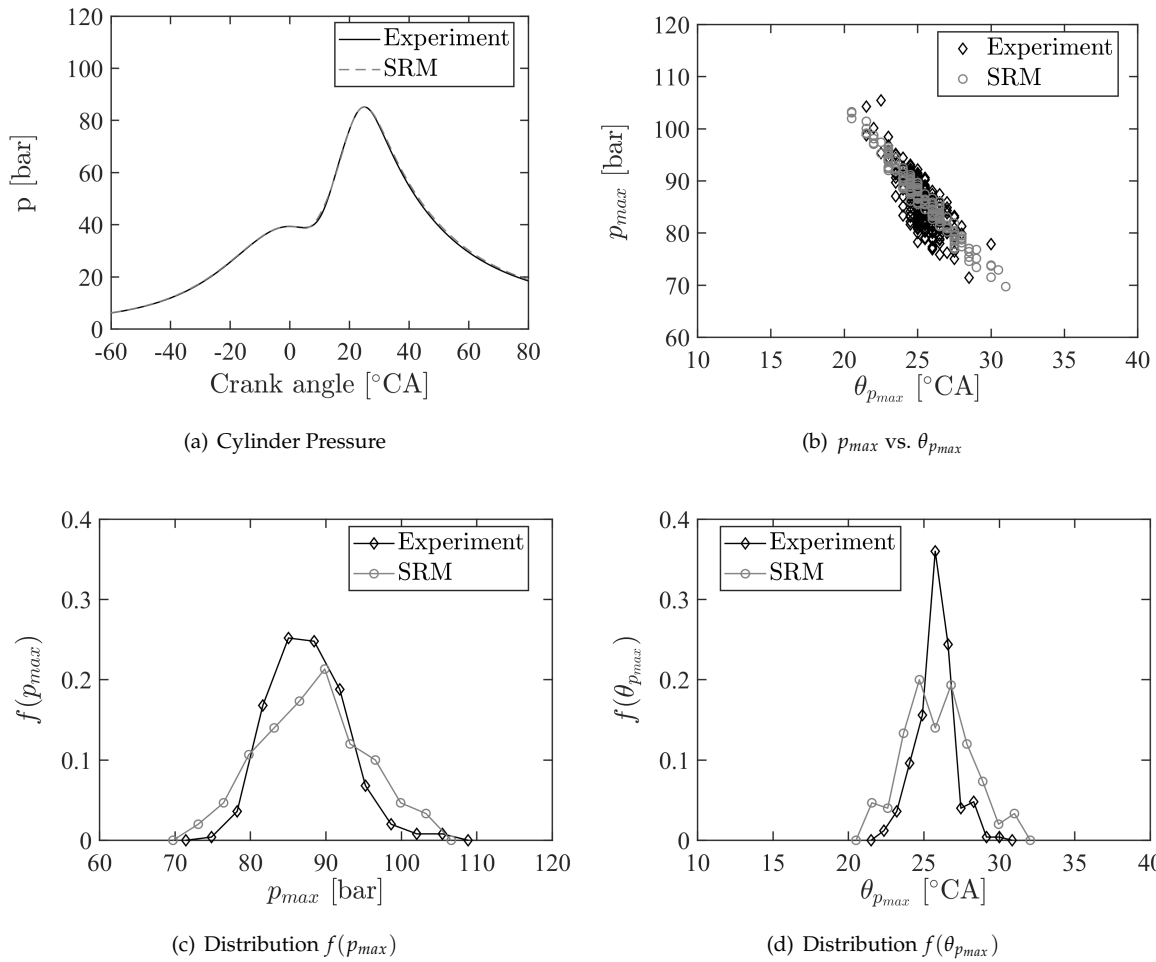


Figure 24: SRM simulation results for cyclic variation at 2000 rpm and 20 bar IMEP. 150 stochastic cycles are calculated by SRM and 150 cycles are recorded in the experiment.

Cyclic variation algorithm The cyclic variation model is initialized at the beginning of the simulation run. The standard deviation of the normal distribution of spark timing $\sigma_{\theta_{ST}}$ and turbulence frequency $\sigma_{u'}$ are defined a priori. Then, a homogeneously

distributed random number RN_1 is drawn.

$$RN_1 \in \{0, 1\} \quad (4.125)$$

The random number RN_1 and the standard deviation of spark timing are used to calculate a normal distributed value for every stochastic cycle (m)

$$\theta_{ST,(m)} = \theta_{ST} + \sqrt{2} \cdot \sigma_{\theta_{ST}} \cdot erf^{-1}(2 \cdot RN_1 - 1) \quad (4.126)$$

where $(m) = [1..N_c]$. Subsequently, a second homogeneously distributed random number RN_2 is drawn to determine the normal distribution of the turbulence frequency.

$$RN_2 \in \{0, 1\} \quad (4.127)$$

Again the normal distributed value of the turbulence frequency is calculated for every stochastic cycle using the inverse error function.

$$u'_{(m)} = u' + \sqrt{2} \cdot \sigma_{u'} \cdot erf^{-1}(2 \cdot RN_2 - 1) \quad (4.128)$$

4.4 Modeling of compression ignition engine

The SRM for compression ignition engines with direct injection (DI-SRM) defines the combustion chamber as one zone. The gas composition and enthalpy is described by an ensemble of notional particles. The turbulence in the system is modeled using a $k - \varepsilon$ turbulence model that calculates the generation and dissipation of turbulent kinetic energy k and the change of angular momentum of swirl flow L_S .

4.4.1 $k - \varepsilon$ turbulence model

The $k - \varepsilon$ turbulence model for CI engines is implemented according to the work of Qirui [45]. The model is based on the work of Bossung [10] and the derived equations are based on Wilcox [44]. The model calculates the change of turbulent kinetic energy dk/dt by a set of differential terms which describe the production and dissipation of k in a cylinder-shaped geometry with a swirl motion around the center-axis of the cylinder. The differential terms for valve flow, axial flow, squish flow, local tumble motion, direct injection, swirl flow, compressibility and dissipation outlined in equation (4.129) are described more in detail in the following paragraphs.

$$\begin{aligned} \frac{dk}{dt} = & \left(\frac{dk}{dt} \right)_{inflow,IV/EV} + \left(\frac{dk}{dt} \right)_{axial} \left(\frac{dk}{dt} \right)_{squish} + \left(\frac{dk}{dt} \right)_{local\ tumble} + \left(\frac{dk}{dt} \right)_{injection} \\ & + \left(\frac{dk}{dt} \right)_{swirl} \left(\frac{dk}{dt} \right)_{compressibility} - \varepsilon \end{aligned} \quad (4.129)$$

The production of turbulent kinetic energy is goverend by the flow of gas into the system

through the intake valves ($m_{i,IV}$) and exhaust valves ($m_{i,EV}$) in equation (4.130) and (4.131). The kinetic energy of the inflow is depending on the relative velocity difference between inflow $v_{i,in}$ and instantaneous piston speed c_{pis} *. The characteristic length scale $r_{i,in,IV}$ of the inflow is determined by the valve diameter d_{IV} and the instantaneous valve lift L_{IV} in equation (4.132), where C_{ε_2} is a scaling parameter between the turbulent and integral length scale.† The characteristic length scale $r_{i,in,EV}$ is defined in a similar manner by equation (4.133).*

$$\left(\frac{dk}{dt}\right)_{inflow,IV} = \sum_{i=1}^{N_{in, valve}} 2 \cdot v_t \cdot \left(\frac{v_{i,in} - c_{pis}}{r_{i,in,IV}}\right)^2 \cdot \frac{m_{i,IV}}{m_{gas}} \quad (4.130)$$

$$\left(\frac{dk}{dt}\right)_{inflow,EV} = \begin{cases} \sum_{i=1}^N 2 \cdot v_t \cdot \left(\frac{v_{i,out} - c_{pis}}{r_{i,in,EV}}\right)^2 \cdot \frac{m_{i,EV}}{m_{gas}}, & -360^\circ \leq \theta \leq -180^\circ \\ 0 & \end{cases} \quad (4.131)$$

$$r_{in,IV} = (0.125 \cdot d_{IV} + 0.003) + \frac{L_{IV}}{C_{\varepsilon_2}} \quad (4.132)$$

$$r_{in,EV} = (0.125 \cdot d_{EV} + 0.003) + \frac{L_{EV}}{C_{\varepsilon_2}} \quad (4.133)$$

The model parameter C_{ε_2} affects the amount of turbulent kinetic energy produced by the mass flow of gas into the system. It affects the turbulent kinetic energy in the system during the valve opening as shown in figure 25. Increasing the C_{ε_2} parameter leads to a reduction of the characteristic length scale of the valve flow and an increase of turbulent kinetic energy. The increase of turbulent kinetic energy during the intake valve flow shows no impact during the combustion due to the strong dissipation.

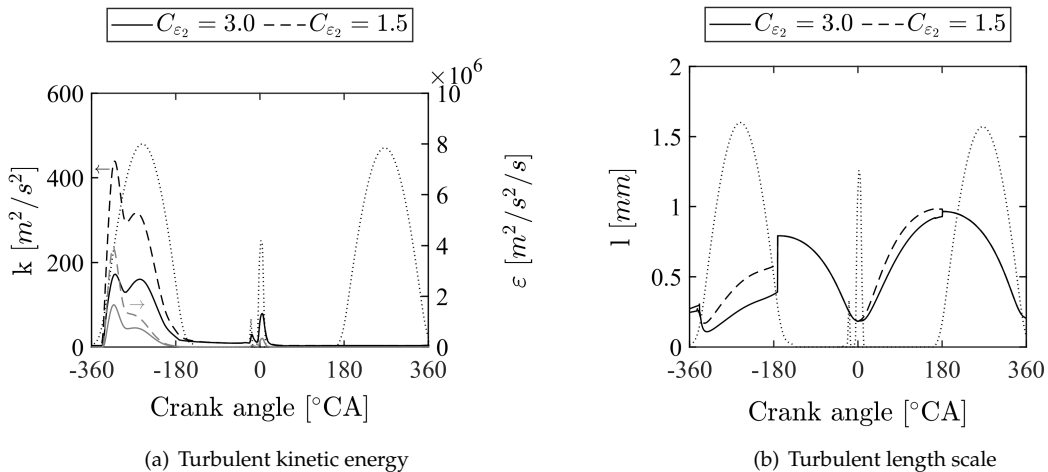


Figure 25: Turbulent kinetic energy, dissipation and length scale in dependence of C_{ε_2} parameter at 1750 rpm and 12 bar IMEP. The dashed lines highlight the intake and exhaust valve lift. The start of fuel injection is at -41°CA .

*The instantaneous piston speed is calculated according to equation (9.8)

†The same scaling parameter C_{ε_2} is also introduced in the Bossung turbulence model in equation (4.75).

*The masses flowing through the valves $m_{i,IV}$ and $m_{i,EV}$, the valve flow velocities $v_{i,in}$ and $v_{i,out}$ and the valve lifts L_{IV} and L_{EV} are determined by the gas exchange model in section 4.2.4.

The source term for production of turbulent kinetic energy from secondary axial flows is outlined in equation (4.134). It follows the same definition as it is used in the Bossung model in equation (4.61).[†]

$$\left(\frac{dk}{dt}\right)_{axial} = \frac{e_{kin,sec}}{\tau_{axial}} \quad (4.134)$$

The production of kinetic energy of secondary flows is depending on the production of kinetic energy of axial flows and the production of turbulent kinetic energy as outlined in equation (4.135).

$$\frac{e_{kin,sec}}{dt} = \max\left(-\frac{de_{kin,axial}}{dt}, 0\right) - \left(\frac{dk}{dt}\right)_{axial} \quad (4.135)$$

The production of kinetic energy of axial flow is calculated according to equation (4.136) and determines a higher energy level during the expansion stroke and exhaust gas exchange.

$$e_{kin,axial} = \begin{cases} \frac{1}{2} \cdot u_{axial}^2, & -360^\circ CA \leq \theta \leq 0^\circ CA \\ \frac{2}{3} \cdot u_{axial}^2 & \end{cases} \quad (4.136)$$

The axial flow velocity u_{axial} is determined according to equation (4.137). During the intake gas exchange the instantaneous piston speed c_{pis} determines the axial flow velocity.* During the compression and expansion stroke additional axial squish flows $u_{sq,axial}$ are induced by the piston bowl geometry.[†]

$$u_{axial} = \begin{cases} c_{pis}, & -360^\circ CA \leq \theta \leq -180^\circ CA \\ 0.5 \cdot \frac{c_{pis} \cdot V + u_{sq,axial} \cdot \left(V_{bowl} + H_1 \cdot \pi \cdot \frac{d_{bowl}^2}{4}\right)}{V} & \end{cases} \quad (4.137)$$

The axial squish velocity $u_{sq,axial}$ is derived from the radial squish velocity $u_{sq,radial}$ assuming a idealized flow field and considering the geometrical dimensions of the piston bowl volume V_{bowl} and the cylinder-shaped volume above the piston bowl [45].

$$u_{sq,axial} = u_{sq,radial} \cdot (H_1 \cdot \pi \cdot d_{bowl}) \cdot \frac{\frac{V_{bowl}}{V_{bowl} + H_1 \cdot \pi \cdot \frac{d_{bowl}^2}{4}}}{\pi \cdot \frac{d_{bowl}^2}{4}} \quad (4.138)$$

$$u_{sq,radial} = -\frac{dV}{dt} \cdot \frac{V_{bowl}}{(V - V_{bowl})} \cdot \frac{d_B^2 - d_{bowl}^2}{4 \cdot d_{bowl}} \quad (4.139)$$

The effect of the axial flow factor on the turbulent kinetic energy and scalar mixing time is shown in figure 26. The decrease of the axial flow factor results in a minor increase of the turbulent kinetic energy during the intake valve flow. The scalar mixing time is decreasing with increasing axial flow factor during the compression and expansion stroke while no effect

[†]The time scale is calculated according to $\tau_{axial} = C_{axial} \cdot \frac{h_s}{c_m}$ where C_{axial} is a model parameter, h_s is the stroke and c_m is the mean piston speed.

*The instantaneous piston speed is calculated according to equation (9.8).

[†]The instantaneous stroke H_1 is determined by $H_1 = \frac{V - V_{bowl}}{\pi \cdot \frac{d_B^2}{4}}$ where V_{bowl} is the piston bowl volume and d_{bowl} is the piston bowl diameter.

is observed during the combustion phase.

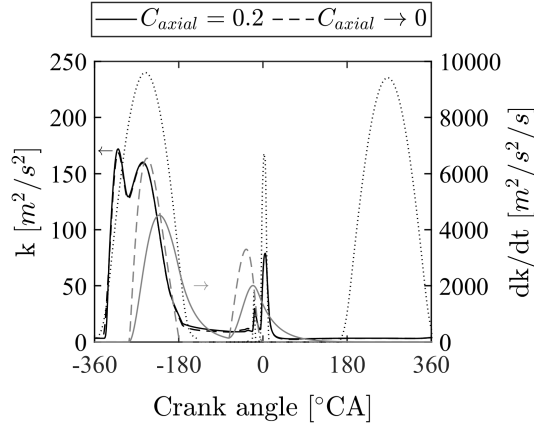


Figure 26: Turbulent kinetic energy and axial flow production term in dependence of C_{axial} parameter at 1750 rpm and 12 bar IMEP. The dashed lines highlight the intake and exhaust valve lift. The start of fuel injection is at -41°CA .

The change of kinetic energy of the squish flow $de_{kin,sq}/dt$ is proportional to the radial squish flow velocity in equation (4.139).

$$\frac{de_{kin,sq}}{dt} = 0.5 \cdot u_{sq,radial}^3 \cdot \frac{H_1 \cdot \pi \cdot d_{bowl}}{V} \quad (4.140)$$

Introducing the scaling parameter $C_{kin,sq}$ the squish flow can split into another kinetic energy of secondary flows within the piston bowl e_{bowl} .

$$\frac{de_{bowl}}{dt} = \begin{cases} (1 - C_{kin,sq}) \cdot \frac{de_{kin,sq}}{dt}, & -180^\circ\text{CA} \leq \theta \leq 180^\circ\text{CA} \\ 0 & \end{cases} \quad (4.141)$$

The first source term in equation (4.142) describes the production of turbulent kinetic energy during the compression stroke where large scale flow motion is squished and decayed into turbulent kinetic energy.*

$$\left(\frac{dk}{dt}\right)_{squish} = \begin{cases} C_{kin,sq} \cdot \frac{de_{kin,sq}}{dt}, & -180^\circ\text{CA} \leq \theta \leq 0^\circ\text{CA} \\ 0 & \end{cases} \quad (4.142)$$

The second term in equation (4.143) describes the production of turbulent kinetic energy during the compression and expansion stroke. The mass flow between squish and piston volume has to pass the edge of the piston bowl. At the edge of the bowl the flow detaches due to its high inertia and forms a secondary tumble flow motion which decays into turbulent kinetic energy.†

$$\left(\frac{dk}{dt}\right)_{local\ tumble} = e_{bowl} \cdot v_t \cdot \beta \quad (4.143)$$

The terms for squish injection and local tumble contribute to the production of turbulent kinetic energy close to the firing TDC as shown in figure 27. The model parameter $C_{kin,sq}$ can

*The default value for the squish flow parameter $C_{kin,sq}$ is 0.3.

†The geometry parameter β is calculated according to $\beta = \pi^2 \cdot 2 \cdot \frac{d_{bowl}^4 + 6 \cdot d_{bowl}^2 \cdot h_{bowl}^2 + 4 \cdot h_{bowl}^4}{d_{bowl}^2 \cdot h_{bowl}^2 \cdot (d_{bowl}^2 + h_{bowl}^2)}$.

be changed to distribute the squish flow kinetic energy differently to the two production terms. However, the contribution of the two squish flows to turbulent kinetic energy production is assumed to be much lower compared to direct injection.

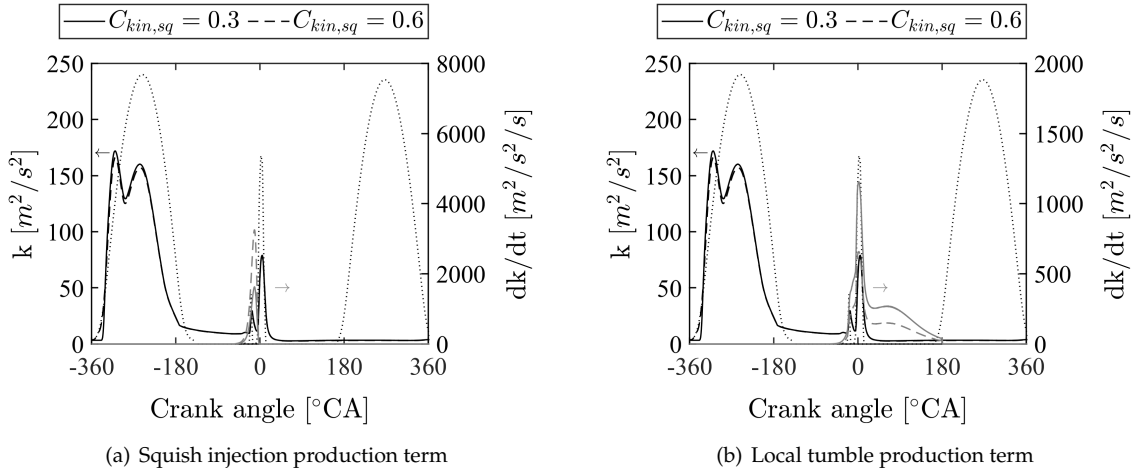


Figure 27: Turbulent kinetic energy, squish injection and local tumble production term in dependence of $C_{kin,sq}$ parameter at 1750 rpm and 12 bar IMEP. The dashed lines highlight the intake and exhaust valve lift. The start of fuel injection is at -41°CA .

The production of turbulent kinetic energy due to direct injection is defined the same way as in the $k - \varepsilon$ turbulence model for SI engines in equation (4.62).

$$\left(\frac{dk}{dt}\right)_{injection} = C_{inj} \cdot \dot{m}_f \cdot \frac{p_{inj} - p_{cyl}}{\rho_f} \cdot \frac{1}{m_g} \quad (4.144)$$

The results of the variation of the model parameter C_{inj} are shown in figure 28. Increasing the C_{inj} parameter leads to higher production of turbulent kinetic energy during fuel injection.

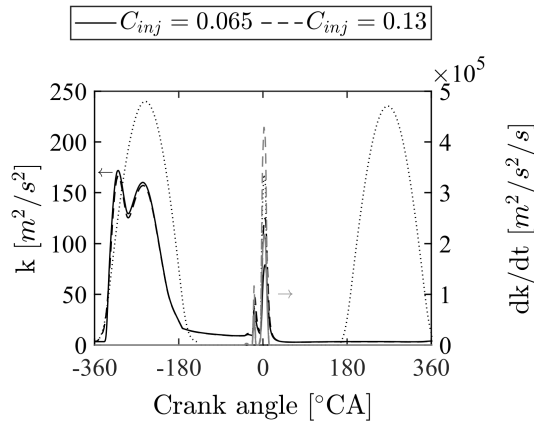


Figure 28: Turbulent kinetic energy and direct injection production term in dependence of C_{inj} parameter at 1750 rpm and 12 bar IMEP. The dashed lines highlight the intake and exhaust valve lift. The start of fuel injection is at -41°CA .

The swirl production term in equation (4.145) is divided into two terms which describe the decay of swirl angular momentum L_S into turbulent kinetic energy.

$$\left(\frac{dk}{dt}\right)_{swirl} = \left(\frac{dk}{dt}\right)_{shear} + \left(\frac{dk}{dt}\right)_{wall\ friction} \quad (4.145)$$

The shear force term describes the decay of angular momentum due to inner friction in the fluid which is governed by the turbulent viscosity ν_t and the geometric dimensions.

$$\left(\frac{dk}{dt}\right)_{shear} = \nu_t \cdot \left(\frac{28.55}{\rho^2}\right) \cdot \left(\frac{H_1 + h_{bowl}}{H_1 \cdot d_B^3 + h_{bowl} \cdot d_{bowl}^3}\right)^2 \cdot \left(H_1 \cdot d_B^2 + h_{bowl} \cdot d_{bowl}^2\right) \cdot L_S^2 \quad (4.146)$$

The differential equation of swirl angular momentum L_S in equation (4.147) includes different production and consumption terms based on valve flow, shear forces, wall friction and shift of mass into the piston bowl.

$$\frac{dL_S}{dt} = \frac{dL_{S,intake}}{dt} + \frac{dL_{S,exhaust}}{dt} + \frac{dL_{S,shear}}{dt} + \frac{dL_{S,friction}}{dt} + \frac{dL_{S,piston}}{dt} \quad (4.147)$$

The generation of angular momentum due to mass flowing into the system is described by equation (4.148). It depends on the volume flow through the valves \dot{m}_{in}/ρ and the lever length $d_B/2$.

$$\frac{dL_{S,intake}}{dt} = S_{Tipp} \cdot \frac{\dot{m}_{in}^2}{\frac{d_B}{2} \cdot \rho} \quad (4.148)$$

The effectiveness of intake flow generating angular momentum is described by the Toppelmann swirl number S_{Tipp} as shown in figure 29. It accounts for the type of intake port and how it directs the flow into the system to form a swirl motion. Increasing the Toppelmann swirl number leads to an increase of swirl angular momentum and higher swirl ratio over the whole engine cycle.*

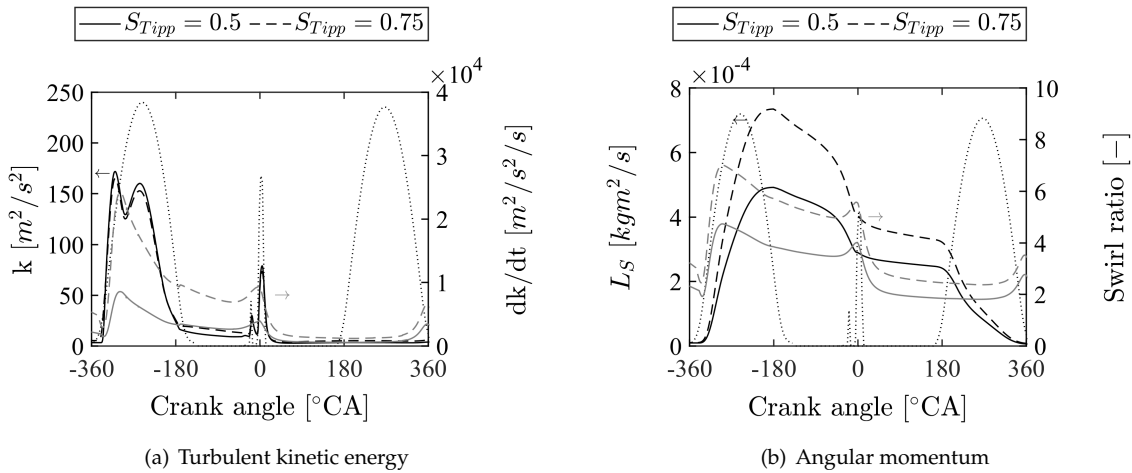


Figure 29: Turbulent kinetic energy, swirl production term, swirl angular momentum and swirl ratio in dependence of S_{Tipp} parameter at 1750 rpm and 12 bar IMEP. The dashed lines highlight the intake and exhaust valve lift. The start of fuel injection is at -41 °CA.

The flow out of the system \dot{m}_{out} can transport swirl angular momentum and is a sink term in equation (4.147). The amount of swirl angular momentum leaving the system is scaling with the total mass m_g .

*The swirl ratio is calculated according to section 9.7.

$$\frac{dL_{S,exhaust}}{dt} = L_S \cdot \frac{\dot{m}_{out}}{m_g} \quad (4.149)$$

Another sink term describes the decay of swirl angular momentum due to shear forces and production of turbulent kinetic energy and is outlined in the following equation. The decay due to shear forces occurs mainly during the compression stroke because of the high angular momentum created by the mass flow through the intake valves.*

$$\frac{dL_{S, shear}}{dt} = \begin{cases} -2.175 \cdot \nu_t \cdot \frac{H_1 + h_{bowl}}{H_1 \cdot d_B^2 + h_{bowl} \cdot d_{bowl}^2} \cdot L_S, & \theta > -180^\circ CA \\ 0 & \theta < -180^\circ CA \end{cases} \quad (4.150)$$

The sink term due to swirl flow and wall interaction is described by equation (4.151) and it diminishes angular momentum during the compression stroke. It is scaling with the local tangential velocity U^* and the dynamic viscosity μ .*

$$\frac{dL_{S, wall friction}}{dt} = \begin{cases} -(0.05 \cdot (H_1 \cdot d_B^{1.8} + h_{bowl} \cdot d_{bowl}^{1.8}) + C_{friction} \cdot (0.0136 \cdot d_B^{2.8} + 0.0071 \cdot d_{bowl}^{2.8}) \cdot \rho^{0.8} \cdot \mu^{0.2} \cdot |U^*|^{1.8}), & \theta > -180^\circ CA \\ 0 & \theta < -180^\circ CA \end{cases} \quad (4.151)$$

The local tangential velocity U^* is derived from the angular momentum L_S using the relationship $L_S = r \cdot m \cdot U^*$ where r is the lever length and m is the mass. Accounting for the instantaneous stroke H_1^\dagger , the piston bowl depth h_{bowl} and diameter d_{bowl} and the density ρ , the tangential velocity can be determined for the system by the following equation.

$$U^* = \pi^2 \cdot \frac{L_S}{2 \cdot (\pi - 2) \cdot \rho \cdot (H_1 \cdot d_B^3 + h_{bowl} \cdot d_{bowl}^3)} \quad (4.152)$$

The increase of the model parameter $C_{friction}$ leads to a decrease of the angular momentum and swirl ratio during the compression and expansion stroke as shown in figure 30.

The reduction of angular momentum due to shift of mass from the cylinder to the piston bowl during the compression stroke is described by the following equation.

$$\frac{dL_{S, piston}}{dt} = \begin{cases} 2 \cdot \frac{\pi-2}{\pi^2} \cdot U^* \cdot \left(\rho \cdot d_B^3 \cdot c_{pis} + (H_1 \cdot d_B^3 + h_{bowl} \cdot d_{bowl}^3) \cdot \frac{d\rho}{dt} \right), & -180^\circ CA \leq \theta \leq 0^\circ CA \\ 0 & \theta < -180^\circ CA \end{cases} \quad (4.153)$$

The wall friction term describes the production of turbulent kinetic energy due to decay of angular momentum from swirl flow and wall interaction and is governed by the local tangential velocity U^* and the kinematic viscosity μ/ρ .

*The turbulent viscosity ν_t is calculated by equation (4.64).

*The dynamic viscosity μ is calculated according to following empirical equation $\mu = 0.612 \cdot 10^{-6} \cdot T^{0.609}$ where μ has the unit $Pa \cdot s$ and T has the unit K .

†The instantaneous distance between piston and cylinder head is calculated with $H_1 = \frac{V}{\pi \cdot \frac{d_B^2}{4}}$.

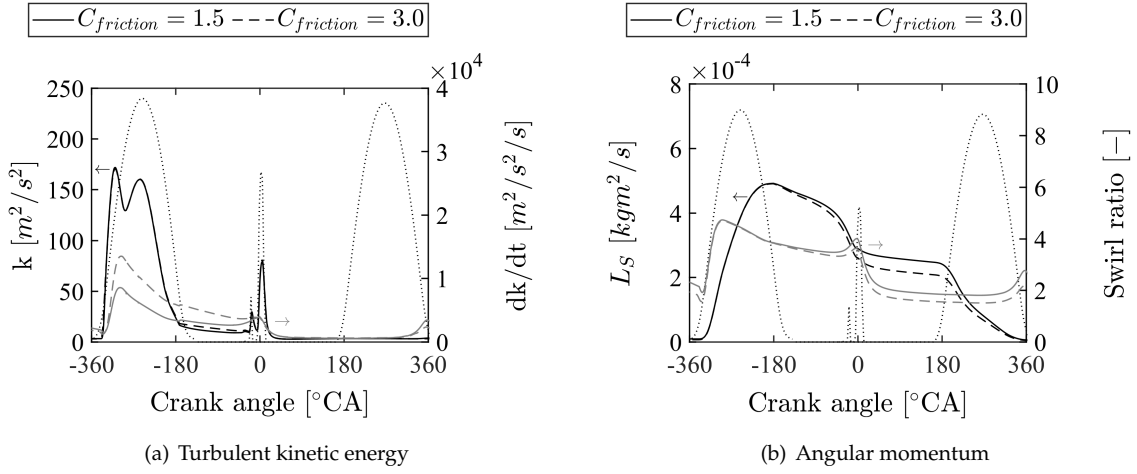


Figure 30: Turbulent kinetic energy, swirl production term, swirl angular momentum and swirl ratio in dependence of $C_{friction}$ parameter at 1750 rpm and 12 bar IMEP. The dashed lines highlight the intake and exhaust valve lift. The start of fuel injection is at -41 °CA.

$$\left(\frac{dk}{dt}\right)_{wall\ friction} = \left(\frac{0.083 \cdot d_B^{1.7} + 0.044 \cdot d_B^{1.7} + C_{friction} \cdot 0.254 \cdot (H_1 \cdot d_B^{0.7} + h_{bowl} \cdot d_{bowl}^{0.7})}{V}\right) \cdot \left(|U^*|^{1.8} \cdot \left(\frac{\mu}{\rho}\right)^{0.2}\right)^{1.5} \quad (4.154)$$

The closure term of the Reynolds stress tensor for compressible flows [44] is included in a similar manner as for the $k - \varepsilon$ turbulence model of SI engines in equation (4.70).

$$\left(\frac{dk}{dt}\right)_{compressibility} = \begin{cases} -\frac{2}{3} \cdot \frac{dV}{dt} \cdot \frac{k}{V}, & -180^\circ CA \leq \theta \leq 180^\circ CA \\ 0 & \end{cases} \quad (4.155)$$

The dissipation ε is the last term of equation (4.129) and is the sink for turbulent kinetic energy. It is calculated proportional to the turbulent kinetic energy k and inversely proportional to the integral length scale l_I .

$$\varepsilon = C_\varepsilon \cdot \frac{k^3}{l_I} \quad (4.156)$$

The ratio of C_ε and C_μ reflects the proportionality of the integral length scale l_I to the turbulent length scale l .

$$l_I = \frac{C_\varepsilon}{C_\mu} \cdot l \quad (4.157)$$

If the model parameter C_ε is increased the turbulent kinetic energy is reduced as shown in figure 31.

The turbulent length scale l is determined by the characteristic turbulent length scale $l_{turb,vol}$ of the cylinder, the characteristic turbulent length scale $l_{turb,avg}$ of the inflow in the

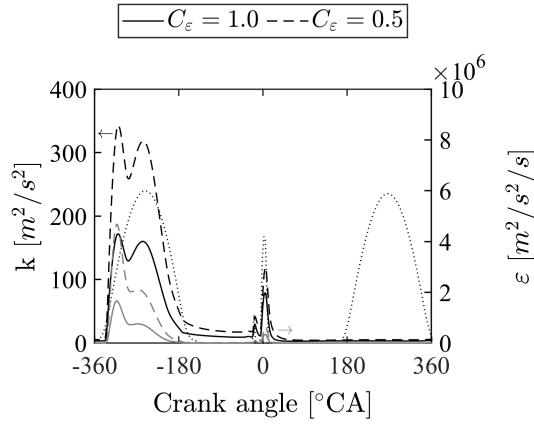


Figure 31: Turbulent kinetic energy and dissipation in dependence of C_ε parameter at 1750 rpm and 12 bar IMEP. The dashed lines highlight the intake and exhaust valve lift. The start of fuel injection is at -41°CA .

system and the characteristic turbulent length scale $l_{turb,sq}$ of the squish flow.

$$l = \frac{m_g}{\frac{m_{vol}}{l_{turb,vol}} + \frac{m_{inflow}}{l_{turb,avg}} + \frac{m_{sq}}{l_{turb,sq}}} \quad (4.158)$$

The characteristic turbulent length scale $l_{turb,vol}$ is determined based on the model parameters C_μ and C_{ε_1} and the product of the swirl number S^* and the characteristic length scale l_{vol} .

$$l_{turb,vol} = \frac{C_\mu}{C_{\varepsilon_1}} + |S| \cdot l_{vol} \quad (4.159)$$

The characteristic length scale l_{vol} is determined based on the cylinder length scale $l_{cyl,1}$ and the bowl length scale l_{bowl} .

$$l_{vol} = \frac{l_{cyl,1} \cdot (V - V_{bowl}) + l_{bowl} \cdot V_{bowl}}{V} \quad (4.160)$$

$$l_{cyl,1} = \left(6 \cdot \frac{V - V_{bowl}}{\pi} \right)^{\frac{1}{3}} \quad (4.161)$$

$$l_{bowl} = \left(4 \cdot \frac{V_{bowl}}{\pi^2} \right)^{\frac{1}{3}} \quad (4.162)$$

The model parameter C_{ε_1} influences the turbulent length scale over the whole engine cycle as shown in figure 32. The largest effect on the turbulent kinetic energy can be observed for the inflow during the intake valve opening. During the combustion no significant effect can be observed.

The turbulent length scale $l_{turb,avg}$ is determined based on the intake valve length scale $l_{turb,IV}$ and the exhaust valve length scale $l_{turb,EV}$.

*The swirl number is determined according to equation (9.12).

*The mass m_{inflow} is calculated based on the accumulated inflow mass of the intake ($m_{inflow,IV}$) and exhaust valves ($m_{inflow,EV}$) using the following definition $m_{inflow} = \sum m_{inflow,IV} + \sum m_{inflow,EV}$.

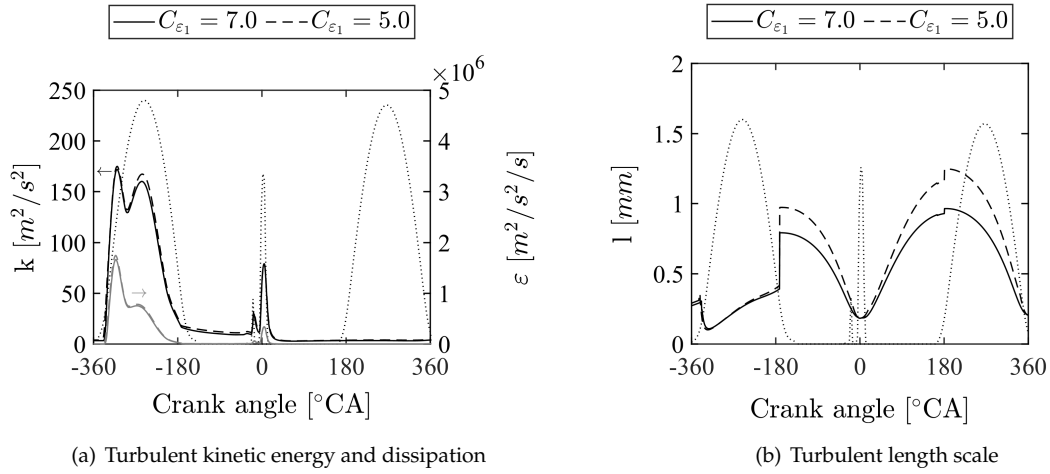


Figure 32: Turbulent kinetic energy, dissipation and turbulent length scale in dependence of C_{ε_1} parameter at 1750 rpm and 12 bar IMEP. The dashed lines highlight the intake and exhaust valve lift. The start of fuel injection is at -41°CA .

$$l_{turb,avg} = \frac{l_{turb,IV} \cdot m_{inflow,IV} + l_{turb,EV} \cdot m_{inflow,EV}}{m_{inflow}} \quad (4.163)$$

The two length scales can be calculated according to equation (4.164) and (4.165). They are depending on the characteristic length scale L_{IV} and L_{EV} which are related to the instantaneous valve lift l_{IV} and l_{EV} . The proportionality between the turbulent length scales l and the characteristic length scales L is governed by the model parameters C_μ and C_{ε_2} .

$$l_{turb,IV} = \frac{C_\mu}{C_{\varepsilon_2}} \cdot L_{IV} \quad (4.164)$$

$$l_{turb,EV} = \frac{C_\mu}{C_{\varepsilon_2}} \cdot L_{EV} \quad (4.165)$$

The length scale $l_{turb,sq}$ of the squish flow is proportional to the characteristic length scale L_{sq} .

$$l_{turb,sq} = \frac{C_\mu}{C_{\varepsilon_2}} \cdot L_{sq} \quad (4.166)$$

The characteristic length scale L_{sq} is relevant during the time when mass is flowing back from the bowl into the squish. This backflow occurs during the expansion stroke while for the remaining parts of the engine cycle the characteristic length scale L_{sq} is zero.

$$L_{sq} = \begin{cases} \sum \frac{dL_{sq}}{dt} \cdot \Delta t, & 0^\circ\text{CA} \leq \theta \leq 180^\circ\text{CA} \\ 0 & \end{cases} \quad (4.167)$$

The change of the characteristic length scale L_{sq} is dependent on the backflow rate $\dot{m}_{back,sq}$, the instantaneous stroke H_1 and the current characteristic length scale L_{sq} .

$$\frac{dL_{sq}}{dt} = \dot{m}_{back,sq} \cdot \frac{H_1 - L_{sq}}{m_{sq}} \quad (4.168)$$

The mass in the squish volume m_{sq} is based on the backflow rate $\dot{m}_{back,sq}$ and the mass flow into the bowl which is dependent on the characteristic time scale $\tau_{m,sq}$.

$$\dot{m}_{sq} = \dot{m}_{back,sq} - \frac{m_{sq}}{\tau_{m,sq}} \quad (4.169)$$

The characteristic time scale $\tau_{m,sq}$ is proportional to the piston bore d_B and the mean piston speed c_m .[†] The model parameter $C_{\tau,m}$ can be changed to adjust the mass flow rate between squish and bowl volume.

$$\tau_{m,sq} = C_{\tau,m} \cdot \frac{d_B}{c_m} \quad (4.170)$$

The backflow rate $\dot{m}_{back,sq}$ is proportional to the radial squish velocity $u_{sq,radial}$ in equation (4.139) and the mass in the cylindrical volume above the piston bowl.

$$\dot{m}_{back,sq} = \begin{cases} |u_{sq,radial}| \cdot H_1 \cdot \pi \cdot d_{bowl} \cdot \rho, & 0^\circ CA \leq \theta \leq 180^\circ CA \\ 0 & \end{cases} \quad (4.171)$$

The scalar mixing time τ_ϕ can now be determined based on the turbulent kinetic energy k and dissipation ε . The model parameter C_ϕ relates the turbulent mixing time τ_t with the scalar mixing time τ_ϕ and can be adjusted depending on the application.

$$\tau_\phi = C_\phi \cdot \frac{k}{\varepsilon} \quad (4.172)$$

4.5 Numerical solution method

The *mdf* in equation (4.1) is numerically solved using an operator split method which was proposed by Tunér [14] for SRM. The differential equations for turbulent kinetic energy (4.51) and (4.129), dissipation (4.71) and (4.156) and angular momentum (4.65) and (4.147) are solved using an explicit Runge-Kutta solver. The structure of the operator split method and Runge-Kutta solver are briefly introduced in the subsequent sections.

4.5.1 Explicit Runge-Kutta Solver

The differential equations for turbulent kinetic energy k , dissipation ε and angular momentum L are solved using the explicit Runge-Kutta algorithm in equation (4.173).

$$\mathbf{y}_{n+1} = \mathbf{y}_n + h \cdot \left(\frac{1}{6}\mathbf{k}_1 + \frac{1}{3}\mathbf{k}_2 + \frac{1}{3}\mathbf{k}_3 + \frac{1}{6}\mathbf{k}_4 \right) \quad (4.173)$$

Therein, \mathbf{y}_n is a vector including the solutions of k , ε and L of the current operator split step n . h is the sample size of the Runge-Kutta algorithm and is equal to the operator split time step Δt . \mathbf{k}_{1-4} are vectors and consist of the solutions of the intermediate steps 1 – 4 and \mathbf{y}_{n+1} is the solution of the Runge-Kutta algorithm.

The solutions of the intermediate steps \mathbf{k}_{1-4} are determined by the following equations.*

[†]The mean piston speed c_m is determined according to equation (9.7).

* t_n denotes the current time step of the operator split method.

$$k_1 = f(t_n, \mathbf{y}_n) \quad (4.174)$$

$$k_2 = f\left(t_n + \frac{h}{2}, \mathbf{y}_n + \frac{h}{2}k_1\right) \quad (4.175)$$

$$k_3 = f\left(t_n + \frac{h}{2}, \mathbf{y}_n + \frac{h}{2}k_2\right) \quad (4.176)$$

$$k_4 = f(t_n + h, \mathbf{y}_n + hk_3) \quad (4.177)$$

The flow chart of the solutions steps for the $k - \varepsilon$ turbulence model are outlined in figure 33.

Runge-Kutta algorithm The Runge-Kutta algorithm is initialized for the current operator split time step t_n and the turbulent viscosity ν_t is calculated first. Next, the turbulent length scale l is calculated based on the current solutions \mathbf{y}_n . The maximum number of iteration steps is set to 20. The iteration loop for the Runge-Kutta solver is started and the solutions of k_i , ε_i and L_i for the current iteration step i are calculated. If convergence is not achieved the next iteration step $i + 1$ is executed. Convergence of the solution is achieved when the following criteria is fulfilled:

$$\left| \frac{\mathbf{y}_{n+1,i} - \mathbf{y}_{n+1,i-1}}{\mathbf{y}_{n+1,i}} \right| < 10^{-4} \quad (4.178)$$

The iteration loop is finished if convergence is achieved or the maximum iteration number is reached. After leaving the iteration loop the solutions $\mathbf{y}_{n+1,i}$ are stored in \mathbf{y}_{n+1} for the next operator split time step t_{n+1} . The scalar mixing time scale τ_ϕ is calculated and the Runge-Kutta algorithm is finalized.

4.5.2 Operator split method

The models outlined in the previous sections are solved sequentially using the operator split algorithm in SRM [14]. The flow chart in figure 34 outlines the solution steps for the SI-SRM. For the DI-SRM the solution steps for flame propagation and crevice are omitted. At the start the notional particles and zones are initialized and all model parameters are set according to the user input. Subsequently, the solutions for piston movement, gas exchange, injection and vaporization, flame propagation, crevice, turbulence and particle mixing, chemical reaction and convective heat transfer are determined. All calculation steps are performed assuming constant pressure. Therefore, a pressure correction is performed at the end of the operator split time step. The operator split algorithm is continued until the end of the simulation is reached. The calculations are finalized and the results are written to output files.

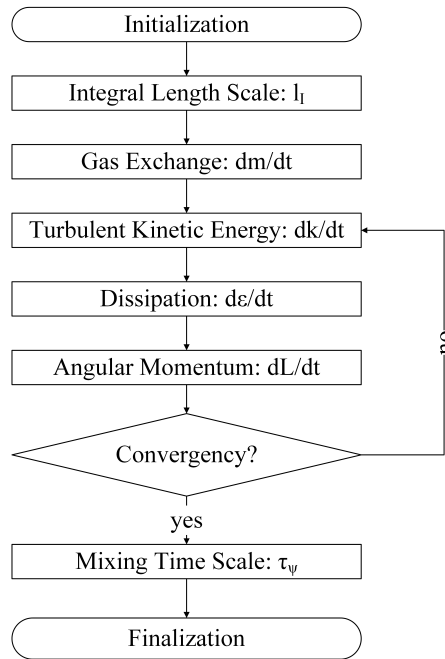


Figure 33: Solution steps during the current SRM operator split time step for the differential equations of the $k - \varepsilon$ turbulence model.

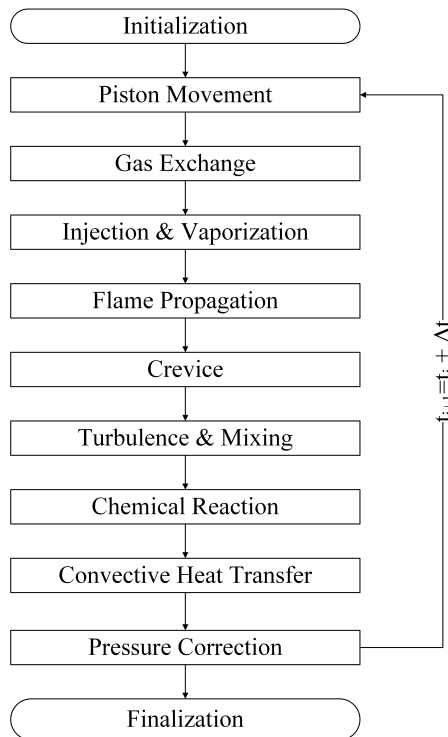


Figure 34: Solution steps of the operator split algorithm in SRM.

4.6 Conclusions for stochastic reactor models

This chapter introduces the numerical models which are implemented in the SRM and optimized during the course of this thesis. The novelty is the implementation of the $k - \varepsilon$

turbulence models for SI and CI engines. The model determines the turbulent time and length scales which occur in piston engines in a physical manner. Even though the implementation of the $k - \varepsilon$ turbulence model for SI and CI engines is still separated in the code both models share a common physical basis which allow to merge them in the future. Other models for turbulent flame propagation, particle mixing, convective heat transfer and crevice flow are developed and improved during this thesis by incorporating the turbulent kinetic energy k and integral length scale l_I .

5 The Multi-Objective Optimization Platform

The multi-objective optimization (MOO) platform is introduced for the automated SRM training over the whole engine operation map. It incorporates models for design space filling, error calculation, response surface modeling, optimization and decision making. The models are explained in the following sections and their performance is evaluated. The MOO platform is developed in the software package modeFRONTIER v2020R2 from ESTECO [64].

5.1 General idea of optimization

A multi-objective optimization aims to find the best solution for the optimization parameters \vec{x} by minimizing or maximizing multiple objective functions $f_i(\vec{x})$. Thereby, the optimum solutions of the defined objective functions can be opposed yielding not one optimum solution but many which are defined as Pareto solutions. The optimum solution is defined as follows: \vec{x}_0 belongs to the Pareto front when no better solution $f_i(\vec{x}^*)$ for the objective function $f_i(\vec{x}_0)$ exists.

$$\forall i \nexists (\vec{x}^*) : f_i(\vec{x}^*) \leq f_i(\vec{x}_0) \quad (5.1)$$

Further, constraints $g_j(\vec{x})$ can be defined to restrict certain parameter or objective function ranges and narrow down the design space of optimum solutions. The optimization run is divided into several generations which in turn consist of a number of individuals or designs. Each design is evaluated during the optimization run and has its own results for the objective functions and constraints.

$$\begin{cases} \min f_i(\vec{x}) = (f_1(\vec{x}), f_2(\vec{x}), \dots, f_k(\vec{x}))^T \\ = \{ \vec{x} \in R^p | g_j(\vec{x}) \leq 0, (j = 1, \dots, m) \} \end{cases} \quad (5.2)$$

The objective functions $f_i(\vec{x})$ and constraints $g_j(\vec{x})$ are defined in dependence of the optimization parameters \vec{x} as shown in equation (5.3). The parameter vector \vec{x} consists of p different parameters which characterize the individual designs of the optimization. In this thesis the objective functions are also referred to as errors ε and their definition is explained in the subsequent section. Increasing the number of objective functions and constraints will increase the computational cost of the multi-objective optimization. The optimization algorithms investigated in this thesis usually perform well with up to three objective functions defined [65] while for higher number of objectives many-objective optimization algorithms are recommended [66, 67].

$$\begin{cases} f_i(\vec{x}) = f_i(x_1, x_2, \dots, x_p), i = 1, \dots, k \\ g_j(\vec{x}) = g_j(x_1, x_2, \dots, x_p), j = 1, \dots, m \end{cases} \quad (5.3)$$

The single steps involved in the multi-objective optimization using the SRM are outlined in figure 35. The selection of the optimization parameters, objective functions and constraints

is already done during the setup of the optimization problem.

Optimization procedure The initial population^a is created using a space filler algorithm and the newly created designs are evaluated using the SRM. Based on the simulation results of the SRM the user-defined error functions ε are evaluated. The results are stored in the design database and are ranked according to the criteria set by the optimization algorithm. A new population of designs is created and evaluated using the SRM and the procedure is repeated until all generations are evaluated. The optimization procedure can be extended by an internal optimization run using response surface models (RSM) [68]. The RSM library includes polynomial singular value decomposition (SVD), Kriging, Radial Basis Function (RBF) and Neural Network models. The RSMs are trained for each objective function and constraint based on the existing design database.^b Their performance is evaluated by calculating a mean normalized error. Subsequently they are competing with each other in a tournament process. The tournament process always selects the best RSM for the next upcoming generation. The internal optimization is performed using an initial population consisting of 50% of designs from the best last evaluated designs and 50% of designs created by a space filler algorithm.^c The best designs of the internal optimization are selected and added to the new population which will be evaluated by the SRM in the next step. After the optimization is finished a multi-criteria decision making process is started to select the best designs from the Pareto solutions. The weights of the objectives can be adjusted to influence the decision making process and retrieve the desired design from the database.

^aA population describes the set of designs of a generation. This term is typical for genetic optimization algorithms while it can be named differently for heuristic optimization algorithms.

^bThe number of designs used for RSM training is limited to 1000 in this thesis.

^cAdding 50% randomly generated designs improves the exploration capability and robustness of the optimization algorithm.

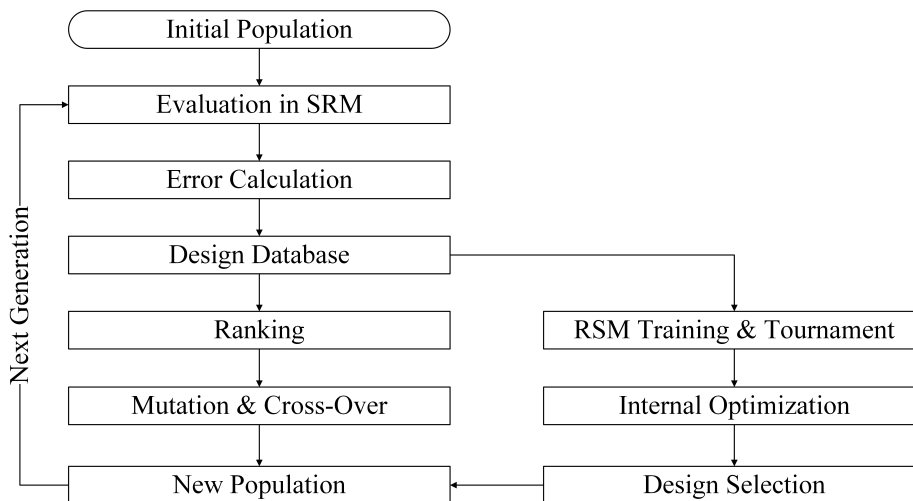


Figure 35: Flow chart for multi-objective optimization with SRM.

5.2 Error calculation

A sum of least square method is used in this thesis to determine the error functions of the SRM simulation results in comparison to the experimental reference data.* The first error function $\varepsilon_{Pressure}$ in equation (5.4) determines the normalized least square error of the cylinder pressure for a number of time steps N and a number of training points R . The weight of the training points w_j can be adjusted.†

$$\varepsilon_{Pressure} = \sum_{j=1}^R w_j \cdot \left\{ \sum_{i=1}^N \left(\frac{p_{sim,ij} - p_{ref,ij}}{p_{ref,ij}} \right)^2 \right\} \quad (5.4)$$

The second error function ε_{PCP} in equation (5.5) determines the normalized least square error of the peak cylinder pressure (PCP)* for a number of training points R .

$$\varepsilon_{PCP} = \sum_{j=1}^R w_j \cdot \left\{ \left(\frac{PCP_{sim,j} - PCP_{ref,j}}{PCP_{ref,j}} \right)^2 \right\} \quad (5.5)$$

The third error function ε_{PCPCA} in equation (5.6) determines the normalized least square error of the peak cylinder pressure crank angle (PCPCA)† for a number of training points R .

$$\varepsilon_{PCPCA} = \sum_{j=1}^R w_j \cdot \left\{ \left(\frac{PCPCA_{sim,j} - PCPCA_{ref,j}}{PCPCA_{ref,j}} \right)^2 \right\} \quad (5.6)$$

The fourth error function $\varepsilon_{y_{A,EVO}}$ determines the normalized least square error of species mass fraction y_A where A is a place holder for different species‡ and is defined more in general in equation (5.7). The species mass fraction is determined at exhaust valve opening (EVO). The difference of simulated and measured species mass fraction is normalized by the maximum measured species mass fraction of the training points R . The natural logarithm accounts for differences of several magnitudes in measured species mass fraction.

$$\varepsilon_{y_{A,EVO}} = \sum_{j=1}^R w_j \cdot \left\{ \left(\frac{\ln(y_{A,EVO,sim,j}) - \ln(y_{A,EVO,ref,j})}{\ln(\max(y_{A,EVO,ref}))} \right)^2 \right\} \quad (5.7)$$

The fifth error function $\varepsilon_{y_{A,gradient}}$ calculates the difference of species mass fraction of two training points for the simulation and reference data and determines the sum of least square error. This error function should ensure that the trend of the measurements between the training points is matched by the SRM simulation.

$$\varepsilon_{y_{A,gradient}} = \sum_{k=1}^{R-1} w_k \cdot \left\{ (\Delta y_{A,EVO,sim,k} - \Delta y_{A,EVO,ref,k})^2 \right\} \text{ with } \Delta y_A = y_{A,k+1} - y_{A,k} \quad (5.8)$$

*The SRM results are denoted by *sim* and the experiments are denoted by *ref*.

†The optimizations investigated in this thesis are performed using equi-weighted training points.

*The peak cylinder pressure is defined as the maximum of the crank-angle-based cylinder pressure profile $PCP = \max(p_i)$ where $i = 1, \dots, N$.

†The peak cylinder pressure crank angle is defined as the crank angle of maximum cylinder pressure.

‡Species mass fraction is used as an example while the error can also be defined based on mole fraction, total mass or specific mass.

5.3 Space filling algorithms

The space filler algorithm is applied for the initial population generation and the design space exploration. The design space is a hypercube with the dimension equal to the number of optimization parameters p .^{*} A measure of a good performance of a space filler algorithm is the uniformity of the sample distribution in the hypercube [69] especially for low number of samples. In the literature the uniformity is defined as the distances between the samples in the design space [70].[†]

The Random, Uniform Latin Hypercube (ULHC), Sobol and Incremental Space Filler (ISF) algorithms are introduced briefly while more detailed information can be found in the literature. The algorithms are tested during the course of the thesis but finally the ULHC algorithm is selected as best practice.

Random The random space filler algorithm creates samples of the optimization parameters according to a uniform distributed random number. This algorithm often suffers from clustering and low uniformity of the design samples [69].

Uniform Latin Hypercube The ULHC algorithm is the generalization of the Latin Square for hypercube dimensions [71]. The Latin Square is a $n \times n$ matrix filled with n different values each of them occurring only once in each column and row. Therefore, the ULHC algorithm provides a good representation of all values of the optimization parameters. The ULHC algorithm shows usually good performance for low number of samples and high-dimensional design spaces.

Sobol The Sobol sequence is based on the more general defined Faure and Halton sequences [72] which in turn are based on the Van-der-Corput sequence [73]. The Faure and Halton sequences are calculated using different prime numbers as base while the Sobol sequence uses the prime number 2 as base. With Sobol the samples of the first dimension of the design space are calculated using the Van-der-Corput sequence while the samples for all subsequent dimensions are permutations of the first dimension. Since the Sobol algorithm is based on a sequence it naturally considers previous samples when it calculates new samples wherefor design spaces created by Sobol are easily extendable.

Incremental Space Filler The ISF algorithm generates new samples by trying to maximize the minimum distance between the samples [70]. It is using a Greedy algorithm to determine the maximum distance of the samples. The algorithm selects incrementally the maximum distance from the previously included samples which will not always be the overall maximum distance of all samples.

Figure 36 compares the distributions for 10 samples and it includes the measure for uniformity U_D of each algorithm. The best performing algorithms regarding uniformity are

^{*}We are using the same notation as it is introduced in equation (5.2) and (5.3).

[†]Discrepancy is another measure of uniformity [69]. The definition of Montrone et al. [70] is outlined in section 9.8.

ULHC and ISF. Even though the Sobol algorithm shows visually a good uniformity it does not perform as good as ULHC and ISF. The Random algorithm shows some clustering and large gaps in the distribution while it is only slightly worse than the Sobol algorithm.

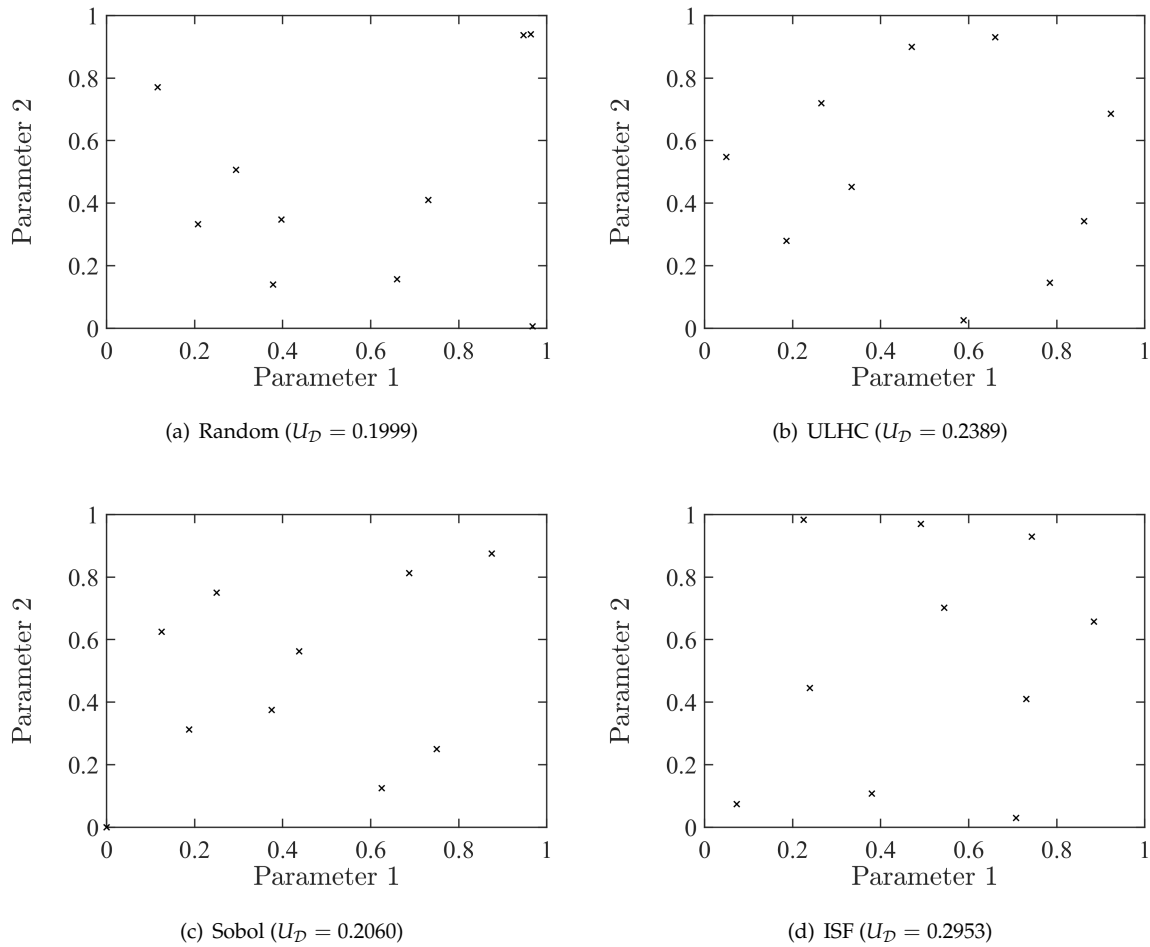


Figure 36: Distribution of 10 samples in a two-dimensional design space using Random, Uniform Latin Hypercube, Sobol and Incremental Space Filler algorithms.

Figure 37 repeats the comparison of the space filler algorithms for 100 samples. The Random algorithm shows more clustering and gaps in the distribution wherefor the uniformity measure is the lowest. The Sobol sequence performs better compared to the ULHC algorithm which highlights the strength of the algorithm for large number of samples. The best performance is obtained by the ISF algorithm which shows by far the highest uniformity measure. During the optimization the number of samples is low wherefor the choice of the ULHC or ISF algorithm is reasonable. Finally, the ULHC algorithm is chosen because the computational cost of the ISF algorithm is higher.

5.4 Response surface models

As shown in figure 35 the internal optimization loop uses RSM models. There are four types of RSM applied in this thesis: Polynomials, Neural Networks, RBF and Gaussian regression (Kriging). Each of the models will be briefly introduced while more detailed information can be found in the literature.

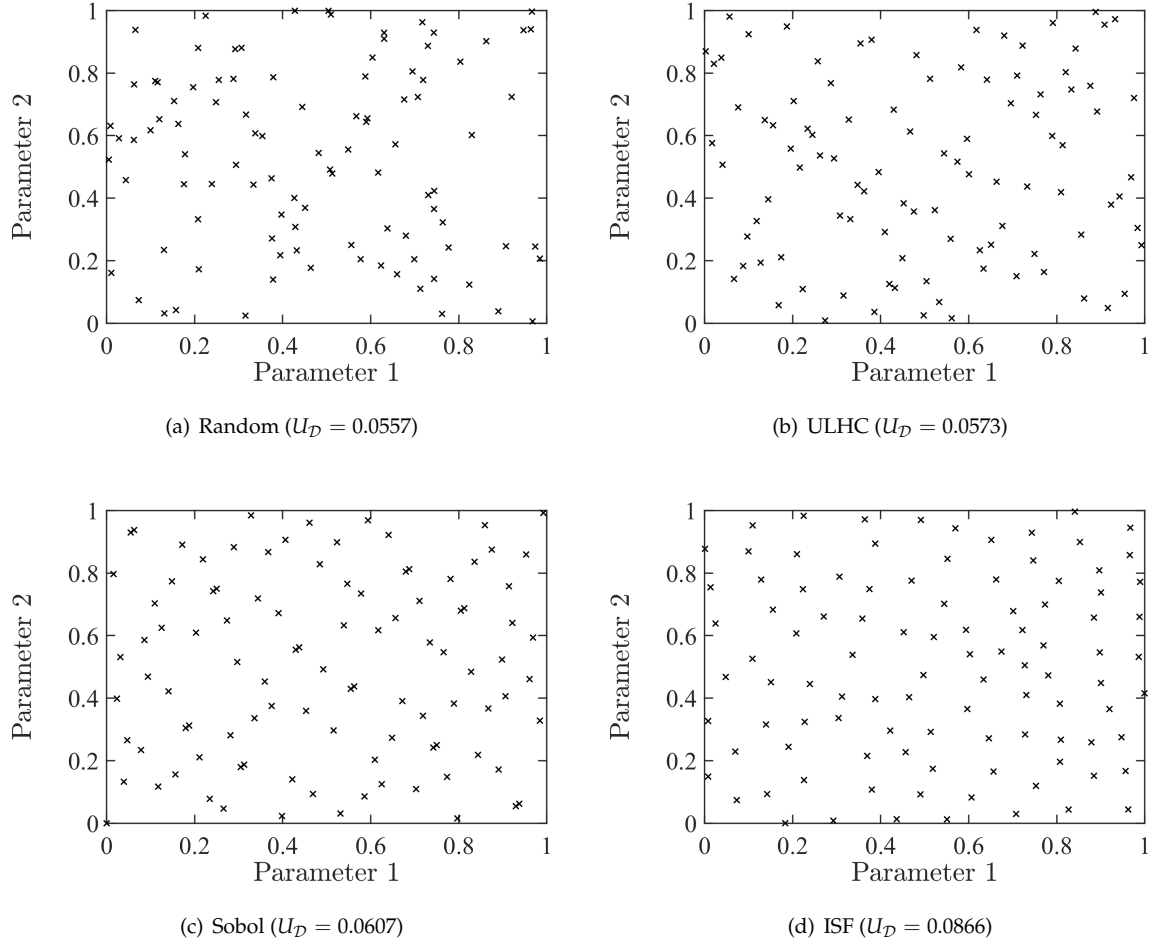


Figure 37: Distribution of 100 samples in a two-dimensional design space using Random, Uniform Latin Hypercube, Sobol and Incremental Space Filler algorithms.

Polynomial Singular Value Decomposition A set of measurements $Y_m(\mathbf{x})$ can be approximated by m number of polynomials of order n .

$$Y_m(\mathbf{x}) = c_1 + c_2x_m + c_3x_m^2 + c_4x_m^3 + \dots + c_{n+1}x_m^n \quad (5.9)$$

The polynomial in equation (5.9) can also be expressed as a linear system of equations with $A \in \mathbb{R}^{m \times n}$.

$$Ac = Y \quad (5.10)$$

Using singular value decomposition (SVD) yields the expression of A where $U \in \mathbb{R}^{m \times m}$ and $V \in \mathbb{R}^{n \times n}$ are orthogonal matrices and $\Sigma \in \mathbb{R}^{m \times n}$ is a diagonal matrix [74].

$$A = U\Sigma V^T \quad (5.11)$$

Combining equation (5.11) and (5.10) and rearrangement of the equation to c yields the following expression that can be used to determine the coefficients c of the polynomial to approximate the measured data.

$$c = V\Sigma^{-1}U^T(Y) \quad (5.12)$$

Neural network A classic feedforward neural network with one hidden layer is utilized in this thesis. It is extended with a back-propagation algorithm, where the RSM output is compared with the training data, to optimize the network weights. The number of neurons in the hidden layer is calculated based on the number of input and output parameters from the training data set [75, 76, 77].

Radial basis function To approximate a set of measured points $Y(x_j)$ a weighted sum of RBF can be calculated [78]. Thereby, a RBF model is similar in structure to a Neural Network with one hidden layer. The method divides the set of measured points x_j into n smaller shares each of them defined by a centroid c_i . Thereby, the number of neurons σ of the RBF is equal to the number of centroids c . The approximation $Y_s(x_s)$ can be determined by the inverse of the weight matrix θ' and the activation function ϕ_s^{**} .

$$Y_s = \theta' \cdot \phi_s^* \quad (5.13)$$

The activation function ϕ_{is} of a centroid c_i can be described by a Gaussian function.

$$\phi_{is} = \exp(-\beta \cdot \Delta_{is}) \quad (5.14)$$

Therein, β is calculated according to $\beta = \frac{1}{2 \cdot \sigma}$ and Δ_{is} is the distance between the centroid c_i and the x_s points according to $\Delta_{is} = (c_i - x_s)^2$.

Kriging Gaussian process regression [79] is a suitable tool for predicting the relationship of non-linear responses. In equation (5.15) for an ordinary Kriging model, the interpolated value vector \vec{b}^* is determined by the expectation μ , the sample vector \vec{b} and the weight matrix β .

$$\vec{b}^* = \mu - \beta \cdot (\vec{b} - \mu) \quad (5.15)$$

The weight matrix β describes the mutual correlation between the sample points, using a Gaussian correlation function. The function is based on the distance x between the sample points and the correlation length θ . Other correlation functions can be selected to obtain a better fit of the data.

$$f(x) = \exp\left(-\pi \cdot \left(\frac{x}{\theta}\right)^2\right) \quad (5.16)$$

5.5 Multi-criteria decision making

The selection of the best solution from the Pareto front is performed using a Multi-Criteria Decision Maker (MCDM) [80]. The MCDM is executed as a post-process at the end of the

* x_s denotes the sample points of the measured points $Y(x)$. The * marks that a bias term is added to the activation function ϕ_s to increase its robustness.

optimization process.

MCDM procedure First, the normalized objective vector $\vec{f}_{k,norm}(\vec{x}_0)$ is determined according to the following equation.

$$\vec{f}_{k,norm}(\vec{x}_0) = \frac{\vec{f}_k(\vec{x}_0) - f_{k,min}(\vec{x}_0)}{f_{k,max}(\vec{x}_0) - f_{k,min}(\vec{x}_0)} \quad (5.17)$$

Therein, $f_{k,min}$ and $f_{k,max}$ correspond to the minimum and maximum values of the objective vector \vec{f}_k . Subsequently, a rank value vector \vec{R} is determined based on the normalized objective vector $\vec{f}_{k,norm}$ and weight factors for the objectives $w_k \in \{0, 1\}$ are introduced as outlined in equation (5.18). Changing the value of the weight factors puts more emphasize on one of the objectives.

$$\vec{R} = \sum_{i=1}^k w_i \cdot \vec{f}_{i,norm}(\vec{x}_0)^\alpha \quad (5.18)$$

Therein, the exponent α is set to 1 to determine a linear rank value. The best solution corresponds to the design with the minimum rank value $\min(\vec{R})$.

5.6 Optimization algorithms

Different optimization algorithms are tested for the training of the model parameters of the SRM. From the family of heuristic optimizers the MOSA and MOPSO algorithms are chosen and from the family of genetic optimizers the MOGA-II and NSGA-II are chosen. Additionally, the RSM based optimization (FAST) is tested using the NSGA-II algorithm. First a short outline of the optimization algorithms is provided while more detailed information can be found in the literature. Subsequently, the performance of the optimization algorithms is tested for a SRM sample case of a CI engine.*

NSGA-II The Non-dominated Sorting Genetic Algorithm II (NSGA-II) introduced by Deb et al. [1, 2] categorizes the solutions based on a domination count into different Pareto fronts. Additionally, the diversity and equal spread of solutions along the Pareto front is ensured by a crowding distance function. The reproduction of solutions is obtained by using crossover and mutation. Crossover ensures the convergency towards the currently best Pareto front while mutation ensures the diversity of the solutions.

The settings of the NSGA-II algorithm used in this thesis are outlined in table 11. The number of generations is set to 500 to have a large number of Pareto solutions. The number of individuals per generations is set to 10 wherefor in total 5000 designs are evaluated by the NSGA-II algorithm. The crossover probability is set to 0.9. The mutation probability is determined according to n which denotes the number of optimization parameters. A low distribution index for crossover and mutation means a wide spread of offspring designs

*The SRM model is set up with 100 notional particles, 1.0°CA time step, 1 stochastic cycle and initial random seed equal to 1.

while a large distribution index means a narrow spread of offspring designs. The initial random seed is set to 1.

Parameter	Value
Number of generations	500
Number of individuals	10
Crossover probability $\in \{0, 1\}$	0.9
Mutation probability $\in \{0, 1\}$	$1/n$
Distribution index for crossover	20.0
Distribution index for mutation	20.0
Initial random seed	1

Table 11: NSGA-II optimization algorithm settings.

The aim of the NSGA-II optimization is to find the best set of SRM parameters for minimizing the sum of least squares of cylinder pressure $\varepsilon_{Pressure}$, peak cylinder pressure ε_{PCP} , peak cylinder pressure crank angle ε_{PCPCA} and carbon monoxide mass fraction ε_{yCO} . The optimization parameters include the coefficients B_1 , B_2 and B_3 which belong to the SOV correction function in equation (9.5), the C_{pilot1} and C_{pilot2} parameters which are multipliers of the pilot injection masses, the injection parameter C_{inj} , the turbulent length scale parameter C_{ε_2} and the scalar mixing time parameter C_{ϕ} . The four-dimensional objective and Pareto solution space is translated into two two-dimensional plots shown in figure 38. The NSGA-II is able to drive the designs towards the area of low optimization errors ε . However, there is a trade-off between the lowest combustion progress related error ($\varepsilon_{Pressure}$) and the lowest engine-out emission related error (ε_{yCO}). Overall, the NSGA-II achieves the lowest error for $\varepsilon_{Pressure}$ compared to the other optimization algorithms.

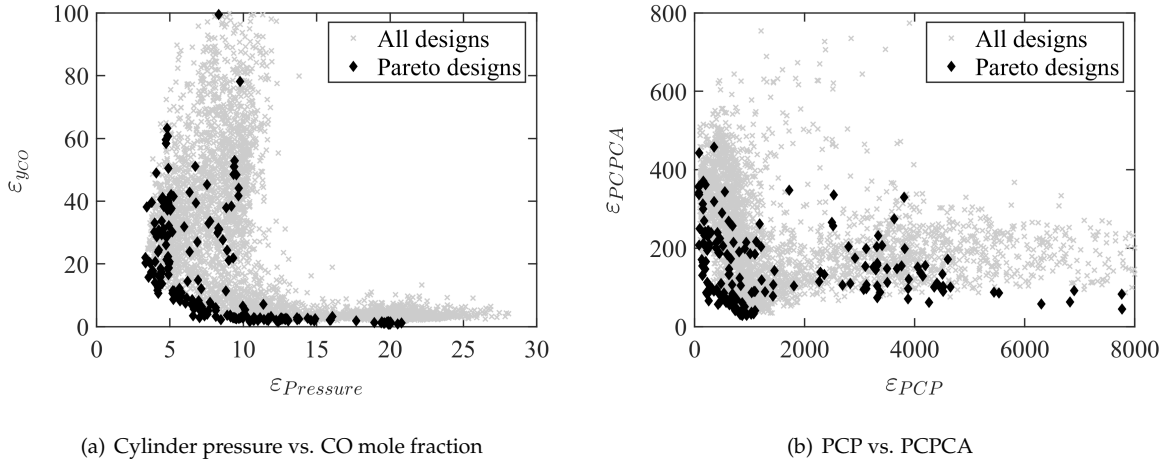


Figure 38: Pareto solutions for the NSGA-II optimization run with 5000 designs.

Further analysis of the Pareto solutions is done by using the parallel coordinates plot in figure 39. The Pareto solutions are now shown as grey-colored lines while the best selected design is highlighted with a bold black line.* The NSGA-II shows some distinct clustering of designs where it tries to minimize either $\varepsilon_{Pressure}$ or ε_{yCO} . This makes it behave distinctly different than other genetic algorithms investigated in this thesis.

*The best design is selected using the MCDM from section 5.5 with the weights $w_{\varepsilon_{Pressure}} = w_{\varepsilon_{PCP}} = w_{\varepsilon_{PCPCA}} = 0.33$.

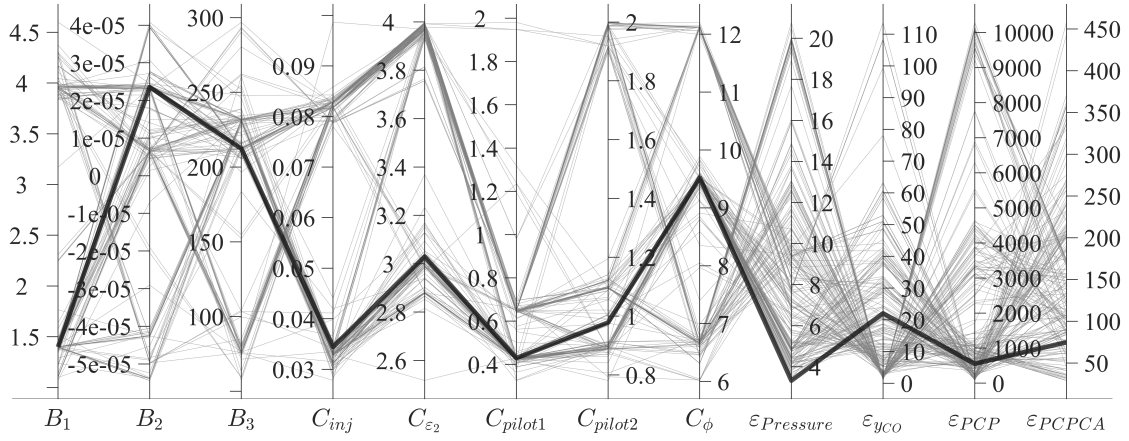


Figure 39: Parallel coordinates of optimization parameters and objectives for the NSGA-II optimization run with 5000 designs. The grey lines show the Pareto solutions. The black thick line shows the design selected by MCDM with equi-weighted objectives.

FAST NSGA-II The principle of the FAST optimization is already introduced in figure 35. This method extends the external optimization using the NSGA-II and SRM with an internal optimization using NSGA-II and RSMs [68]. The FAST NSGA-II algorithm settings are shown in table 12. The NSGA-II settings are the same as shown in table 11. As for the NSGA-II the number of generations is set to 500 and the number of individuals is set to 10. The Polynomial SVD, Kriging and Neural Network models are selected for the internal optimization. The training set size for the RSMs is set to 1000 designs. The external/internal optimization ratio is set to 0 so that only internal optimization is performed. The internal exploration / exploitation ratio is set to 0.5 so that 50% of designs in one generation are created by the space filler algorithm and the other 50% of designs are created by the optimization algorithm.

Parameter	Value
Number of generations	500
Number of individuals	10
Response surface model	Polynomial, Kriging, Neural Network
RSM training data set size	1000
External/internal optimization ratio $\in \{0, 1\}$	0
Internal exploration/exploitation ratio $\in \{0, 1\}$	0.5
Initial random seed	1

Table 12: FAST NSGA-II optimization algorithm settings.

The optimization results in figure 40 show a more widely distributed set of feasible designs compared to the NSGA-II algorithm. The FAST NSGA-II algorithm performs slightly better finding lower ε_{yCO} errors while it does not perform as good as the NSGA-II regarding the $\varepsilon_{Pressure}$ and ε_{PCPA} errors.

The MCDM selection of the best design applies the same weights for the objectives as for the NSGA-II. The ranges of the optimization parameters of the best design are similar to the NSGA-II. However, the distribution of the Pareto solutions is much more diverse for the FAST NSGA-II compared to the NSGA-II and all optimization parameter ranges seem to be covered.

The robustness of the NSGA-II and FAST NSGA-II algorithm is further investigated by

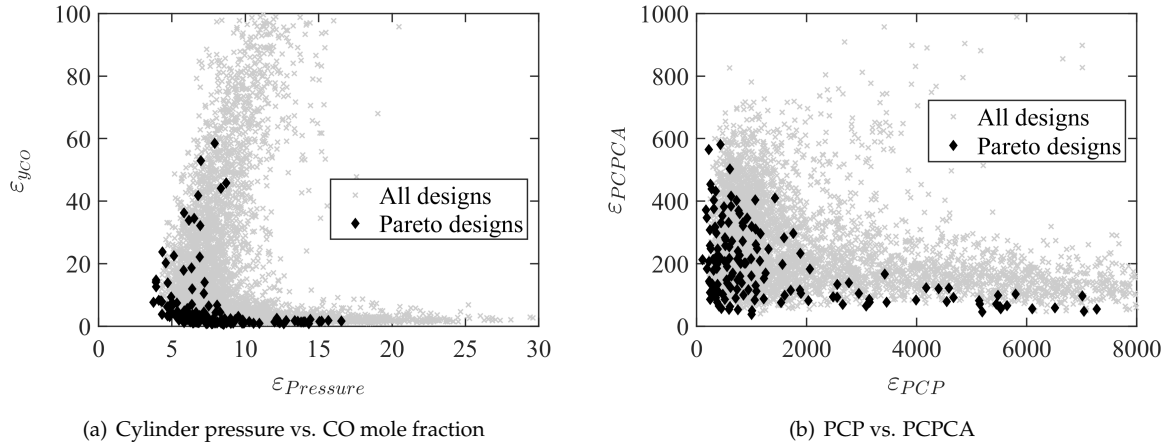


Figure 40: Pareto solutions for the FAST NSGA-II optimization run with 5000 designs.

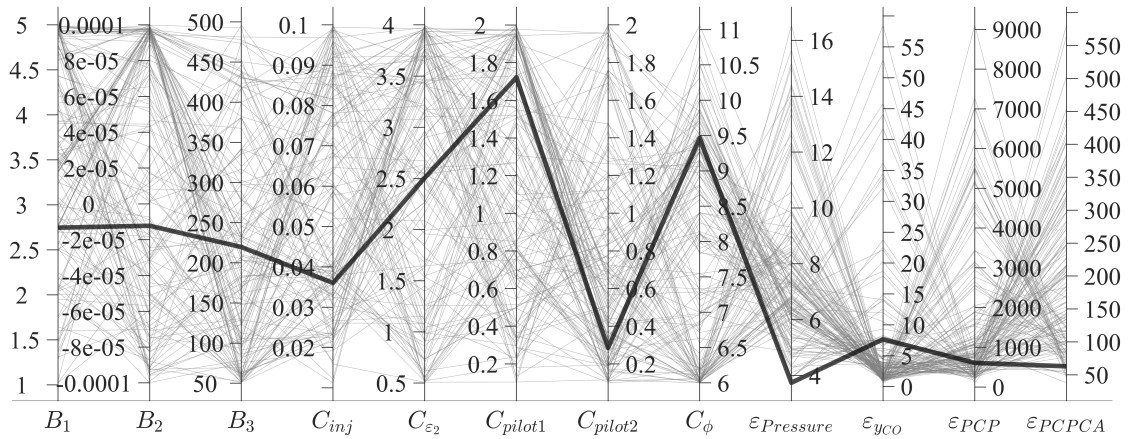


Figure 41: Parallel coordinates of optimization parameters and objectives for the FAST NSGA-II optimization run with 5000 designs. The grey lines show the Pareto solutions. The black thick line shows the design selected by MCDM with equi-weighted objectives.

comparing the empirical attainment function (EAF) [81, 82]. To generate the EAF of the two algorithms the optimizations are repeated 10 times and for each repetition the initial seed is increased by one. This yields a different random number sequence during the optimization and it is a reliable test for the robustness of the algorithms. Figure 42 shows the difference of the two EAFs by using a grey colormap. The darker the color the better the performance of the algorithm in comparison to the other algorithm. Further the solid black lines indicate the variation of the Pareto solutions for the 10 different runs. Overall, the NSGA-II shows a slightly better performance compared to the FAST NSGA-II especially for low errors of ϵ_{yCO} .

MOGA-II The Multi-Objective Genetic Algorithm II (MOGA-II) [83] is an extension of MOGA introduced by Poloni [84]. MOGA-II evolves the designs by using genetically inspired reproduction and elitism. The reproduction step consists of one-point crossover, directional crossover and mutation. One-point crossover takes two designs and randomly cuts them in half at the crossing point. The two corresponding halves of the designs are swapped and the designs are rejoined. Directional crossover accounts for the fitness of the designs and performs the crossover according to it. Mutation randomly perturbs the parameters of the

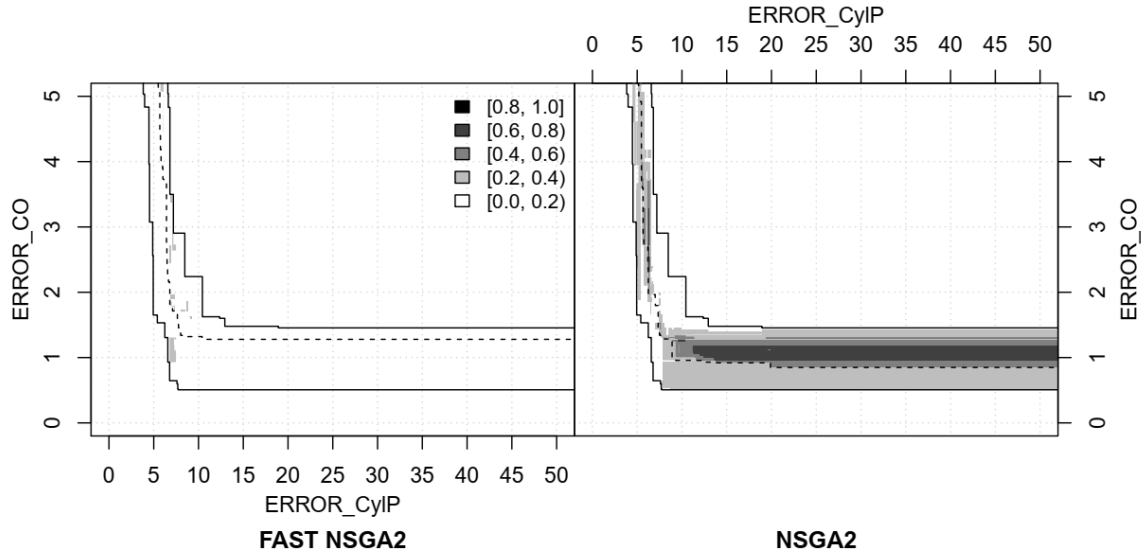


Figure 42: Comparison of the EAF of FAST NSGA-II and NSGA-II. The solid black lines indicate the best and worst Pareto front and the dashed black line indicates the median Pareto front of each algorithm. The darker the color of the colormap the better the performance of the algorithm in comparison to the other algorithm.

designs and ensures diversity of the solutions [83]. Elitism keeps the best designs of the previous generations and ensures convergency towards the Pareto front.

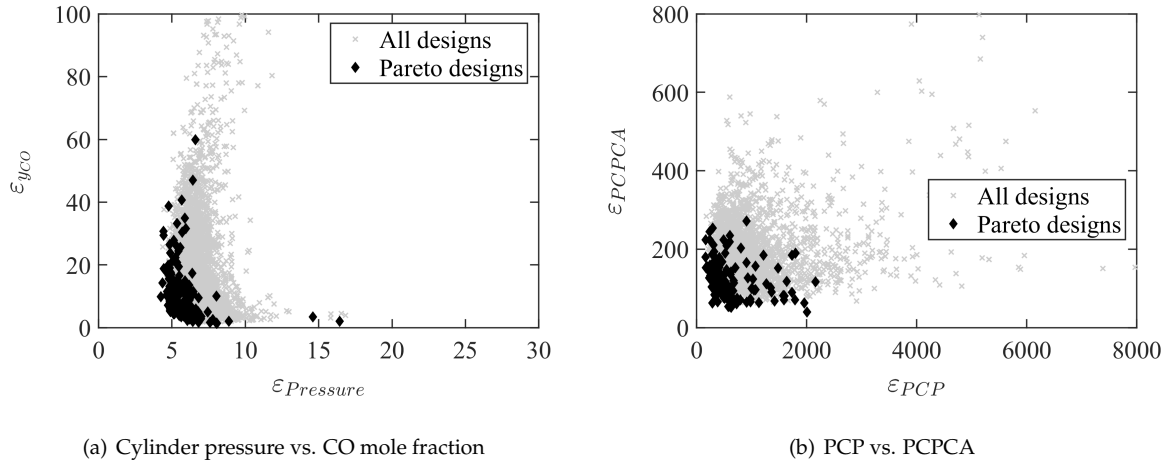
The settings of the MOGA-II algorithm are shown in figure 13. The directional crossover considers additional designs from the current generation with a high fitness value to decide in which direction to push the optimization and its probability is set to 0.5. The selection probability defines how many of the good designs of the previous generations are kept and its value is set to 0.05. The mutation procedure is driving the exploration of the design space and its probability is set to 0.1. The mutation ratio defines how many of the optimization parameters will be mutated at once. The classic crossover probability is automatically calculated from the values of the other probabilities assuming that they all sum up to 1.

Parameter	Value
Number of generations	500
Number of individuals	10
Directional crossover probability $\in \{0, 1\}$	0.5
Selection probability $\in \{0, 1\}$	0.05
Mutation probability $\in \{0, 1\}$	0.1
Mutation ratio $\in \{0, 1\}$	0.05
Initial random seed	1

Table 13: MOGA-II optimization algorithm settings.

The MOGA-II results in figure 43 show a different behaviour compared to the other optimization algorithms. The feasible and Pareto solutions are much closer together in the objective space compared to NSGA-II and FAST NSGA-II. Further, the MOGA-II predicts low ε_{yCO} errors similar to the FAST NSGA-II while it does not perform so well for the minimization of the ε_{PCP} and ε_{PCPCA} errors.

Evaluating the Pareto solutions and the best design in figure 44 underlines the different



(a) Cylinder pressure vs. CO mole fraction

(b) PCP vs. PCPCA

Figure 43: Pareto solutions for the MOGA-II optimization run with 5000 designs.

behaviour of the MOGA-II algorithm compared to NSGA-II and FAST NSGA-II. The NSGA-II and FAST NSGA-II algorithms showed a wide distribution of optimum solutions while the MOGA-II converges to one optimum solution. The optimized parameters are also in a different range compared to the other optimization algorithms.

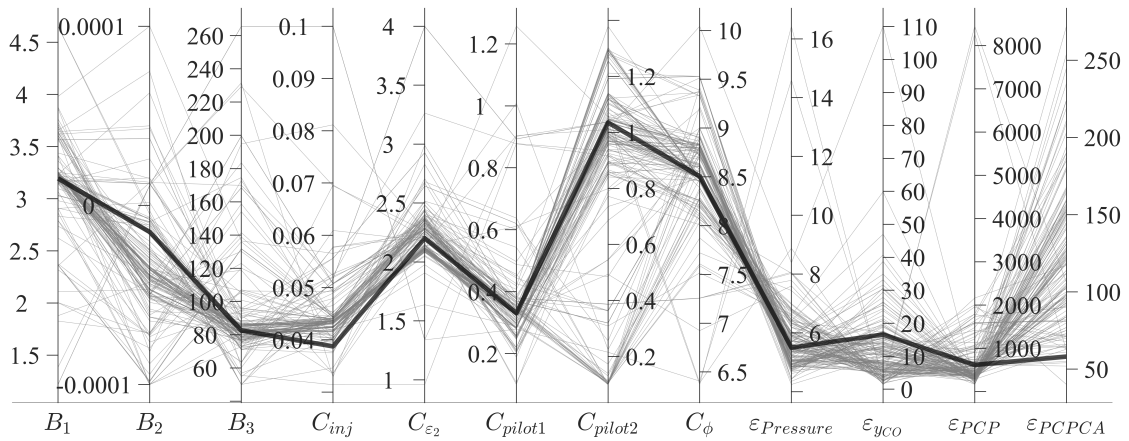


Figure 44: Parallel coordinates of optimization parameters and objectives for the MOGA-II optimization run with 5000 designs. The grey lines show the Pareto solutions. The black thick line shows the design selected by MCDM with equi-weighted objectives.

MOSA The Multi-Objective Simulated Annealing (MOSA) algorithm is an extension of the Simulated Annealing (SA) algorithm introduced by Kirkpatrick et al. [85, 86] and belongs to the family of heuristic optimizers. The SA is a single-objective optimization algorithm and is based on the analogy of a hot metal that cools down over time following an exponential function. Thereby, the hot temperature phase represents the exploration phase and the cold temperature phase represents the exploitation phase in the optimization. A temperature scheduler is applied to describe the change of temperature T in dependence of the number of iterations N [87].

$$T = T_0 \left(1 - \frac{N}{N_{hot}}\right)^2 \quad (5.19)$$

Therein, T_0 is the initial temperature and N_{hot} is the number of iterations of the hot phase. For the cold phase the case $T = 0$ is always true. For the multi-objective SA a dominance criteria is introduced which ranks the designs according to their position in the objective space [87].

The settings of the MOSA algorithm are shown in table 14. The initial temperature T_0 is a normalized value and it is set to 0.1. A large value for T_0 increases the variation of designs and improves the robustness of finding the global best solutions. A low value of T_0 improves the convergence towards the optimum solution. The perturbation length defines the distance between the newly created designs where a large perturbation length creates far distant designs. The initial perturbation length is set to 1 at the beginning of the hot phase and is continuously decreased until it reaches the minimum perturbation length with a value of 0.05 at the beginning of the cold phase.

Parameter	Value
Number of generations	500
Number of individuals	10
Initial temperature (T_0) $\in \{0, 1\}$	0.1
Fraction of hot iterations (N_{hot}) $\in \{0, 1\}$	0.5
Minimum perturbation length of the cold phase $\in \{10^{-6}, 1\}$	0.05
Initial random seed	1

Table 14: MOSA optimization algorithm settings.

The feasible and Pareto solutions in figure 45 show a good performance of the MOSA algorithm minimizing the selected errors. Thereby, it shows a similar good performance as the FAST NSGA-II and MOPSO algorithms. The MOSA algorithm shows a good performance regarding minimization of $\varepsilon_{y_{CO}}$ and $\varepsilon_{Pressure}$ at the same time.

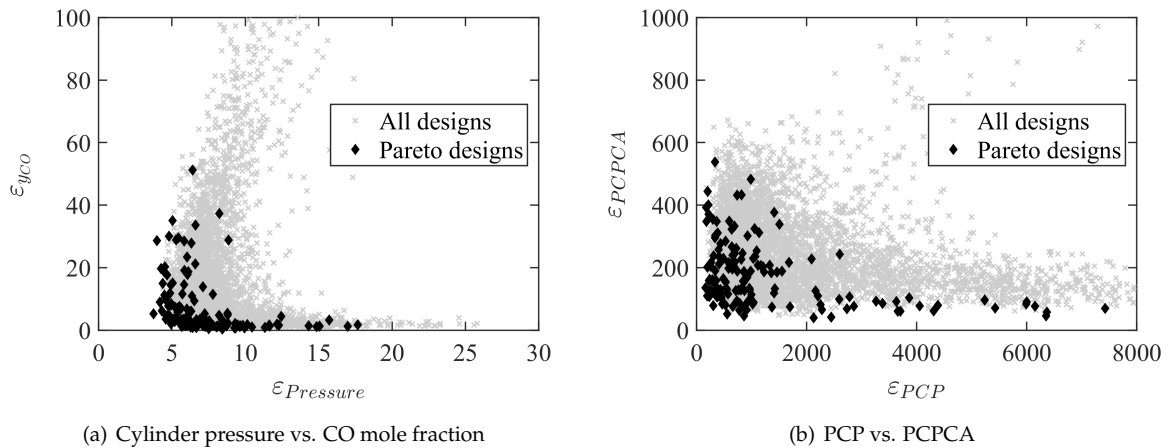


Figure 45: Pareto solutions for the MOSA optimization run with 5000 designs.

The parallel coordinates in figure 46 show an even distribution of the solutions. The best design selected by MCDM is different compared to all other algorithms with a lower integral length scale during intake valve flow and higher injection masses for the pilot injections.

MOPSO The Multi-Objective Particle Swarm Optimizer (MOPSO) belongs to the group of heuristic optimizers. Its initial purpose was to use it to study the behaviour of a swarm

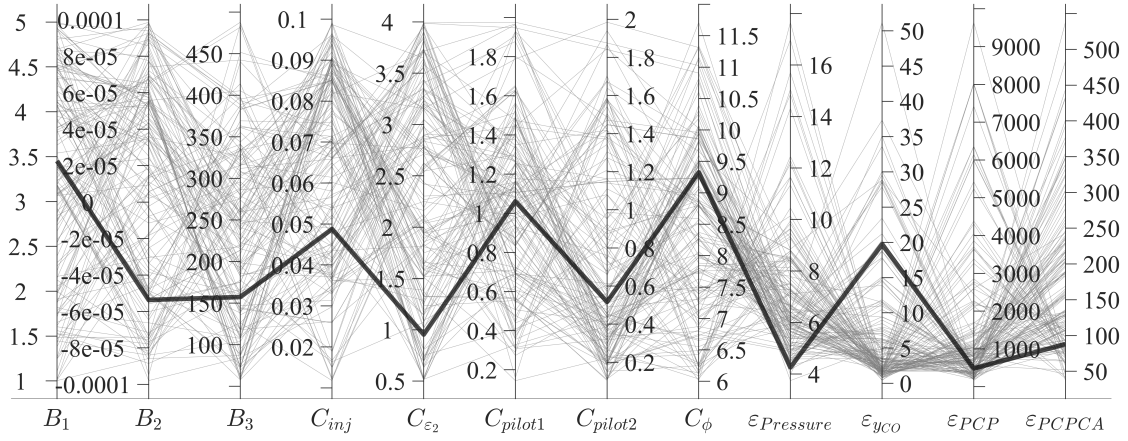


Figure 46: Parallel coordinates of optimization parameters and objectives for the MOSA optimization run with 5000 designs. The grey lines show the Pareto solutions. The black thick line shows the design selected by MCDM with equi-weighted objectives.

of birds that rapidly changes direction while it keeps its internal organization intact [88]. Comparing it to a genetic algorithm the swarm is similar to a population and the particle is similar to an individual. The particle evolution over time $x_i(t + 1)$ is driven by its velocity $v_i(t + 1)$ which can be determined by the following equation [89]

$$v_{ij}(t + 1) = v_{ij}(t) + c_1 r_{1j}(t) [y_{ij}(t) - x_{ij}(t)] + c_2 r_{2j}(t) [\hat{y}_j(t) - x_{ij}(t)] \quad (5.20)$$

where $v_{ij}(t)$ is the velocity of particle i in dimension j at time t , $x_{ij}(t)$ is the position of particle i in dimension j at time t and c_{1j} and c_{2j} are model constants used to scale the contribution of cognitive learning and social learning [89]. The cognitive learning is influenced by the best position $y_{ij}(t)$ of particle i in dimension j ever obtained since the beginning of the optimization. The social learning is influenced by the best position $\hat{y}_j(t)$ of all particles in dimension j ever obtained since the beginning of the optimization. $r_{1j}(t)$ and $r_{2j}(t)$ represent uniformly distributed random numbers in the range $r \in \{0, 1\}$ that account for a stochastic influence in the optimization [89].

The MOPSO algorithm additionally incorporates an elite set which contains the best swarm according to the Pareto dominance criteria [90]. New particles are added to the elite set after each iteration. The elite set can influence the velocity of a particle to drive it towards the direction of the current best Pareto front.

The settings of the MOPSO algorithm are outlined in table 15. The elite set size is set to 10. The inertia weight defines the importance of the current particle velocity to continue moving in the same direction. The inertia weight is set to 0.721. The cognitive learning weight and social learning weight are set to 0.745. The elite learning weight is set higher to 1.49. Turbulence defines a probability of adding a random offset to the particle position and it increases the robustness of the algorithm. Lifecycle is the number of iterations in which a particle does not change its position. If the Lifecycle limit is reached without any change the particle position is changed randomly.

The results of the MOPSO algorithm in figure 47 resemble the ones of FAST NSGA-II and MOSA. The feasible and Pareto solutions are widely distributed across the objective space

Parameter	Value
Number of generations	500
Number of individuals	10
Elite set size $\in \{10, 100\}$	10
Inertia weight $\in \{0, 1\}$	0.721
Cognitive learning weight $\in \{0, 2\}$	0.745
Social learning weight $\in \{0, 2\}$	0.745
Elite learning weight $\in \{0, 2\}$	1.49
Turbulence $\in \{0, 0.9\}$	0.1
Lifecycle $\in \{0, 100\}$	20
Initial random seed	1

Table 15: MOPSO optimization algorithm settings.

and the optimization errors are minimized effectively.

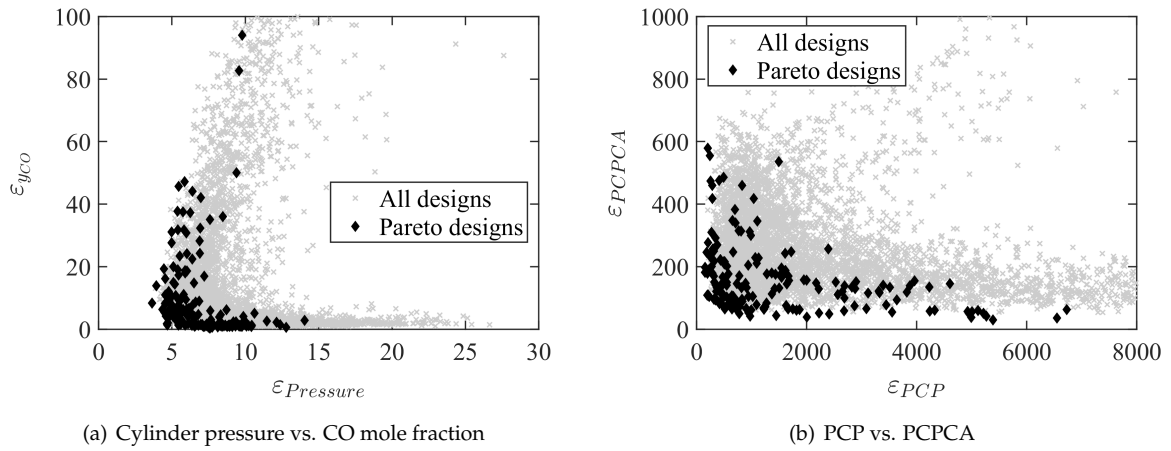


Figure 47: Pareto solutions for the MOPSO optimization run with 5000 designs.

The parallel coordinates of the MOPSO algorithm results in figure 48 show that the algorithm covers the optimization parameter ranges evenly. The best design selected by the MCDM is similar to the one from NSGA-II and FAST NSGA-II which is an excellent confirmation of the robustness of the optimization approach. Limitations of further minimization of the error values are attributed to the SRM setup and selection of optimization parameters.

Comparison of the algorithms The predicted scalar mixing times τ_ϕ for the selected designs using equi-weighted objectives of the five investigated optimization algorithms are shown in figure 49. The scalar mixing time is depicted using a logarithmic scale to account for the different magnitudes of time scales. The comparison shows overall the same trend for the different algorithms with small deviations for the pilot injections due to the different values of C_{pilot1} and C_{pilot2} parameters, and differences in the main injection for the MOPSO algorithm because of the higher value of the C_{inj} parameter.

The predicted cylinder pressure of the five optimization algorithms is shown in figure 50. The coarse setup of the SRM with 100 notional particles, 1 °CA time step size and 1 stochastic cycle chosen for this investigation results in jagged pressure profiles. The cylinder pressure shows some larger deviations between the different optimization algorithms which is reasonable given that the optimization errors $\varepsilon_{Pressure}$, ε_{yCO} and ε_{PCPCA} of the selected

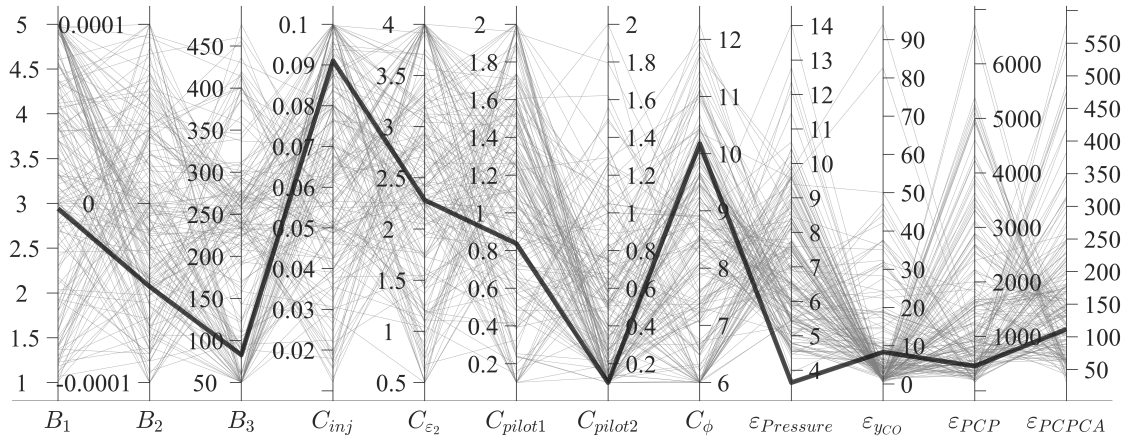


Figure 48: Parallel coordinates of optimization parameters and objectives for the MOPSO optimization run with 5000 designs. The grey lines show the Pareto solutions. The black thick line shows the design selected by MCDM with equi-weighted objectives.

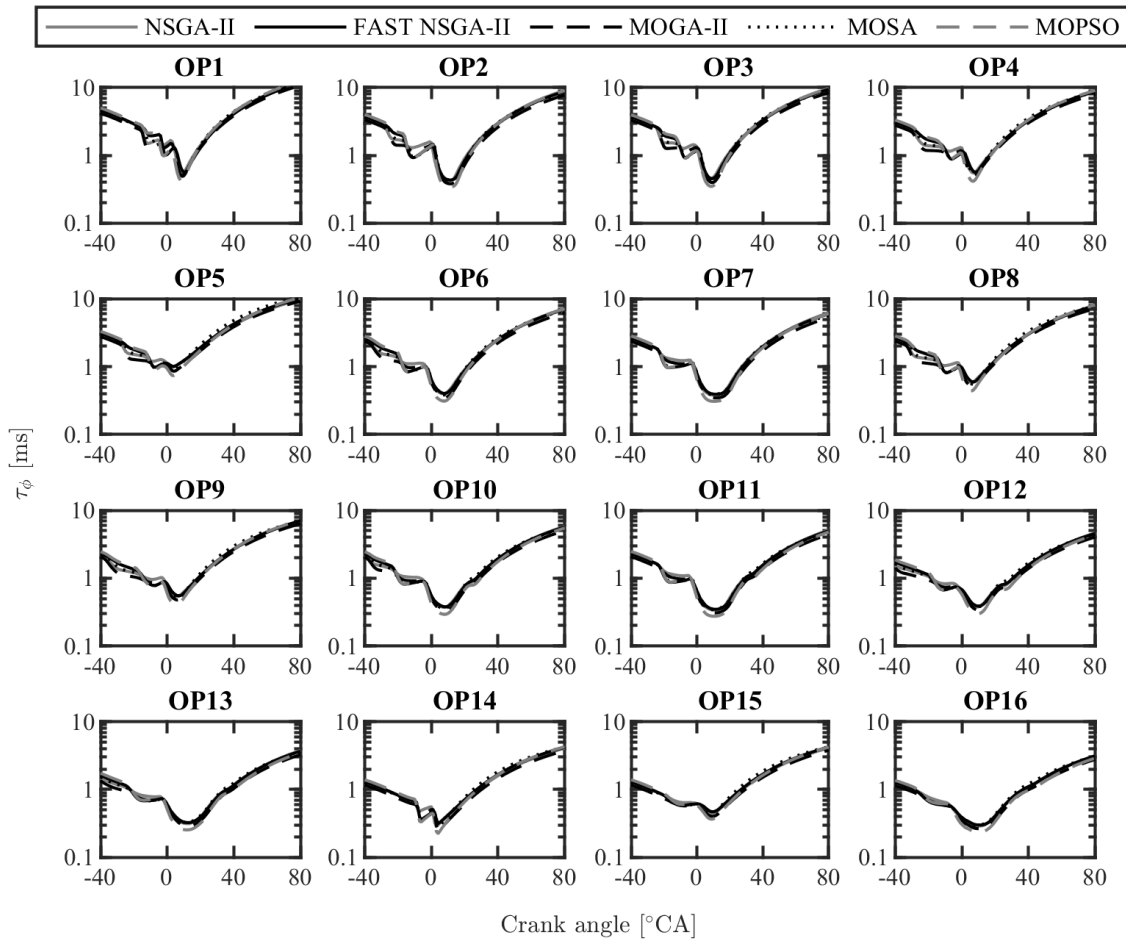


Figure 49: Comparison of scalar mixing time of the selected designs of the five different optimization runs with NSGA-II, FAST NSGA-II, MOGA-II, MOSA and MOPSO.

designs are different.

The CO mole fractions outlined in figure 51 show jagged profiles as well. The CO profiles show variations for the different optimization algorithms especially during the expansion stroke. The MOPSO algorithms shows the lowest CO mole fractions during the expansion stroke for most of the operating points because of the lower scalar mixing time at that time as

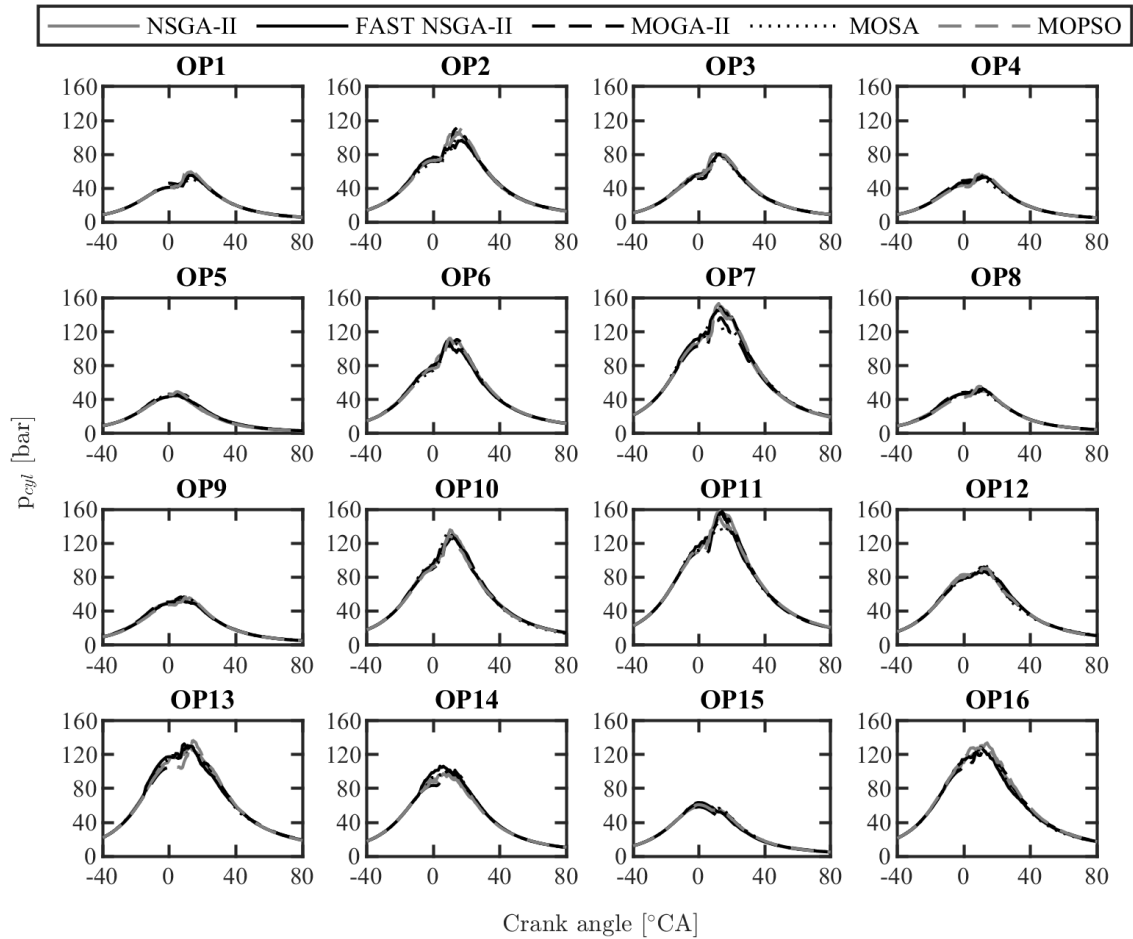


Figure 50: Comparison of cylinder pressure of the selected designs of the five different optimization runs with NSGA-II, FAST NSGA-II, MOGA-II, MOSA and MOPSO.

a result of the higher value of the C_{inj} parameter.

5.7 Conclusions for multi-objective optimization

The aspects of multi-objective optimization of the SRM model parameters are introduced in this chapter. Among them is the definition of the optimization errors $\varepsilon_{Pressure}$, $\varepsilon_{y_{CO}}$, ε_{PCP} and ε_{PCPCA} for multiple operating points which are defined to measure the fitness of SRM towards the experimental combustion progress and engine-out emissions. The exploration of the design space is handled by the space filler algorithm and different algorithms are tested. The ISF algorithm showed overall the best performance regarding uniformity of the design space while finally the ULHC algorithm was chosen because of the lower computational demand. The selection of the best design is performed using a MCDM algorithm which allows to adjust the weights of the optimization errors to influence the decision process. Different genetic and heuristic optimization algorithms are compared for the multi-objective optimization of SRM model parameters for a CI engine. Overall, all five optimization algorithms are able to minimize the optimization errors. However, the absolute values of the optimization errors of the optimization algorithms are different wherefor the optimum SRM model parameters are deviating from each other. The FAST NSGA-II, MOSA and

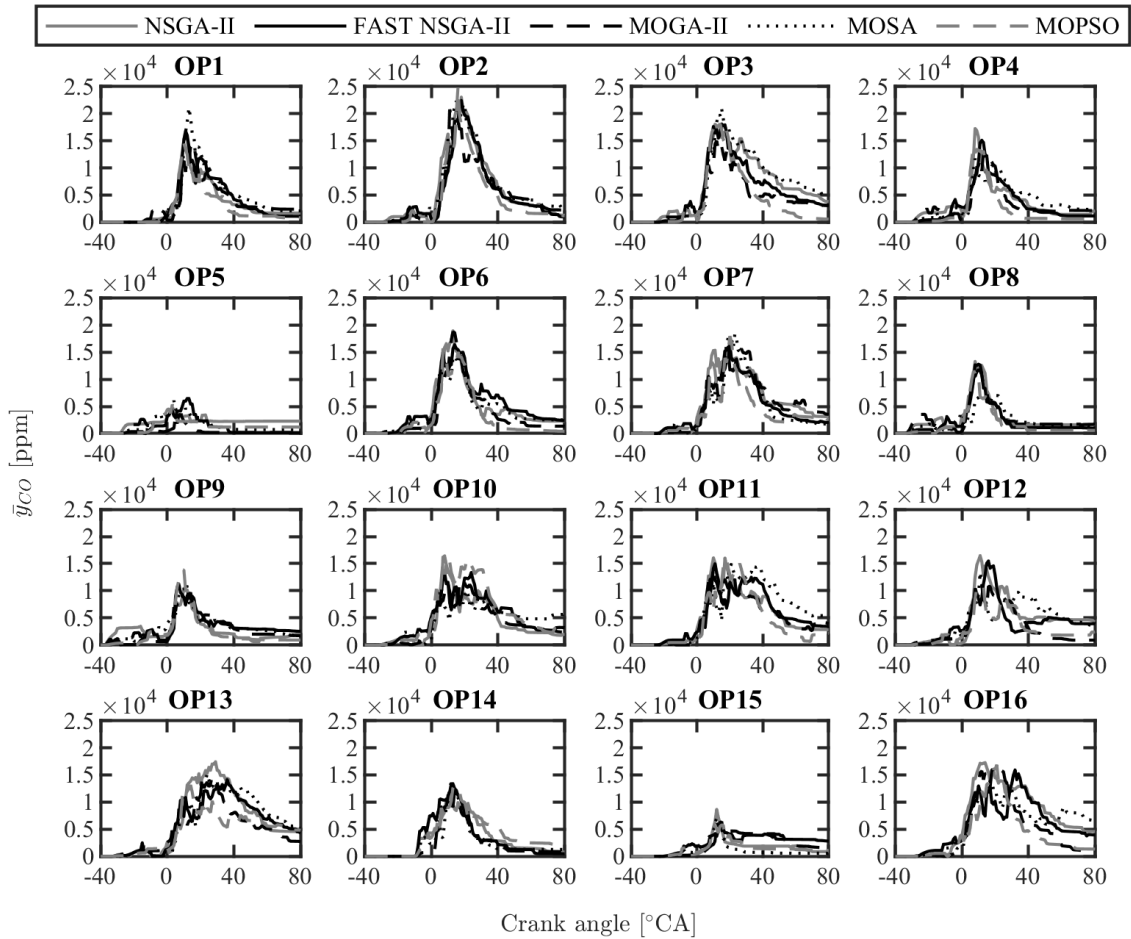


Figure 51: Comparison of CO mole fraction of the selected designs of the five different optimization runs with NSGA-II, FAST NSGA-II, MOGA-II, MOSA and MOPSO.

MOPSO algorithms showed the overall best performance minimizing all four optimization errors and they yield a diverse distribution of Pareto solutions. Finally, the RSM-based optimization (FAST NSGA-II) together with the ULHC space filler is selected as best practice since it showed a good performance minimizing the $\varepsilon_{Pressure}$ and $\varepsilon_{y_{CO}}$ errors at the same time. Further, it shows a diverse distribution of the Pareto solutions even when reducing the number of generations from 500 to 300. Overall, the multi-objective optimization of 5000 designs for 16 training points using 100 notional particles, $1.0^{\circ}CA$ time step size and 1 stochastic cycle took 55 hours on a AMD Epyc 7551 32-core processor.

6 Optimization of a spark ignition engine model

The SI-SRM introduced in chapter 4.3 and the MOO platform introduced in chapter 5 are validated for two single-cylinder research engines. The two SI engines are investigated in the industry funded research projects “Water injection in SI engines” [91] and “Fuel composition for CO₂ Reduction” [92]. The experimental measurements were provided by the project partners from TU Berlin and RWTH Aachen. The engine specifications and operating conditions are outlined in the next sections.

6.1 Engine specifications

The SI engine from the research project [92] is named as *Engine A* in the following sections and its specifications are outlined in table 16. The engine bore is similar to a passenger car sized engine while the stroke is longer to support the tumble flow motion. The crank is slightly offset. The base compression ratio is 10.8:1 and the modified compression ratio is increased to 13:1. The engine is equipped with a six hole direct injector mounted centrally in the cylinder head.

Parameter	Unit	Value
Bore	mm	75.0
Stroke	mm	113.2
Rod Length	mm	220
Crank Offset	mm	-0.4
Compression Ratio (Base)	–	10.8:1
Compression Ratio (Modified)	–	13:1
Crevice Volume	%	4

Table 16: Specification of engine parameters of Engine A.

The cylinder head and piston geometry of *Engine A* are adapted in SI-SRM using the model introduced by Bjerkborn et al. [18]. The result is shown in figure 52 where the blue dot highlights the spark plug. The same method is applied for the second SI engine investigated in this work.

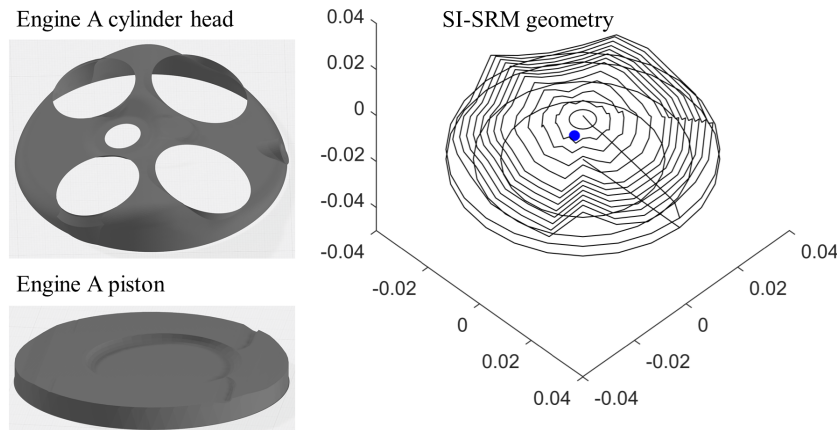


Figure 52: Engine A cylinder head and piston geometry.

The SI engine from the research project [91] is named *Engine B* in the following sections

and its specifications are outlined in table 17. The engine bore, stroke and connecting rod length are smaller compared to *Engine A*. The compression ratio is slightly larger compared to *Engine A*. The relative piston crevice volume is found to be similar for both investigated engines.

Parameter	Unit	Value
Bore	mm	71.9
Stroke	mm	82.0
Rod Length	mm	137
Compression Ratio	–	11.07:1
Crevice Volume	%	4

Table 17: Specification of engine parameters of Engine B.

6.2 Physical properties of gasoline fuel

The *Engine A* is operated with a standard gasoline fuel with research octane number (RON) 95.4 and motored octane number (MON) 85.0. The fuel is blended with 9.9 liquid volume percent of ethanol. The complexity of the gasoline fuel composition is represented by a multi-component surrogate which is developed based on the method of Seidel [93, 94]. The method is validated extensively using SRM and detailed 3D CFD simulations to predict knocking combustion in SI engines by Netzer et al. [59, 95, 96]. The surrogate model *Fuel A* is compared with the experiment fuel in table 18. The surrogate closely matches the RON and MON, lower heating value (LHV), C:H:O ratio and density of the experiment fuel.

Parameter	Unit	Experiment	Surrogate
RON	–	95.4	95.4
MON	–	85.0	86.8
LHV	MJ/kg	41.62	41.32
C:H:O	–	6.6:12.8:0.21	6.31:12.2:0.21
Density	kg/m ³	747.2	748.6

Table 18: Comparison of experiment gasoline fuel and ETRF surrogate for Fuel A.

The composition of *Fuel A* in liquid volume percent is outlined in table 19. It consists of four species to adjust the properties to the experiment fuel. The n-heptane and iso-octane fractions are adjusted to match the RON, and the toluene fraction represents the aromatic content of the experiment fuel. The Modified linear by Volume Method from Morgan et al. [97] is used to determine the Toluene Reference Fuel (TRF) mixture. The composition of the ethanol - TRF (Ethanol Toluene Reference Fuel) mixture is calculated by the assumption of linear blending on a molar basis according to Anderson et al. [98]. The equations are implemented and validated in LOGEtable v2.0 [99] based on the work of Seidel [93].

Species	Unit	Liquid Volume Fraction
iso-Octane	%	47.9
n-Heptane	%	14.7
Toluene	%	27.5
Ethanol	%	9.9

Table 19: Liquid volume fraction of ETRF surrogate species of Fuel A.

The *Engine B* is operated as well with a standard gasoline fuel with RON 96.7 and MON 85.8. The fuel is blended with 10.1 liquid volume percent of ethanol. The surrogate *Fuel B* is developed using the same method as for *Fuel A*.

Parameter	Unit	Experiment	Surrogate
RON	–	96.7	96.7
MON	–	85.8	87.4
LHV	MJ/kg	41.78	41.13
C:H:O	–	6.6:12.8:0.21	6.3:11.8:0.21
Density	kg/m ³	748.7	756.4

Table 20: Comparison of experiment gasoline fuel and ETRF surrogate for Fuel B.

The composition of *Fuel B* in liquid volume percent is outlined in table 21. It consists of the same four species as the *Fuel A* surrogate. However, the aromatic and alcohol content is slightly increased compared to *Fuel A* wherefor RON and MON are higher. The liquid properties of *Fuel A* and *Fuel B* are summarized in table 51.

Species	Unit	Liquid Volume Fraction
iso-Octane	%	44.0
n-Heptane	%	14.1
Toluene	%	31.8
Ethanol	%	10.1

Table 21: Liquid volume fraction of ETRF surrogate species of Fuel B.

6.3 Operating conditions

The operating conditions of *Engine A* used for the investigation in this thesis are outlined in figure 53. The base engine map covers the operating range from 1000 to 4000 rpm and 10 to 70 mg/stroke injected fuel mass at stoichiometric conditions. Additionally, a relative air-fuel ratio (λ) sweep at 1500 and 2000 rpm engine speed and a spark timing sweep at 1500 and 2000 rpm high load are investigated. The spark timing sweep is conducted at the modified compression ratio of 13:1. The data set is distributed into 8 training points (full black diamonds) and 73 validation points (hollow circles). The selection of the training points covers two different engine speeds, part and high load conditions and stoichiometric and lean mixtures.

The SI-SRM simulation is started at intake valve closure (IVC) and a full engine cycle is calculated. The valve lift profiles are provided by the experiments and are the same for all operating conditions. The timings of the intake and exhaust valves are changing for the different operating conditions. The intake and exhaust manifold pressures are measured using a low-pressure indication system and this information is provided as boundary conditions to the SI-SRM. The start of fuel injection is at -300 °CA with 200 bar injection pressure and the injection duration is adjusted according to the injected mass. The cylinder liner, head and piston wall surface temperatures are calculated using the correlation function in equation (9.4). The resulting wall surface temperatures are outlined in figure 115. The initial turbulent kinetic energy k_{init} is calculated using the equation (6.1) and the results are shown in figure 54 (c).

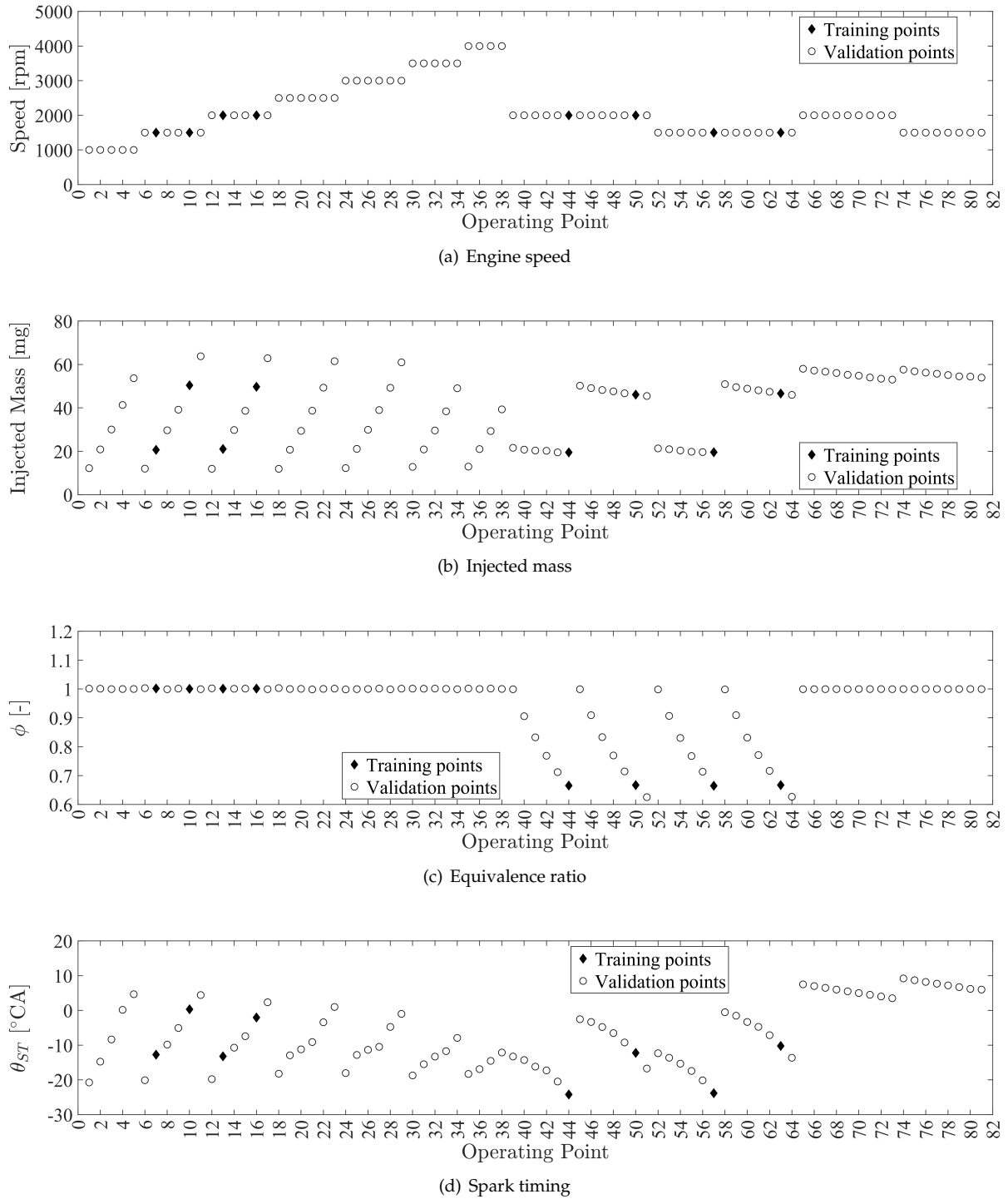


Figure 53: Training and validation points of Engine A.

$$k_{init} = 0.45 \cdot \dot{m}_{air}^2 \quad (6.1)$$

The pressure, temperature and EGR at IVC are determined using the thermodynamic analysis of LOGEngine v3.2 [100]. The thermodynamic analysis matches the experimental compression stroke pressure by optimizing the aforementioned parameters. The results are shown in figure 54 (a), (b) and (d).

The operating conditions of *Engine B* are outlined in figure 55. The data set just comprises

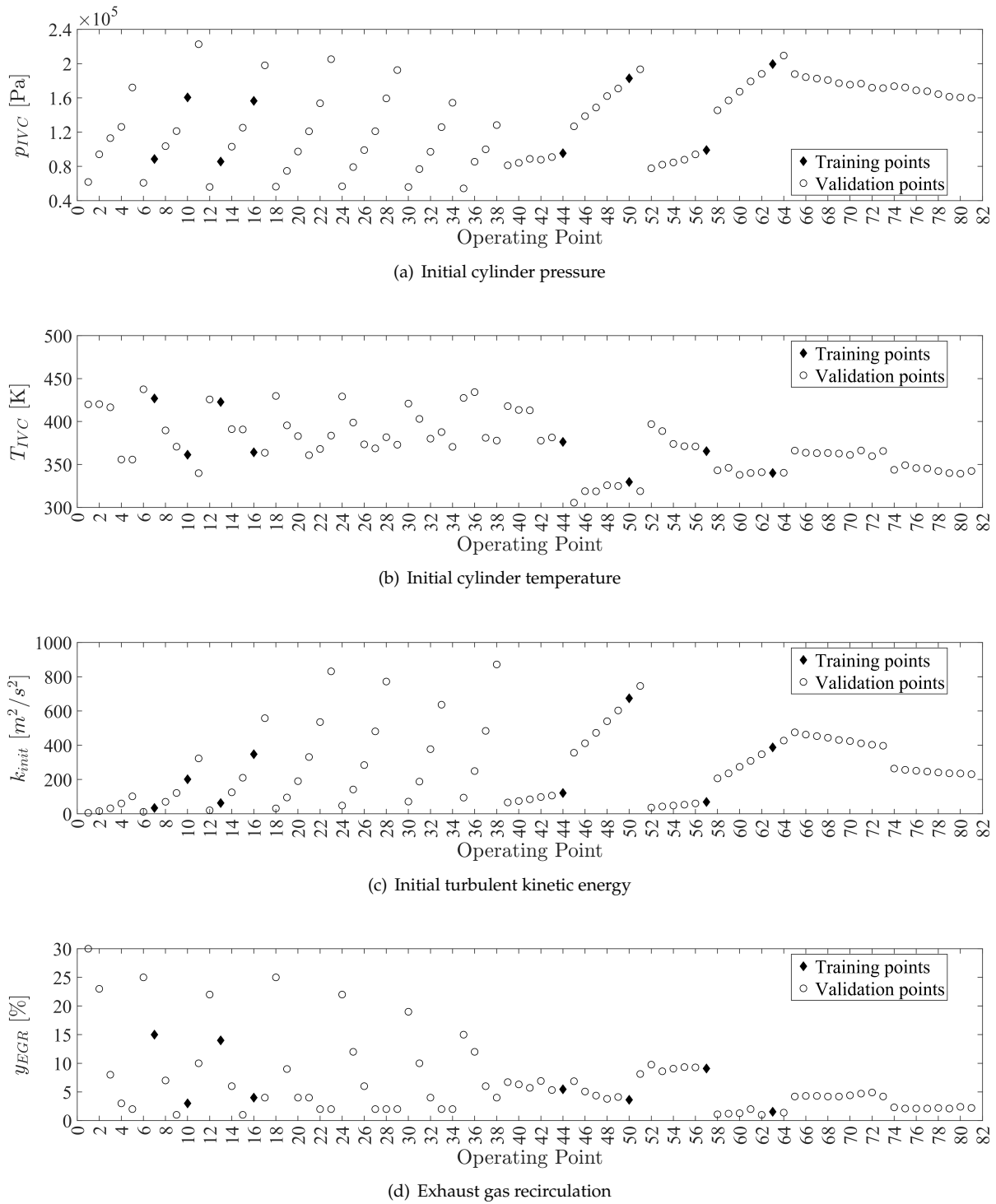


Figure 54: Initial conditions of Engine A.

8 operating points which will be used for the validation of the SI-SRM. The operating range includes 1500 to 2500 rpm engine speed and 10 to 50 mg/stroke injected fuel mass at stoichiometric conditions. The start of fuel injection is at -270°CA with 150 bar injection pressure. The intake and exhaust valve lift profiles and timings are the same for all operating points. The pressure and temperature in the intake and exhaust manifold are measured using a low-pressure indication system and are provided as boundary conditions to the SI-SRM. Further detailed investigations on *Engine B* were conducted regarding water injection and fuel sensitivity using 3D CFD in the work of Vacca et al. [101, 102] and Franken et al. [24, 103].

More details on the experimental setup and measurement devices can be found in the work of Gern et al. [104, 105, 106].

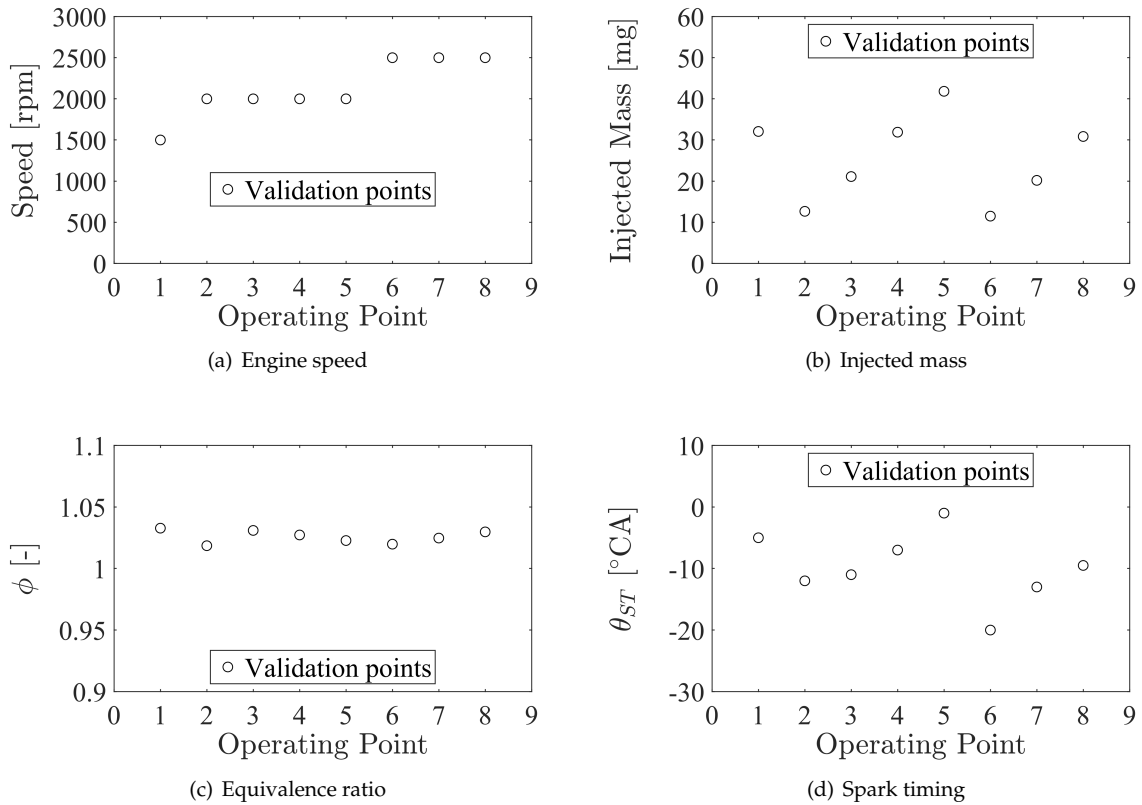


Figure 55: Validation points of Engine B.

The initial conditions of *Engine B* are obtained by a thermodynamic analysis of the measured cylinder pressure profiles. The pressure, temperature and EGR at IVC are shown in figure 56. The initial turbulent kinetic energy k_{init} is determined using equation (6.1). The calculated wall surface temperatures are shown in figure 116.

6.4 Chemistry model

The tabulated chemistry model for *Fuel A* is based on the detailed chemistry model from Seidel [93]. The settings of the tabulated chemistry model are summarized in table 22. The pressure is tabulated from 1 to 200 bar with non-equidistant fix points. The temperature is tabulated from 300 to 1400 K and the equivalence ratio from 0.05 to 6.0 to cover the broad range of mixture conditions during direct fuel injection. The EGR is tabulated from 0 to 40% to account for the high EGR rates of the engine.

The tabulated chemistry model for *Fuel B* is outlined in table 23. The model is based as well on the detailed chemistry model by Seidel [93] and it was also used in the work of Franken et al. [24]. The model applies the same ranges as for *Fuel A*. The model was validated by Matrisciano et al. [23] by comparison with direct solution of the detailed chemistry in SI-SRM.

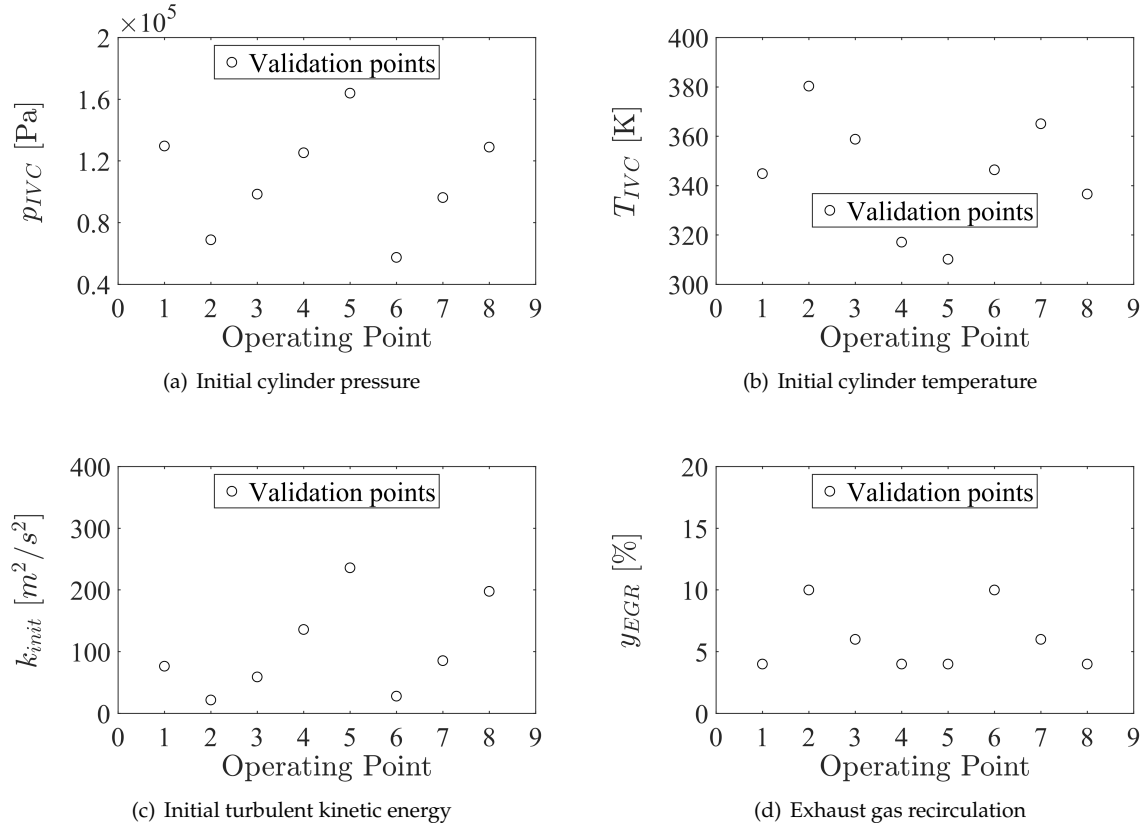


Figure 56: Initial conditions of Engine B.

Parameter	Value
Surrogate composition	see table 19
Detailed chemistry model	see Seidel [93]
Pressure (min, max)	1 bar, 200 bar
Temperature (min, max)	300 K, 1400 K
Equivalence ratio (min, max)	0.05, 6.0
EGR (min, max)	0%, 40%

Table 22: Tabulated chemistry model settings for Fuel A.

6.5 Optimization sensitivity study

The optimization sensitivity study is conducted using the FAST NSGA-II algorithm introduced in section 5.6. The algorithm settings for *Engine A* optimization are outlined in table 24. The remaining parameters use the default settings of NSGA-II in table 11 and FAST NSGA-II in table 12.

The SI-SRM models and settings applied for the sensitivity study are outlined in table 25. The stochastic heat transfer coefficient (C_h) is set to 15 even though a value of 1 is recommended in section 4.2.2. The crevice volume is set to 4% of the clearance volume in the crevice model as it is already outlined in the engine specification table 16. The cyclic variation model is only active when the number of stochastic cycles is larger than 1.

Selection of optimization parameters The objective of the optimization is to minimize the errors $\varepsilon_{Pressure}$, ε_{PCP} and ε_{PCPCA} . To determine the best set of optimization parameters a sensitivity study is performed by switching off one parameter by another and evaluate

Parameter	Value
Surrogate composition	see table 21
Detailed chemistry model	see Seidel [93]
Pressure (min, max)	1 bar, 200 bar
Temperature (min, max)	300 K, 1400 K
Equivalence ratio (min, max)	0.05, 6.0
EGR (min, max)	0%, 40%

Table 23: Tabulated chemistry model settings for Fuel B.

Parameter	Value
Algorithm	FAST NSGA-II
Space filler algorithm	Uniform Latin Hypercube
Number of generations	300
Number of individuals	10
Response surface models	Polynomials, Kriging, Neural Network
RSM training data set size	1000
Initial random seed	1

Table 24: FAST NSGA-II algorithm settings for Engine A optimization.

the influence on the Pareto solutions. The selected optimization parameters and its ranges for this investigation are summarized in table 26.

The Pareto solutions of the different optimization runs are outlined in figure 57. The first optimization run *All* is performed using all optimization parameters. Following the order of parameters in the legend of figure 57 the parameters are switched off and the Pareto solutions are depicted. The lowest errors for $\varepsilon_{Pressure}$, ε_{PCP} and ε_{PCPCA} are obtained using all optimization parameters. Switching off the parameters B_{2-3} of the early flame propagation correlation function shows an increase of the errors. Switching off the parameter b_1 of the turbulent flame propagation model of Peters shows a minor decrease of the errors while switching off C_ε of the $k - \varepsilon$ turbulence model shows a noticeable increase of all errors. Finally, the set of optimization parameters and ranges presented in table 26 is used for the investigations in the following sections.

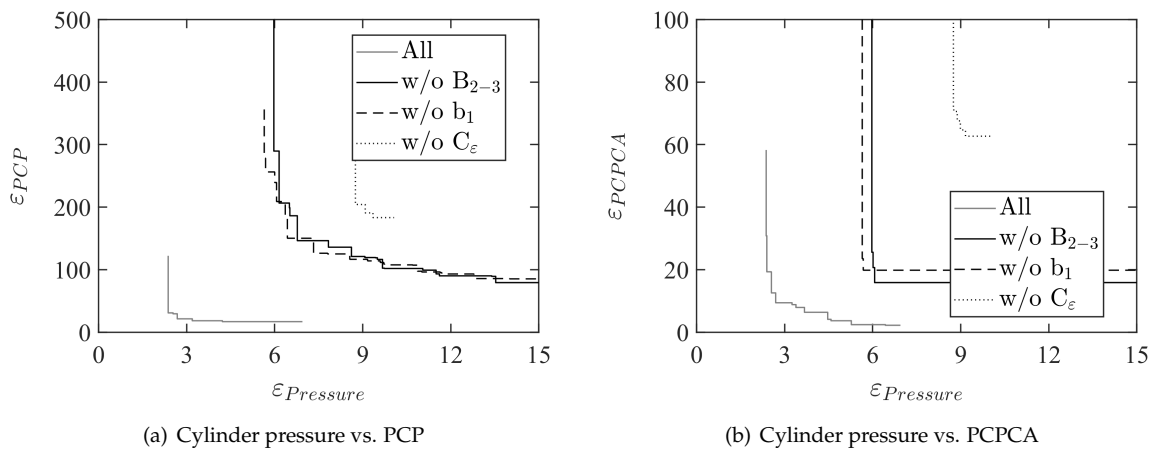


Figure 57: Pareto front of optimization runs with different optimization parameters and 3000 designs of Engine A.

Process	Model
Convective heat transfer	Heinle model (section 4.2.1)
Stochastic heat transfer coefficient (C_H)	15.0 (section 4.2.2)
Direct injection	yes (section 4.2.3)
Gas exchange	yes (section 4.2.4)
Particle mixing	Curl model (section 4.2.5)
Turbulence	$k - \epsilon$ model (section 4.3.1)
Flame propagation	Peters model with early flame propagation (section 4.3.2)
Crevice	yes (section 4.3.4)
Cyclic variation	yes (section 4.3.5)

Table 25: SI-SRM settings for optimization sensitivity study for Engine A.

Parameter	Lower Limit	Upper Limit
C_ϵ	0.1	2.0
C_{ϵ_1}	0.1	1.5
C_{ϵ_2}	0.1	1.5
b_1	2	3
B_1	-0.003	0.003
B_2	-0.016	-0.008
B_3	0	1.5E-7
B_4	-100	100

Table 26: Optimization parameters and objectives for Engine A.

Influence of SI-SRM setup The parameter variation for the SI-SRM setup sensitivity study is shown in table 27. Five different sets are investigated using different number of notional particles, different time step sizes and different number of stochastic cycles. For sets with number of stochastic cycles larger than 1 the initial random seed is set to variable (*var*) to generate a different sequence of random numbers in each stochastic cycle.

Parameter	Set 1	Set 2	Set 3	Set 4	Set 5
Number of particles	100	100	100	100	500
Time step size	1.0°CA	0.5°CA	0.5°CA	0.5°CA	0.5°CA
Number of cycles	1	1	5	30	1
Initial random seed	1	1	<i>var</i>	<i>var</i>	1

Table 27: SI-SRM settings for investigation of setup sensitivity for Engine A.

The Pareto fronts of the investigated sets 1-5 are compared in figure 58. Decreasing the time step size from 1.0 °CA to 0.5 °CA slightly reduces all errors (Set 1 → Set 2). Further, increasing the number of stochastic cycles to 5 reduces the error of the Pareto solutions (Set 2 → Set 3) while further increasing the number of cycles to 30 shows a slight increase of the $\epsilon_{Pressure}$ error (Set 3 → Set 4). The reason is the larger stochastic variance with low number of stochastic cycles which can randomly lead to a better mean Pareto solution compared to the case with higher number of stochastic cycles. The increase of number of notional particles shows a slight increase of the errors (Set 2 → Set 5).

The validation results of Set 1-5 are shown in figure 59. The figure compares the 10% and 50% combustion progress and the NO_x and CO engine-out emissions. The correlation coefficient (R^2) and root mean squared error ($RMSE$) are included in the plots to evaluate the performance. Decreasing the time step size from 1.0 °CA to 0.5 °CA shows an increase of R^2 and decrease of $RMSE$. The increase of number of stochastic cycles to 5 further improves

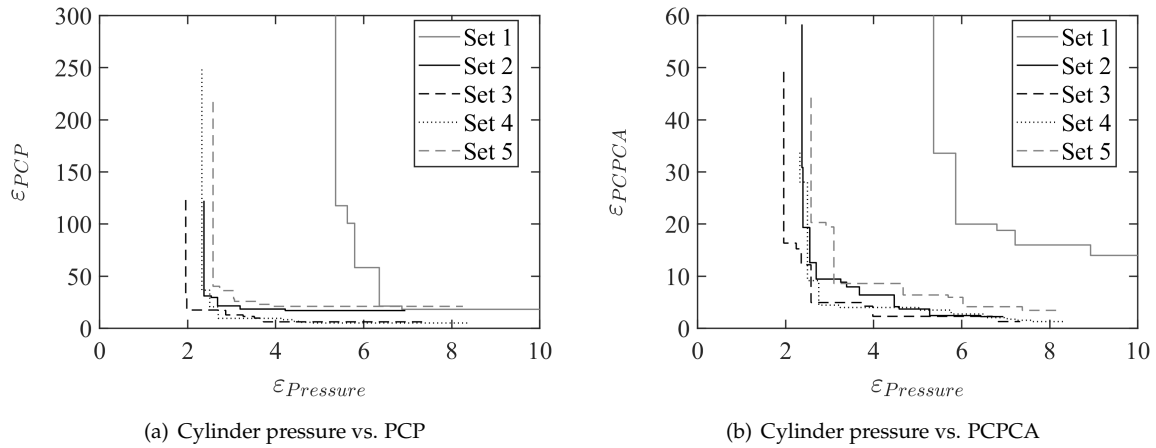


Figure 58: Pareto front of optimization runs with Set 1-5 and 3000 designs of Engine A.

the R^2 and $RMSE$ values while the increase to 30 stochastic cycles slightly reduces the R^2 and increases the $RMSE$ values. The increase of number of notional particles from 100 to 500 shows a slight reduction of R^2 and increase of $RMSE$.

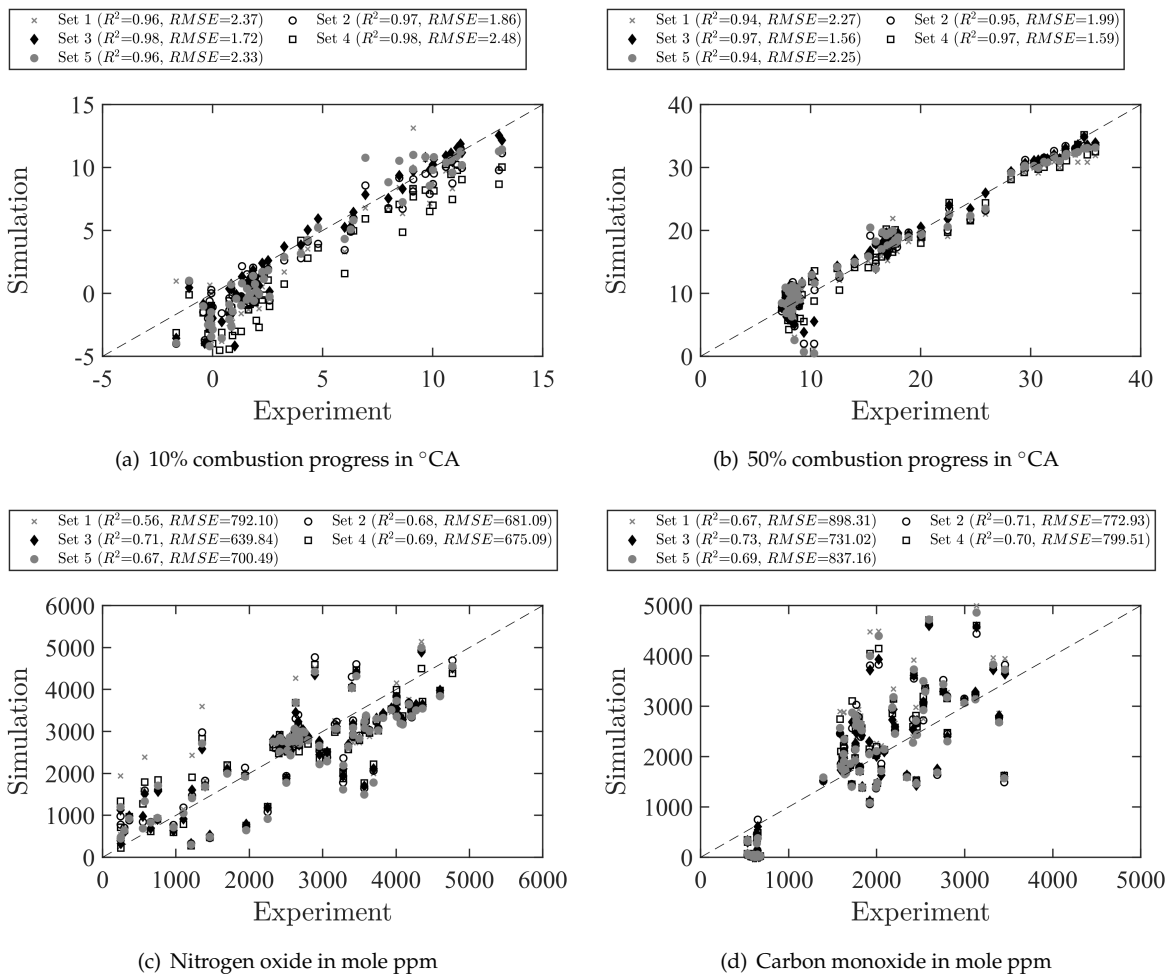


Figure 59: Validation results for the best designs of Set 1-5 of Engine A using equi-weighted objectives in the MCDM. The plots include the R^2 and $RMSE$ values.

Influence of number of operating points The selection of the training points is outlined in figure 60. The set with 4 training points just covers two different engine speeds and loads. For the set with 8 training points four additional points are added with lean air-fuel ratio. The third set extends the operation range to lower and higher engine speeds and lower and higher loads. The optimizations are performed using the SI-SRM setup Set 2 from table 27.

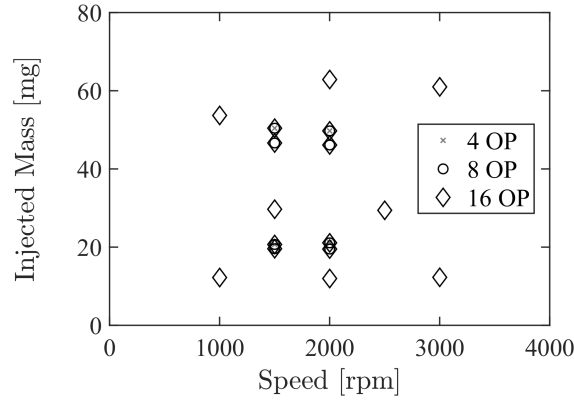


Figure 60: Selected operating points for the optimization runs with 4, 8 and 16 training points of Engine A.

The Pareto fronts shown in figure 61 are normalized for the number of operating points to account for the difference in the accumulated errors. The Pareto fronts show a significant difference in the errors $\varepsilon_{Pressure}$, ε_{PCP} and ε_{PCPCA} while all optimization runs show the minimization of the errors. With increasing number of training points the errors are increasing while for the optimization with 16 training points the errors are increasing much more. The operating points at lowest engine load at 1000, 2000 and 3000 rpm show the large deviations wherefor the overall error is increasing. Further, the number of Pareto solutions for the optimization with 16 operating points is much lower compared to the other two cases.

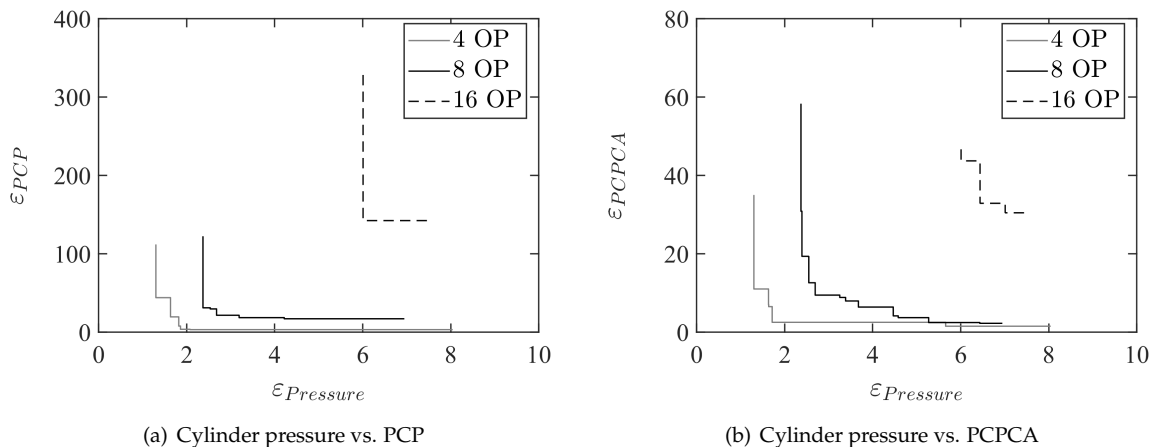


Figure 61: Pareto front of optimization runs with 4, 8 and 16 training points and 3000 designs of Engine A.

The best design from the Pareto solutions is selected by the MCDM with equi-weighted objectives. The validation results are shown in figure 62. The lowest R^2 and largest $RMSE$ values for 10% and 50% combustion progress are found for the case with 4 training points.

Increasing the number of training points to 16 shows a slight increase of R^2 and decrease of $RMSE$. For NO_x emissions the R^2 value is decreasing and the $RMSE$ value is increasing with increasing number of training points so that the case with 4 training points achieves the best fit of the experiments. For the CO emissions no significant change can be found regarding R^2 while $RMSE$ is increasing by increasing the number of training points.

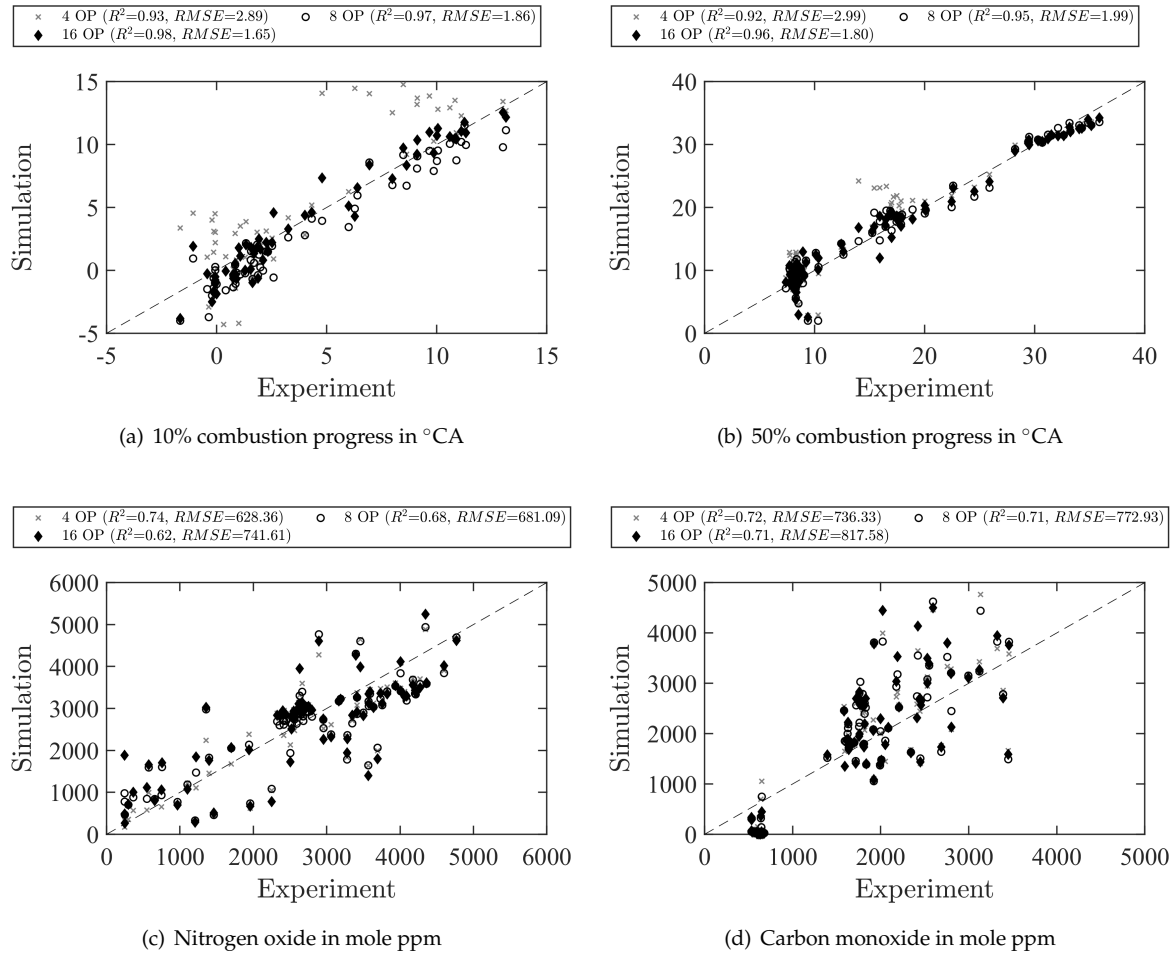


Figure 62: Validation results for number of training points 4, 8 and 16 of Engine A using equi-weighted objectives in the MCDM. The plots include the R^2 and $RMSE$ values.

Influence of set of training points The three different training sets shown in figure 63 consist each of 8 training points with different distribution of the points in the engine map. The Set B is covering a larger operating range for speed and load while it does not contain any lean operating point. The Set C focuses on the variation of spark timing at the higher compression ratio 13:1 and only covers one high load operating condition at two different engine speeds.

The optimization results of the different sets are shown in figure 64. The lowest errors are obtained by Set A while Set B and Set C show higher errors. The Set B shows a significant over-prediction of the cylinder pressure profiles for the three low load operating points at 1000, 2000 and 3000 rpm engine speed. The optimizer is not able to find one set of SI-SRM parameters that is able to match the combustion at low and high load operating

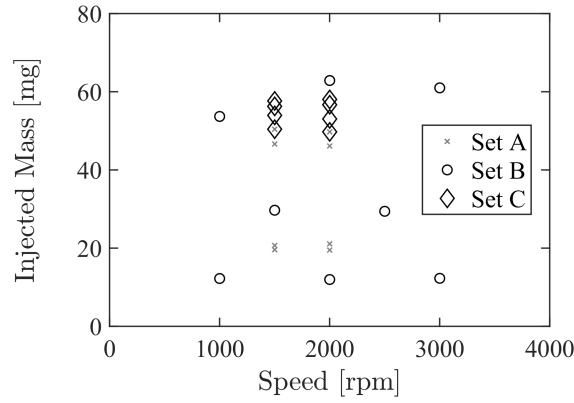


Figure 63: Selected operating points for the sets A, B and C.

conditions at the same time. For Set C six out of the eight operating points are measured with a higher compression ratio of 13.5 compared to the default compression ratio of 10.8. The operating points with the higher compression ratio predict a higher maximum cylinder pressure and advanced center of combustion. To obtain a better match with the experimental cylinder pressure the dissipation factor C_ϵ should be higher. Since the optimizer changes the dissipation factor the same way for all eight operating points it is not able to find lower $\epsilon_{Pressure}$, ϵ_{PCP} and ϵ_{PCPCA} errors.

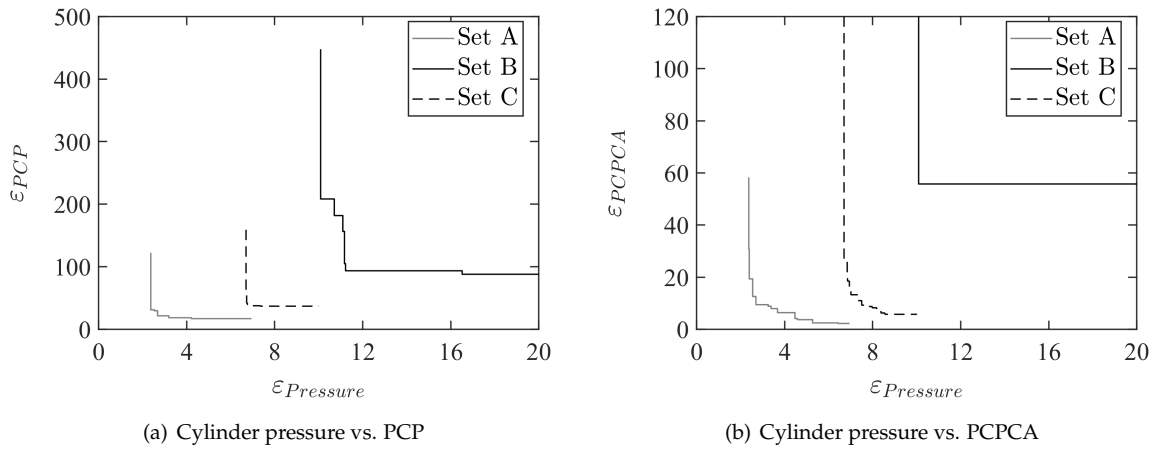


Figure 64: Pareto front of optimization runs with training set A, B and C and 3000 designs of Engine A.

The validation results of Set A, B and C are highlighted in figure 65. Set A shows the highest R^2 and lowest $RMSE$ values for 10% and 50% combustion progress while Set B and C predict the 10% combustion progress too early and the 50% combustion progress too late. The R^2 and $RMSE$ values of the NO_x emissions are worse for Set A compared to Set B and C. For the R^2 and $RMSE$ values of the CO emissions the Sets B and C are performing better again compared to Set A.

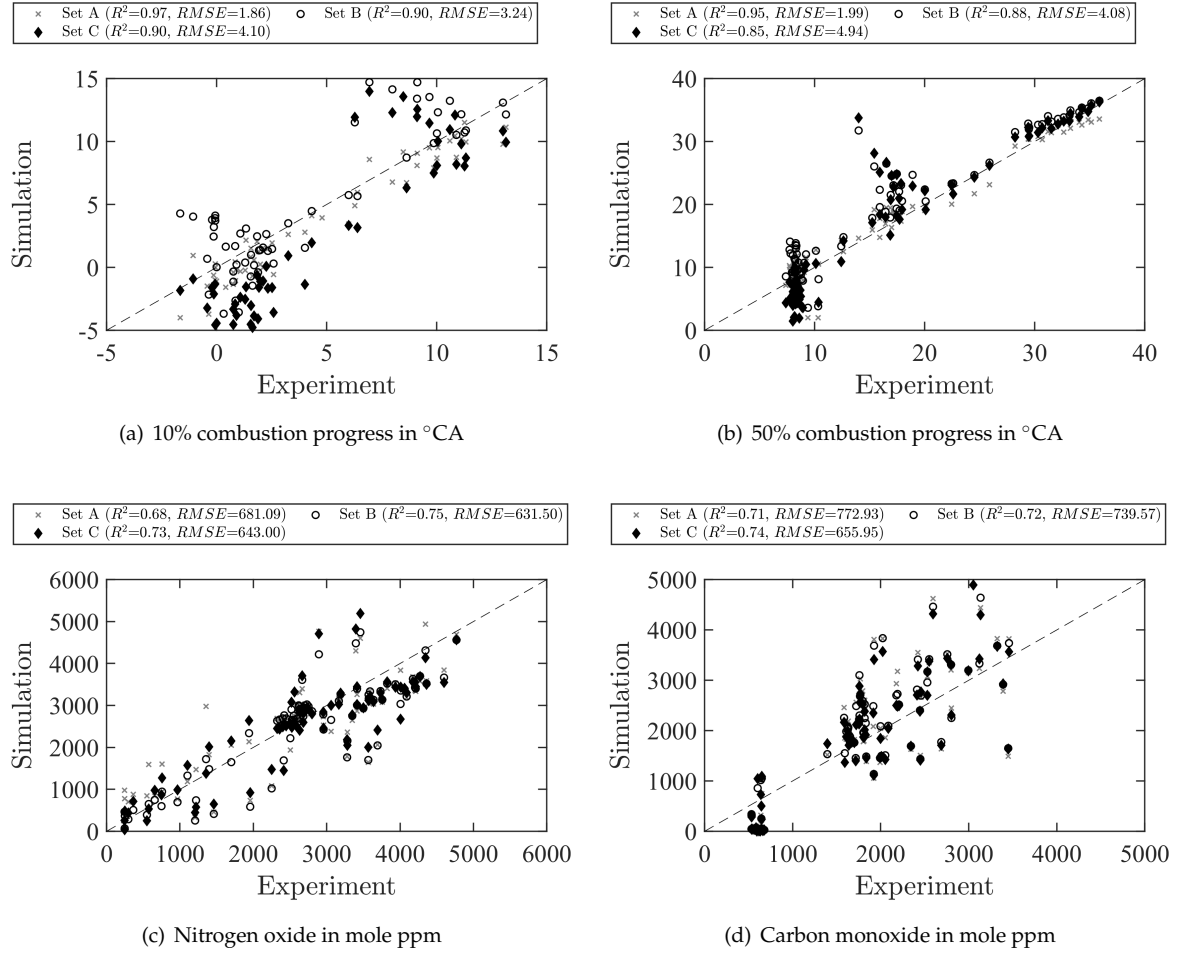


Figure 65: Validation results for the training sets A, B and C of Engine A using equi-weighted objectives in the MCDM. The plots include the R^2 and RMSE values.

6.6 Final validation

The final validation of the optimized SI-SRM setup is conducted for the validation data set of *Engine A* and *Engine B*. It is important to notice that no additional optimization is performed for *Engine B* and the optimized SI-SRM parameters of *Engine A* are just transferred to *Engine B*. The optimization results of Set 5 from table 27 are selected to generate the final SI-SRM setup. In the following paragraphs the Set 5 will be denoted as training set and the SI-SRM setup accounting for cyclic variation will be denoted as validation set as it is summarized in table 28. The cyclic variation model parameters $\sigma_{\theta_{ST}}$ and $\sigma_{u'}$ are calibrated using the experimental measurements of PCP standard deviation.

Parameter	Training Set	Validation Set
Number of particles	500	500
Time step size	$0.5^{\circ}CA$	$0.5^{\circ}CA$
Number of cycles	1	150
Initial random seed	1	<i>var</i>

Table 28: SI-SRM model setup for validation of Engine A.

Optimization results of Engine A The optimization results of *Engine A* using the training set from table 28 are presented in figure 66. The optimization algorithm is able to find minimized solutions of the errors $\varepsilon_{Pressure}$, ε_{PCP} and ε_{PCPCA} . Further, it is noticed that the Pareto solutions are quite close to each other and a correlation between the three objectives is observed. Objectives for minimization of CO and HC engine-out emissions are not defined. The NO_x engine-out emissions are predicted in SI-SRM by the tabulated chemistry model using a source term submodel [16]. The parameters of the NO_x source terms are adjusted after the optimization of the $k - \varepsilon$ model parameters is finished.

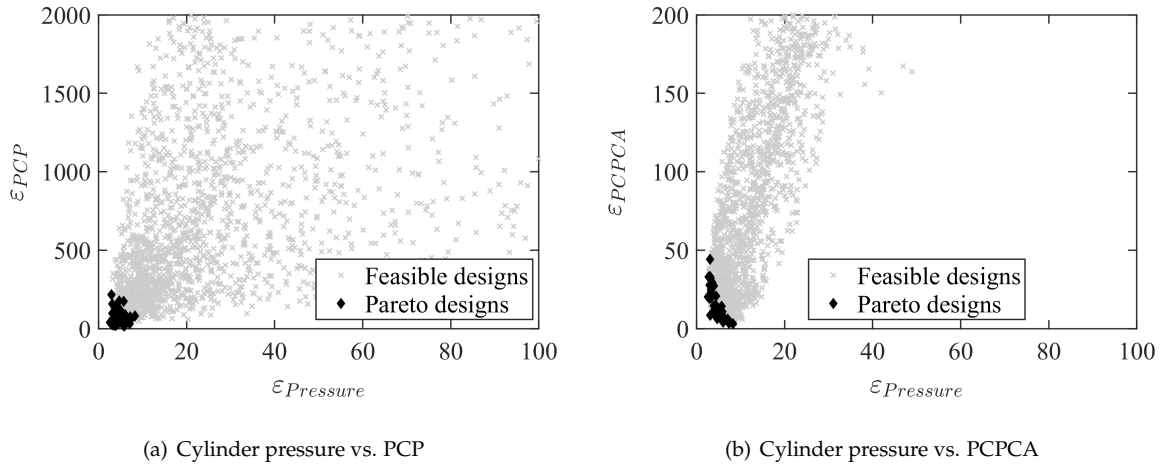


Figure 66: Pareto solutions of the FAST NSGA-II optimization run with 3000 designs for Engine A.

Using the MCDM from section 5.5 with different weights of the objectives three designs are selected from the Pareto solutions and are investigated more in detail. The design ID 476 is selected by setting the weight of objective ε_{PCP} to zero and use equi-weights for the remaining two objectives. The design ID 1987 is selected by using equi-weights for all three objectives. The design ID 2638 is selected by increasing the weight of objective ε_{PCP} to be twice as much as the weights of the other two objectives. The three selected designs are shown in figure 67 and define the edges of the Pareto solution space.

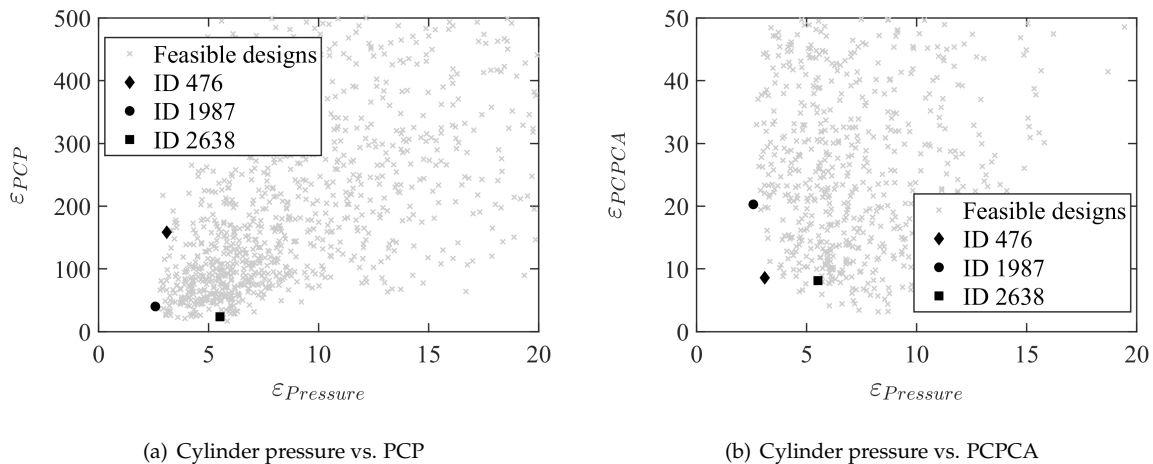


Figure 67: Selected Pareto solutions of the FAST NSGA-II optimization run with 3000 designs for Engine A.

Validation results of Engine A Using the validation data set of *Engine A* and the training set settings from table 28 the results in figure 68 for 1 stochastic cycle are obtained. The design ID 476 shows a slightly higher R^2 value and lower $RMSE$ for 10% and 50% combustion progress compared to design ID 1987 and ID 2638. The selection of ID 476 put more decision weight on the error for crank angle of the maximum pressure ε_{PCPCA} wherefor the match of the center of combustion for the validation data set is better as well. Nevertheless, some operating points with early 50% combustion progress are under-predicted for all three designs. For NO_x engine-out emissions the design ID 1987 shows a higher R^2 value while the lowest $RMSE$ is obtained for design ID 476. For CO engine-out emissions the design ID 476 is showing the highest R^2 value and lowest $RMSE$.

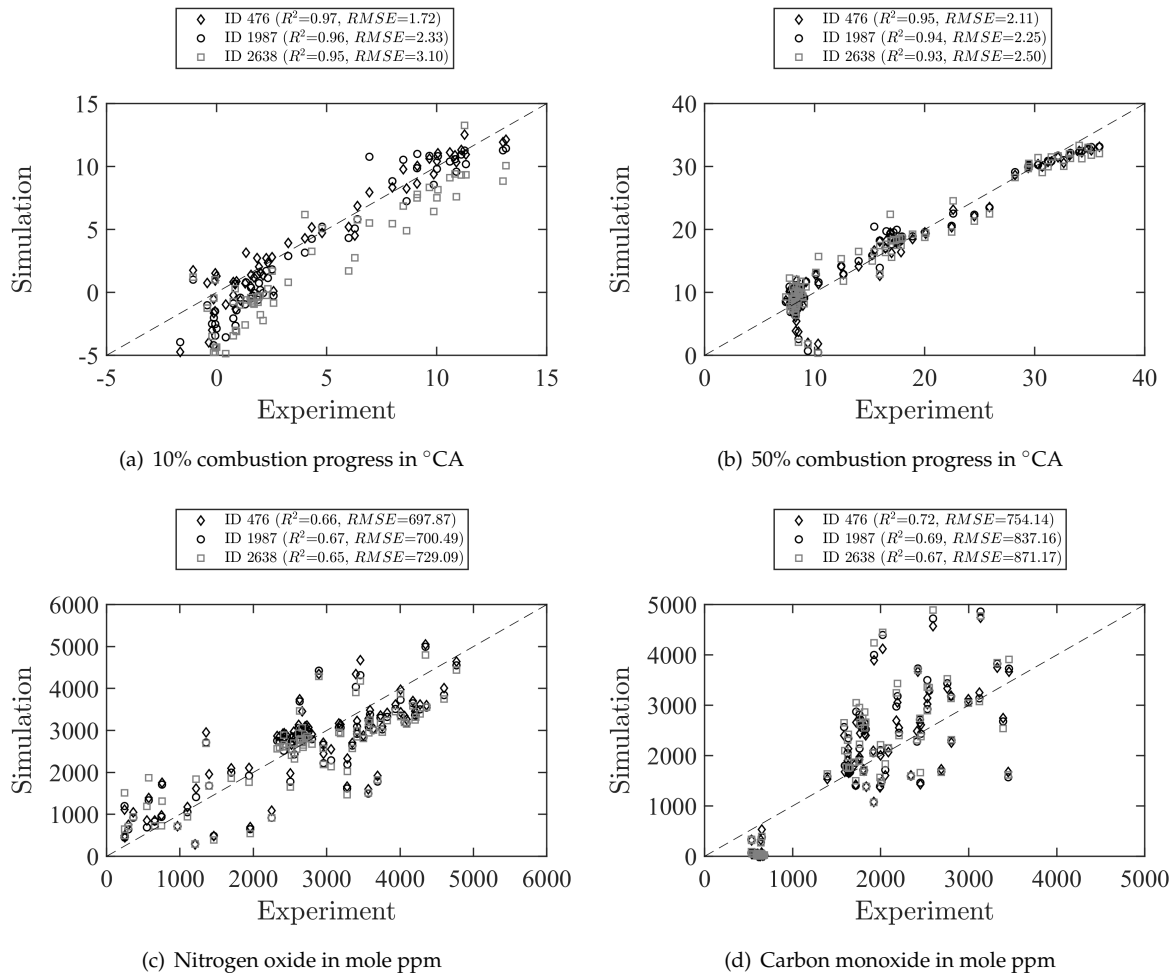


Figure 68: Validation results with 1 stochastic cycle for the designs ID 476, ID 1987 and ID 2638 of Engine A. The plots include the R^2 and $RMSE$ values.

The three designs are further investigated by using the validation set from table 28 and account for cyclic variations. It has to be noted that the experimental measurements used for training and validation of the SI-SRM model parameters consist of the average results of 150 consecutive cycles. Therefore, the SI-SRM simulation with cyclic variation model is conducted for 150 stochastic cycles as well. The 10% and 50% combustion progress results in figure 69 show a higher R^2 value and $RMSE$ compared to the results using 1 stochastic cycle in figure 68. Regarding the NO_x engine-out emissions an increase of the R^2 and reduction of

$RSME$ can be observed for design ID 1987 and ID 2638 which perform better compared to design ID 476. For CO engine-out emissions the R^2 value decreases and $RSME$ increases for the designs ID 1987 and ID 2638 while R^2 increases and $RSME$ decreases for design ID 476 which performs better in this case. The different sensitivity of the two designs ID 1987 and ID 2638 compared to design ID 476 is related to the difference in combustion progress shown in figure 68. Both designs show a shift of combustion progress to later crank angles using the validation set wherefor the emissions change as well. Overall, the match of combustion becomes worse for design ID 1987 and ID 2638 using the validation set. Design ID 476 shows an improvement of combustion progress and engine-out emissions running with 150 stochastic cycles and cyclic variation model.

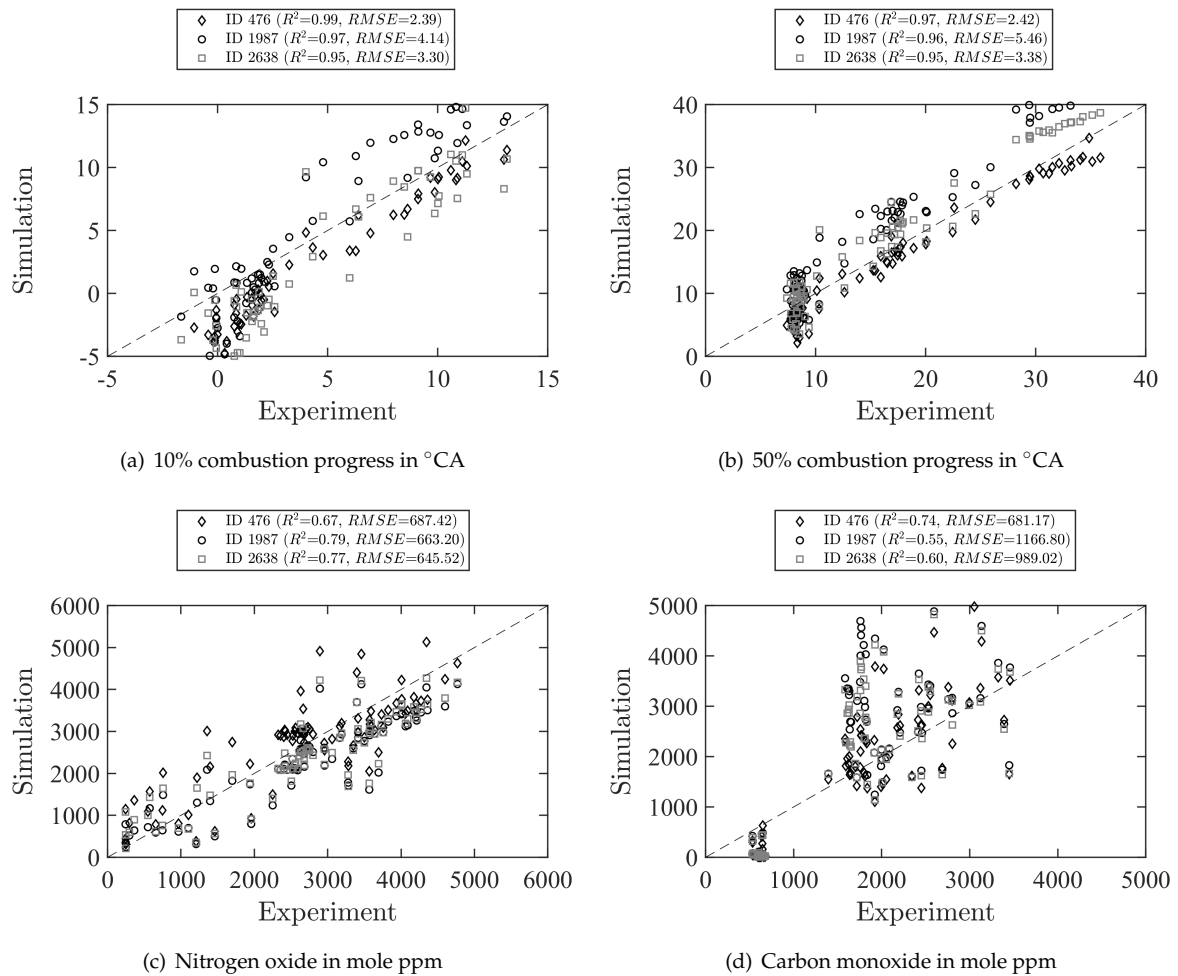


Figure 69: Validation results with 150 stochastic cycles and cyclic variation model for the designs ID 476, ID 1987 and ID 2638 of Engine A. The plots include the R^2 and $RMSE$ values.

The design ID 476 is selected as the final best design. The SI-SRM setup is one more time revised by modifying the η_c value of the early flame propagation model as shown in figure 70 (a) and (b). Even though the optimized coefficients B_{1-5} of the correlation function in equation (9.6) provide a good approximation of the start of flame propagation in dependence of the equivalence ratio and engine load, it does not capture well the dependence on engine speed. The η_c parameter is generally increasing with decreasing equivalence ratio and decreasing engine load. With the modification, the η_c model parameter is additionally decreasing with

increasing engine speed (see figure 70 (b)). Furthermore, the low load operating points in the ϕ range of 0.7 to 0.8 show a drop for the η_c parameter which is not captured by the optimized correlation function in figure 70 (a). Since a spark ignition energy model is not implemented in SI-SRM at the moment the η_c model parameter indirectly captures the longer ignition delay for lean and low load operating conditions.

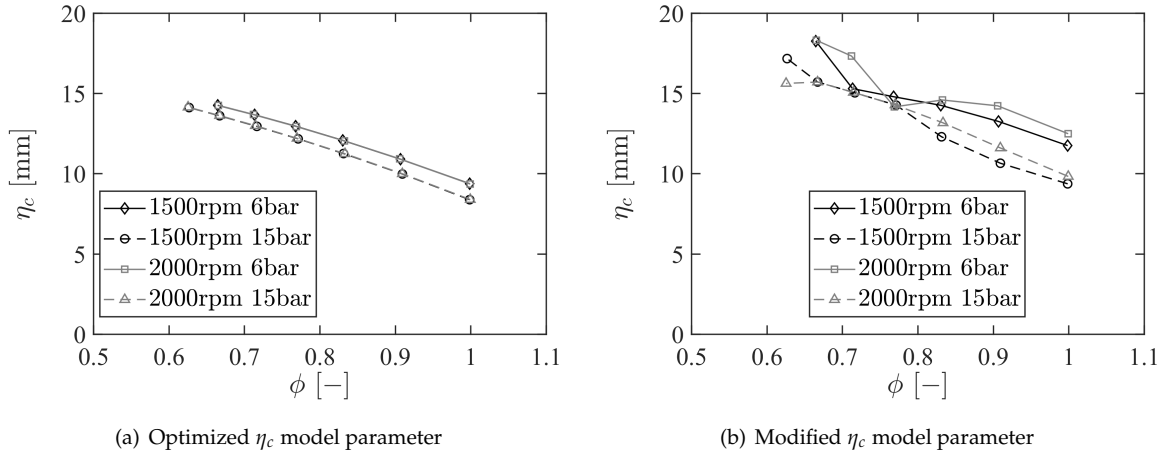


Figure 70: Comparison of the optimized and modified early flame propagation model parameter η_c for different equivalence ratios, engine speeds and loads for Engine A.

The second term of the early flame propagation model in equation (4.110) is governed by the Gibson length scale l_G . The predicted Gibson length scale is compared in figure 71 for different equivalence ratios, engine speeds and loads. It is overall two magnitudes lower compared to the η_c parameter and shows an inverted trend in dependence of equivalence ratio. Further, for the operating point at high engine speed and load the Gibson length scale is significantly lower compared to the other operating conditions which is because of the stronger turbulence fluctuation.

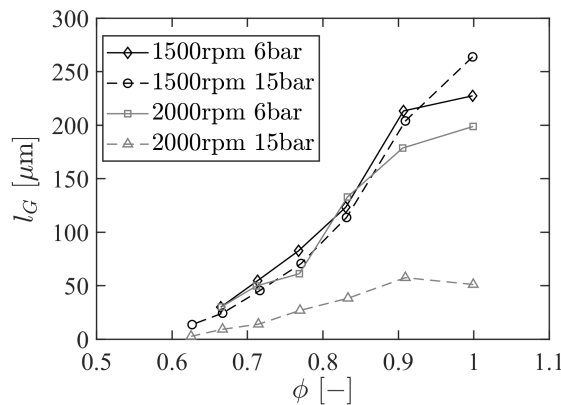


Figure 71: Comparison of the Gibson length scale at 10% combustion progress for different equivalence ratios, engine speeds and loads for Engine A.

The low burning velocity (see figure 72 (a)) and high stretch rate ($Ka > 1$) of lean mixtures thicken the flame front so that smaller eddies can corrugate it more easily [107]. As a result, the Gibson length scale is smaller for lean mixtures. On the other hand side, the dissipation

ε does not change significantly for ϕ greater than 0.8, so that the turbulent flow field can be assumed to be stable. At higher load operating conditions and ϕ smaller than 0.8, the turbulence intensity and dissipation increase (see figure 72 (b)), causing smaller eddies to corrugate the flame front, further lowering the Gibson length scale.

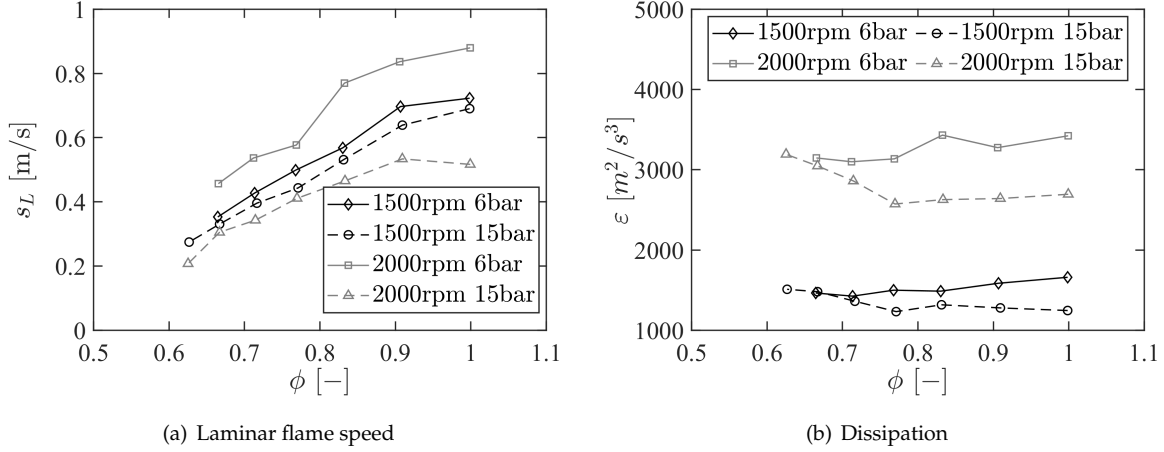


Figure 72: Comparison of the laminar flame speed s_L and dissipation ε at 10% combustion progress for different equivalence ratios, engine speeds and loads for Engine A.

For the operating conditions with increased compression ratio of 13:1 and late spark timing the C_ε model parameter is increased by 0.5 points. The C_ε value of design ID 476 predicts turbulence dissipation too low for these operating conditions wherefor combustion is accelerated too much by high u'/s_L values.

The standard deviation of spark timing $\sigma_{\theta_{ST}}$ and turbulence fluctuation $\sigma_{u'}$ of the cyclic variation model from section 4.3.5 are shown in dependence of equivalence ratio, engine speed and load in figure 73. The standard deviation for spark timing is increasing with decreasing equivalence ratio and decreasing engine load because of the increasing combustion instability. The standard deviation for turbulence fluctuation $\sigma_{u'}$ is not changed for different operating conditions.

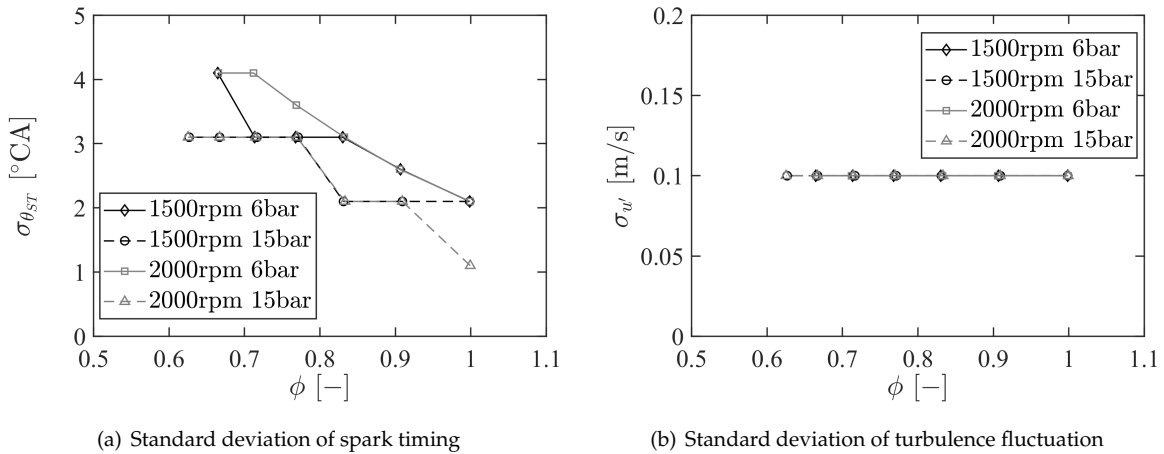


Figure 73: Standard deviation of spark timing $\sigma_{\theta_{ST}}$ and turbulence fluctuation $\sigma_{u'}$ in dependence of equivalence ratio for Engine A.

The cyclic variation of the SI-SRM simulation and experiment for *Engine A* is compared by evaluating the mean and standard deviation of PCP in figure 74. The SI-SRM shows a slight over-prediction of both quantities compared to the experiment but it accurately predicts the trend between the different operating conditions of the engine.

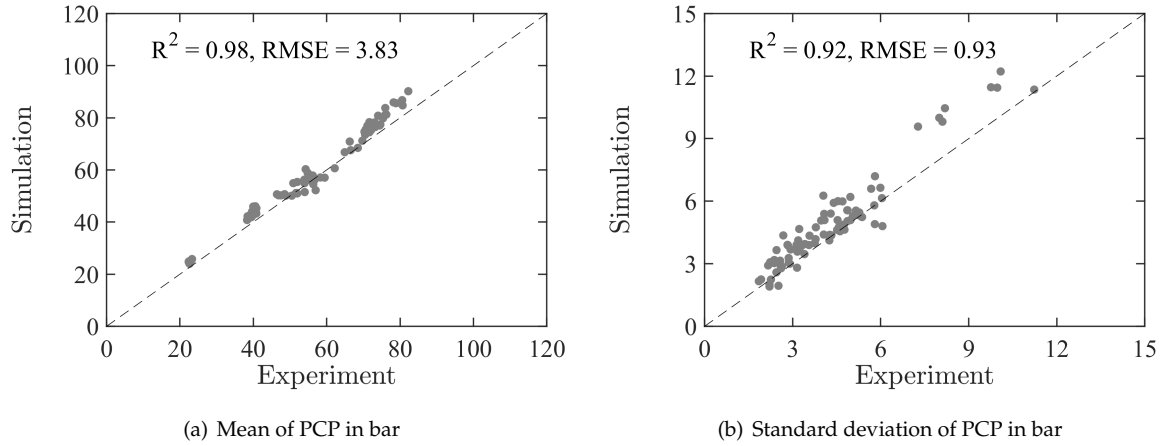


Figure 74: Comparison of the mean and standard deviation of PCP of modified design ID 476 of Engine A.

The validation results of the optimized and modified design ID 476 are compared in figure 75. The adjustments of the early flame propagation model show an improvement of the 10% and 50% combustion progress. The operating points at the high values of 50% combustion progress belong to the spark timing variation and are predicted too late by the modified design ID 476. The NO_x engine-out emissions are showing a better fit with the experimental data while the CO engine-out emissions have not changed much.

Validation results of Engine B The SI-SRM setup of the modified design ID 476 is transferred to the second validation data set which belongs to *Engine B*. In total eight validation points with stoichiometric air-fuel ratio are tested for *Engine B* as outlined in section 6.3. The η_c model parameter is adjusted for the engine case because the combustion chamber geometry is much different compared to *Engine A*. The η_c model parameter and calculated Gibson length scale l_G for *Engine B* are outlined in figure 76. Similar to *Engine A* the η_c model parameter is decreasing with increasing engine load and decreasing engine speed. The Gibson length scale shows a trade-off for the engine load where it increases for the 10 bar IMEP operating points but decreases towards lower and higher engine loads. Similar to *Engine A* the Gibson length scale decreases with increasing engine speed.

The significantly higher Gibson length scale for operating point 1 at 1500 rpm and 15 bar IMEP is because of the low dissipation wherefor the small turbulent eddies cannot distort the flame front. With increasing engine speed the turbulence intensity and dissipation in the cylinder increase wherefor the Gibson length scale is reduced. The trade-off of the Gibson length scale for different engine loads is due to the laminar flame speed which is highest for 10 bar IMEP for 2000 rpm and 2500 rpm engine speed.

The $\sigma_{\theta_{ST}}$ and σ_u model parameters of the cyclic variation model are set constant for all operating conditions of *Engine B* as shown in figure 78. Compared to *Engine A* the cyclic

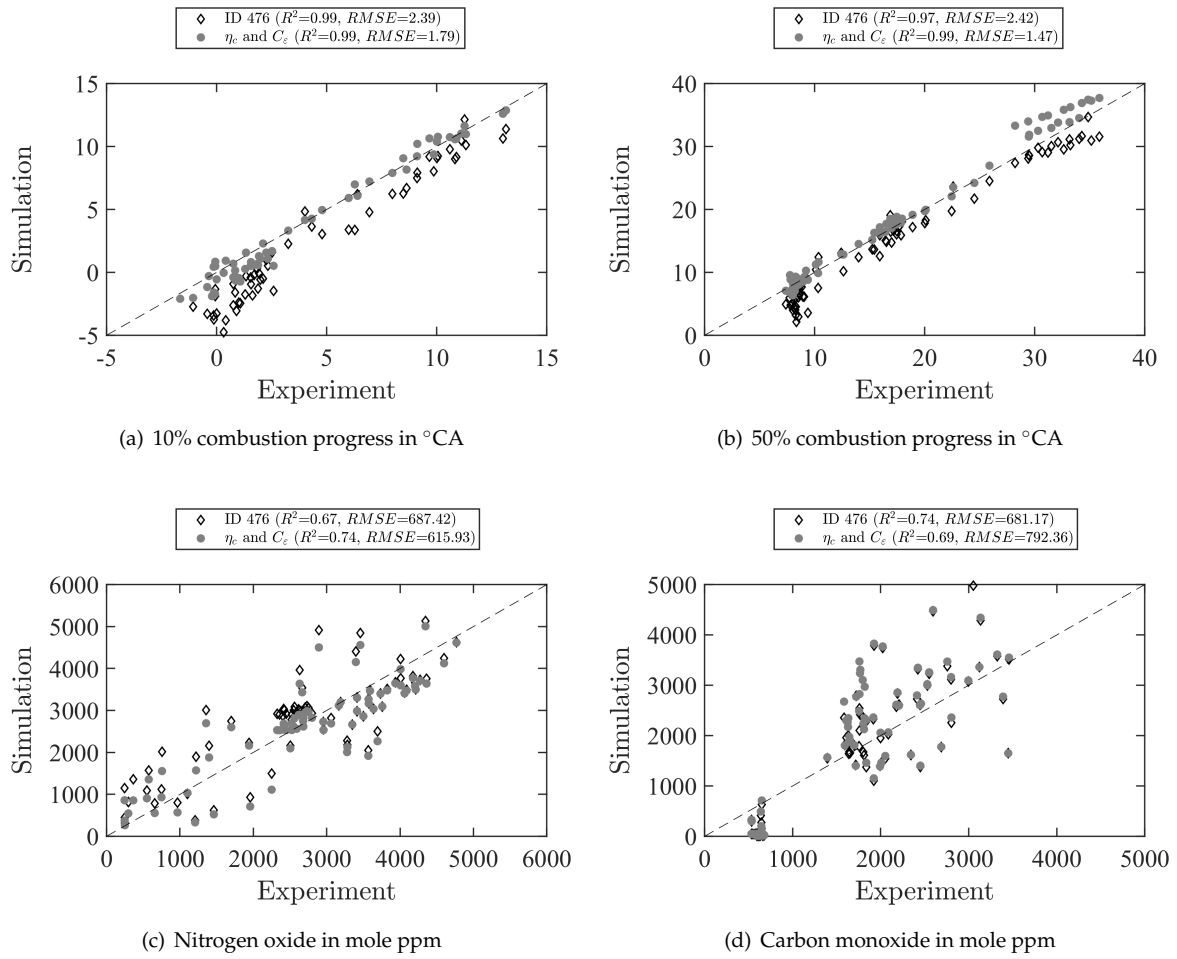


Figure 75: Validation results with 150 stochastic cycles and cyclic variation model for the optimized and modified design ID 476 of Engine A.

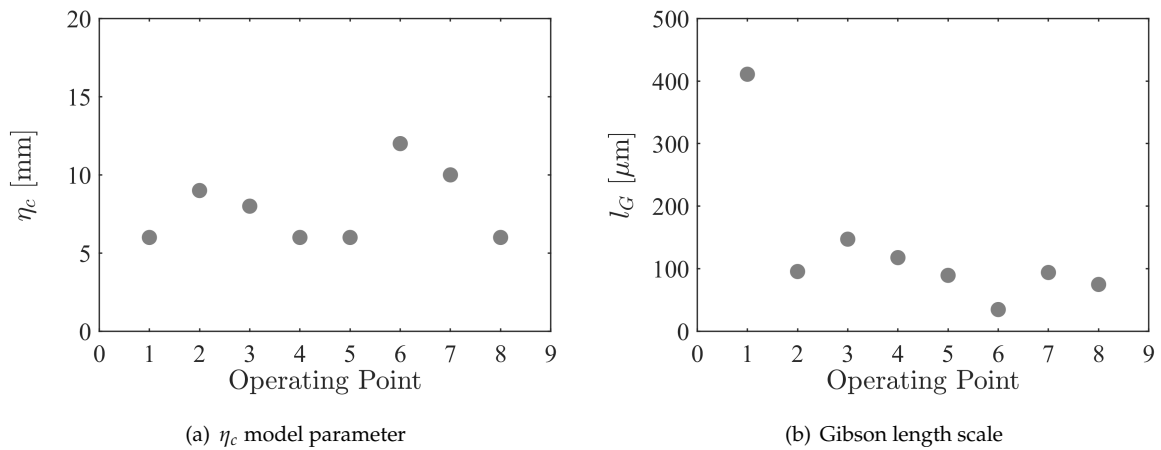


Figure 76: Comparison of the η_c model parameter and Gibson length scale at 10% combustion progress for different operating conditions for Engine B.

variation is lower for *Engine B* wherefor the spark timing parameter $\sigma_{\theta_{ST}}$ is just set to 1.1°CA .

The simulation results for 10% and 50% combustion progress and NO_x engine-out emissions in figure 79 show a good agreement with the experiments and the $RMSE$ are much lower compared to *Engine A*. The NO_x engine-out emissions shown in figure 79 (c) follow

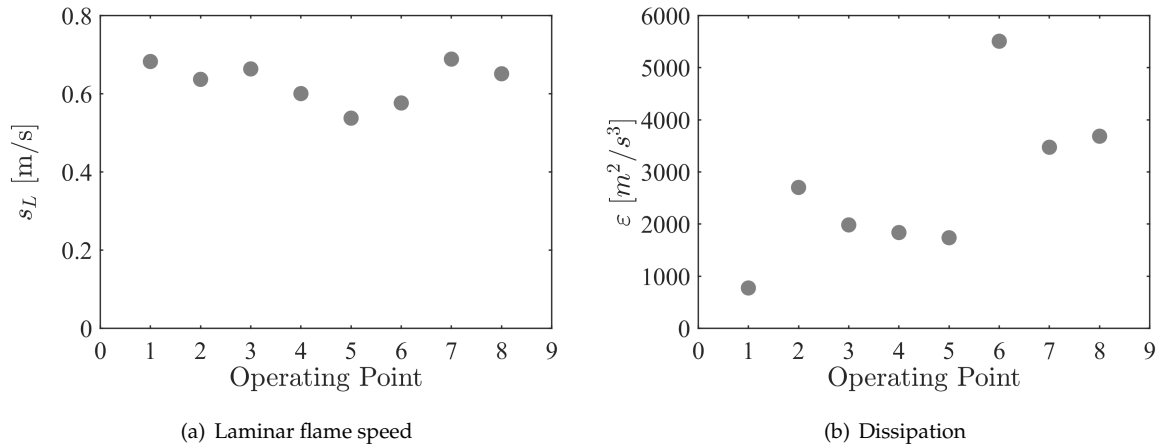


Figure 77: Comparison of the laminar flame speed s_L and dissipation ε at 10% combustion progress for different operating conditions for Engine B.

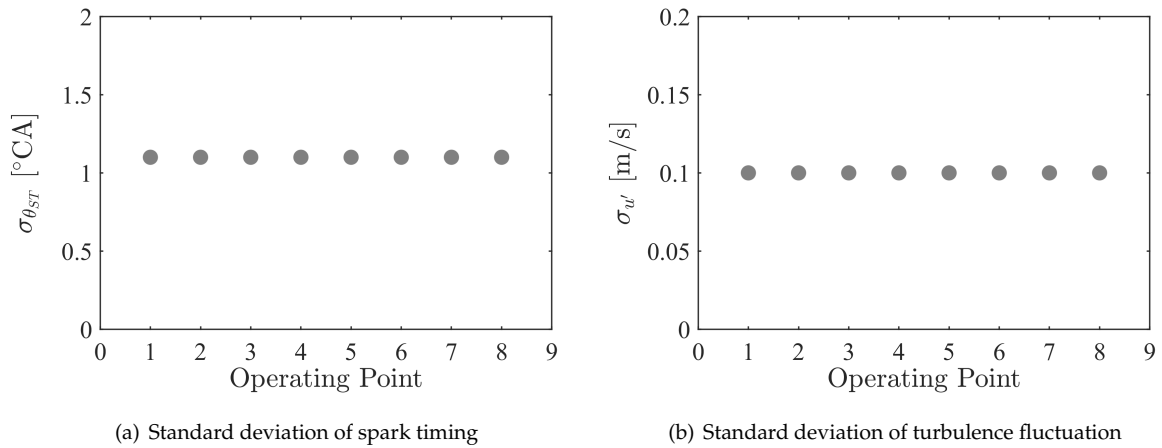


Figure 78: Standard deviation of spark timing $\sigma_{\theta_{ST}}$ and turbulence fluctuation $\sigma_{u'}$ in dependence of different operating conditions for Engine B.

the trend of the experiments while they are over-predicted for high load operating conditions. The $RMSE$ is in the same range as for the *Engine A* case. The CO engine-out emissions in figure 79 (d) are significantly higher for the experiment than for the SI-SRM simulation.* In general, the experimentally measured CO and HC emissions are significantly higher for *Engine B* compared to *Engine A*. The source of the high CO and HC emissions are not determined for the experiment while 3D CFD simulation results published in the FVV project report of “Water injection in SI engines II” [108] indicated liquid wall film vaporization during the expansion stroke of *Engine B* which could be a possible source of unburnt HC and CO emissions.

The predicted average PCP and its standard deviation are outlined in figure 80. The SI-SRM simulation predicts the average PCP of the experiments closely. However, the standard deviation of PCP is predicted higher by the SI-SRM but can follow the trend of the experiments. Overall, the $RMSE$ is in the same range as for the *Engine A* case.

*HC emissions are not shown in the figure but they are generally under-predicted by the SI-SRM simulation.

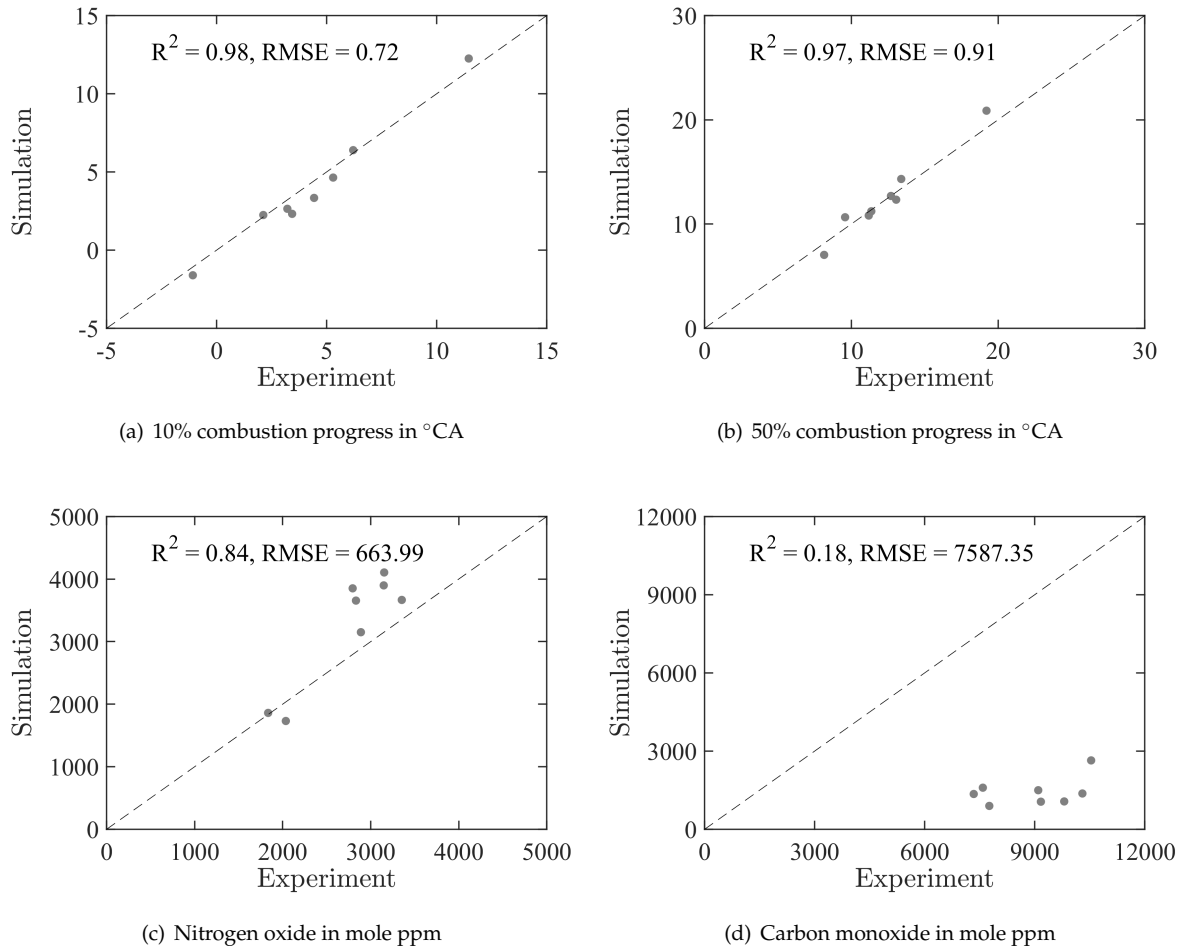


Figure 79: Validation results with 150 stochastic cycles and cyclic variation model for the modified design ID 476 of Engine B.

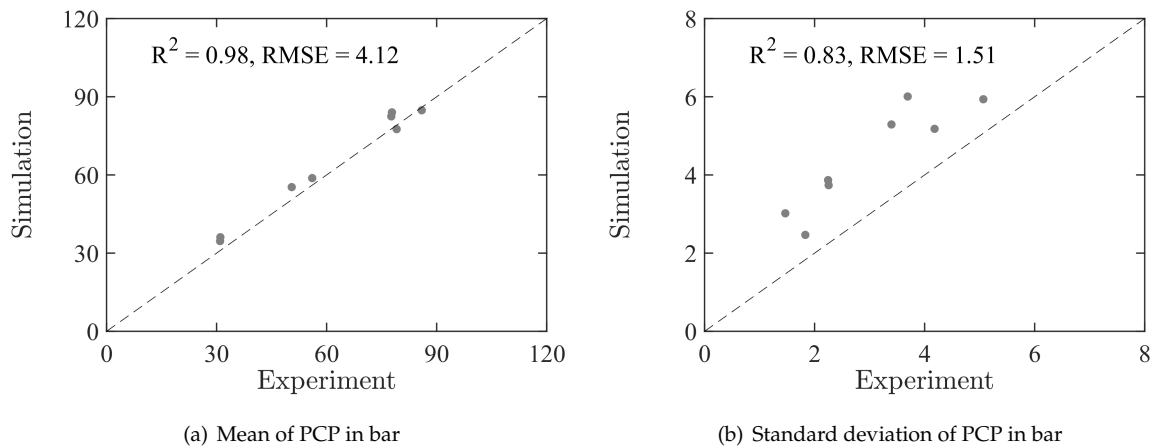


Figure 80: Comparison of the mean and standard deviation of PCP of modified design ID 476 of Engine B.

6.7 Verification with 3D CFD

The SI-SRM simulation results of modified design ID 476 of *Engine A* are further verified by comparing them to 3D CFD Reynolds-Averaged Navier Stokes (RANS) simulation results. The details of the 3D CFD simulation setup are summarized in section 9.9 and will not be

discussed in detail at this point. A relative air-fuel ratio (λ) sweep at 2000 rpm and 6 bar IMEP is selected for the investigation. The SI-SRM simulations are performed using the validation set from table 28 and the 3D CFD simulations are performed for one full engine cycle. The predicted cylinder pressure profiles of SI-SRM and 3D CFD are compared to the experiments in figure 81. The SI-SRM shows an accurate match of the compression stroke pressure while it over-predicts the maximum cylinder pressure for all λ values. The 3D CFD simulation over-predicts the compression stroke pressure and for some λ values over-predicts the maximum cylinder pressure as well. Both models show a decrease of the maximum cylinder pressure with increasing λ which is because of the lower burning velocity at lean conditions.

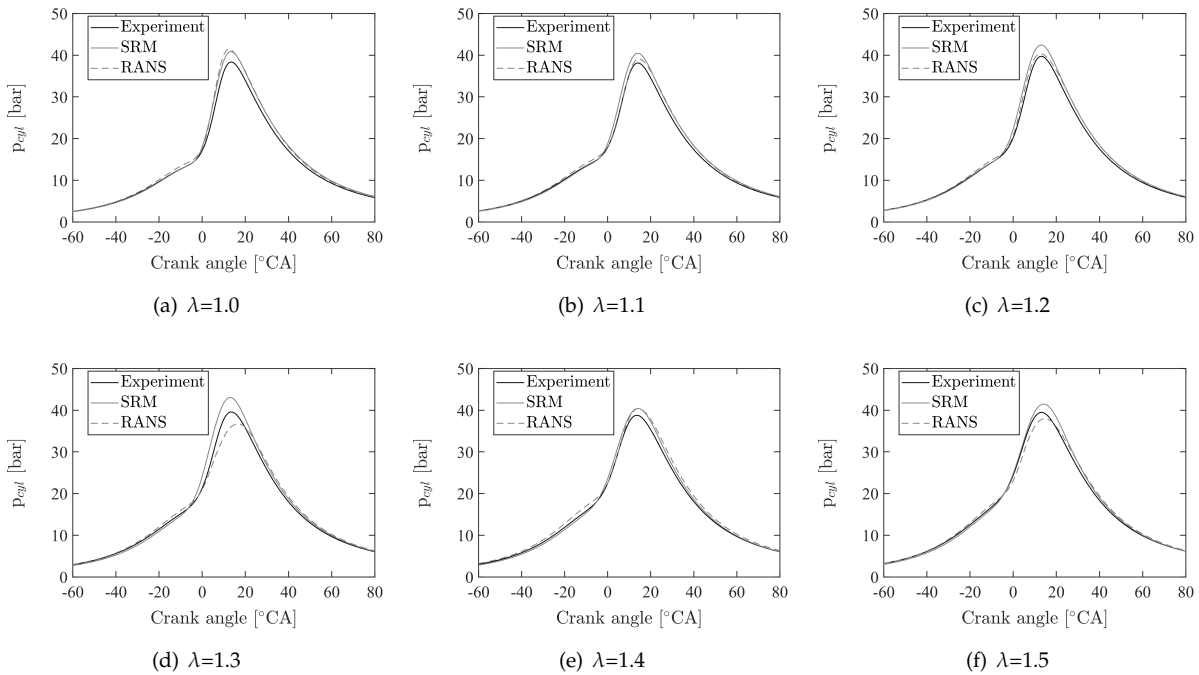


Figure 81: Cylinder pressure of experiment, SI-SRM and 3D CFD RANS for operating point 2000 rpm and 6 bar IMEP and different λ of Engine A.

The corresponding heat release rate profiles are shown in figure 82. The SI-SRM shows higher energy release during the initial phase of combustion wherefor the maximum cylinder pressure is increased. However, the maximum heat release rate is slightly under-predicted and the burn out during the expansion stroke is accurately matched. The 3D CFD simulation shows a similar early combustion phase as the SI-SRM with exception of $\lambda=1.3$ case where the 3D CFD simulation under-predicts the heat release rate of experiment noticeably. Further, the 3D CFD simulation shows an extended energy release during the expansion stroke which is more pronounced for lean operating conditions.

The $k - \varepsilon$ turbulence model performance of SI-SRM using the optimized parameters is further investigated by comparing with the 3D CFD results in figure 83. The SI-SRM predicts a much larger turbulent length scale l compared to 3D CFD during the combustion and exhaust valve opening phase which is because of the optimum $C_{\varepsilon 1}$ parameter is found at 0.14. During the intake valve opening the turbulent length scale predicted by SI-SRM is dropping

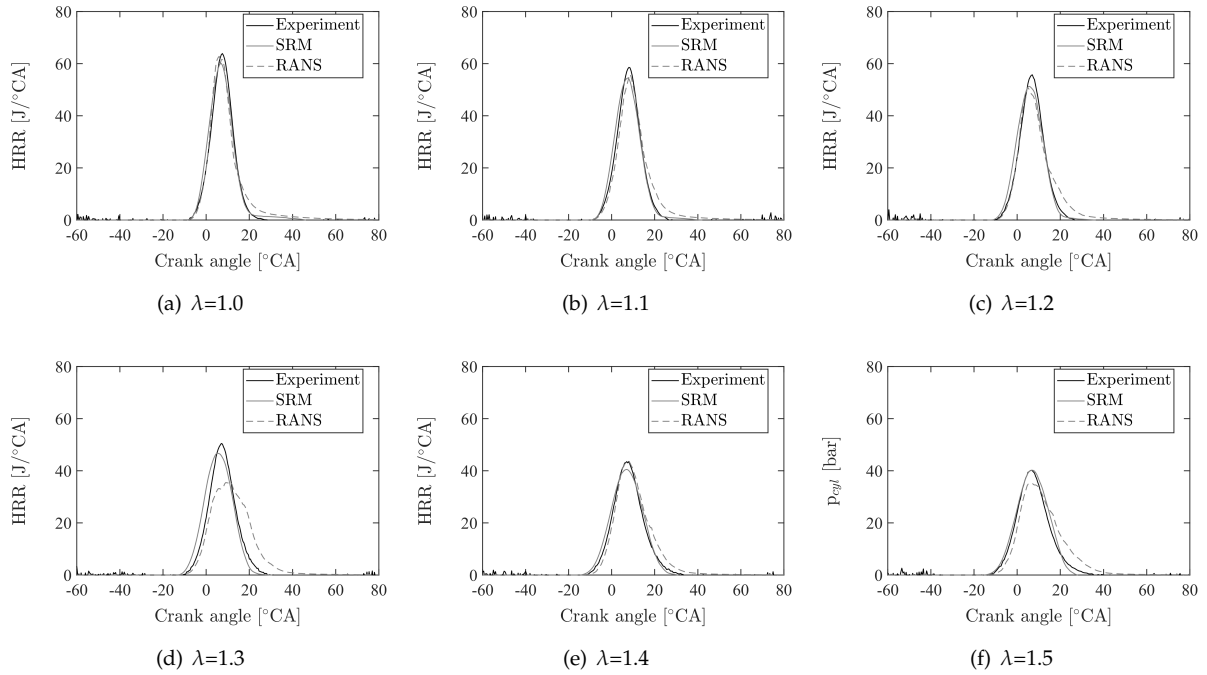


Figure 82: Rate of heat release of experiment, SI-SRM and 3D CFD RANS for operating point 2000 rpm and 6 bar IMEP and different λ of Engine A.

strongly because the optimum C_{ε_2} parameter is much higher than C_{ε_1} with a value of 0.67. The reduced turbulent length scale during intake valve opening leads to a lower formation of turbulent kinetic energy due to inflowing mass. The sharp increase of turbulent length scale at intake valve closure is because the C_{ε_2} parameter is larger than C_{ε_1} which further causes a strong increase of turbulent kinetic energy. Following, the turbulent kinetic energy predicted by SI-SRM is higher during the compression stroke and at spark timing compared to 3D CFD. The increased turbulent length scale further causes a lower dissipation rate for SI-SRM. The increase of turbulent kinetic energy between 120 °CA and 360 °CA in the 3D CFD simulation is because of backflow of mass through the exhaust valves into the cylinder. This backflow is not predicted by the SI-SRM wherefor no turbulent kinetic energy is produced during that time. On the other hand, the angular momentum of the tumble flow is well captured by the SI-SRM compared to 3D CFD using a Toppelmann tumble number (T_{Tipp}) of 0.5.

The combustion regimes for different λ values predicted by SI-SRM and 3D CFD are compared using the Borghi-Peters diagrams as shown in figure 84. The change of λ is indicated by the grey color scale where stoichiometric conditions are colored black and lean conditions are colored light grey. The single points of each λ case represent a different point of time during flame propagation. The largest deviation between the two models are the higher predicted length scale ratios l/δ_L of SI-SRM and the different time evolution of 3D CFD. For both models the flame propagation starts at high Ka numbers and moves towards lower Ka and higher Da numbers which are characterized by low turbulence intensity u' and small flame thicknesses δ_L . In difference to the SI-SRM flame propagation which finishes at the low Ka numbers, the 3D CFD predicted flame continues propagating to lower Re numbers and continues further on to lower Ka numbers. During the late phase of combustion of 3D CFD

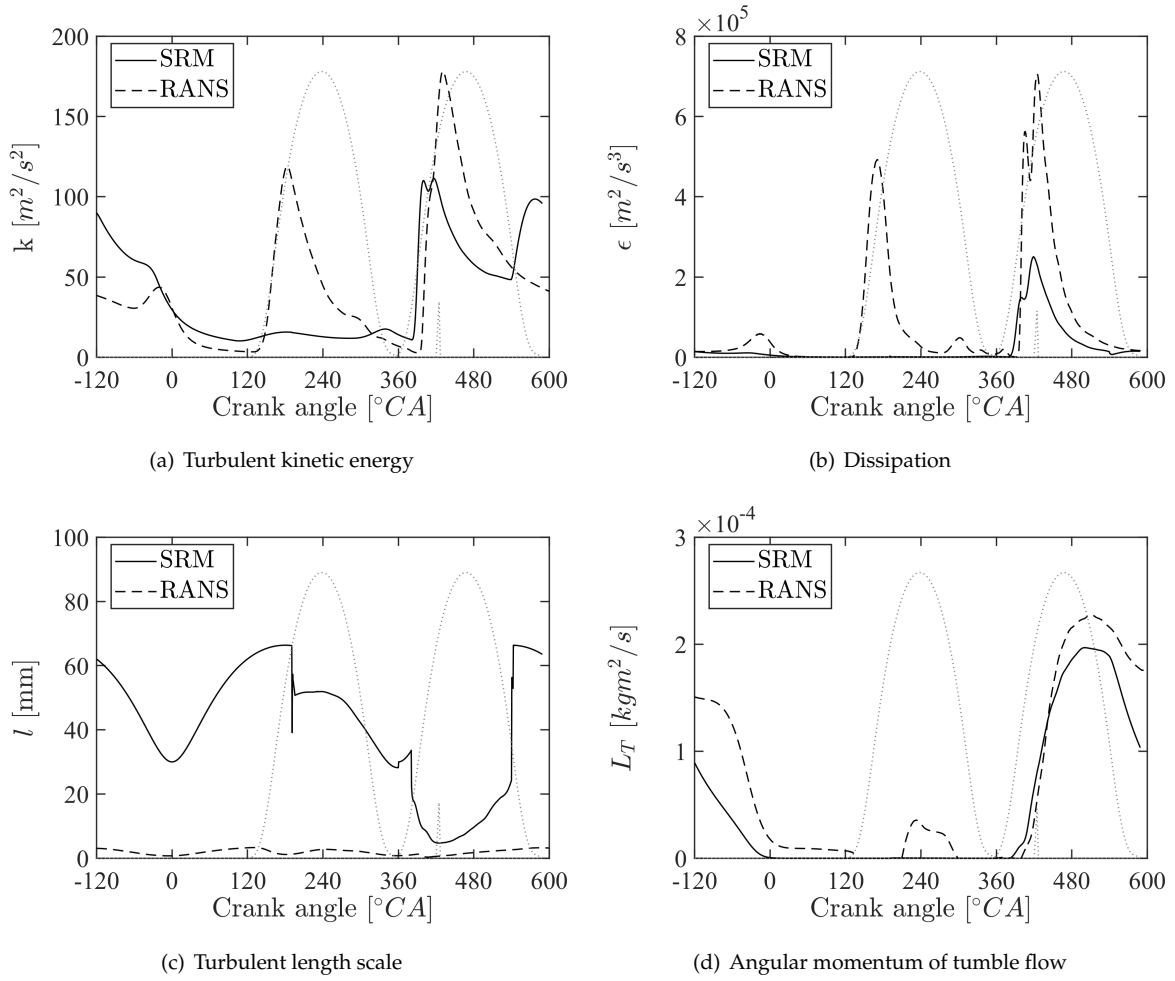


Figure 83: Turbulent kinetic energy, dissipation, turbulent length scale and angular momentum of tumble flow predicted by SI-SRM and 3D CFD RANS for operating point 2000 rpm, 6 bar IMEP and $\lambda=1.0$ of Engine A.

the decrease of the Ka number is due to the increasing turbulent length scale wherefor the stretching of the flame front due to turbulence is further reduced (see figure 83 (a)).

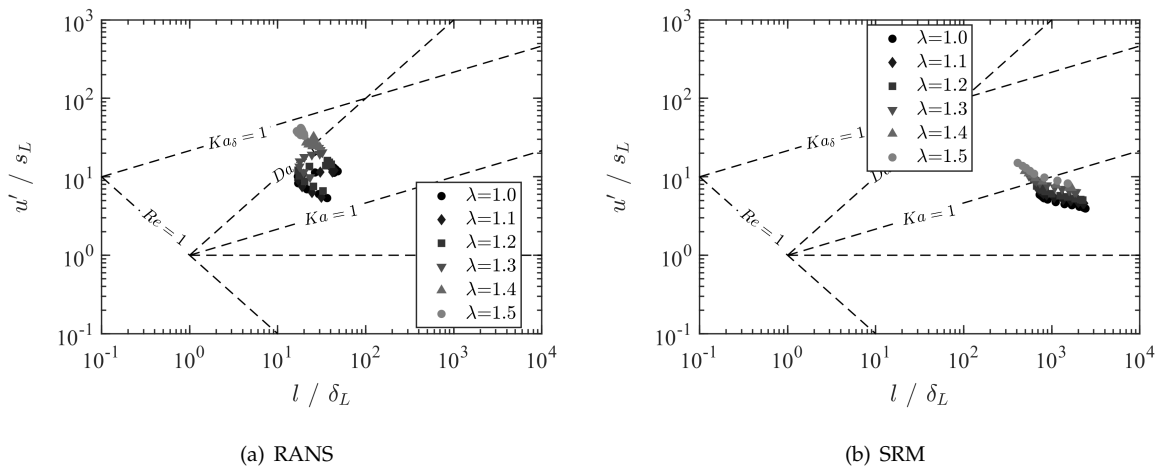


Figure 84: Combustion regimes for λ variation of 3D CFD RANS and SI-SRM at 2000 rpm and 6 bar IMEP of Engine A.

The initial phase of flame propagation in SI-SRM is determined by initialization of the

flame kernel and the laminar-to-turbulent transition which is sensitive for lean burning conditions. With increasing λ the laminar-to-turbulent transition phase is extended due to the lower laminar flame speed as can be seen in figure 85 (a) and (b). The flame thickness δ_L is continuously decreasing after spark ignition and during flame propagation because the thermal diffusivity (α) is decreasing as shown in figure 85 (c) and (d). The thermal diffusivity is decreasing because of the increasing cylinder pressure and density.

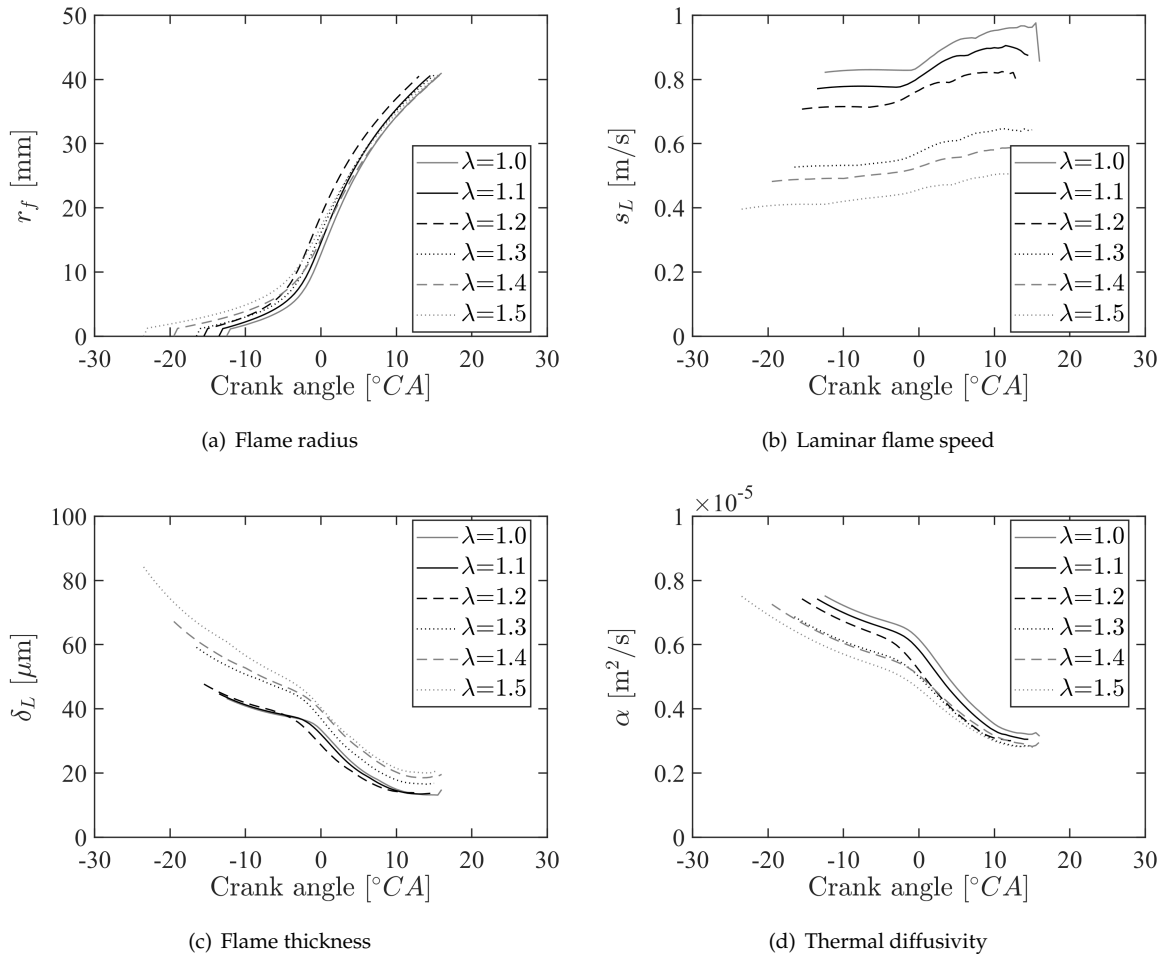


Figure 85: Flame radius, laminar flame speed, flame thickness and thermal diffusivity predicted by SI-SRM for different λ at operating point 2000 rpm and 6 bar IMEP of Engine A.

Following, the combustion regimes of two different engine speeds at 6 bar IMEP are investigated and the results are shown in figure 86. Increasing the engine speed leads to an increase of turbulent intensity wherefor the Re number increases. At the same time the laminar flame speed increases as well as shown in figure 87 (b) which is why the change of Ka number is rather small. The length scale ratio l/δ_L is increasing at the same time as well due to the decreasing flame thickness at higher engine speeds wherefor the Da number is not changing significantly.

The start of flame propagation is predicted earlier for higher engine speed because of the earlier spark timing while the initial flame kernel mass is the same. The flame thickness is reduced for the higher engine speed because of the higher laminar flame speed and thermal diffusivity (see figure 87). As a result of the lower flame thickness, the laminar-to-turbulent

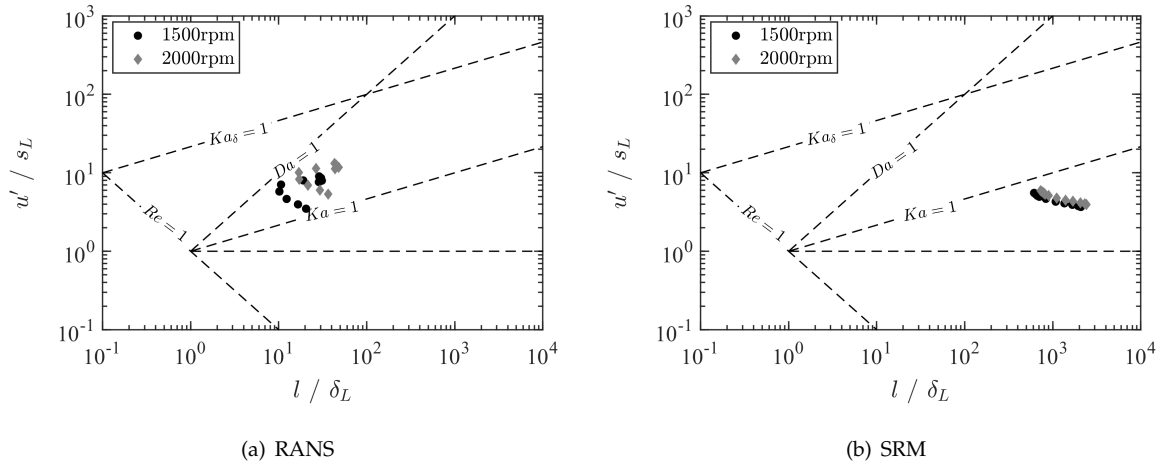


Figure 86: Combustion regimes for two different engine speeds at 6 bar IMEP and $\lambda=1.0$ of 3D CFD RANS and SI-SRM of Engine A.

phase is extended and the flame radius is predicted lower for the higher engine speed.

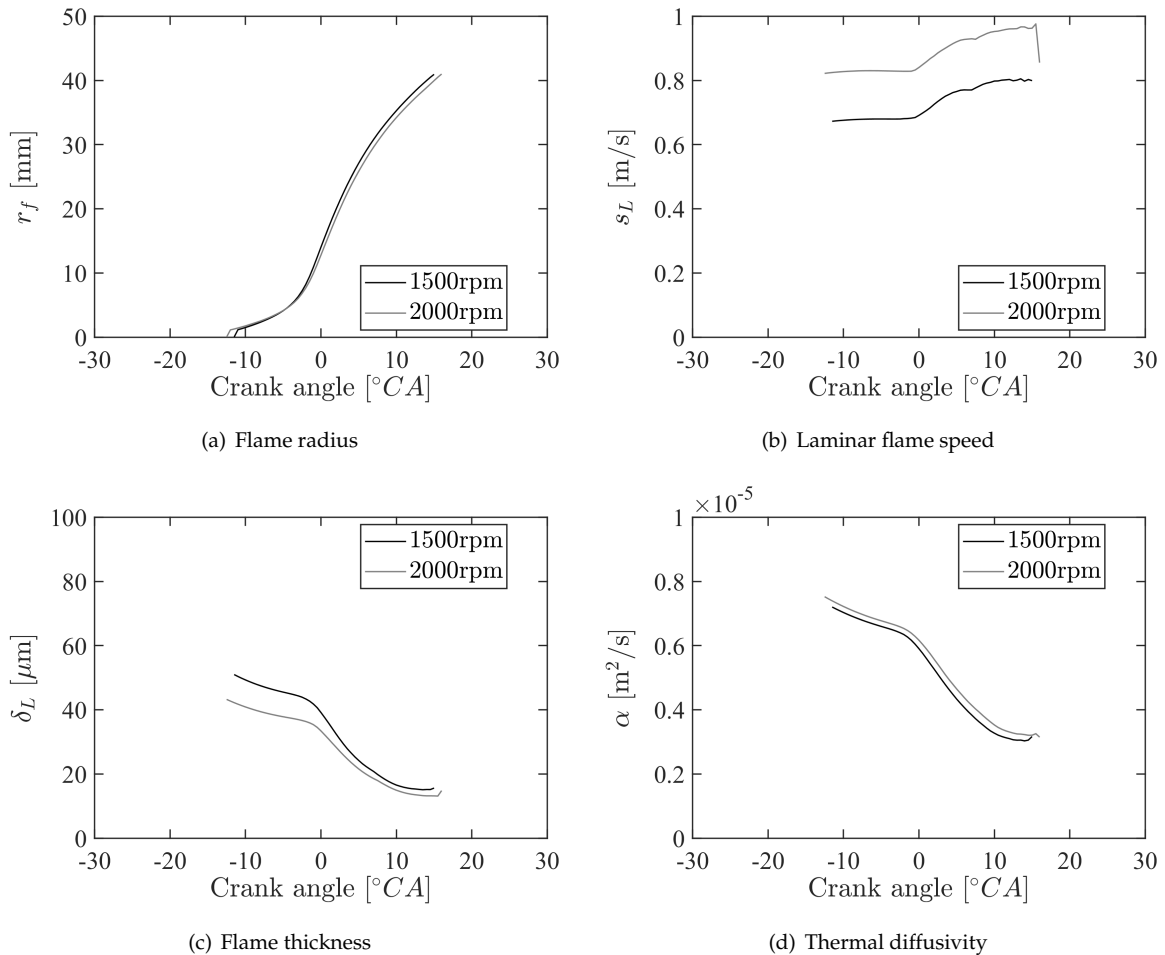


Figure 87: Flame radius, laminar flame speed, flame thickness and thermal diffusivity predicted by SI-SRM for two different engine speeds at 6 bar IMEP and $\lambda=1.0$ of Engine A.

Increasing the IMEP at a constant engine speed of 2000 rpm leads to an increase of the Ka and Re numbers while the Da number is not significantly changing as can be observed

in figure 88 for both models. Thereby, the SI-SRM shows a stronger change of Ka number compared to 3D CFD.

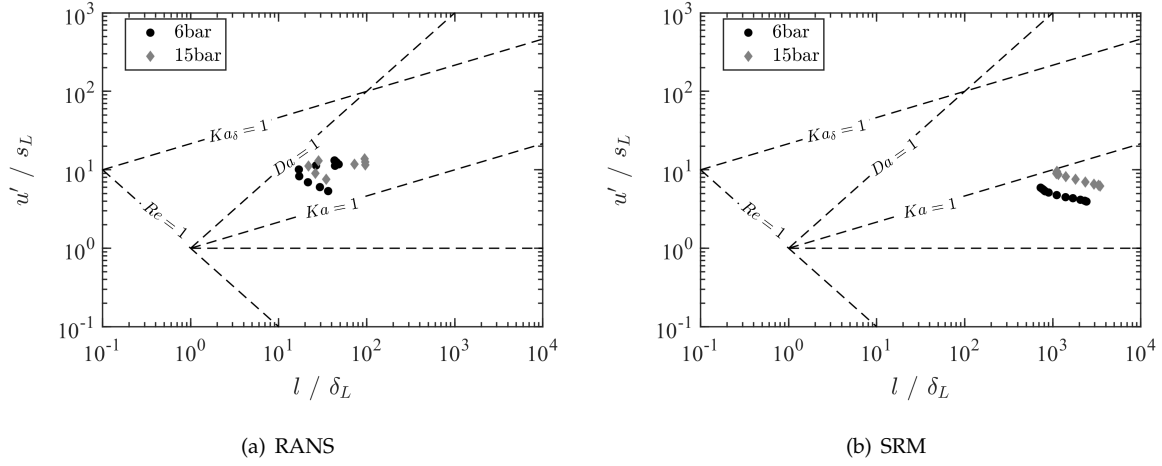


Figure 88: Combustion regimes for two different engine loads at 2000 rpm and stoichiometric conditions of 3D CFD and SI-SRM.

The spark timing is significantly delayed for higher IMEP because of the higher risk of knocking combustion. However, the laminar-to-turbulent transition time is shorter and the combustion duration is reduced. Due to the higher cylinder pressures at high IMEP the laminar flame speed and thermal diffusivity are reduced and as a result the flame thickness is reduced as well.

The influence of the difference in turbulent length scale l and dissipation ε between SI-SRM and 3D CFD shown in figure 83 is further investigated by adjusting the turbulent length scale parameters of the $k - \varepsilon$ model. The C_{ε_1} parameter is set to 3.5 and the C_{ε_2} parameter is set to 2.0 to obtain a better match with the 3D CFD simulation. The simulation results are shown in figure 90 and the turbulent length scale and dissipation of SI-SRM is close to the 3D CFD solution. The turbulent kinetic energy is predicted higher compared to 3D CFD, while the trend is matching. Due to the missing backflow the SI-SRM does not predict the decrease in turbulent length scale and increase of turbulent kinetic energy during exhaust valve opening. The angular momentum L_T predicted by the SI-SRM is slightly lower compared to 3D CFD but matches the trend.

The reduced turbulent length scale leads to a lower Da number according to equation (4.84). Following, the turbulent flame speed is reduced according to equation (4.105), and the heat release rate would be under-predicted by the SI-SRM. To compensate the effect of turbulent length scale, the equation for flame thickness is extended by introducing the model parameter C_{Blint} .

$$\delta_L = C_{Blint} \cdot \frac{\alpha_{th}}{s_L} \cdot \left(1 + \frac{T_{ad} - T_u}{T_u}\right)^{0.7} \quad (6.2)$$

Following, another optimization campaign is performed setting the turbulent length scale parameters C_{ε_1} and C_{ε_2} constant, and selecting C_{ε} , b_1 and C_{Blint} as optimization parameters. The training set from table 28 is used for the optimization. The design ID 227 is selected from

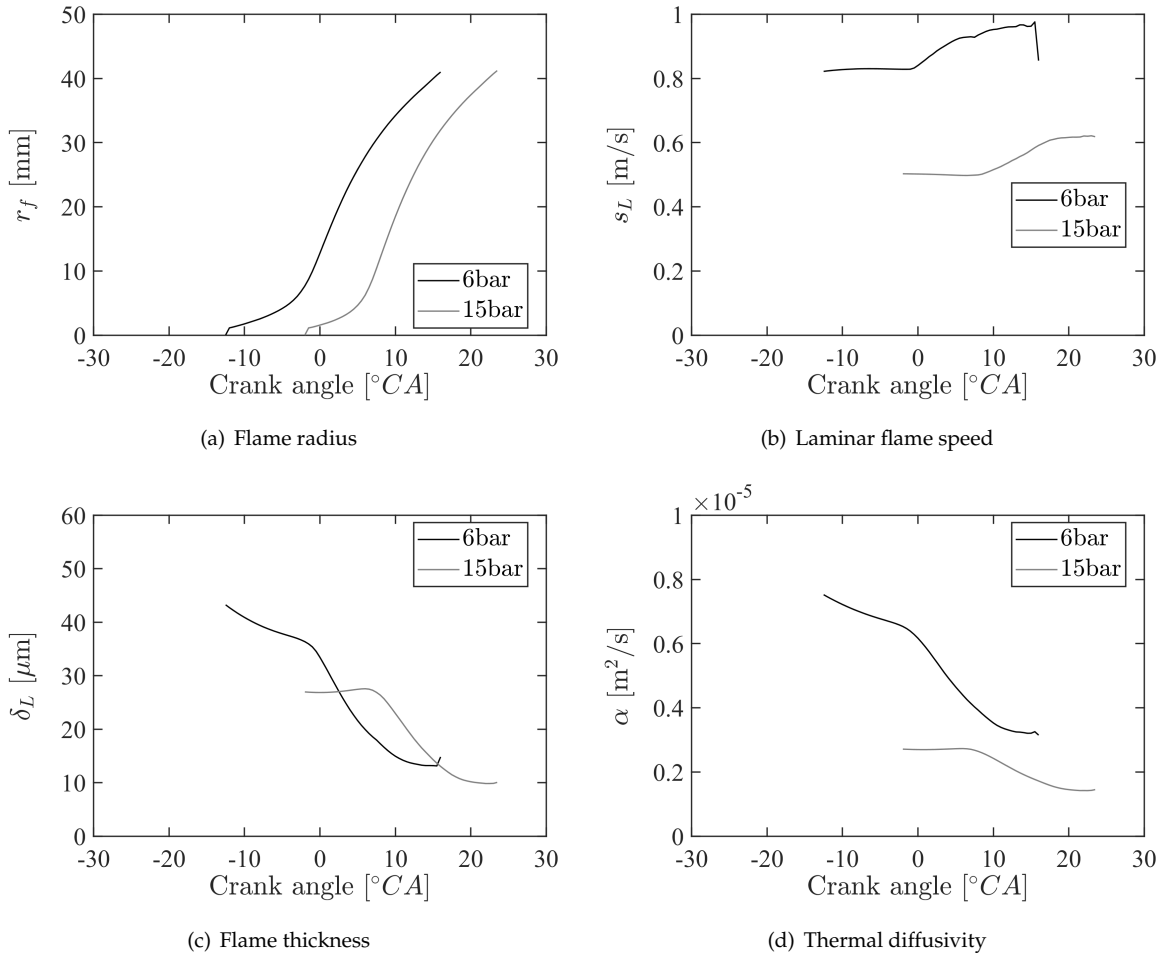


Figure 89: Flame radius, laminar flame speed, flame thickness and thermal diffusivity predicted by SI-SRM for two different engine loads at 2000 rpm and $\lambda=1.0$ of Engine A.

the Pareto solutions and the design parameters are compared with design ID 476 in table 29. The reduced turbulent length scale leads to an increase of dissipation ε wherefor turbulent kinetic energy is reduced. This effect is compensated by the optimization by decreasing the dissipation parameter C_ε which lowers the dissipation according to equation (4.71). The C_{Blint} parameter is decreased by the optimization to balance the effect of the reduced turbulent length scale in regard to the Da number, and the Peters model parameter b_1 is increased to 2.53 to predict the maximum heat release rate. The cyclic variation model parameters are adjusted for design ID 227 by increasing the standard deviation of turbulence fluctuation of velocity $\sigma_{u'}$ for lean mixtures and decrease the standard deviation of spark timing $\sigma_{\theta_{ST}}$ to $0.5^\circ CA$ and keep it constant.

The simulation results of heat release rate for design ID 227 and λ variation are compared to design ID 476 in figure 91. Both designs show overall a good agreement with the experiments, while design ID 227 shows a better match of the maximum heat release rate. Further, both designs over-predict the phase with the highest gradient in heat release rate which indicates that the laminar-to-turbulent transition is too strong at the time shortly before flame propagation becomes fully turbulent.

The combustion regimes for design ID 476 and ID 227 are shown in figure 92. The decrease

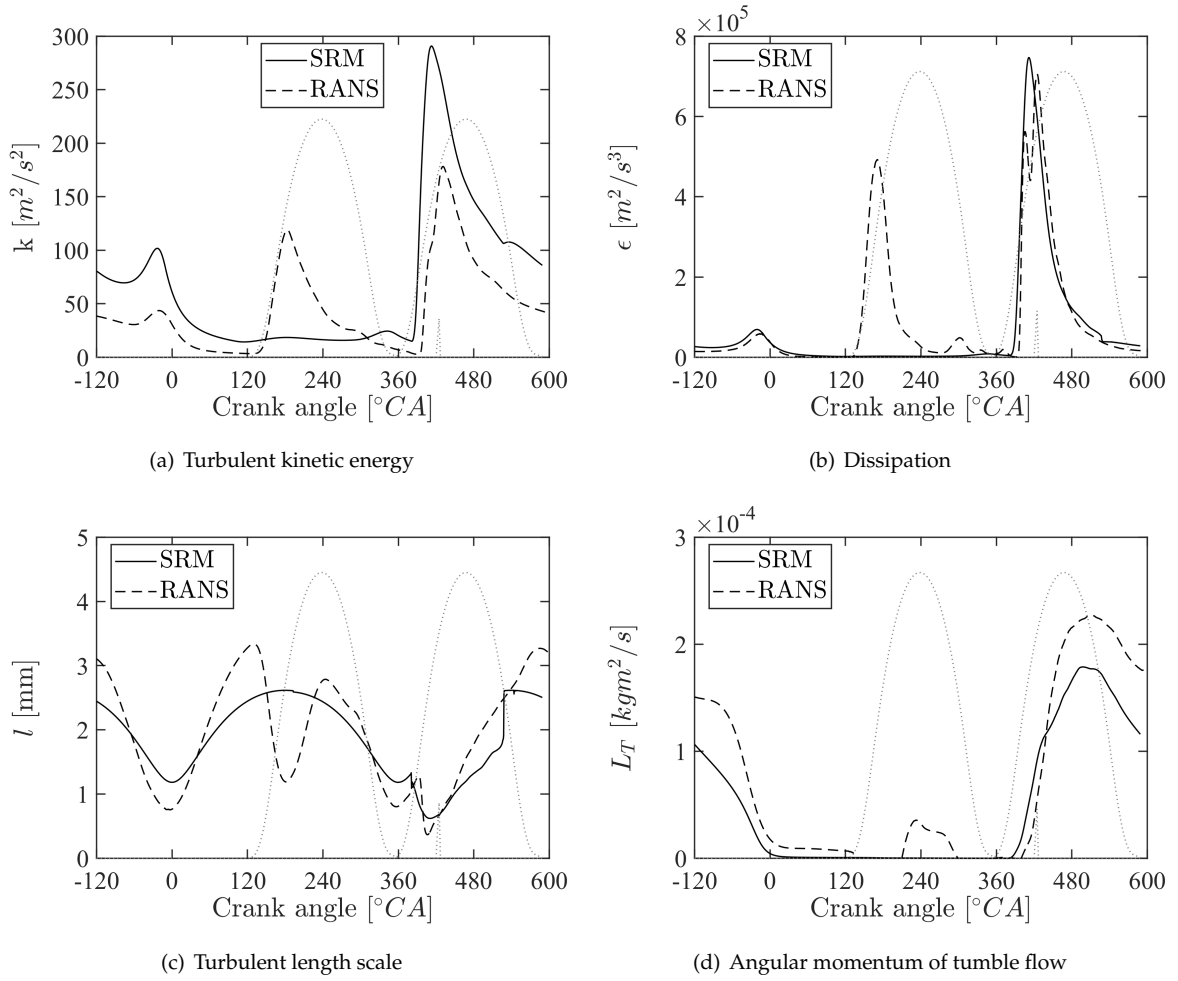


Figure 90: Turbulent kinetic energy, dissipation, turbulent length scale and angular momentum of tumble flow predicted by SI-SRM and 3D CFD RANS for operating point 2000 rpm, 6 bar IMEP and $\lambda=1.0$ of Engine A.

Parameter	ID 476	ID 227
C_ϵ	1.27	0.57
C_{inj}	0	0
C_{axial}	0.2	0.2
$f_{T,spin-up}$	1.0	1.0
T_{Tipp}	0.5	0.5
a_{in}	20	20
b_{in}	0.2	0.2
C_{ϵ_1}	0.14	3.5
C_{ϵ_2}	0.67	2.0
$C_{\phi,u}$	1.0	1.0
$C_{\phi,b}$	0.0025	0.0025
C_{Blint}	2.0	1.0
b_1	2.85	2.53
$\sigma_{\theta_{ST}}$	2.1 °CA - 4.1 °CA	0.5 °CA
$\sigma_{u'}$	0.1 m/s	0.15 m/s - 0.225 m/s

Table 29: Model parameters for the $k - \epsilon$ turbulence model, turbulent flame propagation model and scalar mixing time τ_ϕ .

of the turbulent length scale moves the combustion regime of design ID 227 towards lower Da numbers and higher Ka numbers where it matches closer with the 3D CFD results in figure 84 (a). The increased turbulent kinetic energy shown in figure 90 moves the design ID

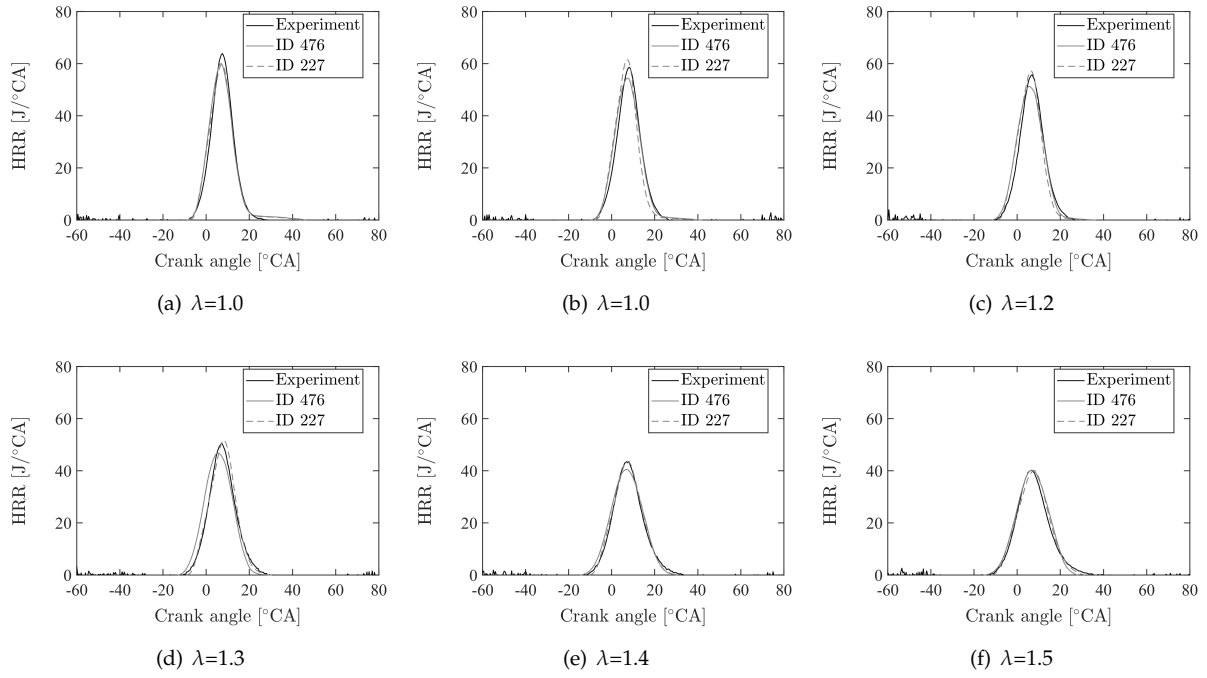


Figure 91: Rate of heat release of experiment and SI-SRM for design ID 476 and ID 227 for operating point 2000 rpm, 6 bar IMEP and different λ of Engine A.

227 further to high Ka numbers.

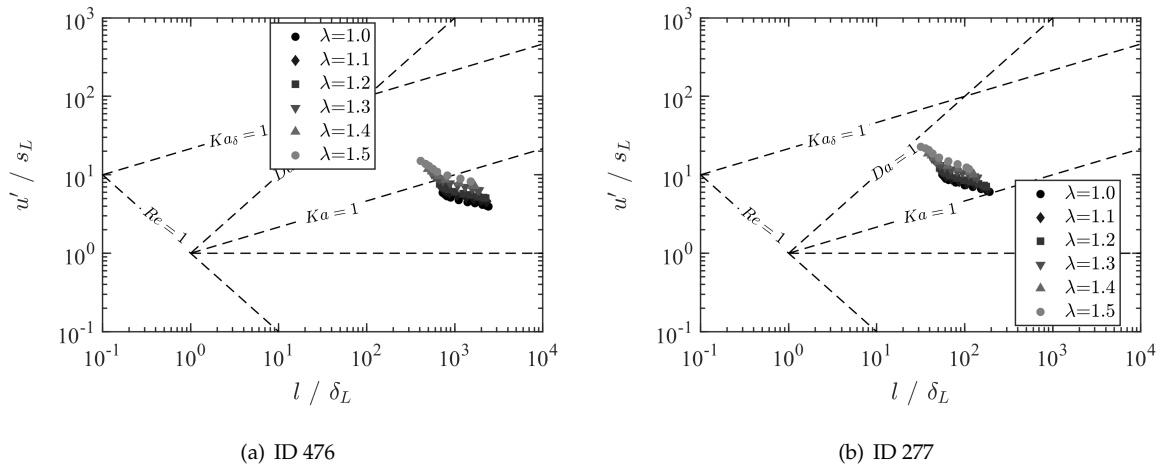


Figure 92: Combustion regimes for λ variation of SI-SRM at 2000 rpm, 6 bar IMEP of Engine A.

The effect of the C_{Blint} parameter on the flame thickness is shown in figure 93. The predicted flame thickness of design ID 227 is only half of the one of design ID 476. The increase of the flame thickness for higher λ values is kept the same. Furthermore, the change of the combustion regimes for different engine speeds and IMEPs are kept the same as shown in figure 86 and 88, while they are moved towards lower l/δ_L ratios.

6.8 Conclusions for spark ignition engine model optimization

The SI-SRM presented in section 4.3 is implemented into the the multi-objective optimization platform from section 5 and validated for two SI single-cylinder research engine cases. The

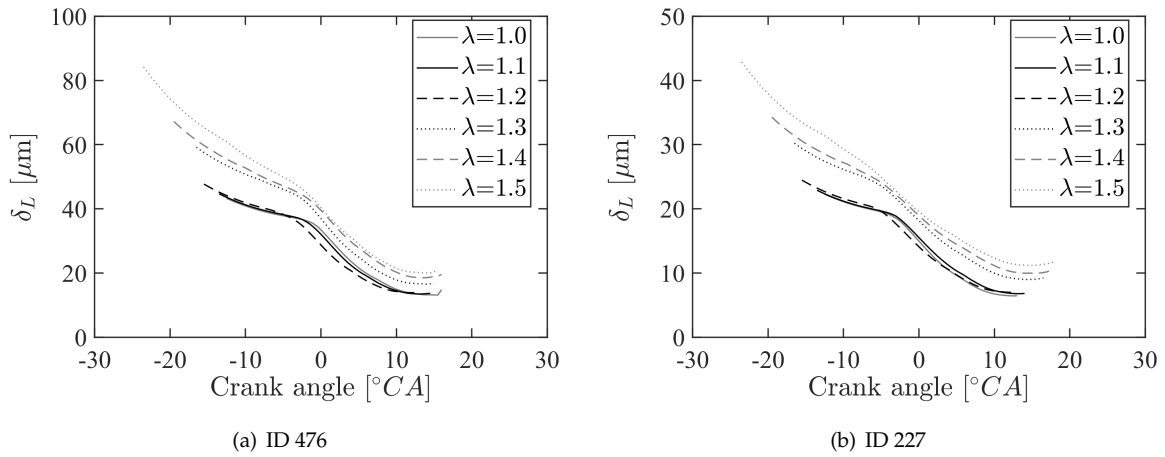


Figure 93: Flame thickness predicted by SI-SRM for different λ at operating point 2000 rpm, 6 bar IMEP of Engine A.

best practice optimization setup comprises the FAST NSGA-II algorithm with 3000 designs evaluated in total. The selection of designs from the Pareto solutions is done using the MCDM. The best practice SI-SRM setup consists of 500 notional particles and 0.5°CA time step size. The cyclic variations of the real engine are reflected by using a probability based modeling approach.

The best performing training procedure included eight operating points selected at 1500 rpm and 2000 rpm engine speed and 6 bar and 15 bar IMEP. Further, the training set included stoichiometric and lean operating conditions. It is found that increasing the number of training points improves the prediction of combustion progress using the validation set while no improvement was found for NO_x and CO engine-out emissions. The parameterization of the η_c model parameter using equation (9.4) allowed to account for the laminar-to-turbulent transition of early flame propagation for different operating conditions.

The $k - \varepsilon$ model is verified using 3D CFD simulation results of one of the SI engine cases. The model predicts the production of turbulent kinetic energy, dissipation and angular momentum of tumble flow accurately for varying operating conditions. Its implementation allowed to capture the different combustion regimes especially for lean operation.

7 Optimization of a compression ignition engine model

The DI-SRM introduced in chapter 4.4 and the MOO platform introduced in chapter 5 are validated for two multi-cylinder engines. The first compression ignition (CI) engine is investigated in the public funded research project “Co-Simulation Platform Connecting Chemistry and Powertrain Dynamics to Traffic Simulation (Connecdt)” and data is published by Picerno et al. [109]. The experimental measurements are provided by the project partner from RWTH Aachen. The second CI engine experimental data is already published by Matrisciano [16] and is used as second validation data set in this thesis.

7.1 Engine specifications

The CI engine from Picerno et al. [109] is named as *Engine C* in the following sections and its specifications are outlined in table 30. The engine bore is similar to a passenger car sized engine. The crank is slightly offsetted. The compression ratio is 15.5:1. The engine is equipped with an eight hole direct injector mounted centrally in the cylinder head.

Parameter	Unit	Value
Bore	mm	83.0
Stroke	mm	92.35
Rod Length	mm	140.006
Pin Offset	mm	0.5
Compression Ratio	–	15.5:1

Table 30: Specification of engine parameters of Engine C.

The CI engine taken from the thesis of Matrisciano [16] is named *Engine D* in the following sections and its specifications are outlined in table 31. The engine bore, stroke and connecting rod length are larger compared to *Engine C* and it belongs to the class of heavy-duty engines. The compression ratio is 16.2:1 which is larger compared to *Engine C*.

Parameter	Unit	Value
Bore	mm	130.0
Stroke	mm	163.0
Rod Length	mm	245.0
Compression Ratio	–	16.2:1

Table 31: Specification of engine parameters of Engine D.

7.2 Physical properties of diesel fuel

Engine C is operated with B7 Diesel with cetane number (CN) 53.3. The fuel is blended with 7 vol-% of biodiesel. The complexity of the diesel fuel composition is represented by a multi-component surrogate which is developed based on the method of Seidel [94]. The surrogate model *Fuel C* is compared with the experiment fuel in table 32. The surrogate closely matches the CN, lower heating value (LHV) and C:H:O ratio of the experiment fuel.

The composition of *Fuel C* in liquid volume percent is outlined in table 33. It consists of three species to adjust the properties to the experimental fuel. The n-decane and α -

Parameter	Unit	Experiment	Surrogate
CN	–	52.5 - 52.9	53.3
LHV	<i>MJ/kg</i>	42.71	42.56
C:H:O	–	13.6:25.1:0.1	10.27:19.4:0.12

Table 32: Comparison of experiment B7 Diesel fuel and surrogate for Fuel C.

methylnaphthalene fractions are adjusted to match the CN, and the α -methylnaphthalene fraction represents the aromatic content of the experimental fuel. The fraction of methyl decanoate represent the biodiesel content of the experimental fuel.

Species	Unit	Liquid Volume Fraction
n-Decane	%	65.0
α -Methylnaphthalene	%	27.0
Methyl decanoate	%	8.0

Table 33: Liquid volume fraction of surrogate species of Fuel C.

Engine D is operated with a standard diesel fuel with CN 53. The surrogate *Fuel D* matches closely the CN, LHV and C:H ratio of the experimental fuel as shown in table 34.

Parameter	Unit	Experiment	Surrogate
CN	–	53.0	52.48
LHV	<i>MJ/kg</i>	42.72	42.78
C:H	–	1.8317:1	1.827:1

Table 34: Comparison of experiment diesel fuel and surrogate for Fuel D.

The composition of *Fuel D* in liquid volume percent is outlined in table 35. It consists of two species n-decane and α -methylnaphthalene. The aromatic content is represented by α -methylnaphthalene and is slightly higher compared to *Fuel C*. The liquid properties of Diesel-2 fuel are used to calculate the vaporization rate of the two surrogates. The liquid property data is summarized in table 55.

Species	Unit	Liquid Volume Fraction
n-Decane	%	69.0
α -Methylnaphthalene	%	31.0

Table 35: Liquid volume fraction of surrogate species of Fuel D.

7.3 Operating conditions

The operating conditions of *Engine C* used for the investigation are outlined in figure 94 and 95. The engine map covers the operating range from 1000 to 4000 rpm and 10 to 70 mg/stroke injected fuel mass at lean conditions. The equivalence ratio range spans from 0.85 down to 0.3. The exhaust gas recirculation (EGR) rate ranges from 0% up to 55%. The intake and exhaust valve timings are adjusted for each operating point as shown in figure 94 (b). The data set is distinguished into 16 training points (full black diamonds) and 11 validation points (hollow circles). The selection of the training points covers a broad range of operating conditions to achieve a robust DI-SRM training.

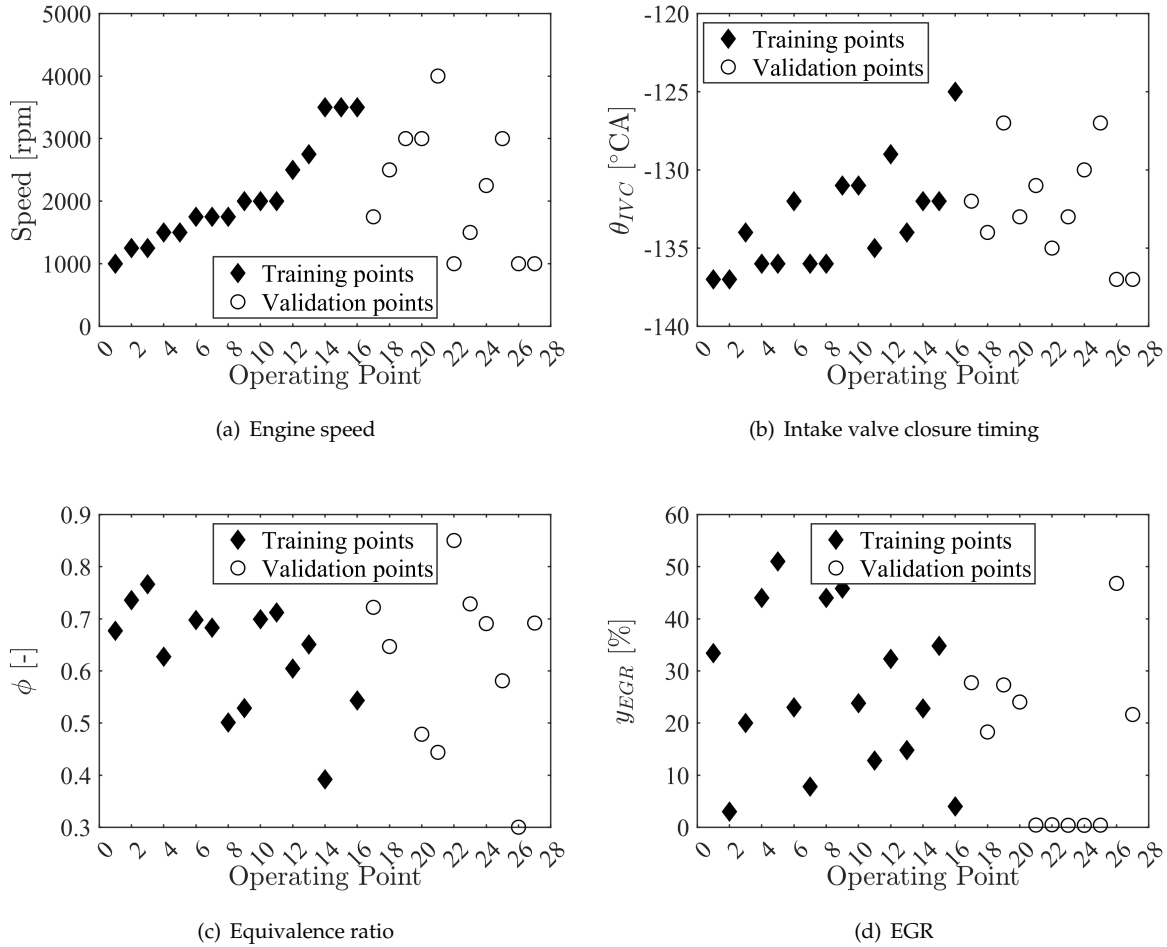


Figure 94: Training and validation points of Engine C.

The injection strategy of *Engine C* is outlined in figure 95. The engine incorporates up to two pilot injections and one post injection. The different injection strategies are covered by the selected training and validation points.

The DI-SRM simulation is started at IVC and a full engine cycle is calculated. The valve lift profiles are provided by the experiments and are the same for all operating conditions. The timings of the intake and exhaust valves are changing for the different operating conditions as shown in figure 94 (b). The intake and exhaust manifold pressures and temperatures are calculated by a one-dimensional (1D) gas exchange model which was calibrated for *Engine C*. The calculated manifold pressure and temperature are provided as boundary conditions to the DI-SRM. The cylinder liner, head and piston wall surface temperatures are set constant to 450 K for all operating points. The initial turbulent kinetic energy k_{init} is calculated using the equation (6.1) and the results are shown in figure 96 (c). The pressure, temperature and EGR at IVC are determined using the thermodynamic analysis of LOGEngine v3.2 [100]. The thermodynamic analysis matches the experimental compression stroke pressure by optimizing the aforementioned parameters. The results are shown in figure 96 (a), (b) and (d).

The validation points for *Engine D* are shown in figure 97. The set include a narrow variation of engine speed between 1000 to 1700 rpm and a broad variation of injection fuel

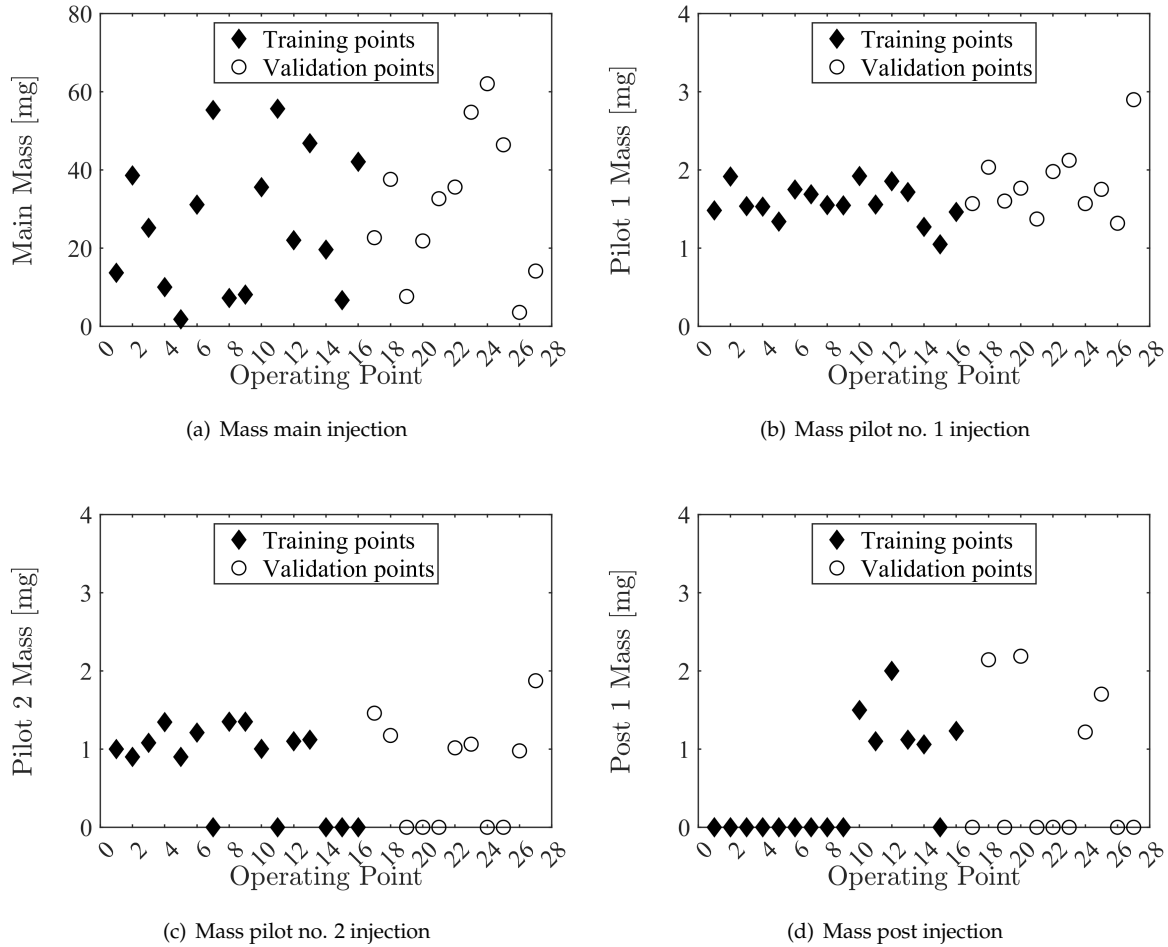


Figure 95: Injection strategy of Engine C.

mass from 70 to 260 mg/stroke. The valve lift profile and timing is the same for all 10 operating points. A single injection strategy is applied for the operating points 1 to 9 and a double injection strategy with one pilot injection is applied for operating point 10. The equivalence ratio ranges from close to stoichiometric down to lean operating conditions.

The initial conditions are outlined in figure 98. The *Engine D* does not incorporate external EGR and the EGR is set to 4% to reflect the internal EGR of the engine. The cylinder liner, head and piston temperatures are set to 403 K, 503 K and 603 K respectively.

7.4 Chemistry model

The tabulated chemistry model for *Fuel C* is based on the detailed chemistry model from Wang [110] and includes the polycyclic aromatic hydrocarbons (PAH) chemistry for detailed soot calculation. The model was also utilized by Picerno et al. [109] for transient driving cycle simulations. The settings of the tabulated chemistry model are summarized in table 36. The pressure is tabulated from 1 to 200 bar with non-equidistant fix points. The temperature is tabulated from 300 to 1400 K and the equivalence ratio from 0.05 to 6.0 to cover the broad range of mixture conditions during direct fuel injection. The EGR is tabulated from 0 to 60% to account for the high EGR rates of the engine.

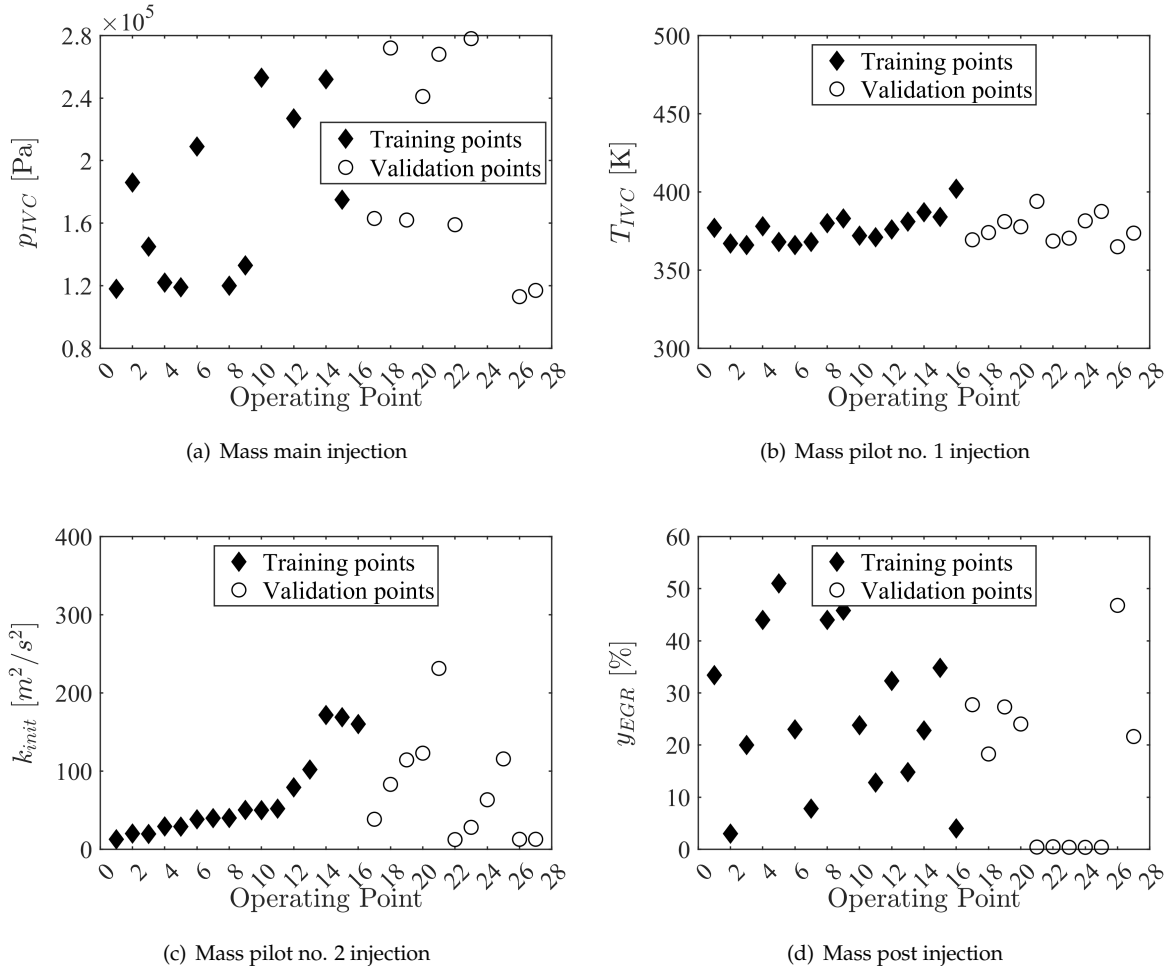


Figure 96: Initial and boundary conditions of Engine C.

Parameter	Value
Surrogate composition	see table 33
Detailed chemistry model	see Wang [110]
Includes PAH chemistry	yes
Pressure (min, max)	1 bar, 200 bar
Temperature (min, max)	300 K, 1400 K
Equivalence ratio (min, max)	0.05, 6.0
EGR (min, max)	0%, 60%

Table 36: Tabulated chemistry model settings for Fuel C.

The tabulated chemistry model for *Fuel D* is outlined in table 37. The model is based on the detailed chemistry model by Wang [110] and was also used in the work of Franken et al. [111]. The model applies the same ranges as for *Fuel C* while only the EGR is tabulated differently in the range of 0 to 40%. The model was validated by Matrisciano et al. [23] by comparison with direct solution of the chemistry equations in DI-SRM.

7.5 Optimization sensitivity study

The optimization sensitivity study is conducted using the FAST NSGA-II algorithm introduced in section 5.6. The algorithm settings for *Engine C* optimization are outlined in table 38. The remaining parameters are set to the default values of NSGA-II in table 11 and FAST NSGA-II

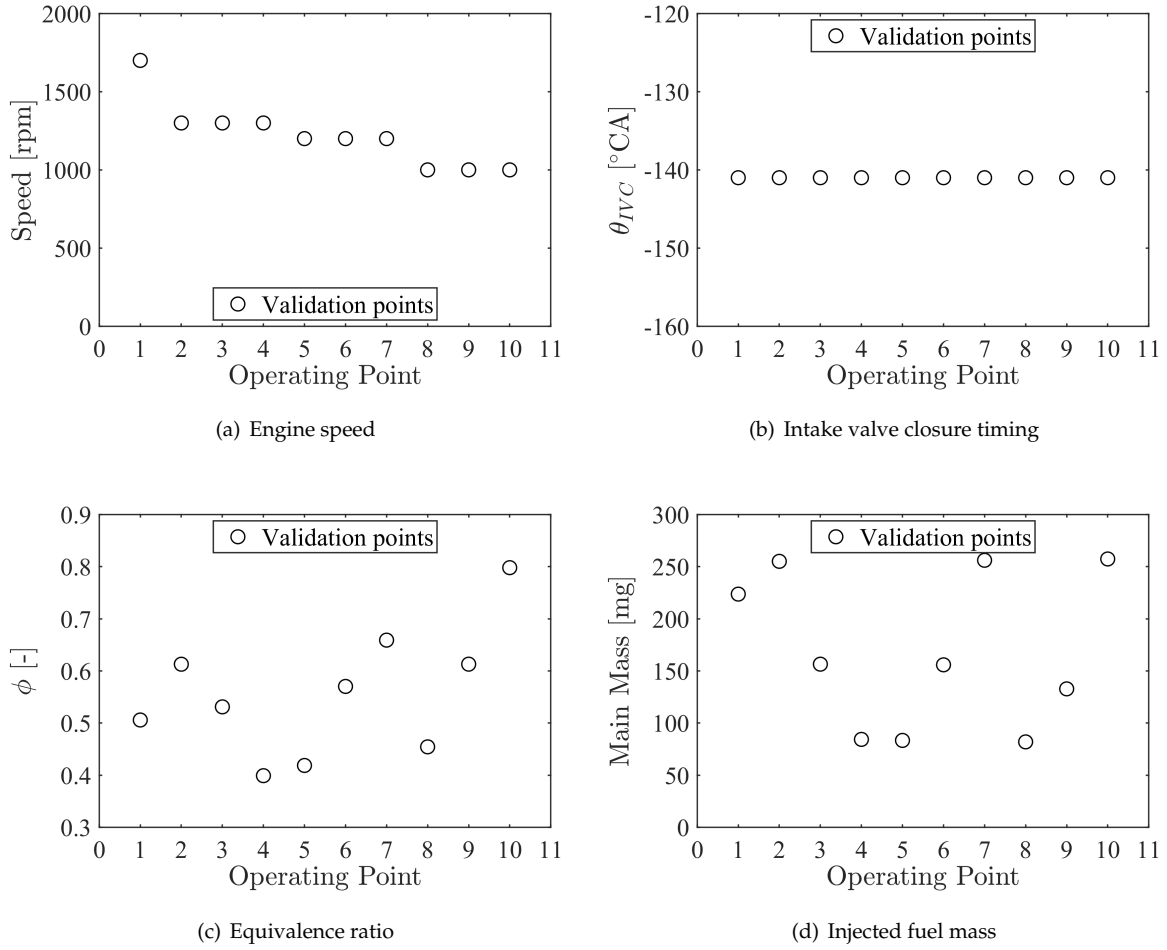


Figure 97: Training and validation points of Engine D.

Parameter	Value
Surrogate composition	see table 35
Detailed chemistry model	see Wang [110]
Includes PAH chemistry	yes
Pressure (min, max)	1 bar, 200 bar
Temperature (min, max)	300 K, 1400 K
Equivalence ratio (min, max)	0.05, 6.0
EGR (min, max)	0%, 40%

Table 37: Tabulated chemistry model settings for Fuel D.

in table 12.

Parameter	Value
Algorithm	FAST NSGA-II
Space filler algorithm	Uniform Latin Hypercube
Number of generations	150
Number of individuals	10
Response surface models	Polynomials, Kriging, Neural Network
RSM training data set size	1000
Initial random seed	1

Table 38: FAST NSGA-II algorithm settings for Engine C optimization.

The DI-SRM models and settings applied for the sensitivity study are outlined in table

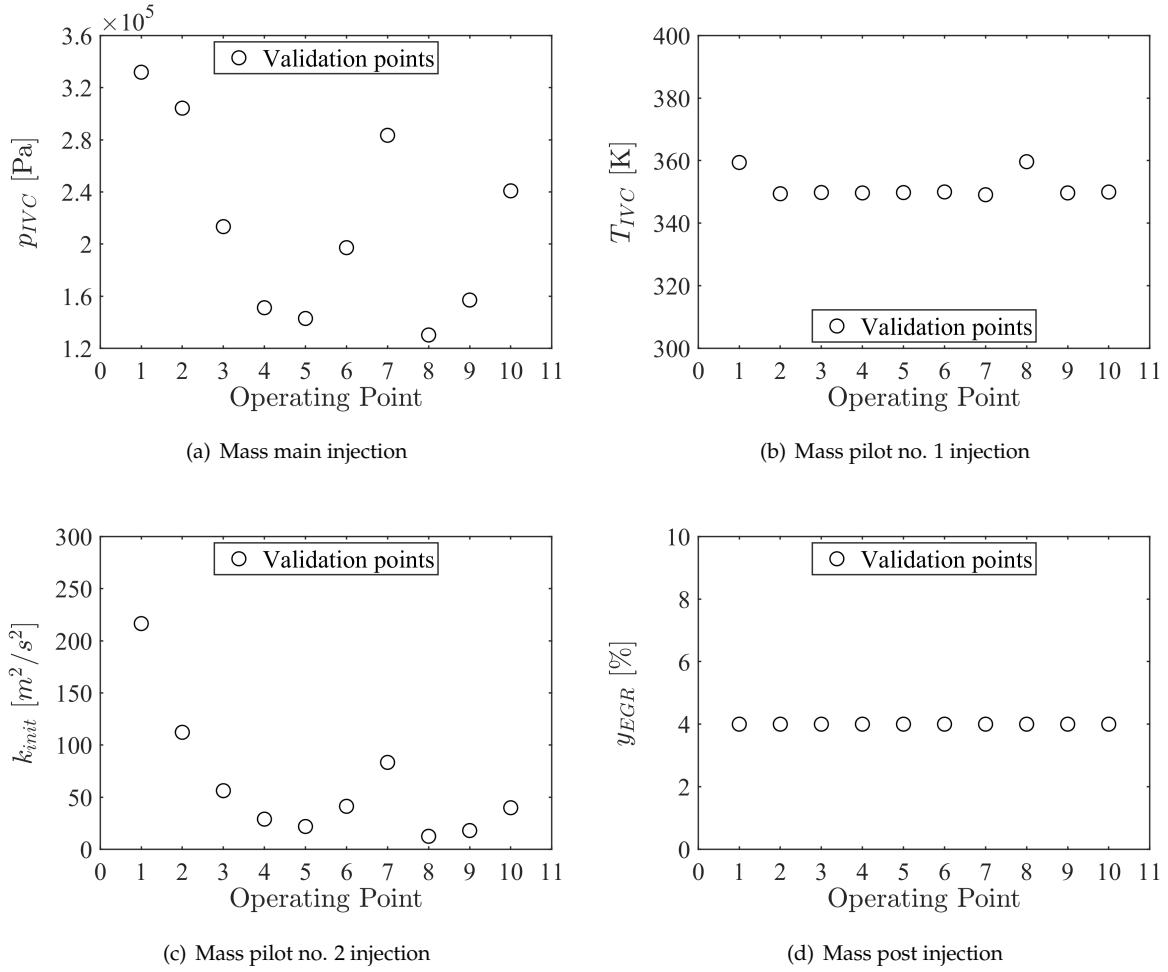


Figure 98: Initial and boundary conditions of Engine D.

39. The stochastic heat transfer coefficient (C_h) is set to 15.0 even though a value of 1 is recommended in section 4.2.2. The particle mixing is modeled using the mixture fraction based EMST model (Z-EMST) as introduced in section 4.2.5.

Process	Model
Convective heat transfer	Woschni model (section 4.2.1)
Stochastic heat transfer coefficient (C_h)	15.0 (section 4.2.2)
Direct injection	yes (section 4.2.3)
Gas exchange	yes (section 4.2.4)
Particle mixing	Z-EMST model (section 4.2.5)
Turbulence	$k - \epsilon$ model (section 4.4.1)

Table 39: DI-SRM settings for optimization sensitivity study for Engine C.

Selection of optimization parameters The objective of the optimization is to minimize the errors $\epsilon_{Pressure}$, $\epsilon_{y_{CO}}$, ϵ_{PCP} and ϵ_{PCPCA} . To determine the best set of optimization parameters a sensitivity study is performed by switching off one parameter by another and evaluate the influence on the Pareto solutions. The selected optimization parameters and its ranges for this investigation are summarized in table 40.

The Pareto solutions of the different optimization runs are outlined in figure 99. The first optimization case *All* is performed using all optimization parameters. Following the order of

Parameter	Lower Limit	Upper Limit
C_ε	0.5	3.0
C_{ε_2}	0.1	3.0
C_{inj}	0.001	0.1
C_ϕ	8	14
B_1	0	8
B_2	-0.0001	0.0001
B_3	50	500
C_{pilot1}	0.1	2.0
C_{pilot2}	0.1	2.0

Table 40: Optimization parameters investigated for Engine C.

parameters in the legend of figure 99 the parameters are switched off and the Pareto solutions are depicted. The lowest errors for $\varepsilon_{Pressure}$, $\varepsilon_{y_{CO}}$, ε_{PCP} and ε_{PCPCA} are obtained using all optimization parameters. Switching off the parameters B_{1-3} and $C_{pilot1-2}$ shows an increase of the errors as seen for case *w/o* B_{1-3} . Switching off the parameters C_ε and C_{ε_2} show only a minor increase of the errors while switching off C_ϕ shows again a noticeable increase of all errors.

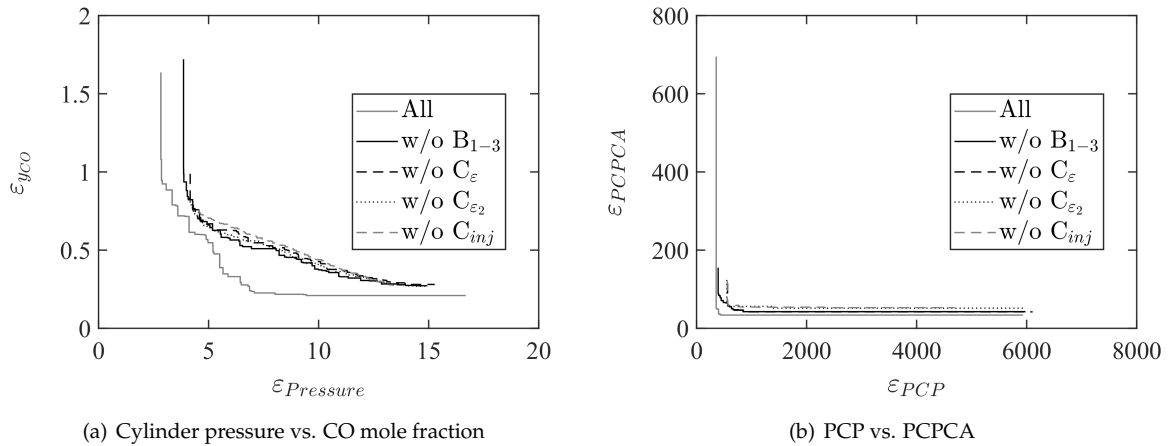


Figure 99: Pareto front of optimization run with different optimization parameters and 1500 designs of Engine C.

Following, the best practice optimization parameters are selected and summarized in table 41. Since C_ε and C_{ε_2} showed only a minor impact on the optimization results they were excluded from the optimization parameters. Further, the range of C_ϕ is increased to allow the optimizer to search for Pareto solutions at lower and higher values of C_ϕ .

Parameter	Lower Limit	Upper Limit
C_{inj}	0.001	0.1
C_ϕ	6	15
B_1	0	8
B_2	-0.0001	0.0001
B_3	50	500
C_{pilot1}	0.1	2.0
C_{pilot2}	0.1	2.0

Table 41: Best practice optimization parameters of Engine C.

Influence of DI-SRM setup To investigate the influence of the DI-SRM setup on the optimization performance different sets are defined and summarized in table 42. The first set uses only 100 notional particles and 1.0 °CA time step size wherefor the simulation times are very short. For set 2, 3 and 4 the number of notional particles is increased to 200 and the number of stochastic cycles is varied from 1 to 30. For the sets 3 and 4 the initial random seed is not fixed but is variable to introduce stochastic. For the set 5 the number of notional particles is further increased to 500 and the number of stochastic cycles is set to 5 with a variable initial random seed. Opposed to table 39 for this investigation the Curl particle mixing model from section 4.2.5 is used.

Parameter	Set 1	Set 2	Set 3	Set 4	Set 5
Number of particles	100	200	200	200	500
Time step size	1.0 °CA	0.5 °CA	0.5 °CA	0.5 °CA	0.5 °CA
Number of cycles	1	1	5	30	5
Initial random seed	1	1	<i>var</i>	<i>var</i>	<i>var</i>

Table 42: DI-SRM model setup for investigation of setup sensitivity for Engine C.

The Pareto solutions of the optimization runs of the different sets are shown in figure 100. Surprisingly the lowest errors are obtained using the set 1 which has a coarse resolution of the cylinder domain and time step and hence was expected to show large inaccuracy. Increasing the number of notional particles show an increase in the errors $\varepsilon_{Pressure}$ and $\varepsilon_{y_{CO}}$ while the errors ε_{PCP} and ε_{PCPCA} are only slightly worse than set 1. Increasing the number of stochastic cycles to 5 shows an increase for the errors $\varepsilon_{Pressure}$ and $\varepsilon_{y_{CO}}$ as well while for 30 number of stochastic cycles the errors are not changing as much.

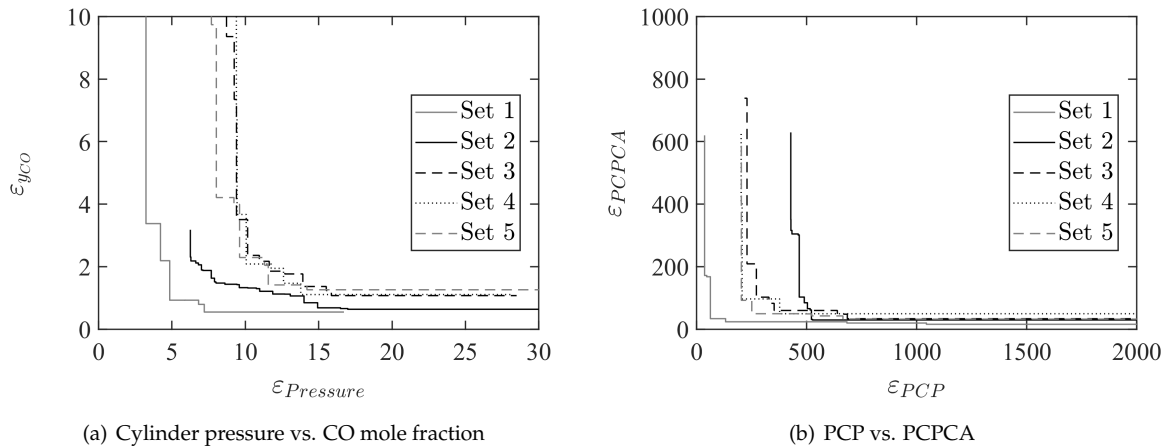


Figure 100: Pareto front of optimization run with set 1-5 and 1500 designs of Engine C.

The validation results of the different SI-SRM setups are shown in figure 101. Surprisingly, the set 1 with lowest number of notional particles and 1.0 °CA time step size is performing better than set 2, 3 and 5 which have a higher number of notional particles and lower time step size. The best performance regarding $RMSE$ is achieved by set 4 with 200 notional particles, 0.5 °CA time step size and 30 stochastic cycles. However, regarding R^2 and $RMSE$ the set 5 is performing best for prediction of 50% combustion progress, NO_x and CO engine-out emissions.

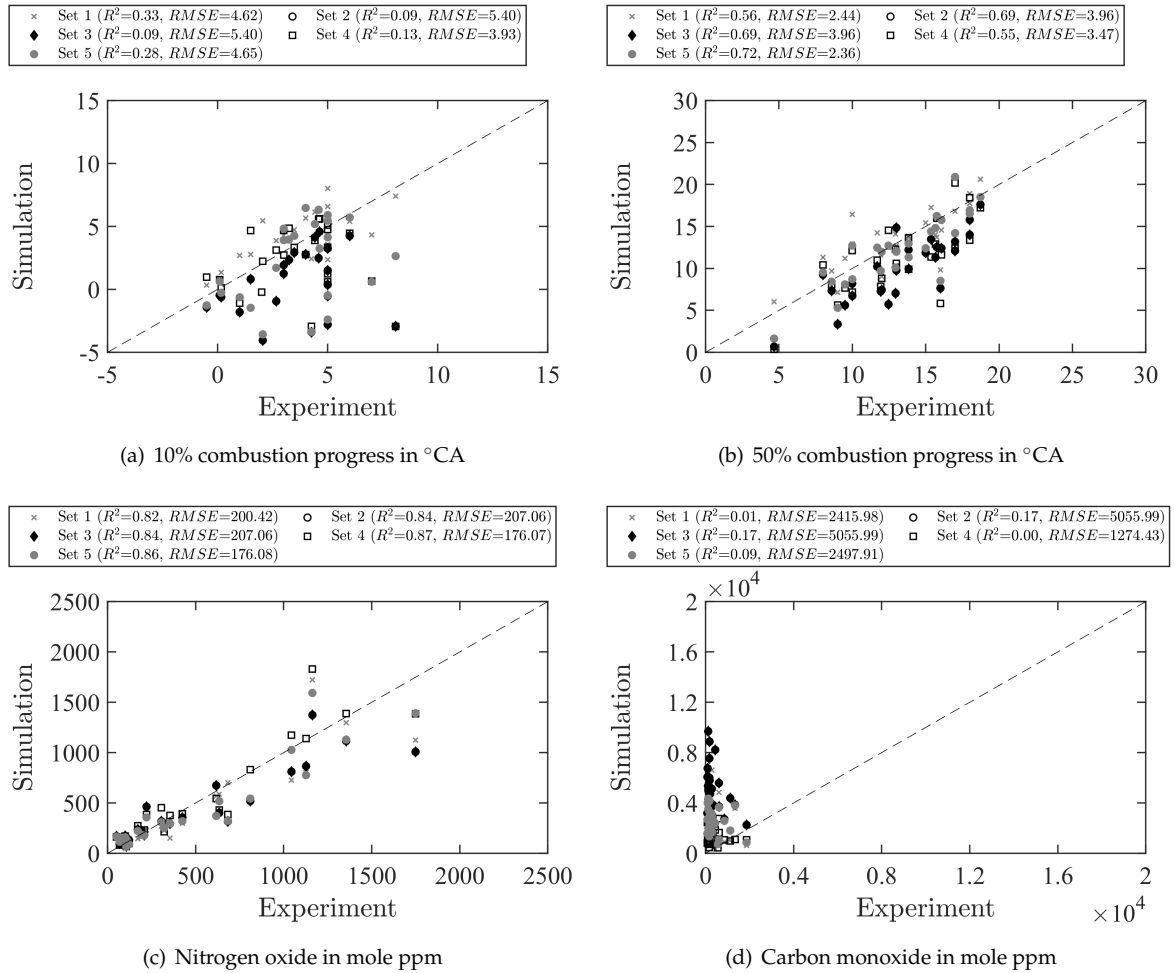


Figure 101: Validation results of different SI-SRM setups of Engine C.

Influence of number of training points The selection of training points for the investigation is shown in figure 102. The three sets of training points show a large span over the engine operation map while the focus is mostly on the low engine speed area. The optimizations are performed using the Curl particle mixing model from section 4.2.5 and the DI-SRM set 1 from table 42.

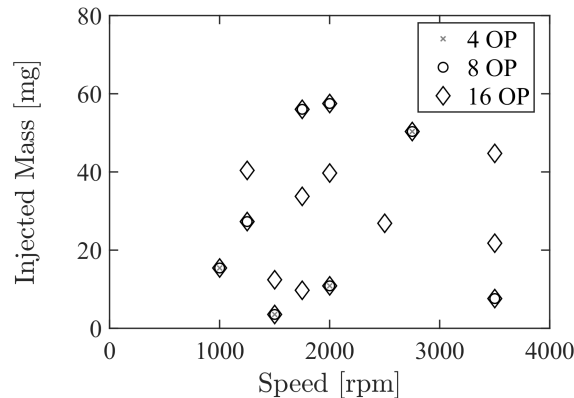


Figure 102: Selected operating points for the optimization runs with 4, 8 and 16 training points for Engine C.

The optimizer tries to push the Pareto front to minimum $\varepsilon_{Pressure}$, $\varepsilon_{y_{CO}}$, ε_{PCP} and ε_{PCPCA}

values for all three sets. Thereby, the lowest errors are achieved by the optimizations with 4 and 8 training points. Further, it can be noticed that with increasing number of training points the number of Pareto solutions is increased and more spread.

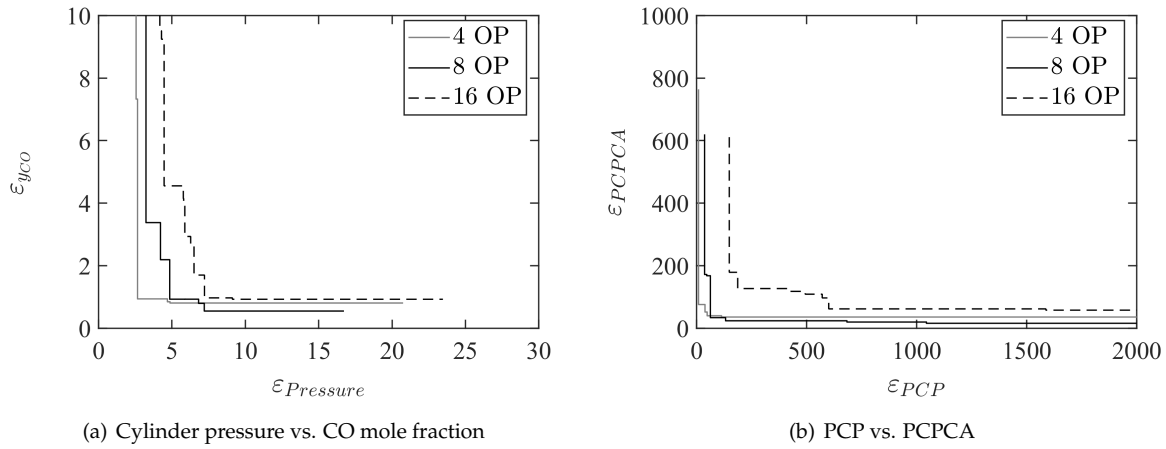


Figure 103: Pareto front of optimization run with 4, 8 and 16 training points and 1500 designs of Engine C.

The best designs of the Pareto solutions are selected using the MCDM with equi-weights for $\epsilon_{Pressure}$, ϵ_{PCP} and ϵ_{PCPCA} while the weight of the $\epsilon_{y_{CO}}$ objective is set to zero. Next, the best designs are tested using the validation data set and the results are shown in figure 104. For 10% combustion progress all three cases show a large variation and the R^2 value is low. For 50% combustion progress the case 4 OP is performing slightly better while all three cases show an acceptable correlation with the experiments. For NO_x emissions an improvement can be observed when using 16 training points and the R^2 value is the highest. The CO emissions are significantly over-predicted for all three cases and show no correlation with the experiments.

7.6 Final validation

The final validation of the optimized DI-SRM setup is conducted for the validation data set of *Engine C* and *Engine D*. It is important to notice that no additional optimization is performed for *Engine D* and simply the optimized DI-SRM parameters of *Engine C* are transferred. The optimization results of Set 3 from table 42 are selected to generate the final DI-SRM setup and the Z-EMST particle mixing model is used. In the following paragraphs the Set 3 will be denoted as Training Set and the DI-SRM setup with increased number of stochastic cycles will be denoted as Validation Set 1 and 2 as it is summarized in table 43.

Parameter	Training Set	Validation Set 1	Validation Set 2	Validation Set 3
Number of particles	200	200	200	200
Time step size	0.5°CA	0.5°CA	0.5°CA	0.5°CA
Number of cycles	5	5	30	100
Initial random seed	var	var	var	var

Table 43: DI-SRM model setup for validation of Engine C.

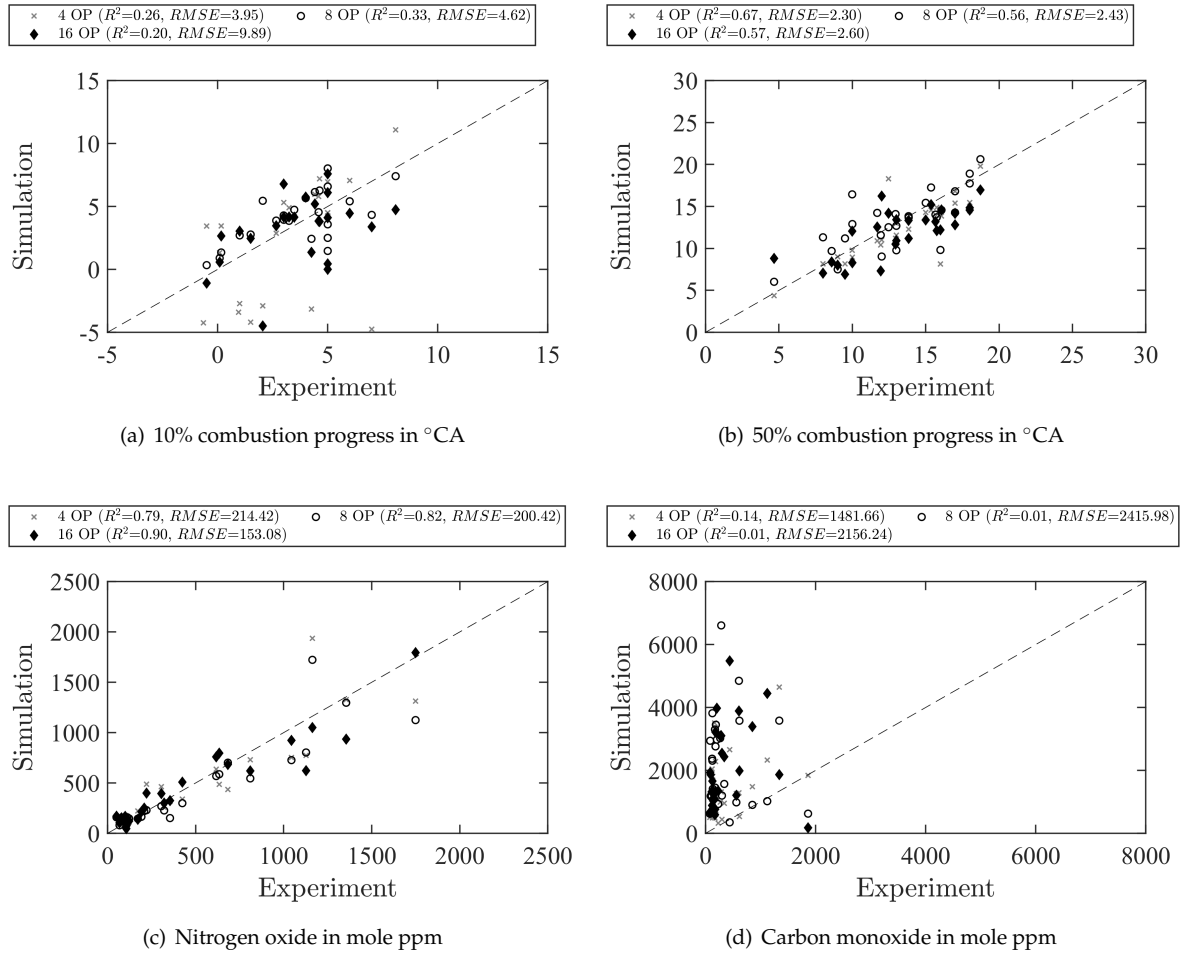


Figure 104: Validation results of number of training points 4, 8 and 16 of Engine C.

Validation results of Engine C The results of the optimization run for *Engine C* using the training set from table 43 are shown in figure 105. Even though the Set 3 is used the results are significantly improved compared to the results shown in figure 100 where the Curl particle mixing model was used. Further, the FAST NSGA-II algorithm shows an even distribution of designs along the Pareto front and a trade-off between $\varepsilon_{Pressure}$ and $\varepsilon_{y_{CO}}$ can be found. This indicates that the designs with best match of combustion do not coincide with the designs with good match of CO emissions. The ε_{PCP} and ε_{PCPCA} errors usually decrease if the $\varepsilon_{Pressure}$ is decreasing.

Using the MCDM three designs are selected from the Pareto solutions as shown in figure 106 to investigate the sensitivity of the selected designs for the validation data set. The design ID 525 is selected by setting the MCDM weight of the $\varepsilon_{Pressure}$ error to one. The design ID 917 puts a higher MCDM weight on $\varepsilon_{y_{CO}}$ error to be able to predict lower CO engine-out emissions. The design ID 526 puts the highest MCDM weight on $\varepsilon_{y_{CO}}$ to get the best match for CO engine-out emissions for the validation data set.

The validation results of the three selected designs are outlined in figure 107. The simulations are performed using the validation set 1 in table 43. The 10% combustion progress is predicted earlier for all three designs. The reason is the faster ignition of the pilot injections for DI-SRM. The predicted 50% combustion progress correlates with the experiments for all

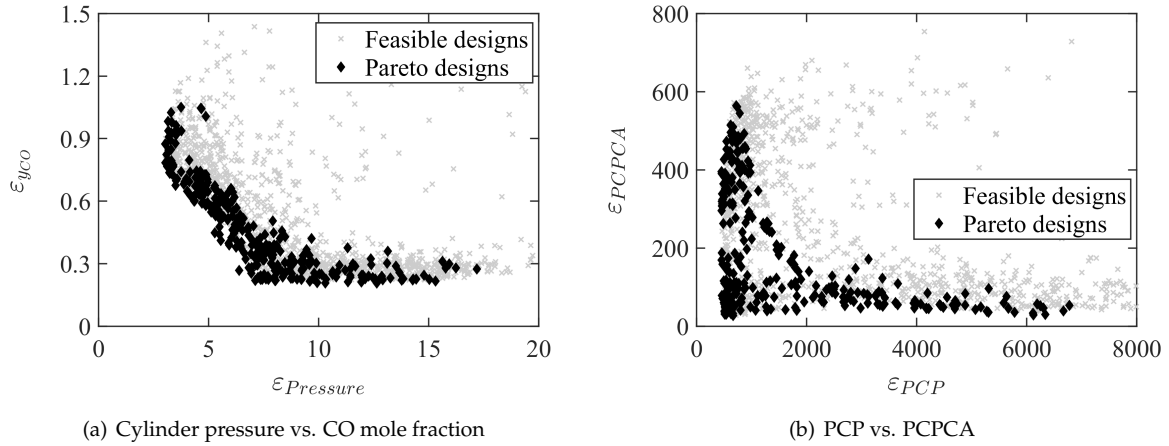


Figure 105: Feasible and Pareto designs of the FAST NSGA-II optimization run with 1500 designs of Engine C.

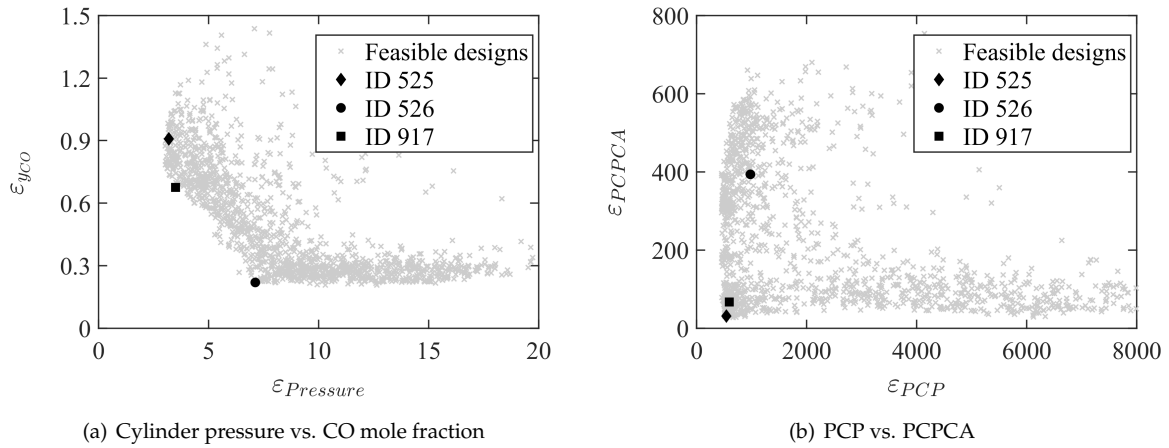


Figure 106: Selected Pareto solutions for the FAST NSGA-II optimization run with 1500 designs of Engine C.

three designs. Even though the combustion progress is matching the design ID 917 shows a high combustion efficiency wherefor the NO_x emissions are predicted higher. The best match for NO_x emissions is obtained for design ID 525 which also predicted the lowest $\varepsilon_{Pressure}$ error. The design ID 526 was selected because of the lower $\varepsilon_{y_{CO}}$ error and it also shows the best match for the validation data set. Nevertheless, all three designs indicate the difficulty to match the experimental CO emissions and having at the same time a reasonable match of the combustion.

Soot optimization for Engine C The design ID 525 is finally selected because of the better prediction of combustion progress and NO_x emissions. Subsequently, the FAST NSGA-II optimization of the soot mass is performed. The set 3 is used for the optimization. The method of soot source term tabulation is introduced by Matrisciano et al. [43, 112, 113] and uses the detailed soot model by Mauß [114] in conjunction with a detailed PAH chemistry. The detailed soot model describes the soot formation and oxidation by incorporating source terms for particle inception, surface reaction, condensation, coagulation and fragmentation. The surface reactions are divided into surface growth by acetylene addition and oxidation

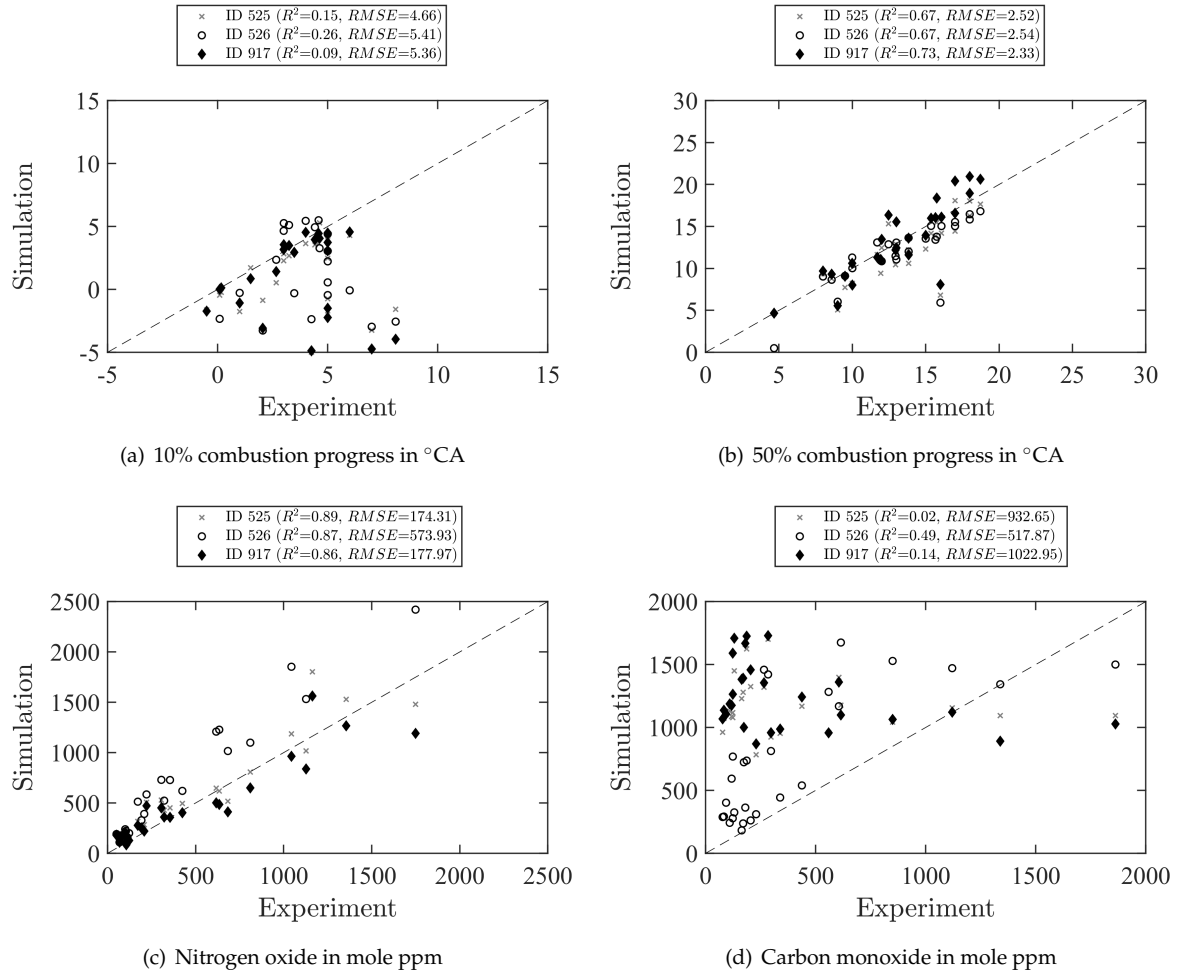


Figure 107: Validation results for design ID 525, ID 526 and ID 917 of FAST NSGA-II optimization run with 1500 designs of Engine C.

by OH and O_2 . The surface sites of a soot particle actually undergoing surface reactions are described by the fraction of active sites which is set to 0.3 according to Pasternak et al. [115]. The shape of a soot particle is mathematical defined by the fractal dimension where a value of 2 denotes a sphere and a value of 3 denotes a chain-like structure. The optimization parameters in table 44 represent scaling factors of the soot source terms.

Parameter	Lower limit	Upper limit
Particle inception source term	0.1	10.0
Surface growth source term	0.1	10.0
Oxidation by OH source term	0.1	10.0
Oxidation by O_2 source term	0.1	10.0
Fractal dimension	2	3

Table 44: Soot optimization parameters for Engine C.

As objectives the ε_{soot} and $\varepsilon_{soot,gradient}$ errors are defined for the soot mass according to the equations (5.7) and (5.8). The feasible designs of the soot optimization show a very large spread in figure 108 and the Pareto solution only consists of a few designs which make the MCDM selection difficult. From the Pareto solutions the three designs ID 2487, ID 2488 and ID 2707 are selected to investigate their performance for the validation data set. Design ID 2487 uses equi-weights in the MCDM for the ε_{soot} and $\varepsilon_{soot,gradient}$ errors while design ID 2488

prefers lower ε_{soot} errors and design ID 2707 focuses on the low $\varepsilon_{soot,gradient}$ errors.

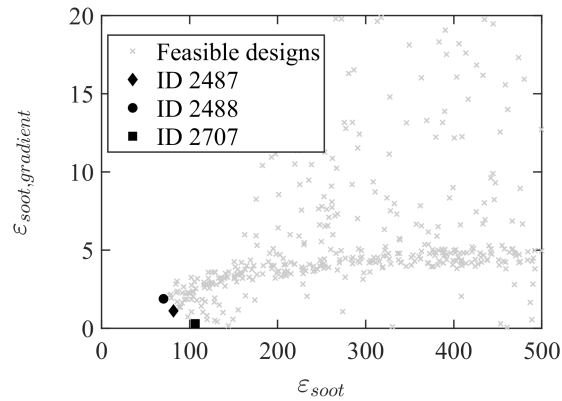


Figure 108: Selected Pareto solutions from the soot optimization run with 1500 designs and FAST NSGA-II of Engine C.

The simulation of the validation data set is performed using the Validation Set 3 from table 43 and the results of the fuel specific fuel mass ($fsSoot$) are outlined in figure 109. The results of all three designs include the standard deviation of soot mass for 100 stochastic cycles which are shown as error bars in the plot. The designs ID 2487 and ID 2707 show a quite similar performance with the tendency to predict higher soot mass compared to design ID 2488. Both designs have a lower particle inception scaling factor ($C_{PI}=8.31 / =8.82$) and oxidation by OH and O_2 scaling factor ($C_{OxOH}=0.96 / =0.86$ and $C_{OxO_2}=4.29 / =3.14$) in comparison to design ID 2488 ($C_{PI}=9.86$, $C_{OxOH}=1.44$ and $C_{OxO_2}=4.80$). All three designs predict the fractal dimension to be close to 2 wherefor the soot particles have a more spherical shape. The design ID 2487 and ID 2707 show a good performance in predicting the high soot masses of the operating points 3, 6, 12, 17 and 18 while the design ID 2488 is performing better predicting the low soot masses of the operating points 2, 15, 19, 21, 22, 24 and 25.

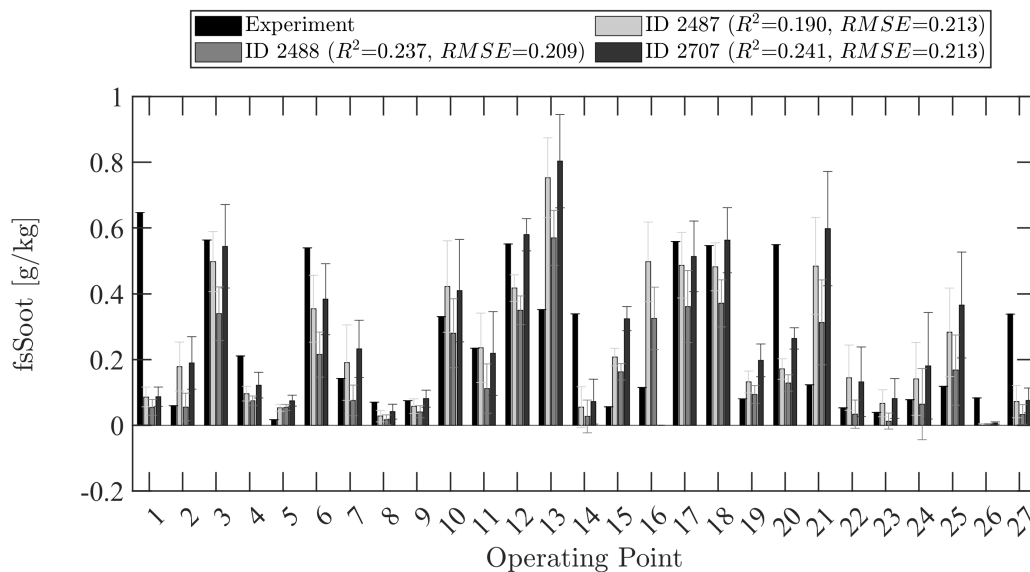


Figure 109: Comparison of fuel specific soot mass for design ID 2487, ID 2488 and ID 2707 including standard deviation as error bars of Engine C. The R^2 values and $RMSE$ are included in the legend.

The sensitivity of the number of stochastic cycles is further investigated for design ID 2707

by running the simulation with validation set 1, 2 and 3. The results in figure 110 include the mean soot mass and its standard deviation. With increasing number of stochastic cycles from 5 to 30 the mean soot mass is significantly decreasing for all operating points. Increasing the number of stochastic cycles even further to 100 shows a slight decrease of soot mass. Further, the standard deviation is the highest for low number of stochastic cycles which indicates the high uncertainty of the soot mass prediction.

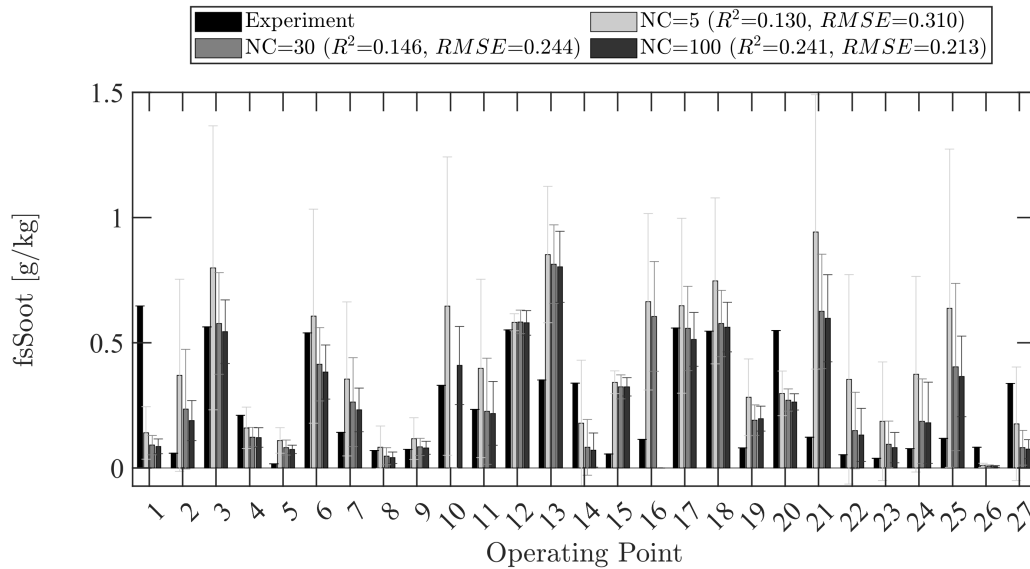


Figure 110: Comparison of fuel specific soot mass for design ID 2707 with 5, 30 and 100 stochastic cycles including standard deviation as error bars of Engine C. The R^2 values and $RMSE$ are included in the legend.

Finally, the design ID 2707 with validation set 3 is selected as the best performing DI-SRM setup. The predicted soot masses using the optimized soot source term scaling factors are compared with the results of design ID 525 without soot source term optimization in figure 111. The design ID 525 under-predicts the soot mass by a margin which indicates the necessity to optimize the soot model parameters. The optimizer fulfilled this task for design ID 2707 by increasing the scaling factor of particle inception wherefor more primary soot particles are formed.

Validation results of Engine D The optimized design ID 2707 with optimized soot model parameters from the previous section is further tested for the case *Engine D*. The initial and boundary conditions are outlined in section 7.3 and the Validation Sets 1 to 3 from table 43 are used for the DI-SRM simulation. It has to be noted that for *Engine D* no measurement data is available for the pressure and temperature in the intake and exhaust manifold. Therefore, the gas exchange model from section 4.2.4 is not used and the turbulent kinetic energy and angular momentum production terms in the $k - \varepsilon$ turbulence model from section 4.4 are not calculated. Further, no experimental data for soot mass is available wherefor only the gaseous emissions are evaluated.

The simulation results are outlined in figure 112. The DI-SRM shows an earlier prediction of 10% combustion progress while 50% combustion progress is slightly higher. The NO_x emissions are under-predicted and the CO emissions are over-predicted using the design ID

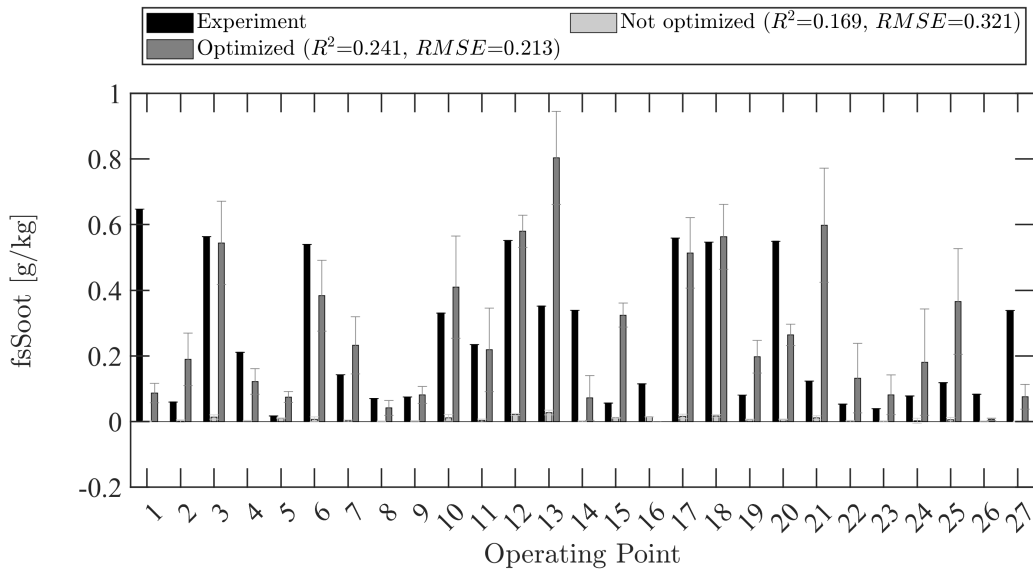


Figure 111: Comparison of fuel specific soot mass for design ID 525 and ID 2707 including standard deviation as error bars of Engine C. The R^2 values and $RMSE$ are included in the legend.

2707 model parameters. Further, increasing the number of stochastic cycles shows no change of the predicted results.

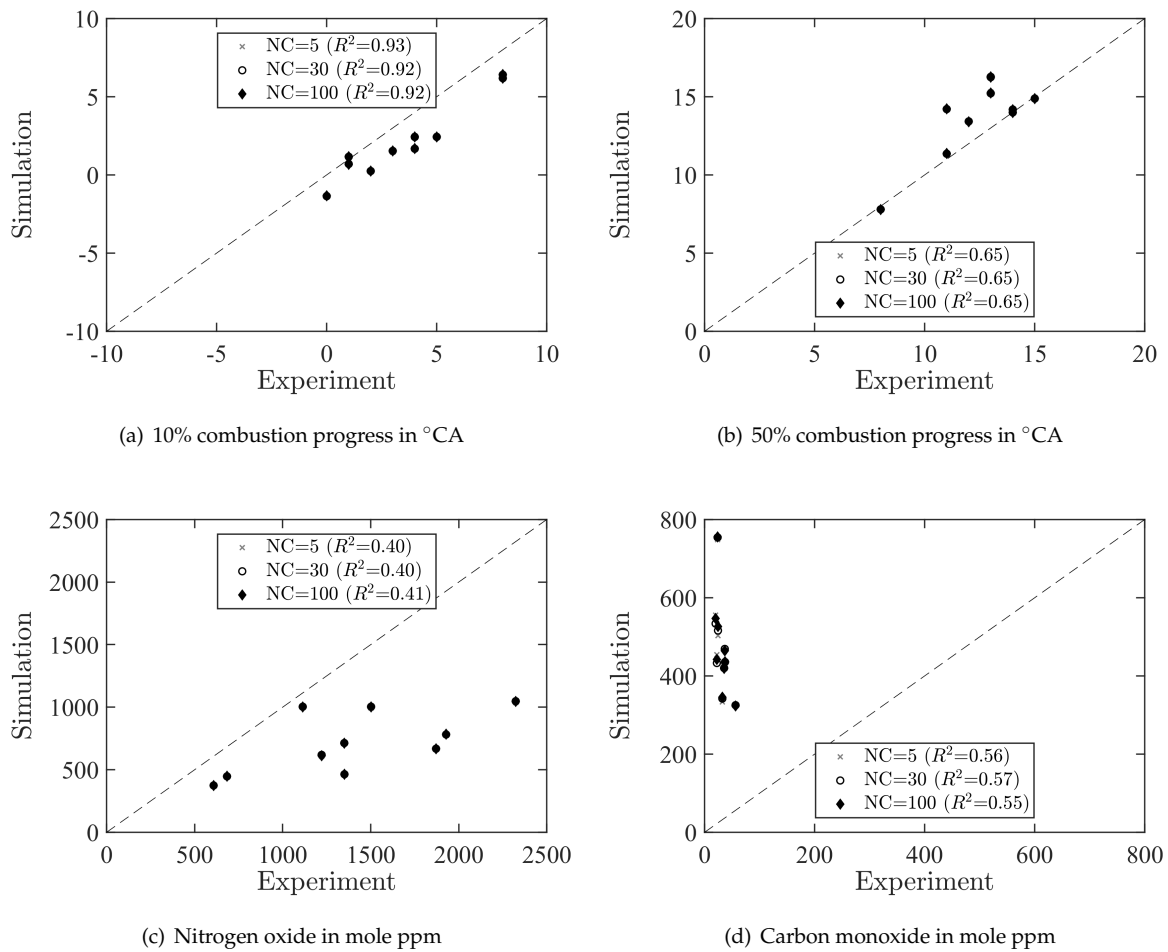


Figure 112: Validation results of design ID 2707 for Engine D.

The simulation results of OP5 and OP10 are investigated more in detail and the cylinder pressure and heat release rate are shown in figure 113. Both cases show a lower predicted maximum cylinder pressure and the combustion duration is longer compared to the experiments. The differences are a result of the inactive gas exchange model wherefor the influence of inflowing mass for turbulent kinetic energy and swirl angular momentum production is not captured. Therefore, the length scale parameter C_{ε_1} of the large-bore engine case *Engine D* is adjusted* to get a better match of the cylinder pressure and heat release rate to investigate the impact on NO_x and CO engine-out emission prediction.

The simulation results for OP5 and OP10 with the modified C_{ε_1} parameter show an improvement of the cylinder pressure and heat release rate. For both operating points the maximum cylinder pressure is closely match and the burn HRR duration matches with the experiments.

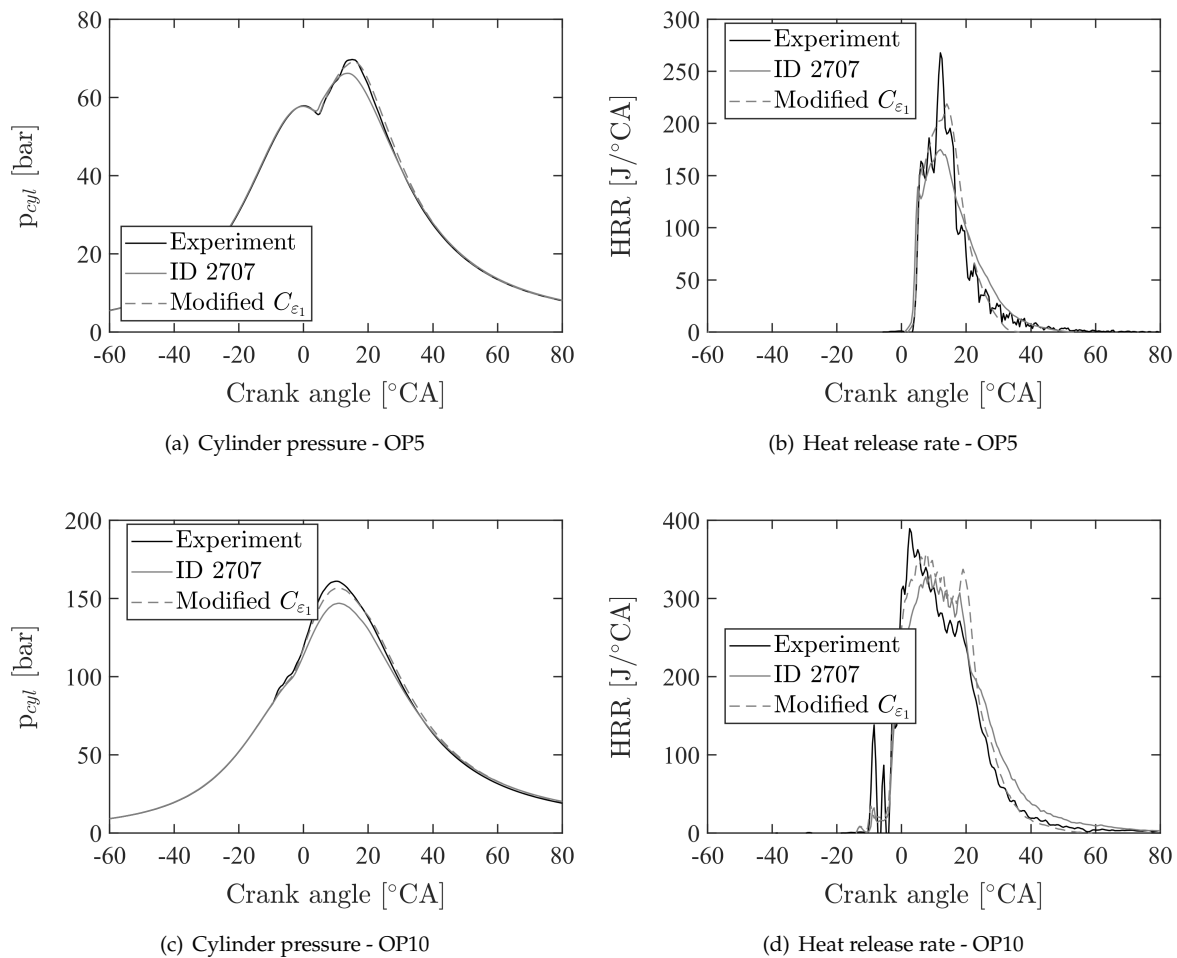


Figure 113: Predicted cylinder pressure and heat release rate of OP5 and OP10 of Engine D.

Reviewing the simulation results in figure 114 of all operating points with modified C_{ε_1} parameter shows an improved match of the 50% combustion progress, NO_x and CO engine out emissions. However, the emissions still differ significantly from the experiments even though the combustion shows a better agreement. For NO_x emissions, especially the operating points with high concentrations in the experiments are under-predicted by the DI-SRM simulation.

*The value of C_{ε_1} is increased from 7 to 9.

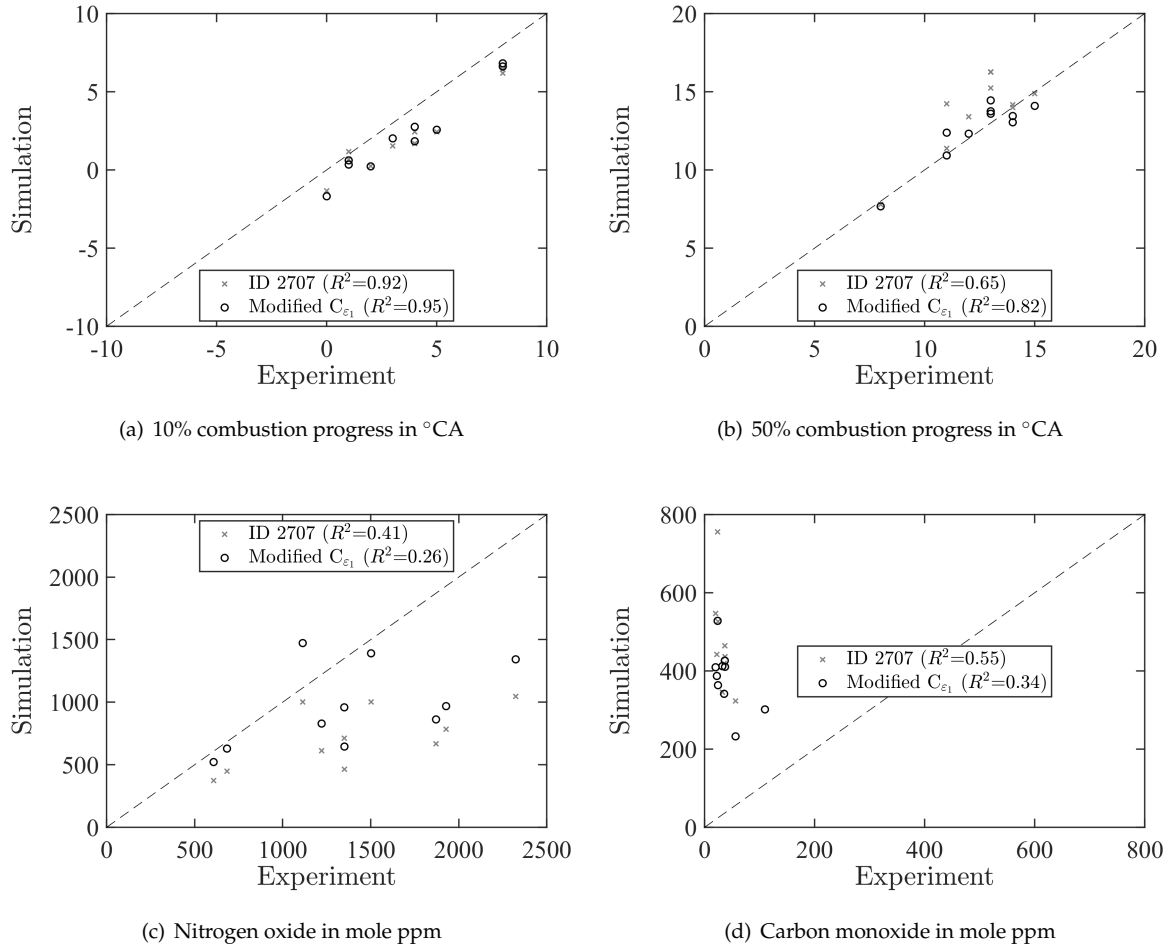


Figure 114: Simulation results of design ID 2707 with modified C_{ϵ_1} parameter for Engine D.

7.7 Conclusions for compression ignition engine model optimization

The DI-SRM presented in section 4.4 is implemented into the multi-objective optimization platform from section 5 and validated for a small-bore and large-bore engine case. The best practice optimization setup comprises the FAST NSGA-II algorithm with 1500 designs evaluated in total. The selection of designs from the Pareto solutions is done using the MCDM. The best practice DI-SRM setup consists of 200 notional particles and 0.5°CA time step size. To determine statistically stable mean results of soot mass 100 stochastic cycles are simulated.

The best performing training procedure included sixteen operating points distributed over the whole engine operation range. The injection strategy of the different operating conditions include up to two pilot injections and for some cases one post injection. It is found that decreasing the number of training points showed no negative impact on the prediction of combustion progress while NO_x emission prediction was diminished. The parameterization of the ΔSOV using equation (9.3) allowed to account for the vaporization delay for different operating conditions.

The soot mass optimization is performed for the small-bore engine case *Engine C*. The optimized $k - \epsilon$ model parameters are used and the soot model source term parameters

of particle inception, surface growth, oxidation by OH and O₂ are optimized. Following, the validation set is tested for different number of stochastic cycles which showed that the standard deviation of soot mass is decreasing with increasing number of stochastic cycles. To obtain a statistical stable result of the mean soot mass 100 stochastic cycles are calculated. The validation of *Engine D* showed larger deviations for combustion progress and engine out emissions. For *Engine D* no experimental data for the intake and exhaust manifold model was available wherefor the gas exchange model from section 4.2.4 is not used. This did not allow to transfer the optimized $k - \epsilon$ model parameters from *Engine C* because the turbulent kinetic energy and angular momentum production due to intake flow is not calculated. The turbulent length scale parameter C_{ϵ_1} is adjusted to obtain an improved match of the combustion progress, however the NO_x emissions are still under-predicted and the CO emissions are still over-predicted by the DI-SRM.

8 Conclusions and Outlook

This thesis summarizes the author's developments in the area of $k - \epsilon$ turbulence models for the prediction of turbulent length and time scales in 0D SRM, and multi-objective optimization methods for automatic model training. The performance of the newly implemented models for the prediction of combustion processes and emission formation was demonstrated for SI and CI engines. Finally, the performance of the developed optimization platform for automated model training is demonstrated for multiple operating points of the engine map. The **convective heat transfer model** in 0D SRM is extended by a term that considers the influence of turbulent scales. Furthermore, a stochastic algorithm describing the influence of turbulence on heat loss is implemented. The models are validated using DNS simulations for temperature stratification in an engine-like geometry. An increase in turbulent kinetic energy leads to higher convective heat loss. The temperature distribution during the compression stroke is in good approximation with the DNS results.

The **injection and vaporization model** was extended by a stochastic algorithm that randomly distributes the injected liquid fuel mass among the notional particles in the cylinder. During the early phase of injection, the ϕ -distribution predicted by the 0D SRM deviates from the 3D CFD RANS results, and is shifted to lean mixtures. The differences are due to a delayed evaporation rate of the injected fuel mass in the 0D SRM. During the compression stroke, the ϕ -distribution converges to the 3D CFD RANS simulation, and at spark ignition, both solutions are close.

The **gas exchange through the valves** is modeled in the 0D SRM using the experimental data of pressure and temperature in the intake manifold and exhaust manifold. The calculated mass flow through the inlet valves agrees well with the 3D CFD RANS results. Backflow of mass through the exhaust valves into the cylinder predicted by 3D CFD RANS is not captured by the 0D SRM. The gas exchange through the valves was coupled with the newly implemented $k - \epsilon$ turbulence model, so that it creates a tumble flow motion and leads to the generation of turbulent kinetic energy during the compression and combustion phases.

The **$k - \epsilon$ turbulence model for SI engines** was implemented in 0D SRM to predict the turbulent length and time scales for different operating points. The model considers the influence of valve flow, axial flow, direct injection, and tumble decay on turbulent kinetic energy generation. The tumble flow motion is described by the angular momentum generated by the valve flows, which decays into turbulent kinetic energy due to shear forces and wall friction forces in the cylinder. The 0D SRM simulation results were compared with 3D CFD RANS results and show good agreement. The $k - \epsilon$ turbulence model is able to predict the change in turbulent time and length scales for different operating conditions.

The **turbulent flame propagation model** of Peters was implemented in 0D SRM, which is valid for flames in the corrugated and thin reaction zone regime. The input parameters for turbulence fluctuation and turbulent length scale are calculated using the $k - \epsilon$ turbulence model. The model was extended to include a **flame propagation model for early flames**, which describes the transition from laminar to turbulent flame propagation as a function of the turbulent time and length scales. The model is able to accurately predict combustion in

gasoline engines for various operating conditions, including lean mixtures. In addition, a **stochastic algorithm** has been implemented to account for the ϕ -distribution in mass transfer between the unburnt and burnt zones. The algorithm allows the calculation of premixed and partially premixed flames.

A source of unburned hydrocarbons is considered by applying a **crevice model** that calculates the volume of the crevice as 2-4% of the cylinder volume. The mass enclosed in the crevice is calculated based on the ideal gas law. Here, the enclosed mass depends on the pressure difference and the turbulent kinetic energy. As the turbulent kinetic energy increases, more mass of unburned hydrocarbons is transported into the crevice. This is based on the assumption that a high turbulent kinetic energy correlates with a strong flow motion toward the piston crevice, which traps more unburned hydrocarbons in the crevice. As a result, the crevice model increases the mass of unburned hydrocarbons, which means that the results of the 0D SRM are in good agreement with the experiments.

The strong cycle variations of cylinder pressure in gasoline engines are accounted for by a *pdf*-based **cyclic variation model**. The model assigns a normally distributed random number for the turbulence variation and the ignition timing. Through this variation, faster or slower firing cycles can be calculated in the 0D SRM. The experimentally measured standard deviation of the maximum cylinder pressure and crank angle is predicted by the model to a good approximation.

The $k - \epsilon$ **turbulence model for CI engines** was implemented in 0D SRM to calculate the generation of turbulent kinetic energy and dissipation for different operating points over the engine map. The model considers the influence of valve flow, axial flow, direct injection, secondary flows in the piston bowl, and swirl flow on the generation of turbulent kinetic energy in the cylinder. The motion of the swirl flow is described by the angular momentum generated by the valve flow, which is amplified by the displacement into the piston bowl during the compression stroke. The shear forces and wall friction forces occurring in the cylinder cause the angular momentum to decay and generate turbulent kinetic energy.

The optimal 0D SRM parameters are determined using the developed **multi-objective optimization platform**. Several genetic and heuristic algorithms were tested to determine the most reliable optimization method. The tested heuristic algorithms are based on the particle swarm method (MOPSO) and the simulated annealing method (MOSA). They show good performance in finding the best Pareto front, exhibiting a diverse distribution of solutions. The genetic algorithms tested are based on the Non-domination Sorting Method (NSGA-II) and the Multi-objective Method (MOGA-II). They show a stronger formation of clusters which is why the solution space is not always evenly covered. The coupling of the RSM-based optimization (FAST) with the genetic algorithm NSGA-II shows a good performance in finding the best Pareto front, with a diverse distribution of solutions. Thus, the FAST NSGA-II algorithm was selected to find the best set of model parameters for 0D SRM. To systematize the selection of solutions from the Pareto front, a multi-criteria decision maker was implemented.

The **0D SRM for SI engines** is trained for a single-cylinder research engine and validated for another single-cylinder research engine. The trained 0D SRM is able to accurately predict

the combustion characteristics of the studied engines, with a correlation factor between $0.98 < R^2 < 0.99$. The prediction of NO_x and CO emissions shows some larger deviations ($R^2 \approx 0.7$). In particular, for the second single-cylinder research engine, the predicted CO and HC emissions are significantly lower compared to the experiments. The reason for the increased measured CO and HC emissions is attributed to a strong spray-wall interaction and evaporation of the liquid wall film during the expansion stroke.

The **0D SRM for CI engines** is trained for a passenger car engine and validated for an additional heavy duty engine. The trained 0D SRM is able to predict the combustion center of the studied engines in a good approximation with a correlation coefficient between $0.67 < R^2 < 0.82$. The 10% combustion advance is predicted too early for low load operating points. CO emissions are predicted too high for high load operating point, indicating that mixture formation is not well predicted. NO_x emissions show good agreement with experiments ($R^2 = 0.89$). Optimization of the soot model parameters shows an improvement in the prediction of the fuel-specific soot mass and the results are in good approximation to the experiments. The trend of soot mass is well matched by the model for most of the operating points, but some operating points show larger deviations. The soot mass predicted by the 0D SRM shows a dependence on the number of calculated stochastic cycles. To achieve a stable prediction of the mean soot mass, 100 stochastic cycles are calculated.

In the future, work will be done on merging the two **$k - \varepsilon$ turbulence models** for SI and CI engines to obtain a general model. This will make it possible to increase the physical significance of the turbulence model by providing a unified definition of the turbulent time and length scales. Furthermore, it will be possible to implement new angular momentum flow terms that can compute mixed swirling and tumbling motions. In addition, the **explicit Runge-Kutta solver** will be extended to include an algorithm that improves convergence at large operator split time steps relevant to real-time simulation.

The simplified stochastic vaporization model is replaced by a **detailed physical vaporization model** that takes into account the multiphase mass transfer of liquid droplets and the distribution of the spray into the cylinder. The information about the distribution of liquids and vapors in the cylinder is needed to implement models that account for the formation of a **wall film** and the interaction between the spray and the piston crevice. The latter is required for the **extension of the crevice model**. In the new model, the rotational speed of the tumble, the penetration depth of the spray and the piston position are related to each other to determine the probability with which unburned hydrocarbons are pushed into the piston crevice. A model for calculating the wall film allows another source of unburned hydrocarbons and soot mass in SI engines to be taken into account.

The onset of flame propagation is predicted using a **spark ignition model** that accounts for discharge energy and discharge duration. The initial mass burned is predicted based on the physical properties of the fuel and the discharge energy. The subsequent flame propagation is calculated by a new model that determines the flame propagation of the individual notional particles. The new model will thus be able to account for **inhomogeneities of the flame front** that lead to different turbulent flame propagation velocities.

9 Appendix

9.1 Thermodynamic polynomials

Heat capacity

$$\frac{c_p(T)}{R} = \left(A_1 + A_2 \cdot \ln(T) + A_3 \cdot T + \frac{A_4}{T^2} \right) \quad (9.1)$$

Enthalpy

$$\frac{H(T)}{R} = \left(A_5 + (A_1 - A_2) \cdot T + A_2 \cdot T \cdot \ln(T) + \frac{1}{2} A_3 \cdot T^2 - \frac{A_4}{T} \right) \quad (9.2)$$

Entropy

$$\frac{S(T)}{R} = \left(A_6 + A_1 \cdot \ln(T) + \frac{1}{2} A_2 \cdot \ln(T)^2 + A_3 \cdot T - \frac{1}{2} \frac{A_4}{T^2} \right) \quad (9.3)$$

9.2 Cylinder wall temperature correlation function

The correlation function in equation (9.4) for the wall temperature of cylinder liner, head and piston is developed based on the work of Barra [116]. Further, experimental measurement data of a single-cylinder spark ignition engine from the FVV project “Water injection in SI engines” [117] is used to investigate the performance of the model.

$$T_{w,i} = (B_1 \cdot T_{oil} + B_2) \cdot \left(T_{w,0,i} + B_3 \cdot \left(n^{B_4} + m_f^{B_5} + |\theta_{SOI}|^{B_6} \right) \right) \quad (9.4)$$

Therein, i is a counter for the cylinder area (liner, head, piston), T_{oil} is the oil temperature, $T_{w,0,i}$ is a default wall temperature, n is the engine speed, m_f is the injected fuel mass and SOI is the start of injection. The values of the parameters $B_1 - B_6$ are given in the table 45. The transient change of wall temperature during the engine cycle is neglected.

Parameter	Unit	Value
B_1	$\frac{1}{K}$	0.00128
B_2	—	0.535
B_3	—	0.008
B_4	—	1.0
B_5	—	2.2
B_6	—	1.5
$T_{w,0,liner}$	K	390
$T_{w,0,head}$	K	430
$T_{w,0,piston}$	K	430

Table 45: Cylinder wall temperature correlation function parameters for a warm engine.

The calculated wall temperatures for the training and validation points of *Engine A* are outlined in figure 115.

The calculated wall temperatures for the validation points of *Engine B* are outlined in figure 116.

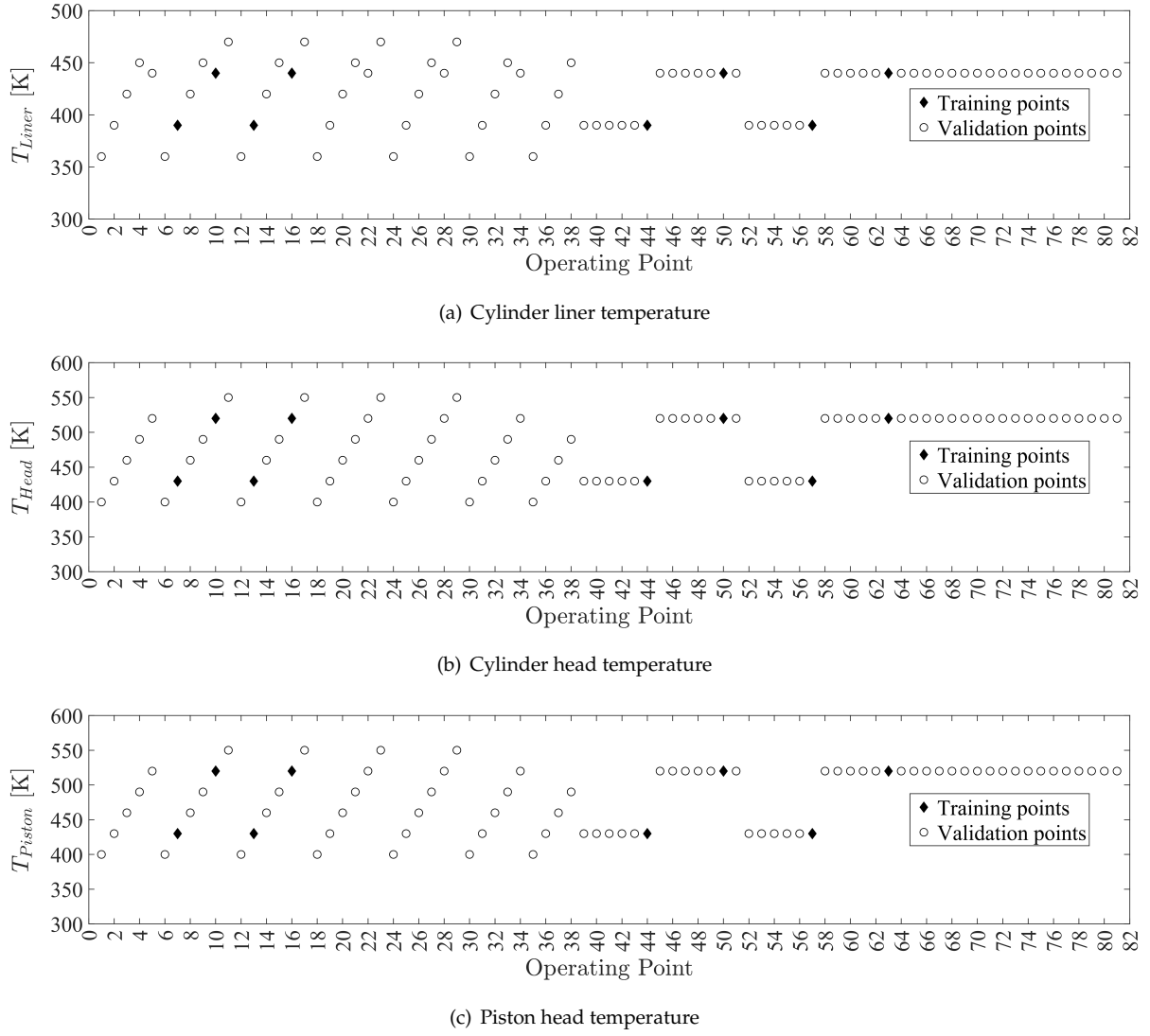


Figure 115: Calculated wall temperatures of cylinder liner, head and piston head of Engine A.

9.3 Start of vaporization correction function

The correction function of $\Delta\theta_{SOV}$ is introduced to account for the time delay of fuel vaporization of direct injection Diesel engines. The stochastic vaporization model introduced in section 4.2.3 underpredicts the vaporization delay wherefor the correction is applied.

$$\Delta\theta_{SOV} = B_1 + B_2 \cdot n + B_3 \cdot (0.06 \cdot m_f)^{3/2} \cdot \exp\left(-1 \cdot (0.06 \cdot m_f)^{5/2}\right) \cdot \sqrt{\frac{1}{n}} \quad (9.5)$$

Therein, B_1 , B_2 and B_3 are model parameters which can be adjusted, n is the engine speed and m_f is the injection fuel mass.

9.4 Early flame propagation correlation function

The correlation function η_c^* estimates the correction parameter η_c of the early flame propagation model in section 4.3.2 based on the equivalence ratio ϕ , injected fuel mass m_f and compression ratio ε_{CR} .

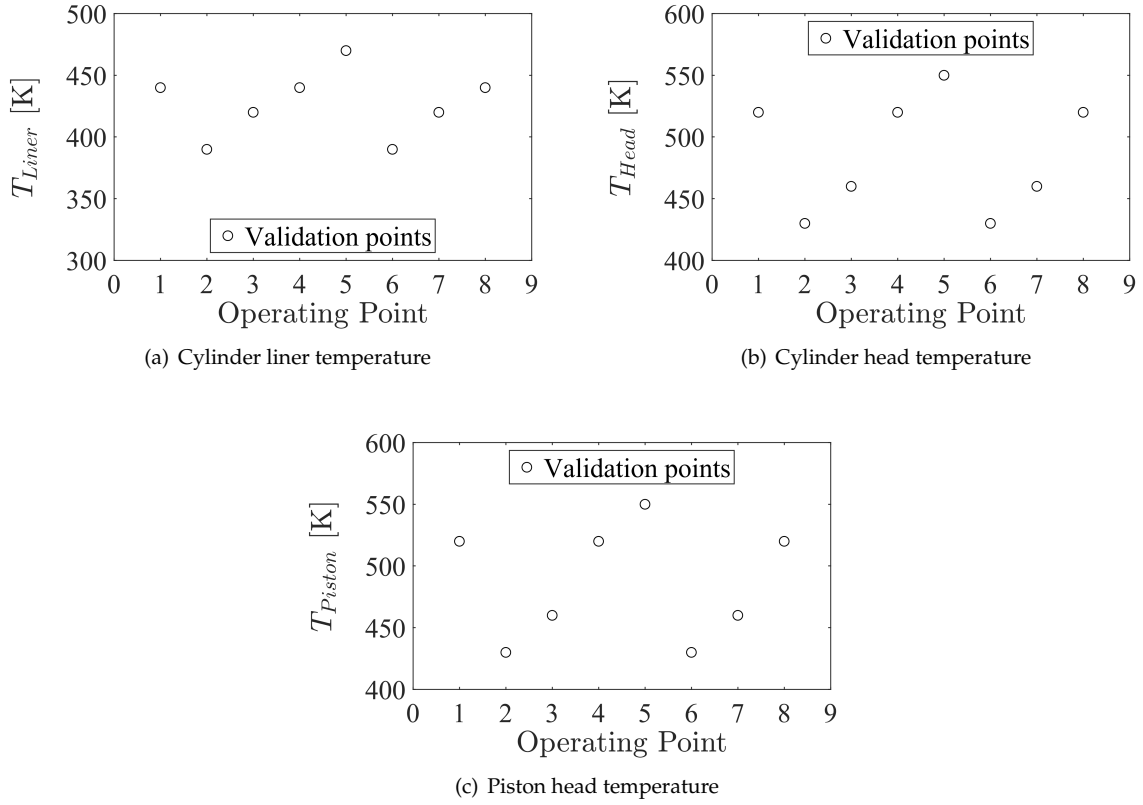


Figure 116: Calculated wall temperatures of cylinder liner, head and piston head of Engine B.

$$\eta_c = B_1 + B_2 \cdot \phi^2 + B_3 \cdot \frac{1}{m_f} + B_4 \cdot \phi \cdot m_f + B_5 \cdot \varepsilon_{CR} \quad (9.6)$$

Therein, B_1 , B_2 , B_3 , B_4 and B_5 are model parameters which can be adjusted.

9.5 Piston speed

The mean piston speed c_m is calculated according to equation (9.7). Therein, h_s is the stroke and n is the engine speed.

$$c_m = 2 \cdot h_s \cdot \frac{n}{60} \quad (9.7)$$

The instantaneous piston speed c_{pis} can be calculated based on the mean piston speed. θ is the current crank angle, l_{rod} is the connecting rod length and h_s is the stroke.

$$c_{pis} = c_m \cdot \frac{\pi}{2} \cdot \sin(\theta) \cdot \left(1 + \left(\frac{\cos(\theta)}{\sqrt{\frac{l_{rod}}{2 \cdot h_s}}} \right)^2 - \sin^2(\theta) \right) \quad (9.8)$$

9.6 Tumble ratio

The tumble ratio T is defined as the ratio of tumble rotation speed n_T and engine speed n .

$$T = \frac{n_T}{n} \quad (9.9)$$

The tumble rotation speed n_T is determined by the angular momentum L_T and the moment of inertia J_T .

$$n_T = \frac{1}{2\pi} \cdot \frac{L_T}{J_T} \quad (9.10)$$

The momentum of inertia J_T of the cylinder is calculated according to the following equation.

$$J_T = m_g \cdot \left(\frac{1}{4} \cdot \left(\frac{d_B}{2} \right)^2 + \frac{1}{12} \cdot H_1^2 \right) \quad (9.11)$$

9.7 Swirl ratio

The swirl ratio S is defined as the ratio of swirl rotation speed n_S and engine speed n .

$$S = \frac{n_S}{n \cdot 60} \quad (9.12)$$

The swirl rotation speed n_S is determined by the angular momentum L_S and the moment of inertia J_S .

$$n_S = \frac{1}{2 \cdot \pi} \cdot \frac{L_S}{J_S} \quad (9.13)$$

The momentum of inertia J_S of the cylinder is calculated according to the following equation.

$$J_S = \pi \cdot \frac{\rho}{32} \cdot \left(H_1 \cdot d_B^4 + h_{bowl} \cdot d_{bowl}^4 \right) \quad (9.14)$$

9.8 Uniformity measure

The uniformity measure is defined according to Montrone et al. [70].

Given a dataset of n points in a d -dimensional space

$$\mathcal{D} = \{x_i | i = 1, \dots, n\} \quad (9.15)$$

for each point x_i one can denote the minimum distance from all other points as q_i

$$q_i = \min_{\forall j \neq i} \{ \|x_i - x_j\| \} \quad (9.16)$$

Considering the whole set of minimum distances

$$\mathcal{Q} = \{q_i | i = 1, \dots, n\} \quad (9.17)$$

the uniformity measure $U_{\mathcal{D}}$ is the median value of this set

$$U_{\mathcal{D}} = \tilde{Q} \quad (9.18)$$

For a fixed number of points, the higher the value of the uniformity measure, the better the uniformity of points.

9.9 3D CFD simulation setup

The 3D CFD simulations are performed for *Engine A* using the CFD code Converge v2.4 [118]. The selected CFD models are outlined in table 46 and references to the original publications are provided in the table as well. More simulation results on the 3D CFD simulation can be found in [92]. Details on the spray model setup can be found in [103]. Details on the combustion model setup can be found in [95].

Model	Unit	Parameter
Base grid size (x,y,z)	mm	2, 2, 2
Adaptive mesh refinement	–	Temperature, velocity, species
Fixed embedding	–	Cylinder, valves and spark
Minimum grid size	mm	0.125 (around spark)
Wall-film model	–	O'Rourke [119]
Collision model	–	NTC [120]
Evaporation model	–	Frossling with boiling model [121]
Liquid mass diffusivity of iso-octane	–	$D_0=7.9E-6 \frac{m^2}{s}$, $n=1.87$ [118]
Initial droplet size distribution	–	Rosin-Rammler ($q_{rr}=5.5$) [122]
Break-up model	–	Kelvin-Helmholtz and Rayleigh-Taylor [123]
Flame propagation	–	G-Equation with CEQ solver in the reaction zone [3, 124, 125]
Laminar flame speed	–	Same look-up table as for SI-SRM
Turbulent flame speed	–	Peters model [3]
Unburnt / burnt zone	–	SAGE with detailed chemistry [126]
Reaction mechanism	–	see section 6.4
Spark model	–	Initialize passive scalar of G-Equation model
Turbulence model	–	RNG $k - \epsilon$ [127]

Table 46: 3D CFD model settings.

9.10 Liquid thermophysical properties

p_s [Pa]	T_s [K]	H_v [J/kg]	p_s [Pa]	T_s [K]	H_v [J/kg]
3.308200E+0	2.000000E+2	3.575500E+5	2.082000E+5	4.000000E+2	2.509200E+5
1.056200E+1	2.100000E+2	3.521600E+5	2.629600E+5	4.100000E+2	2.441500E+5
2.986900E+1	2.200000E+2	3.468700E+5	3.280400E+5	4.200000E+2	2.370100E+5
7.608000E+1	2.300000E+2	3.416600E+5	4.046200E+5	4.300000E+2	2.294700E+5
1.769900E+2	2.400000E+2	3.365400E+5	4.939500E+5	4.400000E+2	2.214700E+5
3.804900E+2	2.500000E+2	3.314800E+5	5.973300E+5	4.500000E+2	2.129400E+5
7.633100E+2	2.600000E+2	3.264800E+5	7.161300E+5	4.600000E+2	2.037900E+5
1.440900E+3	2.700000E+2	3.215200E+5	8.518000E+5	4.700000E+2	1.939000E+5
2.577800E+3	2.800000E+2	3.165700E+5	1.005900E+6	4.800000E+2	1.831100E+5
4.397200E+3	2.900000E+2	3.116300E+5	1.180000E+6	4.900000E+2	1.712100E+5
7.190000E+3	3.000000E+2	3.066700E+5	1.376100E+6	5.000000E+2	1.578800E+5
1.132100E+4	3.100000E+2	3.016700E+5	1.596400E+6	5.100000E+2	1.425800E+5
1.723500E+4	3.200000E+2	2.966100E+5	1.843300E+6	5.200000E+2	1.243600E+5
2.545700E+4	3.300000E+2	2.914600E+5	2.120500E+6	5.300000E+2	1.010300E+5
3.659400E+4	3.400000E+2	2.862000E+5	2.433400E+6	5.400000E+2	6.363100E+4
5.133200E+4	3.500000E+2	2.808100E+5	2.553900E+6	5.500000E+2	2.934200E+4
7.043500E+4	3.600000E+2	2.752600E+5	2.653900E+6	5.600000E+2	0.000000E+0
9.473900E+4	3.700000E+2	2.695300E+5			
1.251500E+5	3.800000E+2	2.635800E+5			
1.626300E+5	3.900000E+2	2.573900E+5			

Table 47: Liquid vapor saturation pressure, temperature and heat of vaporization of iso-Octane [128].

p_s [Pa]	T_s [K]	H_v [J/kg]	p_s [Pa]	T_s [K]	H_v [J/kg]
2.142400E+0	2.000000E+2	4.290700E+5	2.180400E+5	4.000000E+2	2.950900E+5
7.265500E+0	2.100000E+2	4.220100E+5	2.772900E+5	4.100000E+2	2.868500E+5
2.165300E+1	2.200000E+2	4.151200E+5	3.481300E+5	4.200000E+2	2.782000E+5
5.774500E+1	2.300000E+2	4.083900E+5	4.319400E+5	4.300000E+2	2.690500E+5
1.398700E+2	2.400000E+2	4.017900E+5	5.302100E+5	4.400000E+2	2.593500E+5
3.116000E+2	2.500000E+2	3.953100E+5	6.444900E+5	4.500000E+2	2.489800E+5
6.451500E+2	2.600000E+2	3.889200E+5	7.764200E+5	4.600000E+2	2.378100E+5
1.252500E+3	2.700000E+2	3.826000E+5	9.277600E+5	4.700000E+2	2.256900E+5
2.297300E+3	2.800000E+2	3.763400E+5	1.100400E+6	4.800000E+2	2.123800E+5
4.007200E+3	2.900000E+2	3.701000E+5	1.296300E+6	4.900000E+2	1.975600E+5
6.684500E+3	3.000000E+2	3.638600E+5	1.517900E+6	5.000000E+2	1.807400E+5
1.071600E+4	3.100000E+2	3.575900E+5	1.767700E+6	5.100000E+2	1.610900E+5
1.657900E+4	3.200000E+2	3.512600E+5	2.049100E+6	5.200000E+2	1.369900E+5
2.484700E+4	3.300000E+2	3.448600E+5	2.366300E+6	5.300000E+2	1.042400E+5
3.619000E+4	3.400000E+2	3.383400E+5	2.727900E+6	5.400000E+2	2.210300E+4
5.137400E+4	3.500000E+2	3.316700E+5	2.827900E+6	5.500000E+2	0.000000E+0
7.125900E+4	3.600000E+2	3.248400E+5			
9.679500E+4	3.700000E+2	3.178000E+5			
1.290100E+5	3.800000E+2	3.105200E+5			
1.690300E+5	3.900000E+2	3.029600E+5			

Table 48: Liquid vapor saturation pressure, temperature and heat of vaporization of n-Heptane [128].

p_s [Pa]	T_s [K]	H_v [J/kg]	p_s [Pa]	T_s [K]	H_v [J/kg]
1.083300E+0	2.000000E+2	4.754600E+5	2.562200E+5	4.200000E+2	3.354400E+5
3.763200E+0	2.100000E+2	4.683600E+5	3.207500E+5	4.300000E+2	3.278500E+5
1.147900E+1	2.200000E+2	4.614900E+5	3.969800E+5	4.400000E+2	3.199400E+5
3.131400E+1	2.300000E+2	4.548200E+5	4.861900E+5	4.500000E+2	3.116500E+5
7.754200E+1	2.400000E+2	4.483200E+5	5.897400E+5	4.600000E+2	3.029400E+5
1.764900E+2	2.500000E+2	4.419800E+5	7.090500E+5	4.700000E+2	2.937500E+5
3.731200E+2	2.600000E+2	4.357600E+5	8.455900E+5	4.800000E+2	2.840200E+5
7.392300E+2	2.700000E+2	4.296600E+5	1.000900E+6	4.900000E+2	2.736500E+5
1.382900E+3	2.800000E+2	4.236300E+5	1.176600E+6	5.000000E+2	2.625500E+5
2.458600E+3	2.900000E+2	4.176800E+5	1.374500E+6	5.100000E+2	2.505800E+5
4.177400E+3	3.000000E+2	4.117600E+5	1.596400E+6	5.200000E+2	2.375900E+5
6.816500E+3	3.100000E+2	4.058600E+5	1.844400E+6	5.300000E+2	2.233200E+5
1.072700E+4	3.200000E+2	3.999600E+5	2.120700E+6	5.400000E+2	2.074700E+5
1.634000E+4	3.300000E+2	3.940300E+5	2.427900E+6	5.500000E+2	1.895400E+5
2.417000E+4	3.400000E+2	3.880500E+5	2.769100E+6	5.600000E+2	1.687400E+5
3.482100E+4	3.500000E+2	3.820000E+5	3.147900E+6	5.700000E+2	1.436200E+5
4.898000E+4	3.600000E+2	3.758500E+5	3.568800E+6	5.800000E+2	1.106900E+5
6.741800E+4	3.700000E+2	3.695700E+5	4.038500E+6	5.900000E+2	5.056300E+4
9.098800E+4	3.800000E+2	3.631500E+5	4.088500E+6	6.000000E+2	3.529300E+4
1.206200E+5	3.900000E+2	3.565500E+5	4.188500E+6	6.100000E+2	0.000000E+0
1.573100E+5	4.000000E+2	3.497500E+5			
2.021400E+5	4.100000E+2	3.427200E+5			

Table 49: Liquid vapor saturation pressure, temperature and heat of vaporization of Toluene [128].

p_s [Pa]	T_s [K]	H_v [J/kg]	p_s [Pa]	T_s [K]	H_v [J/kg]
1.101800E+0	2.000000E+2	1.008500E+6	5.236800E+5	4.000000E+2	7.516600E+5
4.145600E+0	2.100000E+2	1.000300E+6	6.945200E+5	4.100000E+2	7.259000E+5
1.369400E+1	2.200000E+2	9.921100E+5	9.063600E+5	4.200000E+2	6.979600E+5
4.040400E+1	2.300000E+2	9.838500E+5	1.165300E+6	4.300000E+2	6.677200E+5
1.080400E+2	2.400000E+2	9.754600E+5	1.477600E+6	4.400000E+2	6.350700E+5
2.649900E+2	2.500000E+2	9.668900E+5	1.849900E+6	4.500000E+2	5.998600E+5
6.022900E+2	2.600000E+2	9.580600E+5	2.289000E+6	4.600000E+2	5.617000E+5
1.279500E+3	2.700000E+2	9.489100E+5	2.802300E+6	4.700000E+2	5.198600E+5
2.559700E+3	2.800000E+2	9.393500E+5	3.397600E+6	4.800000E+2	4.728700E+5
4.852900E+3	2.900000E+2	9.292900E+5	4.083900E+6	4.900000E+2	4.176400E+5
8.767900E+3	3.000000E+2	9.186400E+5	4.871900E+6	5.000000E+2	3.461600E+5
1.516900E+4	3.100000E+2	9.072700E+5	5.776700E+6	5.100000E+2	2.211800E+5
2.523800E+4	3.200000E+2	8.950600E+5	6.187500E+6	5.200000E+2	7.161900E+4
4.053100E+4	3.300000E+2	8.818900E+5	6.287500E+6	5.300000E+2	0.000000E+0
6.303300E+4	3.400000E+2	8.676400E+5			
9.520700E+4	3.500000E+2	8.521600E+5			
1.400300E+5	3.600000E+2	8.353400E+5			
2.009900E+5	3.700000E+2	8.170200E+5			
2.821500E+5	3.800000E+2	7.970700E+5			
3.880300E+5	3.900000E+2	7.753300E+5			

Table 50: Liquid vapor saturation pressure, temperature and heat of vaporization of Ethanol [128].

p_s [Pa]	T_s [K]	H_v [J/kg]	p_s [Pa]	T_s [K]	H_v [J/kg]
9.0445E-04	1.6000E+02	5.1572E+05	7.6723E+04	3.6000E+02	3.8074E+05
8.8144E-03	1.7000E+02	5.1007E+05	1.0639E+05	3.7000E+02	3.7223E+05
6.1632E-02	1.8000E+02	5.0433E+05	1.4468E+05	3.8000E+02	3.6344E+05
3.3084E-01	1.9000E+02	4.9850E+05	1.9331E+05	3.9000E+02	3.5436E+05
1.4340E+00	2.0000E+02	4.9258E+05	2.5413E+05	4.0000E+02	3.4497E+05
5.2154E+00	2.1000E+02	4.8657E+05	3.2914E+05	4.1000E+02	3.3522E+05
1.6395E+01	2.2000E+02	4.8046E+05	4.2049E+05	4.2000E+02	3.2508E+05
4.5600E+01	2.3000E+02	4.7424E+05	5.3043E+05	4.3000E+02	3.1451E+05
1.1433E+02	2.4000E+02	4.6791E+05	6.6133E+05	4.4000E+02	3.0344E+05
2.6231E+02	2.5000E+02	4.6146E+05	8.1566E+05	4.5000E+02	2.9181E+05
5.5750E+02	2.6000E+02	4.5490E+05	9.9593E+05	4.6000E+02	2.7953E+05
1.1088E+03	2.7000E+02	4.4820E+05	1.2047E+06	4.7000E+02	2.6648E+05
2.0810E+03	2.8000E+02	4.4137E+05	1.4447E+06	4.8000E+02	2.5254E+05
3.7117E+03	2.9000E+02	4.3440E+05	1.7184E+06	4.9000E+02	2.3748E+05
6.3288E+03	3.0000E+02	4.2728E+05	2.0285E+06	5.0000E+02	2.2104E+05
1.0369E+04	3.1000E+02	4.1999E+05	2.3776E+06	5.1000E+02	2.0280E+05
1.6393E+04	3.2000E+02	4.1254E+05	2.7684E+06	5.2000E+02	1.8207E+05
2.5103E+04	3.3000E+02	4.0490E+05	3.2032E+06	5.3000E+02	1.5761E+05
3.7355E+04	3.4000E+02	3.9706E+05	3.6847E+06	5.4000E+02	1.2665E+05
5.4166E+04	3.5000E+02	3.8902E+05	4.2152E+06	5.5000E+02	7.9339E+04

Table 51: Liquid vapor saturation pressure, temperature and heat of vaporization of RON95E10 [128].

p_s [Pa]	T_s [K]	H_v [J/kg]	p_s [Pa]	T_s [K]	H_v [J/kg]
2.8673E+00	250.00	3.8874E+05	8.3911E+04	440.00	2.8104E+05
7.9180E+00	260.00	3.8282E+05	1.0855E+05	450.00	2.7462E+05
1.9993E+01	270.00	3.7700E+05	1.3855E+05	460.00	2.6797E+05
4.6638E+01	280.00	3.7126E+05	1.7465E+05	470.00	2.6107E+05
1.0141E+02	290.00	3.6560E+05	2.1767E+05	480.00	2.5387E+05
2.0709E+02	300.00	3.6001E+05	2.6846E+05	490.00	2.4633E+05
3.9985E+02	310.00	3.5447E+05	3.2790E+05	500.00	2.3841E+05
7.3415E+02	320.00	3.4898E+05	3.9696E+05	510.00	2.3004E+05
1.2883E+03	330.00	3.4353E+05	4.7664E+05	520.00	2.2115E+05
2.1704E+03	340.00	3.3809E+05	5.6801E+05	530.00	2.1165E+05
3.5240E+03	350.00	3.3266E+05	6.7222E+05	540.00	2.0142E+05
5.5338E+03	360.00	3.2722E+05	7.9054E+05	550.00	1.9028E+05
8.4305E+03	370.00	3.2175E+05	9.2432E+05	560.00	1.7803E+05
1.2495E+04	380.00	3.1623E+05	1.0751E+06	570.00	1.6431E+05
1.8060E+04	390.00	3.1065E+05	1.2447E+06	580.00	1.4862E+05
2.5513E+04	400.00	3.0498E+05	1.4353E+06	590.00	1.3004E+05
3.5300E+04	410.00	2.9921E+05	1.6497E+06	600.00	1.0673E+05
4.7917E+04	420.00	2.9331E+05	1.8918E+06	610.00	7.3445E+04
6.3919E+04	430.00	2.8726E+05			

Table 52: Liquid vapor saturation pressure, temperature and heat of vaporization of n-Decane [128].

p_s [Pa]	T_s [K]	H_v [J/kg]	p_s [Pa]	T_s [K]	H_v [J/kg]
3.3875E-02	250.00	4.3750E+05	1.9452E+05	550.00	3.1695E+05
1.3016E-01	260.00	4.3432E+05	2.3405E+05	560.00	3.1149E+05
4.3464E-01	270.00	4.3110E+05	2.7951E+05	570.00	3.0587E+05
1.2879E+00	280.00	4.2784E+05	3.3144E+05	580.00	3.0007E+05
3.4445E+00	290.00	4.2454E+05	3.9042E+05	590.00	2.9408E+05
8.4301E+00	300.00	4.2120E+05	4.5701E+05	600.00	2.8788E+05
1.9099E+01	310.00	4.1781E+05	5.3180E+05	610.00	2.8145E+05
4.0442E+01	320.00	4.1438E+05	6.1538E+05	620.00	2.7477E+05
8.0680E+01	330.00	4.1090E+05	7.0834E+05	630.00	2.6781E+05
1.5268E+02	340.00	4.0737E+05	8.1127E+05	640.00	2.6054E+05
2.7570E+02	350.00	4.0379E+05	9.2476E+05	650.00	2.5291E+05
4.7740E+02	360.00	4.0016E+05	1.0494E+06	660.00	2.4489E+05
7.9612E+02	370.00	3.9647E+05	1.1857E+06	670.00	2.3640E+05
1.2834E+03	380.00	3.9272E+05	1.3344E+06	680.00	2.2738E+05
2.0065E+03	390.00	3.8891E+05	1.4959E+06	690.00	2.1773E+05
3.0511E+03	400.00	3.8504E+05	1.6707E+06	700.00	2.0731E+05
4.5239E+03	410.00	3.8111E+05	1.8595E+06	710.00	1.9595E+05
6.5547E+03	420.00	3.7710E+05	2.0628E+06	720.00	1.8338E+05
9.2992E+03	430.00	3.7303E+05	2.2810E+06	730.00	1.6919E+05
1.2940E+04	440.00	3.6888E+05	2.5146E+06	740.00	1.5271E+05
1.7689E+04	450.00	3.6465E+05	2.7641E+06	750.00	1.3259E+05
2.3789E+04	460.00	3.6034E+05	3.0299E+06	760.00	1.0550E+05
3.1512E+04	470.00	3.5594E+05	3.3125E+06	770.00	5.3691E+04
4.1162E+04	480.00	3.5145E+05			
5.3075E+04	490.00	3.4686E+05			
6.7615E+04	500.00	3.4217E+05			
8.5177E+04	510.00	3.3737E+05			
1.0619E+05	520.00	3.3246E+05			
1.3109E+05	530.00	3.2742E+05			
1.6037E+05	540.00	3.2226E+05			

Table 53: Liquid vapor saturation pressure, temperature and heat of vaporization of α -Methylnaphthalene [128].

p_s [Pa]	T_s [K]	H_v [J/kg]	p_s [Pa]	T_s [K]	H_v [J/kg]
3.9161E-02	310.00	3.4226E+05	3.8679E+04	560.00	2.2927E+05
1.1918E-01	320.00	3.3654E+05	4.9360E+04	570.00	2.2490E+05
3.3321E-01	330.00	3.3099E+05	6.2335E+04	580.00	2.2043E+05
8.6317E-01	340.00	3.2562E+05	7.7959E+04	590.00	2.1583E+05
2.0872E+00	350.00	3.2039E+05	9.6623E+04	600.00	2.1107E+05
4.7418E+00	360.00	3.1531E+05	1.1876E+05	610.00	2.0614E+05
1.0180E+01	370.00	3.1037E+05	1.4484E+05	620.00	2.0100E+05
2.0759E+01	380.00	3.0555E+05	1.7540E+05	630.00	1.9562E+05
4.0390E+01	390.00	3.0084E+05	2.1100E+05	640.00	1.8996E+05
7.5283E+01	400.00	2.9624E+05	2.5232E+05	650.00	1.8397E+05
1.3491E+02	410.00	2.9174E+05	3.0007E+05	660.00	1.7760E+05
2.3321E+02	420.00	2.8733E+05	3.5510E+05	670.00	1.7076E+05
3.8997E+02	430.00	2.8300E+05	4.1838E+05	680.00	1.6335E+05
6.3251E+02	440.00	2.7873E+05	4.9105E+05	690.00	1.5522E+05
9.9742E+02	450.00	2.7453E+05	5.7451E+05	700.00	1.4615E+05
1.5325E+03	460.00	2.7038E+05	6.7050E+05	710.00	1.3579E+05
2.2989E+03	470.00	2.6627E+05	7.8131E+05	720.00	1.2354E+05
3.3728E+03	480.00	2.6220E+05	9.1012E+05	730.00	1.0819E+05
4.8476E+03	490.00	2.5814E+05	1.0618E+06	740.00	8.6858E+04
6.8360E+03	500.00	2.5409E+05	1.2444E+06	750.00	0.0000E+00
9.4712E+03	510.00	2.5004E+05			
1.2909E+04	520.00	2.4597E+05			
1.7330E+04	530.00	2.4188E+05			
2.2939E+04	540.00	2.3774E+05			
2.9968E+04	550.00	2.3354E+05			

Table 54: Liquid vapor saturation pressure, temperature and heat of vaporization of Methyl Decanoate [128].

p_s [Pa]	T_s [K]	H_v [J/kg]	p_s [Pa]	T_s [K]	H_v [J/kg]
1.85E-02	2.00E+02	4.23E+05	5.32E+04	5.00E+02	2.58E+05
5.10E-02	2.10E+02	4.17E+05	6.83E+04	5.10E+02	2.53E+05
8.35E-02	2.20E+02	4.10E+05	8.68E+04	5.20E+02	2.47E+05
1.16E-01	2.30E+02	4.04E+05	1.09E+05	5.30E+02	2.42E+05
1.48E-01	2.40E+02	3.97E+05	1.36E+05	5.40E+02	2.36E+05
1.81E-01	2.50E+02	3.91E+05	1.67E+05	5.50E+02	2.31E+05
2.13E-01	2.60E+02	3.84E+05	2.04E+05	5.60E+02	2.24E+05
2.46E-01	2.70E+02	3.78E+05	2.47E+05	5.70E+02	2.18E+05
2.78E-01	2.80E+02	3.71E+05	2.96E+05	5.80E+02	2.11E+05
8.22E-01	2.90E+02	3.65E+05	3.53E+05	5.90E+02	2.04E+05
2.22E+00	3.00E+02	3.59E+05	4.18E+05	6.00E+02	1.97E+05
5.53E+00	3.10E+02	3.53E+05	4.93E+05	6.10E+02	1.89E+05
1.28E+01	3.20E+02	3.47E+05	5.77E+05	6.20E+02	1.80E+05
2.79E+01	3.30E+02	3.42E+05	6.72E+05	6.30E+02	1.70E+05
5.75E+01	3.40E+02	3.36E+05	7.80E+05	6.40E+02	1.60E+05
1.12E+02	3.50E+02	3.31E+05	9.00E+05	6.50E+02	1.48E+05
2.09E+02	3.60E+02	3.26E+05	1.04E+06	6.60E+02	1.34E+05
3.73E+02	3.70E+02	3.21E+05	1.19E+06	6.70E+02	1.18E+05
6.40E+02	3.80E+02	3.16E+05	1.36E+06	6.80E+02	9.63E+04
1.06E+03	3.90E+02	3.11E+05	1.55E+06	6.90E+02	6.08E+04
1.70E+03	4.00E+02	3.06E+05			
2.65E+03	4.10E+02	3.01E+05			
4.02E+03	4.20E+02	2.96E+05			
5.95E+03	4.30E+02	2.92E+05			
8.60E+03	4.40E+02	2.87E+05			
1.22E+04	4.50E+02	2.82E+05			
1.69E+04	4.60E+02	2.77E+05			
2.30E+04	4.70E+02	2.73E+05			
3.09E+04	4.80E+02	2.68E+05			
4.08E+04	4.90E+02	2.63E+05			

Table 55: Liquid vapor saturation pressure, temperature and heat of vaporization of Diesel-2 [128].

References

- [1] DEB, Kalyanmoy ; AGRAWAL, Samir ; PRATAP, Amrit ; MEYARIVAN, T.: A fast elitist non-dominated sorting genetic algorithm for multi-objective optimization: NSGA-II. In: *Lecture Notes in Computer Science (including subseries Lecture Notes in Artificial Intelligence and Lecture Notes in Bioinformatics)* 1917 (2000), S. 849–858. http://dx.doi.org/10.1007/3-540-45356-3_83. – DOI 10.1007/3-540-45356-3_83. – ISBN 978-3-540-45356-7
- [2] DEB, Kalyanmoy ; GOEL, Tushar: Controlled elitist non-dominated sorting genetic algorithms for better convergence. In: *Lecture Notes in Computer Science (including subseries Lecture Notes in Artificial Intelligence and Lecture Notes in Bioinformatics)* 1993 (2001), 67–81. http://dx.doi.org/10.1007/3-540-44719-9_5/COVER. – DOI 10.1007/3-540-44719-9_5/COVER. – ISBN 9783540417453
- [3] PETERS, Norbert: *Turbulent Combustion*. Cambridge University Press, 2000. <http://dx.doi.org/10.1017/cbo9780511612701>. <http://dx.doi.org/10.1017/cbo9780511612701>. – ISBN 9780521660822
- [4] BHAVE, A. ; BALTHASAR, M. ; KRAFT, M. ; MAUSS, F.: Analysis of a natural gas fuelled homogeneous charge compression ignition engine with exhaust gas recirculation using a stochastic reactor model. In: *International Journal of Engine Research* 5 (2004), Nr. 1, S. 93–104. <http://dx.doi.org/10.1243/146808704772914273>. – DOI 10.1243/146808704772914273. – ISSN 14680874
- [5] KOŽUCH, Peter: *Ein phänomenologisches Modell zur kombinierten Stickoxid- und Rußberechnung bei direkteinspritzenden Dieselmotoren*, Universität Stuttgart, Diss., 2004. <http://dx.doi.org/10.18419/opus-4031>. – DOI 10.18419/opus-4031. – 214 S.
- [6] SU, Haiyun: *Stochastic Reactor Models for Simulating Direct Injection Homogeneous Charge Compression Ignition Engines*. Cambridge, University of Cambridge, Diss., 2010. <http://131.111.109.57/dissertations/hs309-PhDThesis.pdf>
- [7] DE BELLIS, Vincenzo ; SEVERI, Elena ; FONTANESI, Stefano ; BOZZA, Fabio: Hierarchical 1D/3D approach for the development of a turbulent combustion model applied to a VVA turbocharged engine. Part I: Turbulence model. In: *Energy Procedia* 45 (2014), S. 829–838. <http://dx.doi.org/10.1016/j.egypro.2014.01.088>. – DOI 10.1016/j.egypro.2014.01.088. – ISBN 3908176832
- [8] DE BELLIS, Vincenzo ; SEVERI, Elena ; FONTANESI, Stefano ; BOZZA, Fabio: Hierarchical 1D/3D approach for the development of a turbulent combustion model applied to a VVA turbocharged engine. Part II: Combustion model. In: *Energy Procedia* 45 (2014), 1027–1036. <http://dx.doi.org/10.1016/j.egypro.2014.01.108>. – DOI 10.1016/j.egypro.2014.01.108. – ISBN 3908176832
- [9] DULBECCO, Alessio ; RICHARD, Stephane ; LAGET, Olivier ; AUBRET, Philippe: Development of a Quasi-Dimensional K-k Turbulence Model for Direct Injection Spark

- Ignition (DISI) Engines Based on the Formal Reduction of a 3D CFD Approach. In: *SAE Technical Papers* 2016-October (2016). <http://dx.doi.org/10.4271/2016-01-2229>. – DOI 10.4271/2016-01-2229. – ISSN 01487191
- [10] BOSSUNG, Christoph: *Turbulenzmodellierung für quasidimensionale Motorprozessrechnung*, Universität Stuttgart, Diss., 2017. <http://dx.doi.org/10.18419/opus-9171>. – DOI 10.18419/opus-9171
- [11] YANG, Qirui ; GRILL, Michael ; BARGENDE, Michael: A Quasi-Dimensional Charge Motion and Turbulence Model for Diesel Engines with a Fully Variable Valve Train. In: *SAE Technical Papers* 2018-April (2018), S. 1–23. <http://dx.doi.org/10.4271/2018-01-0165>. – DOI 10.4271/2018-01-0165. – ISSN 01487191
- [12] BOZZA, Fabio ; TEODOSIO, Luigi ; DE BELLIS, Vincenzo ; FONTANESI, Stefano ; IORIO, Agostino: A Refined OD Turbulence Model to Predict Tumble and Turbulence in SI Engines. In: *SAE International Journal of Engines* 12 (2019), Nr. 1, 15–30. <http://dx.doi.org/10.4271/03-12-01-0002>. – DOI 10.4271/03-12-01-0002
- [13] SAMUELSSON, K: *Development and Validation of a Fuel Injection Model for the SRM Code*. Lund, 2004
- [14] TUNÉR, Martin: *Stochastic Reactor Models for Engine Simulations*, Lund University, Diss., 2008. – 1–230 S
- [15] PASTERNAK, Michal: *Simulation of the diesel engine combustion process using the stochastic reactor model*. Berlin, BTU Cottbus - Senftenberg, Diss., 2016
- [16] MATRISCIANO, Andrea: *Development of an efficient solver for detailed kinetics in reactive flows*, Chalmers University of Technology, Diss., 2021. <https://research.chalmers.se/en/publication/525272>
- [17] BJERKBORN, Simon ; PERLMAN, Cathleen ; FROJD, Karin ; MAUSS, Fabian: Predictive Flame Propagation Model for Stochastic Reactor Model Based Engine Simulations. In: *ICDERS* (2011), 1–6. <http://www.icders.org/ICDERS2011/abstracts/ICDERS2011-0325.pdf>
- [18] BJERKBORN, Simon ; FROJD, Karin ; PERLMAN, Cathleen ; MAUSS, Fabian: A Monte Carlo Based Turbulent Flame Propagation Model for Predictive SI In-Cylinder Engine Simulations Employing Detailed Chemistry for Accurate Knock Prediction. In: *SAE International Journal of Engines* 5 (2012), Nr. 4, S. 1637–1647. <http://dx.doi.org/10.4271/2012-01-1680>. – DOI 10.4271/2012-01-1680. – ISSN 19463944
- [19] NETZER, Corinna ; PASTERNAK, Michal ; SEIDEL, Lars ; RAVET, Frédéric ; MAUSS, Fabian: Computationally efficient prediction of cycle-to-cycle variations in spark-ignition engines. In: *International Journal of Engine Research* 21 (2020), Nr. 4, S. 649–663. <http://dx.doi.org/10.1177/1468087419856493>. – DOI 10.1177/1468087419856493. – ISSN 20413149

- [20] FRANKEN, Tim ; SOMMERHOFF, Arnd ; WILLEMS, Werner ; MATRISCIANO, Andrea ; LEHTINIEMI, Harry ; BORG, Anders ; NETZER, Corinna ; MAUSS, Fabian: Advanced Predictive Diesel Combustion Simulation Using Turbulence Model and Stochastic Reactor Model. In: *SAE Technical Papers* 2017-March (2017), Nr. March. <http://dx.doi.org/10.4271/2017-01-0516>. – DOI 10.4271/2017-01-0516. – ISSN 01487191
- [21] MATRISCIANO, Andrea ; FRANKEN, Tim ; PERLMAN, Cathleen ; BORG, Anders ; LEHTINIEMI, Harry ; MAUSS, Fabian: Development of a Computationally Efficient Progress Variable Approach for a Direct Injection Stochastic Reactor Model. In: *SAE Technical Papers* (2017). <http://dx.doi.org/10.4271/2017-01-0512>. – DOI 10.4271/2017-01-0512
- [22] FRANKEN, Tim ; KLAUER, Christian ; KIENBERG, Martin ; MATRISCIANO, Andrea ; MAUSS, Fabian: Prediction of thermal stratification in an engine-like geometry using a zero-dimensional stochastic reactor model. In: *International Journal of Engine Research* 21 (2020), Nr. 9, S. 1750–1763. <http://dx.doi.org/10.1177/1468087418824217>. – DOI 10.1177/1468087418824217. – ISSN 20413149
- [23] MATRISCIANO, Andrea ; FRANKEN, Tim ; GONZALES MESTRE, Laura C. ; BORG, Anders ; MAUSS, Fabian: Development of a computationally efficient tabulated chemistry solver for internal combustion engine optimization using stochastic reactor models. In: *Applied Sciences* 10 (2020), Nr. 24, S. 1–31. <http://dx.doi.org/10.3390/app10248979>. – DOI 10.3390/app10248979. – ISSN 20763417
- [24] FRANKEN, Tim ; MAUSS, Fabian ; SEIDEL, Lars ; GERN, Maike S. ; KAUF, Malte ; MATRISCIANO, Andrea ; KULZER, Andre C.: Gasoline engine performance simulation of water injection and low-pressure exhaust gas recirculation using tabulated chemistry. In: *International Journal of Engine Research* 21 (2020), Nr. 10, S. 1857–1877. <http://dx.doi.org/10.1177/1468087420933124>. – DOI 10.1177/1468087420933124. – ISSN 20413149
- [25] PASTERNAK, Michal ; MAUSS, Fabian ; KLAUER, Christian ; MATRISCIANO, Andrea: Diesel engine performance mapping using a parametrized mixing time model. In: *International Journal of Engine Research* 19 (2018), Nr. 2, S. 202–213. <http://dx.doi.org/10.1177/1468087417718115>. – DOI 10.1177/1468087417718115. – ISSN 20413149
- [26] FRANKEN, Tim ; MAUSS, Fabian: Development of Methodology for Predictive Diesel Combustion Simulation Using 0D Stochastic Reactor Model. In: *SAE Technical Papers* (2016), apr. <http://dx.doi.org/10.4271/2016-01-0566>. – DOI 10.4271/2016-01-0566. – ISSN 0148-7191
- [27] CORREA, S. M.: Turbulence-chemistry interactions in the intermediate regime of premixed combustion. In: *Combustion and Flame* 93 (1993), apr, Nr. 1-2, S. 41–60. [http://dx.doi.org/10.1016/0010-2180\(93\)90083-F](http://dx.doi.org/10.1016/0010-2180(93)90083-F). – DOI 10.1016/0010-2180(93)90083-F. – ISSN 00102180
- [28] CORREA, S. M. ; BRAATEN, M. E.: Parallel simulations of partially stirred methane combustion. In: *Combustion and Flame* 94 (1993), sep, Nr. 4, S. 469–486. [http://dx.doi.org/10.1016/0010-2180\(93\)90083-F](http://dx.doi.org/10.1016/0010-2180(93)90083-F). – DOI 10.1016/0010-2180(93)90083-F. – ISSN 00102180

- [org/10.1016/0010-2180\(93\)90128-P](https://doi.org/10.1016/0010-2180(93)90128-P). – DOI 10.1016/0010-2180(93)90128-P. – ISSN 00102180
- [29] CHEN, J. Y.: Stochastic modeling of partially stirred reactors. In: *Combustion Science and Technology* 122 (1997), Nr. 1-6, 63–94. <http://dx.doi.org/10.1080/00102209708935605>. – DOI 10.1080/00102209708935605. – ISSN 00102202
- [30] POPE, S. B.: PDF methods for turbulent reactive flows. In: *Progress in Energy and Combustion Science* 11 (1985), jan, Nr. 2, S. 119–192. [http://dx.doi.org/10.1016/0360-1285\(85\)90002-4](http://dx.doi.org/10.1016/0360-1285(85)90002-4). – DOI 10.1016/0360-1285(85)90002-4. – ISSN 03601285
- [31] KRAFT, Markus: *Stochastic Modelling of Turbulent Reacting Flow in Chemical Engineering*. Bd. 6. VDI-Verlag, 1998. – 1–109 S. – ISBN 3-18-339106-6
- [32] WOSCHNI, G.: A universally applicable equation for the instantaneous heat transfer coefficient in the internal combustion engine. In: *SAE Technical Papers* (1967). <http://dx.doi.org/10.4271/670931>. – DOI 10.4271/670931. – ISSN 26883627
- [33] HOHENBERG, Günter F.: Advanced approaches for heat transfer calculations. In: *SAE Technical Papers* (1979), S. 2788–2806. <http://dx.doi.org/10.4271/790825>. – DOI 10.4271/790825. – ISSN 26883627
- [34] HEINLE, Moritz ; BARGENDE, Michael ; BERNER, Hans J.: Some Useful Additions to Calculate the Wall Heat Losses in Real Cycle Simulations. In: *SAE International Journal of Engines* 5 (2012), Nr. 2, S. 469–482. <http://dx.doi.org/10.4271/2012-01-0673>. – DOI 10.4271/2012-01-0673. – ISSN 19463944
- [35] SCHMITT, Martin: *Direct numerical simulations in engine-like geometries*, ETH Zurich, Diss., 2014. <http://dx.doi.org/10.3929/ethz-a-010349869>. – DOI 10.3929/ethz-a-010349869. – 1–15 S
- [36] HEYWOOD, John B.: *Internal combustion engine fundamentals*. McGraw-Hill, 1988. – 26-0943-26-0943 S. <http://dx.doi.org/10.5860/choice.26-0943>. <http://dx.doi.org/10.5860/choice.26-0943>. – ISBN 007028637-X
- [37] CURL, R L.: Theory and Effects in Simple Reactors. In: *A.I.Ch.E. Journal* 9 (1963), S. 175–181
- [38] JANICKA, J. ; KOLBE, W. ; KOLLMANN, W.: Closure of the transport equation for the probability density function of turbulent scalar fields. In: *Journal of Non-Equilibrium Thermodynamics* 4 (1979), Nr. 1, S. 47–66. <http://dx.doi.org/10.1515/jnet.1979.4.1.47>. – DOI 10.1515/jnet.1979.4.1.47. – ISSN 14374358
- [39] SUBRAMANIAM, S. ; POPE, S. B.: A mixing model for turbulent reactive flows based on euclidean minimum spanning trees. In: *Combustion and Flame* 115 (1998), Nr. 4, S. 487–514. [http://dx.doi.org/10.1016/S0010-2180\(98\)00023-6](http://dx.doi.org/10.1016/S0010-2180(98)00023-6). – DOI 10.1016/S0010-2180(98)00023-6. – ISSN 00102180

- [40] SVENSSON, Erik: *System Simulation of Partially Premixed Combustion in Heavy-Duty Engines: Gas Exchange, Fuels and In-cylinder Analysis*, Diss., may 2019. <http://lup.lub.lu.se/record/1e44b743-55b7-4ab7-ae96-270fe5dd080d>
- [41] FRANKEN, Tim ; MATRISCIANO, Andrea ; SARI, Rafael ; FOGUÉ ROBLES, Álvaro ; MONSALVE-SERRANO, Javier ; LOPEZ PINTOR, Dario ; PASTERNAK, Michal ; GARCIA, Antonio ; MAUSS, Fabian: Modeling of Reactivity Controlled Compression Ignition Combustion Using a Stochastic Reactor Model Coupled with Detailed Chemistry. In: *SAE Technical Papers* (2021), sep. <http://dx.doi.org/10.4271/2021-24-0014>. – DOI 10.4271/2021-24-0014. – ISSN 01487191
- [42] LEHTINIEMI, Harry ; MAUSS, Fabian ; BALTHASAR, Michael ; MAGNUSSON, Ingemar: Modeling diesel spray ignition using detailed chemistry with a progress variable approach. In: *Combustion Science and Technology* 178 (2006), Nr. 10-11, S. 1977–1997. <http://dx.doi.org/10.1080/00102200600793148>. – DOI 10.1080/00102200600793148. – ISSN 00102202
- [43] LEHTINIEMI, Harry ; BORG, Anders ; MAUSS, Fabian: Combustion Modeling of Diesel Sprays. In: *SAE Technical Papers* 2016-April (2016), Nr. April. <http://dx.doi.org/10.4271/2016-01-0592>. – DOI 10.4271/2016-01-0592. – ISBN 2016010592
- [44] WILCOX, David C.: *Turbulence Modeling for CFD, Volume 1*. Third edit. DCW industries La Canada, 2006. – 522 S. – ISBN 1928729088
- [45] YANG, Qirui: *Quasi-dimensional Charge Motion and Turbulence Model*, University of Stuttgart, Diss., 2022. http://dx.doi.org/10.1007/978-3-658-35774-0_3. – DOI 10.1007/978-3-658-35774-0_3. – 15–78 S.
- [46] DAMKÖHLER, Gerhard: Allgemeine Elektrochemie. In: *Zeitschrift für Elektrotechnik und Elektrochemie* 5 (1898), Nr. 21, 241–245. <http://dx.doi.org/10.1002/bbpc.18980052102>. – DOI 10.1002/bbpc.18980052102. – ISSN 03728323
- [47] BLINT, Richard: The relationship of the laminar flame width to flame speed. In: *Combustion Science and Technology* 49 (1986), Nr. 1-2, S. 79–92. <http://dx.doi.org/10.1080/00102208608923903>. – DOI 10.1080/00102208608923903. – ISSN 1563521X
- [48] PASTERNAK, Michal ; MAUSS, Fabian ; SENS, Marc ; RIESS, Michael ; BENZ, Andreas ; STAPF, Karl G.: Gasoline engine simulations using zero-dimensional spark ignition stochastic reactor model and three-dimensional computational fluid dynamics engine model. In: *International Journal of Engine Research* 17 (2016), Nr. 1, S. 76–85. <http://dx.doi.org/10.1177/1468087415599859>. – DOI 10.1177/1468087415599859. – ISSN 20413149
- [49] KOLLA, Hemanth: *Scalar dissipation rate based flamelet modelling of turbulent premixed flames*, University of Cambridge, Diss., 2010. <http://dx.doi.org/10.17863/CAM.13979>. – DOI 10.17863/CAM.13979

- [50] DUCLOS, J. M. ; VEYNANTE, D. ; POINSOT, T.: A comparison of flamelet models for premixed turbulent combustion. In: *Combustion and Flame* 95 (1993), oct, Nr. 1-2, S. 101–117. [http://dx.doi.org/10.1016/0010-2180\(93\)90055-8](http://dx.doi.org/10.1016/0010-2180(93)90055-8). – DOI 10.1016/0010-2180(93)90055-8. – ISSN 00102180
- [51] LIPATNIKOV, A. N. ; CHOMIAK, J.: Turbulent flame speed and thickness: Phenomenology, evaluation, and application in multi-dimensional simulations. In: *Progress in Energy and Combustion Science* 28 (2002), jan, Nr. 1, S. 1–74. [http://dx.doi.org/10.1016/S0360-1285\(01\)00007-7](http://dx.doi.org/10.1016/S0360-1285(01)00007-7). – DOI 10.1016/S0360-1285(01)00007-7. – ISSN 03601285
- [52] BRAY, K. N.: The interaction between turbulence and combustion. In: *Symposium (International) on Combustion* 17 (1979), jan, Nr. 1, S. 223–233. [http://dx.doi.org/10.1016/S0082-0784\(79\)80024-7](http://dx.doi.org/10.1016/S0082-0784(79)80024-7). – DOI 10.1016/S0082-0784(79)80024-7. – ISSN 00820784
- [53] BRAY, K. N. C. ; LIBBY, Paul A. (Hrsg.) ; WILLIAMS, Forman A. (Hrsg.): *Turbulent flows with premixed reactants*. Berlin, Heidelberg : Springer Berlin Heidelberg, 1980. – 115–183 S. http://dx.doi.org/10.1007/3540101926_10. http://dx.doi.org/10.1007/3540101926_10. – ISBN 978-3-540-38273-7
- [54] KOLLA, H. ; ROGERSON, J. W. ; CHAKRABORTY, N. ; SWAMINATHAN, N.: Scalar Dissipation Rate Modeling and its Validation. In: *Combustion Science and Technology* 181 (2009), mar, Nr. 3, 518–535. <http://dx.doi.org/10.1080/00102200802612419>. – DOI 10.1080/00102200802612419. – ISSN 00102202
- [55] SU, Yunde ; SPLITTER, Derek ; KIM, Seung H.: Laminar-to-turbulent flame transition and cycle-to-cycle variations in large eddy simulation of spark-ignition engines. In: *International Journal of Engine Research* 22 (2021), Nr. 9, S. 2803–2818. <http://dx.doi.org/10.1177/1468087420962346>. – DOI 10.1177/1468087420962346. – ISSN 20413149
- [56] KEUM, Seunghwan ; ZHU, Guangfei ; GROVER, Ronald ; ZENG, Wei ; RUTLAND, Christopher ; KUO, Tang W.: A semi-empirical laminar-to-turbulent flame transition model coupled with G equation for early flame kernel development and combustion in spark-ignition engines. In: *International Journal of Engine Research* 22 (2021), Nr. 2, S. 479–490. <http://dx.doi.org/10.1177/1468087419864748>. – DOI 10.1177/1468087419864748. – ISSN 20413149
- [57] HÉLIE, J. ; TROUVÉ, A.: Turbulent flame propagation in partially premixed combustion. In: *Symposium (International) on Combustion* 27 (1998), jan, Nr. 1, S. 891–898. [http://dx.doi.org/10.1016/S0082-0784\(98\)80486-4](http://dx.doi.org/10.1016/S0082-0784(98)80486-4). – DOI 10.1016/S0082-0784(98)80486-4. – ISSN 00820784
- [58] PASQUIER, N. ; LECORDIER, B. ; TRINITÉ, M. ; CESSOU, A.: An experimental investigation of flame propagation through a turbulent stratified mixture. In: *Proceedings of the Combustion Institute* 31 I (2007), jan, Nr. 1, S. 1567–1574. <http://dx.doi.org/10.1016/j.proci.2006.07.118>. – DOI 10.1016/j.proci.2006.07.118. – ISSN 15407489

- [59] NETZER, Corinna ; SEIDEL, Lars ; PASTERNAK, Michal ; KLAUER, Christian ; PERLMAN, Cathleen ; RAVET, Frederic ; MAUSS, Fabian: Engine Knock Prediction and Evaluation Based on Detonation Theory Using a Quasi-Dimensional Stochastic Reactor Model. In: *SAE Technical Papers* 2017-March (2017), Nr. March. <http://dx.doi.org/10.4271/2017-01-0538>. – DOI 10.4271/2017-01-0538. – ISSN 01487191
- [60] WENTWORTH, J. T.: The piston crevice volume effect on exhaust hydrocarbon emission. In: *Combustion Science and Technology* 4 (1971), sep, Nr. 1, 97–100. <http://dx.doi.org/10.1080/00102207108952475>. – DOI 10.1080/00102207108952475. – ISSN 1563521X
- [61] TANG, Qinglong ; LIU, Xinlei ; RAMAN, Vallinayagam ; SHI, Hao ; CHANG, Junseok ; IM, Hong G. ; JOHANSSON, Bengt: Effects of fuel trapping in piston crevice on unburned hydrocarbon emissions in early-injection compression ignition engines. In: *Combustion and Flame* 231 (2021), sep, S. 111496. <http://dx.doi.org/10.1016/j.combustflame.2021.111496>. – DOI 10.1016/j.combustflame.2021.111496. – ISSN 15562921
- [62] MALFI, Enrica ; DE BELLIS, Vincenzo ; BOZZA, Fabio ; CAFARI, Alberto ; CAPUTO, Gennaro ; HYVÖNEN, Jari: A phenomenological model for the description of unburned hydrocarbons emission in ultra-lean engines. In: *International Journal of Engine Research* 23 (2022), Nr. 6, S. 995–1011. <http://dx.doi.org/10.1177/14680874211005063>. – DOI 10.1177/14680874211005063. – ISSN 20413149
- [63] PERA, Cecile ; KNOP, Vincent ; REVEILLON, Julien: Influence of flow and ignition fluctuations on cycle-to-cycle variations in early flame kernel growth. In: *Proceedings of the Combustion Institute* 35 (2015), Nr. 3, 2897–2905. <http://dx.doi.org/10.1016/j.proci.2014.07.037>. – DOI 10.1016/j.proci.2014.07.037. – ISSN 15407489
- [64] S.P.A., ESTECO: *modeFRONTIER v2020R2*. <https://www.esteco.com/>. Version: 2020
- [65] ZITZLER, E. ; DEB, K. ; THIELE, L.: Comparison of multiobjective evolutionary algorithms: empirical results. In: *Evolutionary computation* 8 (2000), Nr. 2, S. 173–195. <http://dx.doi.org/10.1162/106365600568202>. – DOI 10.1162/106365600568202. – ISSN 10636560
- [66] FARINA, M. ; AMATO, P.: On the optimal solution definition for many-criteria optimization problems. In: *Annual Conference of the North American Fuzzy Information Processing Society - NAFIPS* 2002-Janua (2002), S. 233–238. <http://dx.doi.org/10.1109/NAFIPS.2002.1018061>. – DOI 10.1109/NAFIPS.2002.1018061. ISBN 0780374614
- [67] WAGNER, Tobias ; BEUME, Nicola ; NAUJOKS, Boris: Pareto-, aggregation-, and indicator-based methods in many-objective optimization. In: *Lecture Notes in Computer Science (including subseries Lecture Notes in Artificial Intelligence and Lecture Notes in Bioinformatics)* 4403 LNCS (2007), S. 742–756. http://dx.doi.org/10.1007/978-3-540-70928-2_56/COVER. – DOI 10.1007/978-3-540-70928-2_56/COVER. – ISBN 9783540709275

- [68] POLONI, Carlo ; GIURGEVICH, Andrea ; ONESTI, Luka ; PEDIRODA, Valentino: Hybridization of a multi-objective genetic algorithm, a neural network and a classical optimizer for a complex design problem in fluid dynamics. In: *Computer Methods in Applied Mechanics and Engineering* 186 (2000), Nr. 2-4, S. 403–420. [http://dx.doi.org/10.1016/S0045-7825\(99\)00394-1](http://dx.doi.org/10.1016/S0045-7825(99)00394-1). – DOI 10.1016/S0045-7825(99)00394-1. – ISSN 00457825
- [69] VINET, Luc ; ZHEDANOV, Alexei: *A 'missing' family of classical orthogonal polynomials*. New York : Springer New York, NY, 2011. – 1–373 S. <http://dx.doi.org/10.1088/1751-8113/44/8/085201>. <http://dx.doi.org/10.1088/1751-8113/44/8/085201>. – ISBN 9780387781648
- [70] MONTRONE, Teresa ; RIGONI, Enrico ; SERGI, Elisabetta ; SILVETTI, Simone: *New Greedy Incremental Space Filler in mF 2019 : Benchmark Tests*. 2019
- [71] MCKAY, M. D. ; BECKMAN, R. J. ; CONOVER, W. J.: A comparison of three methods for selecting values of input variables in the analysis of output from a computer code. In: *Technometrics* 42 (2000), Nr. 1, 55–61. <http://dx.doi.org/10.1080/00401706.2000.10485979>. – DOI 10.1080/00401706.2000.10485979. – ISSN 15372723
- [72] COLLINGS, Bruce J. ; NIEDERREITER, Harald: *Random Number Generation and Quasi-Monte Carlo Methods*. Philadelphia, 1993. – 699 S. <http://dx.doi.org/10.2307/2290359>. <http://dx.doi.org/10.2307/2290359>. – ISBN 978-0-898712-95-7
- [73] TAYLOR, L. R. ; PRESS, William H. ; FLANNERY, Brian P. ; TEUKOLSKY, Saul A. ; VETTERLING, William T.: *Numerical Recipes: The Art of Scientific Computing*. Third. Cambridge : Press, Cambridge University, 1987. – 374 S. <http://dx.doi.org/10.2307/4830>. <http://dx.doi.org/10.2307/4830>. – ISBN 978-0-511-33555-6
- [74] CORLESS, Robert M. ; GIANNI, Patrizia M. ; TRAGER, Barry M. ; WATT, Stephen M.: The singular value decomposition for polynomial systems. In: *International Symposium on Symbolic and Computation - ISSAS, Proceedings* (1995), S. 195–207. <http://dx.doi.org/10.1145/220346.220371>. – DOI 10.1145/220346.220371
- [75] HAGAN, Martin T. ; MENHAJ, Mohammad B.: Training feedforward networks with the Marquardt algorithm. In: *IEEE transactions on Neural Networks* 5 (1994), Nr. 6, S. 989–993. <http://dx.doi.org/10.1109/72.329697>. – DOI 10.1109/72.329697
- [76] NGUYEN, Derrick ; WIDROW, Bernard: Improving the learning speed of 2-layer neural networks by choosing initial values of the adaptive weights. In: *1990 IJCNN International Joint Conference on Neural Networks* (1990), S. 21–26. <http://dx.doi.org/10.1109/IJCNN.1990.137819>. – DOI 10.1109/IJCNN.1990.137819
- [77] RIGONI, Enrico ; LOVISON, Alberto: Automatic sizing of neural networks for function approximation. In: *2007 IEEE International Conference on Systems, Man and Cybernetics* (2007), S. 2005–2010. <http://dx.doi.org/10.1109/ICSMC.2007.4413933>. – DOI 10.1109/ICSMC.2007.4413933

- [78] SIEBERTZ, Karl ; BEBBER, David van ; HOCHKIRCHEN, Thomas: *Statistische Versuch-splanung*. Berlin, Heidelberg : Springer-Verlag, 2010. <http://dx.doi.org/10.1007/978-3-642-05493-8>. <http://dx.doi.org/10.1007/978-3-642-05493-8>. – ISBN 978-3-642-05492-1
- [79] RASMUSSEN, Carl E.: Gaussian processes in machine learning. In: *Summer school on machine learning* (2003), S. 63–71. http://dx.doi.org/10.1007/978-3-540-28650-9_4. – DOI 10.1007/978-3-540-28650-9_4
- [80] TRIANTAPHYLLOU, Evangelos: Multi-Criteria Decision Making Methods. (2000), 5–21. http://dx.doi.org/10.1007/978-1-4757-3157-6_2. – DOI 10.1007/978-1-4757-3157-6_2
- [81] FONSECA, Carlos M. ; FLEMING, Peter J.: On the performance assessment and comparison of stochastic multiobjective optimizers. In: *Lecture Notes in Computer Science (including subseries Lecture Notes in Artificial Intelligence and Lecture Notes in Bioinformatics)* 1141 (1996), 584–593. http://dx.doi.org/10.1007/3-540-61723-X_1022/COVER. – DOI 10.1007/3-540-61723-X_1022/COVER. – ISBN 354061723X
- [82] DA FONSECA, Viviane G. ; FONSECA, Carlos M. ; HALL, Andreia O.: Inferential performance assessment of stochastic optimisers and the attainment function. In: *Lecture Notes in Computer Science (including subseries Lecture Notes in Artificial Intelligence and Lecture Notes in Bioinformatics)* 1993 (2001), 213–225. http://dx.doi.org/10.1007/3-540-44719-9_15/COVER. – DOI 10.1007/3-540-44719-9_15/COVER. – ISBN 9783540417453
- [83] POLES, Silvia ; RIGONI, Enrico ; ROBIČ, Tea: MOGA-II performance on noisy optimization problems. In: *Bioinspired Optimization Methods and their Applications - Proceedings of the International Conference on Bioinspired Optimization Methods and their Applications, BIOMA 2004* (2004), S. 51–62. ISBN 9616303619
- [84] POLONI, Carlo: GA coupled with computationally expensive simulations: tools to improve efficiency. In: *Genetic Algorithms in Engineering and Computer Science* 13 (1998)
- [85] KIRKPATRICK, S. ; GELATT, C. D. ; VECCHI, M. P.: Optimization by Simulated Annealing. In: *Science* 220 (1983), may, Nr. 4598, 671–680. <http://dx.doi.org/10.1126/SCIENCE.220.4598.671>. – DOI 10.1126/SCIENCE.220.4598.671. – ISSN 00368075
- [86] KIRKPATRICK, Scott: Optimization by simulated annealing: Quantitative studies. In: *Journal of Statistical Physics* 34 (1984), mar, Nr. 5-6, 975–986. <http://dx.doi.org/10.1007/BF01009452/METRICS>. – DOI 10.1007/BF01009452/METRICS. – ISSN 00224715
- [87] RIGONI, Enrico: *MOSA Multi objective simulated annealing*. 2003
- [88] KENNEDY, J. ; EBERHART, R.: Particle swarm optimization. In: *Proceedings of ICNN'95 - International Conference on Neural Networks* 4 (1995), 1942–1948. <http://dx.doi.org/10.1109/ICNN.1995.488968>. – DOI 10.1109/ICNN.1995.488968. ISBN 0-7803-2768-3

- [89] ENGELBRECHT, Andries P.: Computational Intelligence: An Introduction: Second Edition. In: *Computational Intelligence: An Introduction: Second Edition* (2007), oct, 1–597. <http://dx.doi.org/10.1002/9780470512517>. – DOI 10.1002/9780470512517. ISBN 9780470035610
- [90] MONTRONE, Teresa ; COSTANZO, Stefano ; ENGEL, Maja: *MOPSO Algorithm: General Description*. 2016
- [91] GERN, Maike S. ; FRANKEN, Tim ; VACCA, Antonino: *Water Injection in SI Engines*. Frankfurt am Main, 2020
- [92] BURKARDT, Patrick ; LEHN, Florian vom ; HESSE, Raik ; CHU, Hongchao ; JACOBS, Sascha ; CRÖNERT, Sebastian ; FRANKEN, Tim: *Fuel Composition for CO2 Reduction*. Frankfurt am Main, 2022
- [93] SEIDEL, Lars: *Development and reduction of a multicomponent reference fuel for gasoline*, BTU Cottbus - Senftenberg, Diss., 2017. <https://opus4.kobv.de/opus4-btu/frontdoor/index/index/year/2017/docId/4269>
- [94] SEIDEL, Lars ; NETZER, Corinna ; HILBIG, Martin ; MAUSS, Fabian ; KLAUER, Christian ; PASTERNAK, Michał ; MATRISCIANO, Andrea: Systematic Reduction of Detailed Chemical Reaction Mechanisms for Engine Applications. In: *Journal of Engineering for Gas Turbines and Power* (2017). <http://dx.doi.org/10.1115/ICEF2016-9304>. – DOI 10.1115/ICEF2016-9304
- [95] NETZER, Corinna: *Simulation and Assessment of Engine Knock Events*, BTU Cottbus - Senftenberg, Diss., 2019. <https://opus4.kobv.de/opus4-btu/frontdoor/index/index/year/2019/docId/4877>
- [96] NETZER, Corinna ; SEIDEL, Lars ; RAVET, Frédéric ; MAUSS, Fabian: Impact of the surrogate formulation on 3D CFD engine knock prediction using detailed chemistry. In: *Fuel* 254 (2019), Nr. June, 115678. <http://dx.doi.org/10.1016/j.fuel.2019.115678>. – DOI 10.1016/j.fuel.2019.115678. – ISSN 00162361
- [97] MORGAN, Neal ; SMALLBONE, Andrew ; BHAVE, Amit ; KRAFT, Markus ; CRACKNELL, Roger ; KALGHATGI, Gautam: Mapping surrogate gasoline compositions into RON/MON space. In: *Combustion and Flame* 157 (2010), Nr. 6, S. 1122–1131. <http://dx.doi.org/https://doi.org/10.1016/j.combustflame.2010.02.003>. – DOI <https://doi.org/10.1016/j.combustflame.2010.02.003>
- [98] ANDERSON, J E. ; KRAMER, U ; MUELLER, S A. ; WALLINGTON, T J.: Octane numbers of ethanol- and methanol- gasoline blends estimated from molar concentrations. In: *Energy & Fuels* 24 (2010), Nr. 12, S. 6576–6585. <http://dx.doi.org/https://doi.org/10.1021/ef101125c>. – DOI <https://doi.org/10.1021/ef101125c>
- [99] LOGESOFT: *Manual: LOGEtable v2.0*. www.logesoft.com. Version: 2020
- [100] LOGESOFT: *Manual: LOGE engine v3.0*. www.logesoft.com. Version: 2015

- [101] VACCA, Antonino ; BARGENDE, Michael ; CHIODI, Marco ; FRANKEN, Tim ; NETZER, Corinna ; GERN, Maike S. ; KAUF, Malte ; KULZER, André Casal: Analysis of Water Injection Strategies to Exploit the Thermodynamic Effects of Water in Gasoline Engines by Means of a 3D-CFD Virtual Test Bench. In: *SAE Technical Papers 2019-Septe* (2019), sep, Nr. September. <http://dx.doi.org/10.4271/2019-24-0102>. – DOI 10.4271/2019-24-0102. – ISSN 0148-7191
- [102] VACCA, Antonino: *Potential of Water Injection for Gasoline Engines by Means of a 3D-CFD Virtual Test Bench*, University of Stuttgart, Diss., 2020. <http://dx.doi.org/10.1007/978-3-658-32755-2>. – DOI 10.1007/978-3-658-32755-2
- [103] FRANKEN, Tim ; SHRESTHA, Krishna P. ; SEIDEL, Lars ; MAUSS, Fabian: Effect of Gasoline–Ethanol–Water Mixtures on Auto-Ignition in a Spark Ignition Engine. In: *International Conference on Ignition Systems for Gasoline Engines–International Conference on Knocking in Gasoline Engines* (2022), 175. <http://dx.doi.org/10.24053/9783816985440>. – DOI 10.24053/9783816985440
- [104] GERN, Maike S. ; VACCA, Antonino ; BARGENDE, Michael: Experimental Analysis of the Influence of Water Injection Strategies on DISI Engine Particle Emissions. In: *SAE International Journal of Advances and Current Practices in Mobility 2* (2019), sep, Nr. 2, 598–606. <http://dx.doi.org/10.4271/2019-24-0101>. – DOI 10.4271/2019-24-0101. – ISSN 2641-9637
- [105] KAUF, Malte ; GERN, Maike ; SEEFELDT, Stefan: Evaluation of Water Injection Strategies for NO_x Reduction and Charge Cooling in SI Engines. In: *SAE Technical Papers* (2019), dec, Nr. December. <http://dx.doi.org/10.4271/2019-01-2164>. – DOI 10.4271/2019-01-2164. – ISSN 0148-7191
- [106] SOPHIE GERN, Maike: *Experimentelle Entwicklung einer Einspritzstrategie für Ottomotoren mit Wassereinspritzung*, Technische Universität Berlin, Diss., 2020. <http://dx.doi.org/10.1007/978-3-658-33713-1>. – DOI 10.1007/978-3-658-33713-1
- [107] PETERS, N.: Laminar flamelet concepts in turbulent combustion. In: *Symposium (International) on Combustion 21* (1988), jan, Nr. 1, S. 1231–1250. [http://dx.doi.org/10.1016/S0082-0784\(88\)80355-2](http://dx.doi.org/10.1016/S0082-0784(88)80355-2). – DOI 10.1016/S0082-0784(88)80355-2. – ISSN 0082-0784
- [108] MASSOUD, Ehab ; SHRESTHA, Krishna P. ; ROSSI, Edoardo: *Water Injection in SI Engines II*. Frankfurt am Main, 2022
- [109] PICERNO, Mario ; LEE, Sung Y. ; PASTERNAK, Michal ; SIDDAREDDY, Reddy ; FRANKEN, Tim ; MAUSS, Fabian ; ANDERT, Jakob: Real-Time Emission Prediction with Detailed Chemistry under Transient Conditions for Hardware-in-the-Loop Simulations. In: *Energies 15* (2022), dec, Nr. 1, 261. <http://dx.doi.org/10.3390/en15010261>. – DOI 10.3390/en15010261. – ISSN 19961073

- [110] WANG, Xiaoxiao: *Kinetic mechanism of surrogates for biodiesel*, BTU Cottbus-Senftenberg, Diss., 2017. https://opus4.kobv.de/opus4-btu/files/4668/Wang_Xiaoxiao.pdf
- [111] FRANKEN, Tim ; DUGGAN, Alexander ; MATRISCIANO, Andrea ; LEHTINIEMI, Harry ; BORG, Anders ; MAUSS, Fabian: Multi-Objective optimization of fuel consumption and NOx emissions with reliability analysis using a stochastic reactor model. In: *SAE Technical Papers 2019-April (2019)*, apr, Nr. April. <http://dx.doi.org/10.4271/2019-01-1173>. – DOI 10.4271/2019-01-1173. – ISSN 01487191
- [112] LEHTINIEMI, Harry ; MAUSS, Fabian ; BALTHASAR, Michael ; MAGNUSSON, Ingemar: Modeling diesel spray ignition using detailed chemistry with a progress variable approach. In: *Combustion science and technology* 178 (2006), Nr. 10-11, 1977–1997. <http://dx.doi.org/10.1080/00102200600793148>. – DOI 10.1080/00102200600793148
- [113] MATRISCIANO, Andrea ; BORG, Anders ; PERLMAN, Cathleen ; LEHTINIEMI, Harry ; PASTERNAK, Michal ; MAUSS, Fabian: Soot Source Term Tabulation Strategy for Diesel Engine Simulations with SRM. In: *SAE Technical Papers 2015 (2015)*. <http://dx.doi.org/10.4271/2015-24-2400>. – DOI 10.4271/2015-24-2400. – ISSN 01487191
- [114] MAUSS, Fabian: *Entwicklung eines kinetischen Modells der Rußbildung mit schneller Polymerisation*. Göttingen, RWTH Aachen, Diss., 1998. <http://publications.rwth-aachen.de/record/55085>. – 186 S
- [115] PASTERNAK, Michal ; MAUSS, Fabian ; PERLMAN, Cathleen ; LEHTINIEMI, Harry: Aspects of 0D and 3D modeling of soot formation for diesel engines. In: *Combustion Science and Technology* Bd. 186, 2014. – ISSN 1563521X, S. 1517–1535
- [116] ADOLFO, Carlos ; PARRA, Finol: *Heat Transfer Investigations in a Modern Diesel Engine* Carlos Adolfo Finol Parra, University of Bath, Diss., 2008. <https://purehost.bath.ac.uk/ws/portalfiles/portal/187943792/thesis.pdf>
- [117] GERN, Maike S. ; KAUF, Georg M. ; VACCA, Antonino ; FRANKEN, Tim ; KULZER, André Casal: Ganzheitliche Methode zur Bewertung der Wassereinspritzung im Ottomotor. In: *Motortechnische Zeitschrift* 80 (2019), Nr. 7-8, S. 124–129. <http://dx.doi.org/10.1007/s35146-019-0070-x>. – DOI 10.1007/s35146-019-0070-x. – ISSN 0024-8525
- [118] CONVERGE CFD SOFTWARE: *CONVERGE Manual v2.4*. <https://convergecf.com/>. Version: 2018
- [119] O’ROURKE, Peter J. ; AMSDEN, A A.: A spray/wall interaction submodel for the KIVA-3 wall film model. In: *SAE transactions* (2000), S. 281–298. <http://dx.doi.org/https://doi.org/10.4271/2000-01-0271>. – DOI <https://doi.org/10.4271/2000-01-0271>
- [120] SCHMIDT, David P. ; RUTLAND, C J.: A new droplet collision algorithm. In: *Journal of Computational Physics* 164 (2000), Nr. 1, S. 62–80. <http://dx.doi.org/https://doi.org/10.1006/jcph.2000.6568>. – DOI <https://doi.org/10.1006/jcph.2000.6568>

- [121] AMSDEN, Anthony A. ; O'ROURKE, Peter J. ; BUTLER, T D.: *KIVA-II: A computer program for chemically reactive flows with sprays*. 1989
- [122] VESILIND, P.Aarne: The Rosin-Rammler particle size distribution. In: *Resource Recovery and Conservation* 5 (1980), Nr. 3, 275–277. [http://dx.doi.org/https://doi.org/10.1016/0304-3967\(80\)90007-4](http://dx.doi.org/https://doi.org/10.1016/0304-3967(80)90007-4). – DOI [https://doi.org/10.1016/0304-3967\(80\)90007-4](https://doi.org/10.1016/0304-3967(80)90007-4). – ISSN 0304–3967
- [123] REITZ, Rolf D.: Mechanism of breakup of round liquid jets. In: *Encyclopedia of fluid mechanics* 10 (1986)
- [124] POPE, S B.: *CEQ: A Fortran library to compute equilibrium compositions using Gibbs function continuation*. <https://tcg.mae.cornell.edu/CEQ/>. Version: 2003
- [125] POPE, Stephen B.: Gibbs function continuation for the stable computation of chemical equilibrium. In: *Combustion and Flame* 139 (2004), 222–226. <http://dx.doi.org/10.1016/j.combustflame.2004.07.008>. – DOI 10.1016/j.combustflame.2004.07.008
- [126] SENECA, P. K. ; POMRANING, E. ; RICHARDS, K. J. ; BRIGGS, T. E. ; CHOI, C. Y. ; MCDAVID, R. M. ; PATTERSON, M. A.: Multi-dimensional modeling of direct-injection diesel spray liquid length and flame lift-off length using cfd and parallel detailed chemistry. In: *SAE Technical Papers* (2003), Nr. 724. <http://dx.doi.org/10.4271/2003-01-1043>. – DOI 10.4271/2003–01–1043. – ISSN 26883627
- [127] HAN, Z. ; REITZ, R. D.: Turbulence Modeling of Internal Combustion Engines Using RNG κ - ϵ Models. In: *Combustion Science and Technology* 106 (2007), jan, Nr. 4-6, 267–295. <http://dx.doi.org/10.1080/00102209508907782>. – DOI 10.1080/00102209508907782. – ISSN 1563521X
- [128] HUBER, Marcia L. ; LEMMON, Eric W. ; BELL, Ian H. ; MCLINDEN, Mark O.: The NIST REFPROP Database for Highly Accurate Properties of Industrially Important Fluids. In: *Industrial and Engineering Chemistry Research* 61 (2022), oct, Nr. 42, 15449–15472. <http://dx.doi.org/10.1021/acs.iecr.2c01427>. – DOI 10.1021/acs.iecr.2c01427. – ISSN 15205045